Università degli Studi di Trieste

XXVIII Ciclo del Dottorato di Ricerca in Fisica

Solar modulation of cosmic ray electrons and positrons measured by the PAMELA experiment during the 23rd solar minimum

Settore scientifico-disciplinare: Fisica Sperimentale

Ph.D. program Coordinator:
Prof. Paolo Camerini

Ph.D. student:
Riccardo Munini

Thesis Supervisor:
Dott. Mirko Boezio

Thesis co-Supervisor:
Dott.ssa Anna Gregorio

Academic Year 2014/2015

Riccardo Munini: *Solar modulation of Cosmic Ray electrons and positrons measured by the PAMELA experiment during the 23rd solar minimum,* Phd thesis, © 2015.

E-MAIL:
Riccardo.Munini@ts.infn.it

Picture sideward: mount Montasio, group of Alpi Giuie, Friuli, Italia.

E su quelle montagne ritrovai il cammino per la conoscenza...

ABSTRACT

Cosmic rays (CRs) are energetic particles mainly originating outside the Solar System in extremely powerful environments like supernovae remnants (SNRs). The cosmic radiation is composed primarily of high-energy protons, helium and atomic nuclei while only a small fraction are electrons, anti-protons and positrons. During propagation through the Galaxy, CRs interact with the interstellar matter and the Galactic magnetic field. Because of these interactions CRs lose energy and change their spectral features with respect to the injection spectrum. Moreover, before reaching the Earth, CRs traverse the heliosphere, a region of space formed by the continuously outward expanding solar wind. Propagation inside the solar environment make the CR spectra decrease in intensity and vary with time following the 11-year solar cycle. During solar minimum the intensity of CRs on Earth is maximum; the situation reverses during solar maximum. Above 30 GeV the effects of solar modulation are negligible.

In this work a new measurement of the time dependent Galactic CR positron and electron energy spectra between 70 MeV and 50 GeV is presented. The analysis was conducted on data collected by the space borne PAMELA experiment during the period from July 2006 to January 2009. This was a period of intense solar minimum and negative solar magnetic field polarity. Long flight duration together with high proton rejection power make the PAMELA instrument the ideal apparatus for measuring the long-term variation of CR electrons and positrons. A total of seven spectra was obtained, each measures over six months period. This solution was a compromise between the time resolution and the statistics.

Precise measurement of the electron and positron spectra allows to test the numerical 3D models which describe the transport of charged particles through the heliosphere. The results discussed in this thesis are relevant since they provide long-term observation of electron and positron spectra improving both time resolution and statistical precision with respect to previous experiments. Moreover the measurement is performed down to 70 MeV, an energy region not achievable by other space-borne experiments able to perform charge sign separation like AMS-02. A big effort has been invested to achieve precise results below 200 MeV since a change in the spectral shape is expected from the propagation models. Finally, the simultaneous measure of the positron and electron spectra allow a comprehensive study of the charge-sign dependent modulation of CRs.

SOMMARIO

I raggi cosmici sono particelle cariche che si propagano attraverso lo spazio interstellare. Queste particelle vengono accelerate principalmente in siti estremamente energetici quali i resti di supernovae. L'89% della radiazione cosmica é composta da protoni, il 9% da particelle α mentre il restante 2% é costituito da nuclei via via piu' pesanti fino al ferro, da elettroni e in minima frazione da particelle di antimateria come antiprotoni e positroni. Nel loro viaggio attraverso la galassia i raggi cosmici interagiscono in vario modo con il mezzo e il campo magnetico interstellare perdendo energia e modificando la loro forma spettrale. Prima di raggiungere la terra essi inoltre attraversano l'eliosfera, una zona di spazio elissoidale formata dalla continua espansione radiale del vento solare. A seguito dell'interazione col vento e col campo magnetico solare il flusso dei raggi cosmici decresce rispetto a quello interstellare, fenomeno conosciuto come modulazione solare. In aggiunta l'intensitá del vento solare varia nel tempo seguendo il ciclo undecennale dell'attivitá solare e conseguentemente la modulazione dei raggi cosmici risulta dipendete dal tempo. Piu' precisamente durante i periodi di massimo dell'attivitá solare il flusso di raggi cosmici é al minimo mentre la situazione si ribalta durante i periodi di minimo. Ad alte energie > 30 GeV i raggi cosmici non risentono della modulazione solare e il flusso misurato sulla terra coincide con quello galattico.

Nel presente lavoro viene discussa una nuova misura della variazione temporale della componente di positroni ed elettroni della radiazione cosmica nell'intervallo di energia tra 70 MeV e 50 GeV. I dati utilizzati per condurre questo studio sono stati raccolti da PAMELA, rivelatore costruito per la misura della radiazione cosmica con particolare attenzione alla componente di antimateria. L'esperimento é posizionato a bordo del satellite Resurs DK1 in orbita attorno alla terra dal 15 giugno del 2006. I risultati presentati si riferiscono ai dati raccolti tra il luglio del 2006 e il gennaio del 2009, periodo temporale caratterizzato da un minimo dell'attivitá solare inconsueto sia per la sua bassa intensitá che per la sua lunga durata. La variazione temporale degli spettri di elettroni e positroni é stata misurata su base semestrale ottenendo un totale di sette flussi. Questa scelta é stata considerata il miglior compromesso per avere al tempo stesso una buona risoluzione temporale e una sufficiente statistica per la misura degli spettri.

L'analisi degli spettri di bassa energia dei raggi cosmici permette una accurata valutazione sperimentale dei parametri teorici che descrivono i meccanismi di propagazione delle particelle cariche nell'eliosfera rendendo inoltre possibile attraverso una procedura di demodulazione

interessanti valutazioni sugli spettri interstellari di bassa energia. La misura simultanea di elettroni e positroni consente infine di studiare la dipendenza della modulazione solare dal segno della carica della particella.

CONTENTS

LIST OF FIGURES

LIST OF TABLES

1 COSMIC RAY PROPAGATION

INDEX

Cosmic rays (CRs) are energetic charged particles, originating in outer space, that travel at nearly the speed of light and strike the Earth from all directions. The term CRs usually refers to Galactic CRs, which originate in sources outside the solar system, distributed throughout our Milky Way galaxy. Most of the CRs (about 89%) are hydrogen nuclei (protons), 9% are helium, and about 1% are heavier nuclei. CRs also include high energy electrons and positrons (less than 1%). Not surprisingly the cosmic radiation includes also antiparticles: they are produced in the interaction between cosmic rays and the interstellar matter. Furthermore, novel sources of primary cosmic-ray antiparticles of either astrophysical (e.g. positrons from pulsars) or exotic origin (e.g. annihilation of dark matter (DM) particles) may exist.

Before being detected on Earth, CRs propagate first through the interstellar space and then through the heliosphere[1]. As CRs enter and travel through our heliosphere, they are affected by various modulation processes causing them to lose energy and decrease in intensity before reaching Earth. These effects are especially significant for low energy ($\lesssim$ 30 GeV) CRs. This chapter is devoted to a general discussion of the CR electron and positron propagation through the interplanetary space. Furthermore the main aspects concerning the acceleration at the source and the propagation through interstellar space are discussed.

1 The region of space surrounding our solar system which is formed by the outward expanding solar wind, see 1.5

1.1 COSMIC-RAY ELECTRONS AND POSITRONS

CR electrons are the most abundant negatively charged particle of the cosmic radiation. Their intensity is about 1% of the protons at 10 GeV and decreases to about 0.1% at 1 TeV. Positron intensity is even smaller being roughly 10% of the electron intensity up to a few tens of GeV (see Figure 1.1). Electrons in CRs, because of their low mass and leptonic nature, have unique features, complementary to the other CR components. CR electrons experience different types of energy loss as they travel through interstellar space. Above a few GeV electrons undergo severe energy loss through synchrotron radiation in the magnetic field and inverse Compton scattering with the ambient photons (microwave background). Electrons and positrons are also good candidates to test the propagation model of charged particles inside the heliosphere. Before an exhaustive discussion about cosmic-ray transport in the interplanetary space, a brief introduction about the main features of galactic CRs, the production sites and the propagation through interstellar space, is presented.

1.2 ELECTRON AND POSITRON SOURCES

CR electrons were known to exist long before their direct discovery. Radio astronomers observed the synchrotron radiation from relativistic electrons in such places as supernovae envelopes and other galaxies. The first detection of CR electrons was achieved by Earl [1961] performing a 12 hour high altitude balloon flight with a lead multi-plate cloud chamber. Figure 1.2 shows the shower produced by the first CR electron detected by Earl. He obtained the electron flux above 0.5 GeV and derived the ratio of the electron to the proton flux to be $3 \pm 1\%$. Measurements performed by Earl and other pioneering experiments [Anand et al., 1968; Daniel and Stephen, 1965] were not able to separate electrons from positrons and suffered large systematic uncertainties.

Ginzburg [1958] had already pointed out that a measurement of the charge composition of the electron component of primary CRs would have been crucial in determining the source of the CR electrons. Charge electron–positron separation could be accomplished by measuring the curvature of the incoming particles within a suitable magnetic field. De Shong et al. [1964] developed an instrument made of a permanent magnet, optical spark chambers as track detectors and shower spark chambers. They performed a balloon flight providing the first experimental evidence on the positron fraction $e^+/(e^- + e^+)$, showing that this was much smaller than would have been expected if the electrons originated predominantly from nuclear collisions in interstellar space.

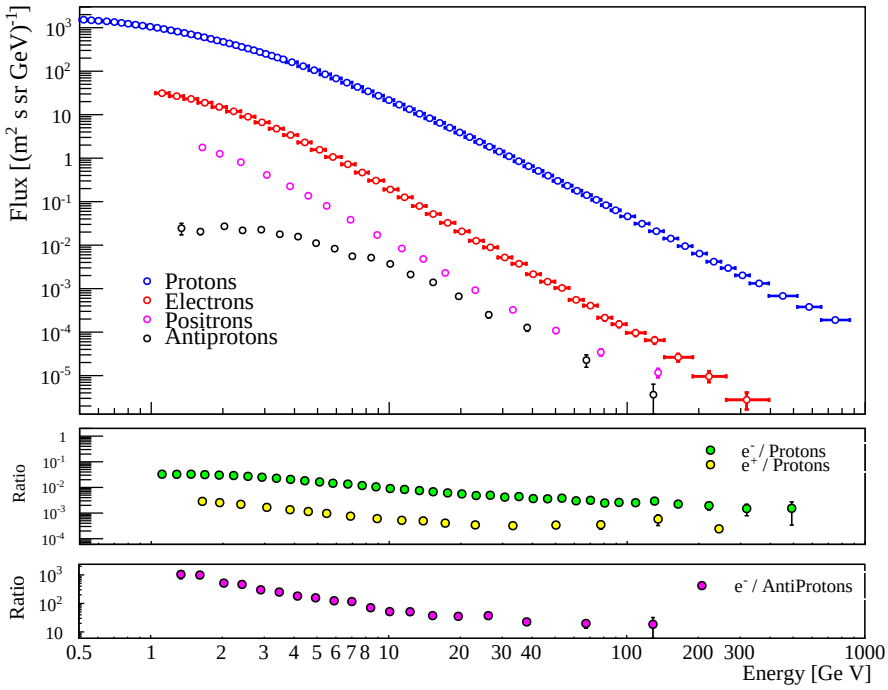

Figure 1.1: Top panel: CR electron [Adriani et al., 2011a], positron [Adriani et al., 2013a], proton [Adriani et al., 2011c] and anti-proton [Adriani et al., 2010] energy spectra measured by the PAMELA experiment. Middle panel: electrons and positron ratio with respect to proton flux. Bottom panel: electron to anti-proton ratio. The error bars are the quadratic sum of the statistical and systematic errors. If not visible, they lie inside the data points.

Their work led to the conclusion that a major portion of the CR electrons must be of primary origin, directly accelerated in sources of CRs. In the following years the CR electrons and positrons were measured by many balloon-borne experiments like TS93 [Golden et al., 1996], HEAT (1994-95) [Barwick et al., 1997] and CAPRICE (1994-98) [Boezio et al., 2000]. Furthermore the AMS-01 [Alcaraz et al., 2000] team in a ten day flight on board the Space Shuttle was the first antimatter experiment outside the atmosphere using a very large magnetic spectrometer (1998). For a more detailed review about the electron and positron measurements see [Picozza and Marcelli, 2014; Yoshida, 2008].

All the experimental observations led to the conclusion that CR electrons are predominantly of primary origin. It was already noticed in the thirties by Baade and Zwicky [1934] and in the early sixties by Ginzburg and Syrovatskii [1964] that energy arguments favored supernovae remnants (SNRs) as possible CR accelerators.

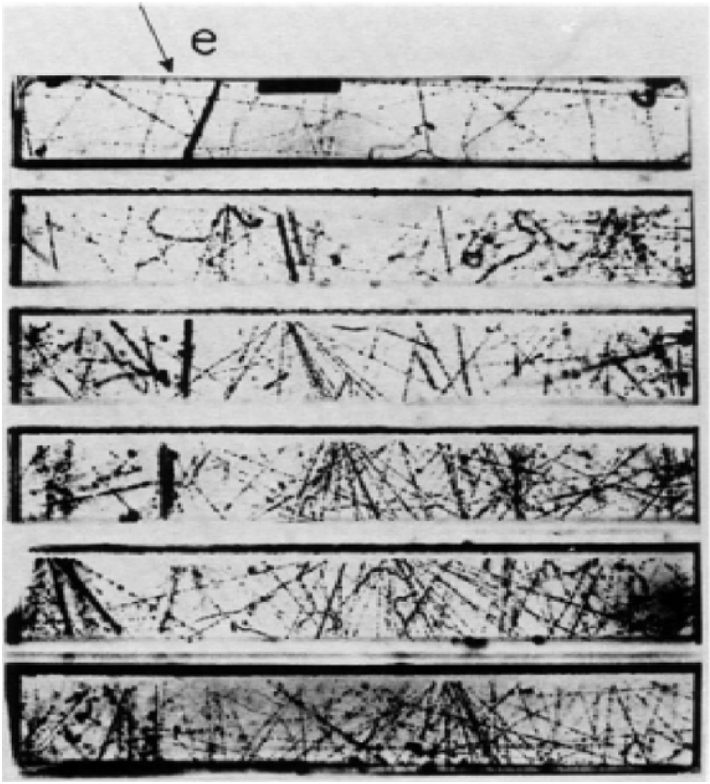

Figure 1.2: A cloud-chamber picture of a shower produced by a high-energy electron from [Earl, 1961].

There are large uncertainties in these numbers, but it appears plausible that an efficiency of a few per cent would be enough for SNRs to energize all the Galactic CRs and account for their observed energy density $\rho_{CR} \sim 1\ \mathrm{eV/cm^3}$. Evidence for synchrotron X-ray emission from several supernova remnant such as Cassiopeia A [Rothschild et al., 1997] strongly supports the hypothesis that primary Galactic CR electrons originate in SNRs. On the contrary positrons were assumed to have a purely secondary origin. In fact both electrons and positrons CR are created from the interactions of hadronic CR species (mainly protons and α particles) with the interstellar material (hydrogen and helium) as the end product of the decay of short-lived particles produced in these interactions, i.e. $\pi^{\pm} \to \mu^{\pm} \to e^{\pm}$ or $K^{\pm} \to \mu^{\pm} \to e^{\pm}$. In this case they are referred to as secondary CRs. Since these processes involve positively charged particles, charge conservation implies that more positrons are generated than electrons. Figure 1.3 shows the results for the secondary electron (left panel) and positron (right panel) fluxes at the Earth from a model by Delahaye, T. et al. [2010] where a slight excess of positrons can be noticed. The yellow band is the flux

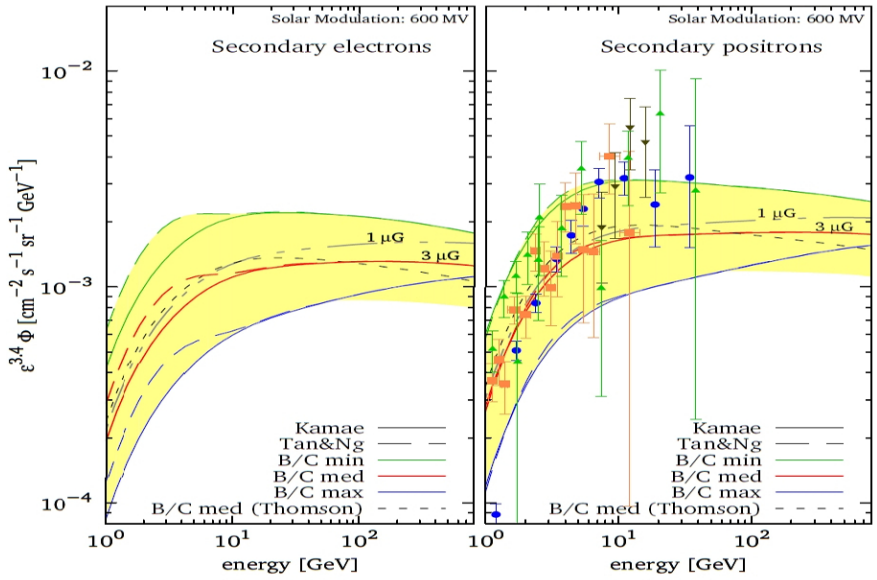

Figure 1.3: Flux predictions of secondary electrons (left) and positrons (right) at the Earth [Delahaye, T. et al., 2010]. The black solid and dashed lines are obtained by considering a relativistic treatment of energy losses (Klein-Nishina, see Section 1.4) and alternative parameterizations of the nuclear cross-sections, respectively from [Kamae et al., 2006] and [Tan and Ng, 1983]. The yellow band is the flux range available for all sets of different propagation parameters (MIN-MED-MAX model, see footnote) compatible with boron/carbon ratio constraints derived in [Maurin et al., 2001]. The small-dashed curves are the predictions calculated in the MED configuration and the Thomson limit for the energy losses (see Equation 1.3). A slight excess of positrons is present. The secondary positron predictions are compared with various experimental measurements. Above 10 GeV an excess of positrons seems to appear with respect to pure secondary production (see text).

range available for all sets of different propagation parameters (MIN-MED-MAX model[2]).

Standard production models consider only secondary positrons. However already the experimental observations discussed above hinted to the presence of a positron excess with respect to a purely secondary production (see also Figure 1.3). The PAMELA magnetic spectrometer, launched in June 2006 on board of a Russian satellite, definitively confirmed this. One of the most interesting outcomes from PAMELA

2 A full scan of the experimental parameter space (e.g. diffusion coefficients) is usually required to estimate uncertainties due to propagation and compare the model predictions to the experimental data. For this reason is very convenient to isolate three sets of the various parameters which, considering the uncertainties, include the lower (MIN) the (MED) and the upper (MAX) values of the parameters.

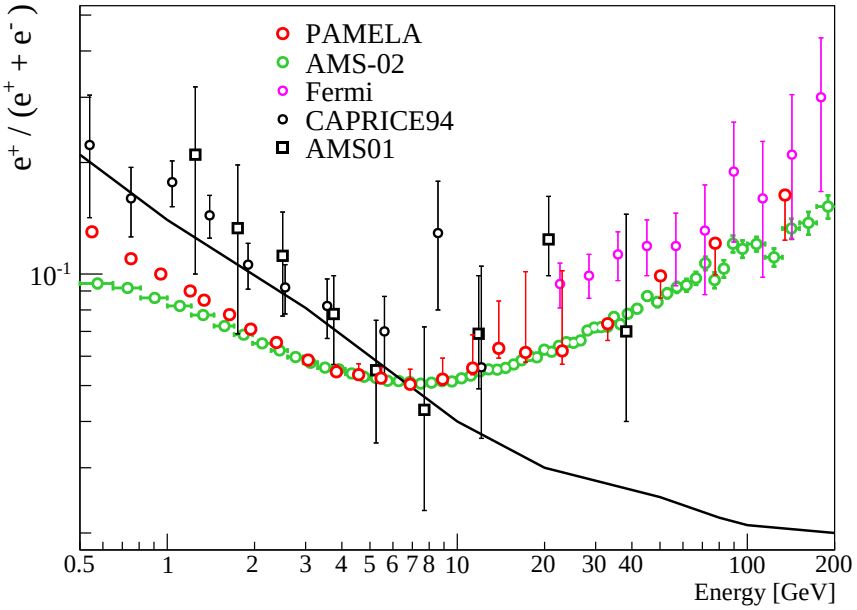

Figure 1.4: Positron fraction data from balloon-borne and satellite experiments. The solid line shows a calculation for pure secondary positron production [Moskalenko and Strong, 1998]. The PAMELA and AMS02 results perfectly agree above ~ 3 GeV. Below this energy the effect of the charge-sign dependence (see Section 1.6) due to solar modulation makes the positron fraction change with time (see Section 1.9).

was the result on the positron fraction [Adriani et al., 2009a]. A clear increase above 10 GeV up to 200 GeV with respect to a pure secondary positron production appeared in the $e^+/(e^- + e^+)$ data, see Figure 1.4. This result was confirmed by the magnetic spectrometer AMS02 on board of the international space station [Accardo et al., 2014] which collected much more statistics with respect to PAMELA. The AMS02 results on the positron fraction are shown by the green points in Figure 1.4, togheter with the results provided by AMS01 [Alcaraz et al., 2000], CAPRICE94 [Boezio et al., 2000] and FERMI [Ackermann et al., 2012]. The PAMELA result on positron fraction has led to many speculations about a primary origin for the positrons.

DARK MATTER AND PULSARS

Discrepancies between measurements and expectations from secondary production of positrons may be indications of potential tracers for new physics, in particular the annihilation of dark matter (DM). Many parti-

cle candidates have been proposed for the dark matter component. The most widely studied are the neutralino from supersymmetric models (e.g. [Kamionkowski et al., 1996]) and the lightest Kaluza Klein particle from extra dimension models (e.g. [Cheng et al., 2002]). The gravitino (e.g. [Buchmüller et al., 2007]) is also an interesting candidate.

However, for example, the interpretation of the PAMELA positron excess in terms of neutralino annihilation is challenged by the asymmetry between the leptonic (positron) and hadronic (antiproton) PAMELA data. The anti-proton spectrum is consistent with secondary production models. Such an asymmetry is difficult to explain in a framework where the neutralino is the dominant DM component. A suitable explanation requires a very high mass neutralino, which is unlikely in the context of allowed supersymmetry models. Better descriptions are obtained for supersymmetric models with purely leptonic annihilation channels for a wide range of the WIMP mass [Cirelli et al., 2009].

Additionaly many authors proposed that pulsars might be associated with the production of primary CR positrons and electrons, e.g. [Serpico, 2012]. Young pulsars are well known particle accelerators. Primary electrons are accelerated in the magnetosphere of pulsars at the polar cap and in the outer gap along the magnetic field lines emitting gamma rays by synchrotron radiation. In the presence of the pulsar magnetic field, these gamma rays can produce positron and electron pairs which can contribute to the high-energy electron and positron CRs.

A reliable model for CR origins able to reproduce the primary energy spectrum is essential to make comparison with the experimental data and search for possible exotic CR component like DM annihilation. Simple CR acceleration and propagation model was already formulated in the late forties-early fifties and are discussed in the next section.

1.3 ACCELERATION MECHANISMS

In 1949 Fermi proposed an acceleration mechanism for relativistic particles in space by means of their collision with interstellar clouds which acted as "magnetic mirrors" [Fermi, 1949]. Particles gained energies in head-on collision with clouds and lost it in a following collision. Fermi showed that on average the particles gained energy in these reflections. In its model the average energy gain is proportional to $(\frac{v}{c})^2$, where v was the velocity of the particle and c the speed of light. This mechanism is referred to as second order Fermi acceleration. Fermi was searching for an acceleration mechanism able to reproduce the spectral features observed in the CR energy spectrum. Nowadays is well known that

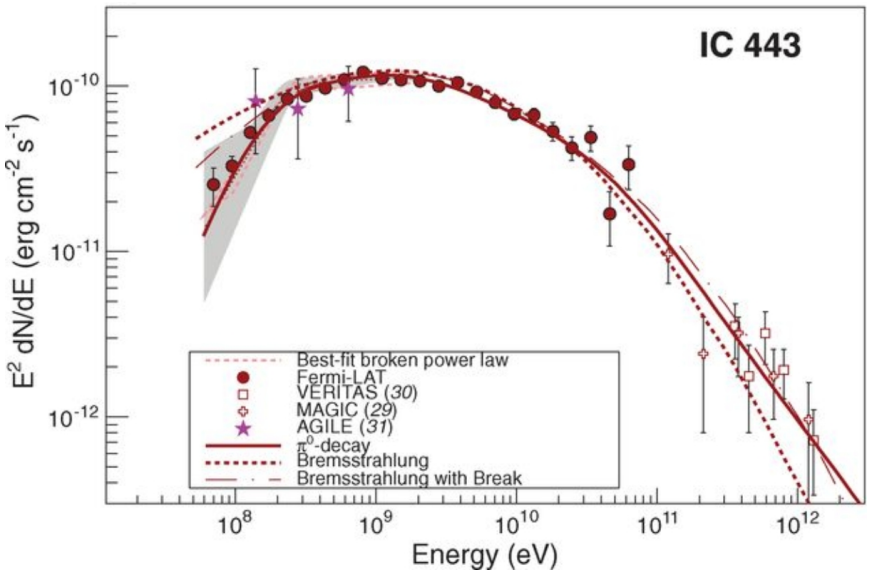

Figure 1.5: Gamma-ray spectrum of SNR IC443 as measured with the Fermi LAT together with MAGIC and VERITAS data [Ackermann et al., 2013]. Gray-shaded bands show systematic errors. Solid lines denote the best-fit pion-decay gamma-ray spectra, dashed lines the best-fit with different models for the emission of bremsstrahlung photons by electrons (see Section A.1).

above 1 GeV the differential energy spectra of the various CR species can be well represented by a power-law distribution as illustrated in Figure 1.1. The spectra are conventionally written:

$$\frac{dN(E)}{dE} = KE^{-\gamma} \tag{1.1}$$

The spectral index γ usually lies in the range roughly $2.2 - 3.0$ depending on the particle type. The second-order Fermi acceleration seemed promising since the resulting energy spectrum turns out to be a power law. Nevertheless, even though second-order acceleration succeeds in generating a power-law spectrum, it is not a completely satisfactory mechanism. First, the random velocities of clouds are relatively small and thus the energy gain is very slow. Second, the theory does not predict the power law exponent.

The mechanism would be much more efficient if there were only head on collisions. This set-up occurs when the relativistic particles collide with strong shock waves, like those produced in supernova explosions. During the diffusive shock acceleration particles bounce back and forth in the upstream and downstream regions and always approach the plasma having head-on collisions. The gain in energy is now proportional to $(\frac{v}{c})$ and is called first order Fermi acceleration. This mechanism accelerates CRs up to energy of $10^{15} - 10^{16}$ eV, the so

called Galactic component. Above 10^{16} eV most of CRs are expected to be of extragalactic origin since their gyro-radius becomes greater than the size of the Galaxy and they cannot be confined in the Milky Way. Possible sources of extragalactic CRs are active galactic nuclei (AGN), gamma ray bursts (GRBs) or pulsars [Fang et al., 2013; Hillas, 2006].

In the last decades the experimental measurements led to an impressive rate of discoveries and more complex and sophisticated models for CR acceleration have been proposed. SNRs remain the most plausible sources of Galactic CR where phenomena like magnetic field amplification at the shock are considered while time escape from the sources becomes a crucial step to determine the spectrum of CRs. Also the phenomenon of CR acceleration at shocks propagating in partially ionized media and the implications of this in terms of width of the Balmer line emission has been analyzed. This field of research has recently experienced a remarkable growth. For a complete review of the newest development of CR acceleration models see [Blasi, 2013].

Many experimental observations point to CR acceleration in SNRs. Figure 1.5 shows the gamma-ray spectrum of SNR IC443 as measured with the Fermi LAT apparatus [Ackermann et al., 2013]. When accelerated protons at the shock front encounter interstellar material, they produce neutral pions, which in turn decay into gamma rays. Focusing on the sub-GeV part of the gamma-ray spectrum, the best-fit is provided by a π^0 decay model (thw model which considered the bremsstrahlung photon emission from energetic electrons does not fit the observed gamma-ray spectra). In particular the prominent peak near 1 GeV and the steep fall below few hundreds of MeV is interpreted as an indication for the π^0-decay origin of the gamma-ray emission [Giuliani et al., 2011]. This measure provides direct evidence that CR hadrons are accelerated in SNRs.

The diffusive shock acceleration model predicts $\gamma = 2$ for the power law spectral index of Equation 1.1. The predicted exponent is slightly different from the value of $\gamma \sim -3.0$ obtained from the differential energy spectrum observed at Earth[3]. Howewer between the emission and the detection at Earth the CRs propagate through the interstellar space changing their spectral features.

3 The observed spectral index of electrons is $\gamma \sim -3.0$, steeper than the protons $\gamma \sim -2.7$. The different spectral index reflects different energy losses during propagation.

1.4 PROPAGATION IN INTERSTELLAR SPACE

In the diffusion model the propagation of electrons can be expressed in terms of the usual current conservation equation [Berezinskii et al., 1990]:

$$\underbrace{\frac{dN(E,x,t)}{dt}}_{a} - \underbrace{\frac{\partial}{\partial E}\{\frac{dE}{dt}N(E,x,t)\}}_{b} - \underbrace{\nabla\{D(E)\nabla N(E,x,t)\}}_{c} = \underbrace{Q(E,x,t)}_{d} \quad (1.2)$$

Here $N(E,x,t)$ is the density of electrons per unit of energy. The physical transport and modulation mechanisms contained in Equation 1.2 are:

- (a) the time-dependent change in the CR distribution function.
- (b) the energy loss term. Above $\sim$ 10 GeV electrons lose energy mainly by synchrotron radiation in the Galactic magnetic field and inverse Compton scattering with the interstellar photons in the Galaxy. The energy loss rate in the Thomson approximation that holds for electrons very well up to energies around a few tens of GeV is given by:

  $$\frac{dE}{dt} = -b(E)E^2 \quad \text{with} \quad b(E) = -\frac{4}{3}\frac{\sigma_T c}{(m_e c^2)^2}(\rho_{ph} + \frac{B^2}{8\pi}) \quad (1.3)$$

  For higher energy the Klein-Nishina fully relativistic model is considered. Here, E is the electron energy, m_e is the mass of electron, c is the speed of light, B is the magnetic field strength in the Galaxy, ρ_{ph} is the energy density of interstellar photons, and σ_T is the Thomson cross section. As derived from Eq. 1.3 electrons lose almost all of their energy after a time:

  $$T(E) = \frac{1}{b(E)E} \quad (1.4)$$

  thus the electron lifetime becomes progressively shorter with increasing energy.

- (c) the diffusion in random magnetic fields that account for the high CR isotropy and relatively long confinement time in the Galaxy. For the diffusion coefficient $D(E)$ a widely adopted expression is [Panov, 2013]:

  $$D(E) = D_0(E/TeV)^{\delta} \quad \text{with} \quad D_0 = (2 \div 5)10^{29}\text{cm}^2\text{s}^{-1} \quad (1.5)$$

  where $\delta = 0.3 \div 0.6$. In a diffusive propagation model, the diffusion coefficient determines the average travel distance of electrons in a given time:

  $$R(E) = \sqrt{2D(E)T(E)} \quad (1.6)$$

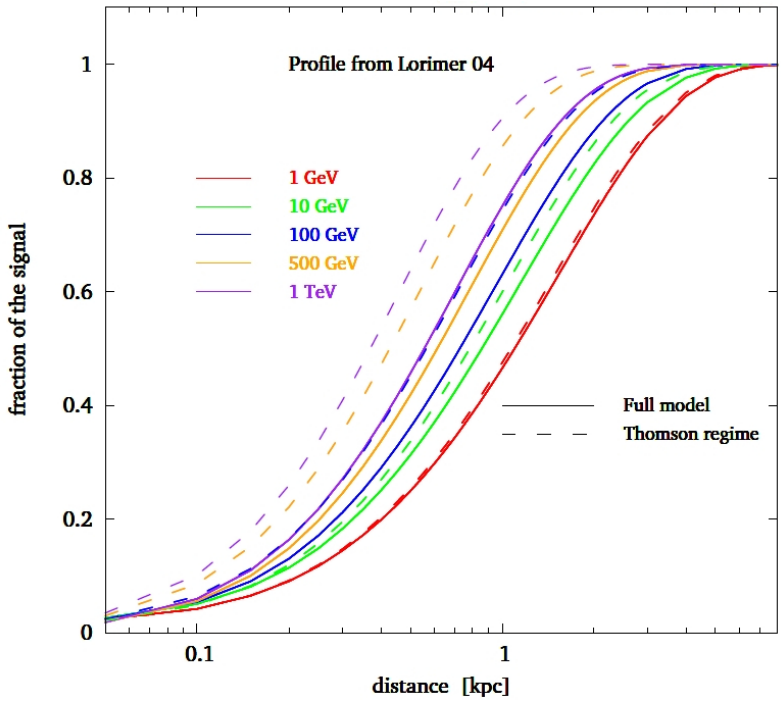

Figure 1.6: Fraction of the electron signal reaching the Earth as a function of the integrated radius [Delahaye, T. et al., 2010]. The Thomson approximation is shown by the dashed line, the solid line represents a different approximation regime for energy losses (fully relativistic Klein-Nishina).

Assuming $B_\perp = 5\mu G$ [4] and taking the Klein-Nishina formula for the Compton process, the lifetime is $T(E) = 2.5 \cdot 10^5 (\text{years})/E$ (TeV). This result implies a short range propagation for high energy electrons, $R(1\text{TeV}) \sim 1.5$ kpc [5]. Thus, TeV electrons detected at Earth are mostly produced by sources in the neighborhood of the solar system within 1 kpc. Fig. 1.6 shows the cumulative fraction of the electron signal received at Earth as a function of the radial integration distance for various energies. Above 1 TeV, the propagation lifetime is so short that only a few nearby CR electron sources can contribute and thus features in the spectral shape are expected [Kobayashi et al., 2004].

- (d) the electron source strength $Q(E, x, t)$ (SNRs in the case of electrons).

4 The local magnetic field strength is derived using the radio synchrotron emission from relativistic electrons. $B_\perp$ means the magnetic field perpendicular to the electron velocity, that is $B_\perp^2 = 2B^2/3$.

5 One parsec (pc) corresponds to approximately 3.26 light-years or $3.09 \cdot 10^{16}$ m.

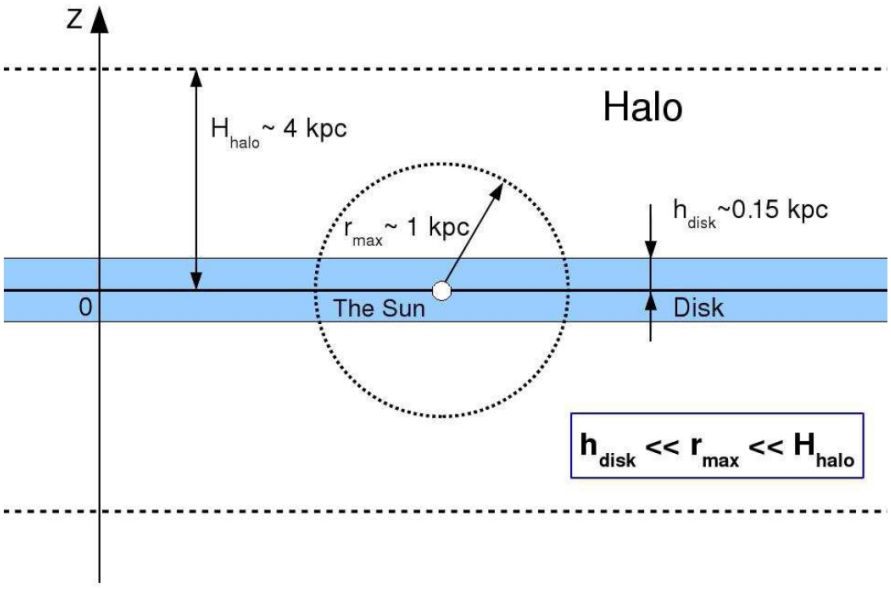

Figure 1.7: The geometry of the Galactic disk and diffusion halo in the "thin disk approximation" [Panov, 2013].

It is useful now to resolve analytically the current conservation equation to show how the experimental observations can be formally linked to the propagation mechanisms.

THIN DISK APPROXIMATION

A simplified solution can be obtained with the so called "thin disk approximation", a model in which the Galactic disk is infinitely thin and homogeneous together with an infinitely thick Galactic halo (see [Panov, 2013] for more details).

As illustrated in Figure 1.7 the half-depth of the diffusion Galatic halo is ~ 4 kpc which, for 1 TeV electrons, is larger than the expected diffusion electron range $R_{max} \sim 1$ kpc. One can assume that the propagation scale is short enough to neglect the vertical boundary condition and thus the depth of the halo may be considered as infinitely large. At the same time, the half-depth of the Galactic disk, at the position of the Sun, is only about 150 pc which is much smaller than R_{max}. The source of electrons located within the Galatic disk, may be considered to be infinitely thin relative to the value of R_{max}. Since the Sun is located very close to the Galatic plane the flux of electrons calculated exactly for $z = 0$, is a reasonable approximation. The source spectrum is assumed

to be mere power law of index γ, constant with time, and distributed homogeneously at $z = 0$ in the infinitely thin plane:

$$Q(x, t, E) = Q_0 E^{-\gamma} \delta(z) \tag{1.7}$$

Given this source term, the solution of the transport Equation 1.2 for $z = 0$, with the diffusion coefficient defined in Equation 1.5, predict the observed spectrum at Earth to be:

$$N(E)\,|_{z=0} = Q_0 E^{-\gamma^*} \quad \text{with} \quad \gamma^* = \gamma + \Delta, \quad \Delta = \delta + \frac{1}{2} \tag{1.8}$$

Therefore, instead of the source spectrum with the index γ, an observer measures the electron spectrum steeper by $\Delta = \delta + \frac{1}{2}$ at Earth. A value of $0.3 < \delta < 0.6$ lead to $\Delta \approx 1$ and the predicted value of the observed spectral index is $\gamma^* \approx 3$. Although a very useful approximation, this spectral analysis is only valid for a smooth and flat distribution of source(s), and significantly differs when local discrete effects are taken into consideration. A more complete solution of the transport equation has been performed considering a more realistic source distribution (e.g. see [Delahaye, T. et al., 2010; GALPROP]).

The CR propagation mechanisms through interplanetary space can be described with a mathematical approach very similar to Equation 1.2. The basic CR transport equation through the heliosphere was derived by Parker in 1965. Before discussing the physical processes described in the Parker equation is important to touch briefly upon the key features of the Sun that are relevant to the propagation of CRs in our Solar System.

1.5 SOLAR ENVIRONMENT

The possibility of performing in-situ measurements make the interplanetary medium the ideal environment in which to test the theory of propagation of charged particles in magnetic fields under conditions which approximate typical cosmic condition. A wealth of information about the structure of the Sun has been gained through the use of many sophisticated observations and analysis techniques.

THE SUN

The Sun is situated near the Orion spiral arm at the outer reaches of the Milky Way Galaxy and is classified as a G-type main-sequence star, informally referred to as a yellow dwarf. With a mass of $2 \cdot 10^{30}$ kg, the Sun accounts for about 98.6% of the total mass of the Solar System.

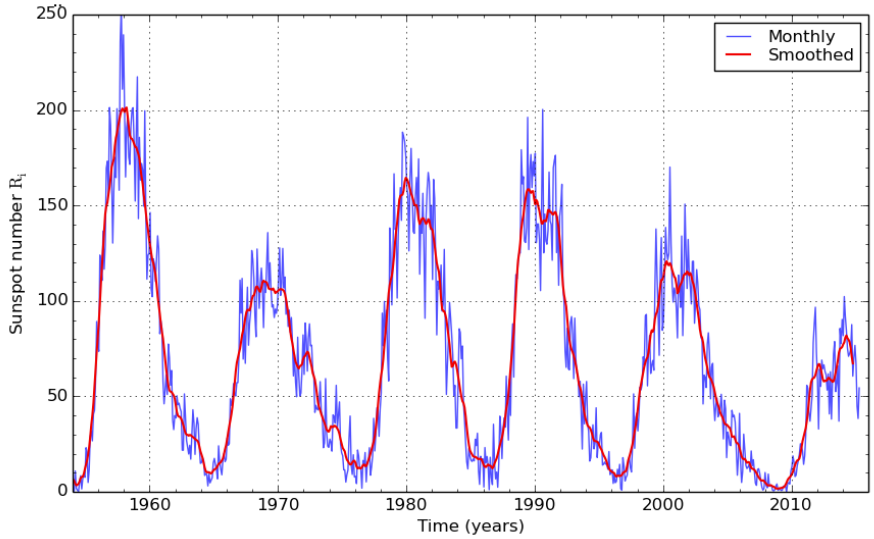

Figure 1.8: Monthly mean number of sunspots from 1950 to 2015. Picture taken from http://sidc.oma.be/.

Hydrogen and helium accounts for about 75% and 23% of the Sun mass, respectively. The residual 2% consists of heavy nuclei.

The Sun has a radius of about $7 \cdot 10^5$ km and can be divided in several regions. The core extends from the center to about 20–25% of the solar radius and is the region where the thermonuclear reactions, which generate the power, take place. The radiative zone, where thermal radiation is the primary means of energy transfer, extend from the core out to about 0.7 solar radii. Inside the convective zone, which extends up to $2 \cdot 10^5$ km below the Sun surface, convective currents dominate the heat transfer. The internal convective motion generates the Sun's magnetic field via a dynamo process [Charbonneau, 2014]. The Sun magnetic field is similar to that of a typical magnetic dipole with the Northern and Southern hemispheres having opposite polarities. Above the convective zone the thin layer called the photosphere defines the surface of the Sun. This region has a temperature of about 5800 K as deduced from the absorption lines observed in the solar spectrum. The next layer of the Sun, the corona, is a region in which the temperature increases to millions of kelvin. The Sun's corona extends millions of kilometers into space and is most easily seen during a total solar eclipse. Although a fraction of the coronal heating is known to be from magnetic reconnection [Erdélyi and Ballai, 2007], the entire mechanism is still unclear.

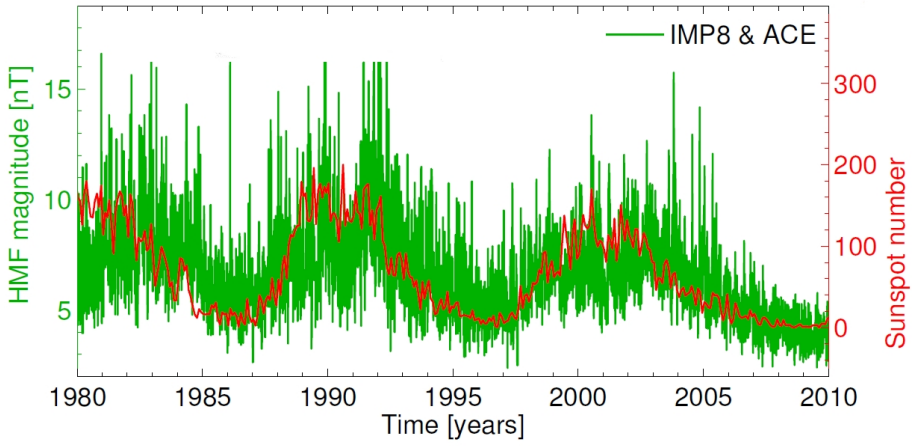

Figure 1.9: The correlation between the sunspot number (red line) and the Sun magnetic field (green line) as measured by IMP8 and ACE. Data obtained from http://nssdc.gsfc.nasa.gov/.

SOLAR ACTIVITY

The solar cycle is the periodic change in the Sun's activity. The longest recorded feature of solar variations are changes in sunspot number. Sunspots are temporary phenomena on the Sun photosphere caused by intense magnetic activity which inhibits convection, forming areas of reduced surface temperature. Sunspots have been observed for hundreds of years. Figure 1.8 shows the monthly average sunspot number from 1950 to 2015 from which is clearly visible a periodic variation with an average duration of about 11 years. The sunspots number is one of the many solar activity indexes and fluctuates between successive maxima and minima, referred to as solar maximum and minimum.

Hale and Nicholson [1925] first reveled that the solar polarity also has a periodic variation with a 22-year periodicity. After every 11-year cycle, the solar magnetic field undergoes a polarity reversal. However, because the vast majority of the manifestations of the solar cycle are insensitive to magnetic polarity, it remains common usage to speak of the "11-year solar cycle". When the solar magnetic field points outward in the Northern hemisphere and inward in the Southern hemisphere, the Sun is said to be in a positive polarity cycle [6], $A > 0$. The opposite situation is referred to as a negative polarity cycle, $A < 0$. In addition, the magnetic field magnitude also shows a periodic fluctuating pattern that correlates with the sunspot number counts. The solar magnetic field is significantly weaker during solar minimum conditions, with an

6 In the complex sun magnetic field the dipole term nearly always dominates the magnetic field of the solar wind. A is defined as the projection of this dipole on the solar rotation axis.

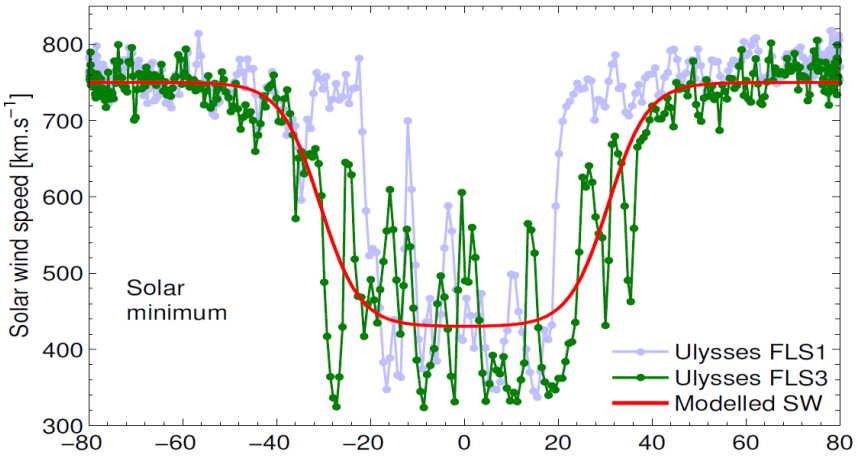

Figure 1.10: The latitudinal dependence of the SW speed at solar minimum measure with the Ulysses spacecraft during two different fast latitudinal scans (FLS) between 1994 and 1995. The red curve represents the assumed SW profile that gives the best fit with Equation 1.9. Data obtained from http://cohoweb.gsfc.nasa.gov/. Figure adapted from [Etienne, 2011].

average magnitude of 5 nT, compared to solar maximum conditions with magnitudes about 10 nT. Figure 1.9 shows a plot of the heliospheric magnetic field (HMF) magnitude from 1980 to 2010 overlaid with the sunspots number. During the solar minimum condition, the Sun's global magnetic field has its simplest form, contrarily during solar maximum the magnetic field tends to assume a chaotic structure. The total solar irradiance as well as many other physical processes are also correlated to changes in the solar activity. The solar wind is one of them.

THE SOLAR WIND

In 1958 Parker presented his theory and predicted the existence of an outflow of material from the corona region of the Sun that was named the solar wind (SW) [Parker, 1958]. In January 1959, the Soviet satellite Luna 1 directly observed the solar wind and measured its strength [LUNA1]. The existence of the SW is ascribed to a difference in pressure between the corona and the interstellar medium. This leads to the corona emitting a continuous stream of ionized gas moving at supersonic velocity. It consists of mostly electrons, protons and alpha particles with energies usually between 1.5 and 10 keV. Since the solar wind is coupled with the corona this structure depends upon the magnetic field configuration present in the corona. During solar minimum conditions the Sun's magnetic field has a simple structure divided in

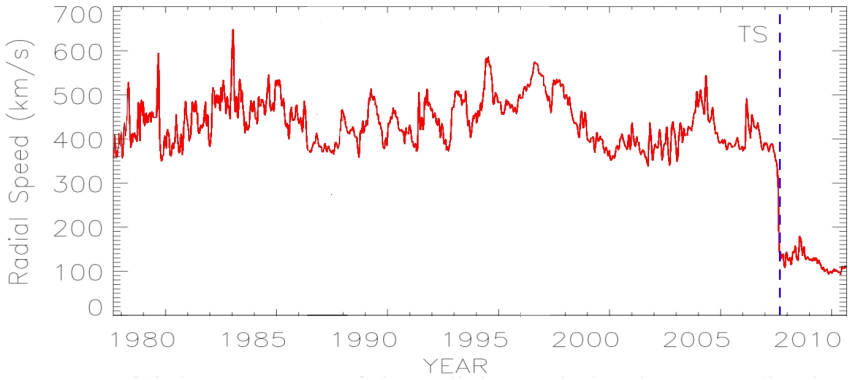

Figure 1.11: The radial solar wind speed as a function of time measured by Voyager 2. The sudden decrease in 2007 correspond to the termination shock crossing approximately at 84 AU from the Sun. Picture from ftp://space.mit.edu/pub/plasma/publications/jdr_burlaga_issi/jdr_burlaga_issi.pdf.

regions with open and closed field lines. Closed field lines are found near the equator. They are perpendicular to the solar wind direction and inhibit its outflow. This component is referred as the slow solar wind with typical velocities of 400 km/s. Conversely, the fast solar wind is thought to originate from coronal holes, which are funnel-like regions of open field lines in the Sun's magnetic field. Such open lines are particularly prevalent around the Sun's magnetic poles. Typical velocities of the SW in these regions are about 800 km/s. The existence of these latitudinal dependence in the SW speed has been confirmed by the Ulysses spacecraft, e.g. [Phillips et al., 1995]. Figure 1.10 shown the solar wind velocity pattern during solar minima measure with the Ulysses spacecraft during two fast latitudinal scans (FLS) between 1994 and 1995. For solar minima the outward directed SW velocity can be parametrize as:

$$\mathbf{V}^{*}_{sw}(r,\theta) = V_0 V_r(r) V_\theta(\theta)\mathbf{e}_r \tag{1.9}$$

where $\mathbf{e}_r$ is a unit vector in the radial direction, r is the radial distance from the Sun, $V_0 = 400$ Km/s. Here it is assumed that the radial $V_r(r)$ and latitudinal $V_\theta(\theta)$ dependencies are independent of each other. The characteristic SW latitude dependence for solar minimum conditions is represented by the red curve in Figure 1.11. Concerning the radial SW speed dependence, Sheeley et al. [1997] found that the SW, across all latitudes, accelerates within 0.1 AU from the Sun, after which it becomes a steady flow at 0.3 AU till the transition shock where the solar wind speed suddenly decreases. Figure 1.10 shows the solar wind speed measured by Voyager 2 as a function of time (or equivalently the radial distance from the Sun). For more detail about the radial and latitudinal dependence of the SW see [Etienne, 2011].

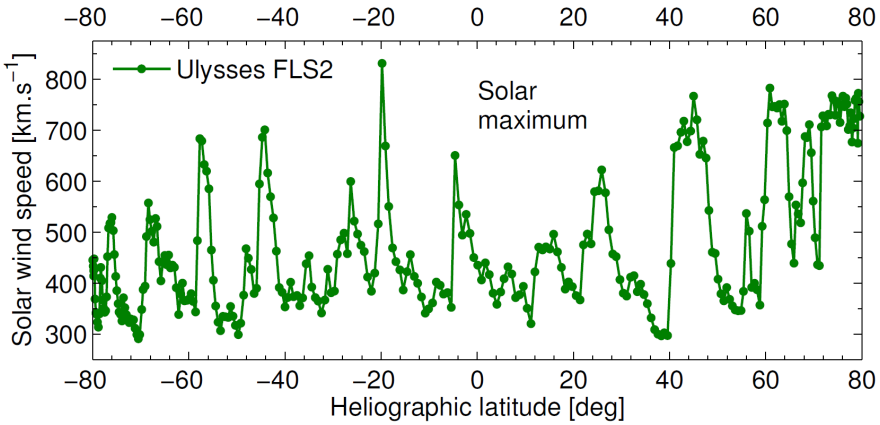

Figure 1.12: The latitudinal dependence of the SW speed at solar maximum measure with the Ulysses spacecraft during a fast latitudinal scans (FLS) between 1994 and 1995. Data obtained from http://cohoweb.gsfc.nasa.gov/. Figure adapted from [Etienne, 2011].

Contrarily to the solar minima periods, during solar maxima, there appears to be a mixture of fast and slow SW streams so that no well-defined speed profile is visible, as can be seen in Figure 1.12 which shown the solar wind velocity pattern during solar maxima measure with the Ulysses spacecraft during a the FLS between 1994 and 1995.

HELIOSPHERE STRUCTURE

The outward expanding solar wind encounters and interacts with the interstellar medium (ISM) to form a region which defines the boundary between the SW plasma and the ISM, the heliopause (HP). At this boundary the solar wind merges with the surrounding local interstellar medium. This bubble-like region of space occupied by the outward flowing of solar wind is called the heliosphere. Figure 1.13 shows a magnetohydrodynamic simulation of the heliosphere structure showing the temperature of the solar wind plasma. At a heliocentric distance between 70 and 100 AU where the solar wind pressure equals the external thermal pressure of the interstellar medium the solar wind slows down to subsonic speed forming a shock called the termination shock (TS). An important goal of the two Voyager spacecrafts has always been to observe the TS and HP. In 2004 at 94 AU Voyager 1 measured a sudden decrease in the solar wind speed which corresponded to the Sun's termination shock crossing, followed by Voyager 2 in 2007 at 84 AU as shown in Figure 1.10. On September 12, 2013, NASA announced that Voyager 1 had exited the heliosphere at 121.7 AU on August 25, 2012, when it measured a sudden increase in the electron and proton CR fluxes [Webber et al., 2012].

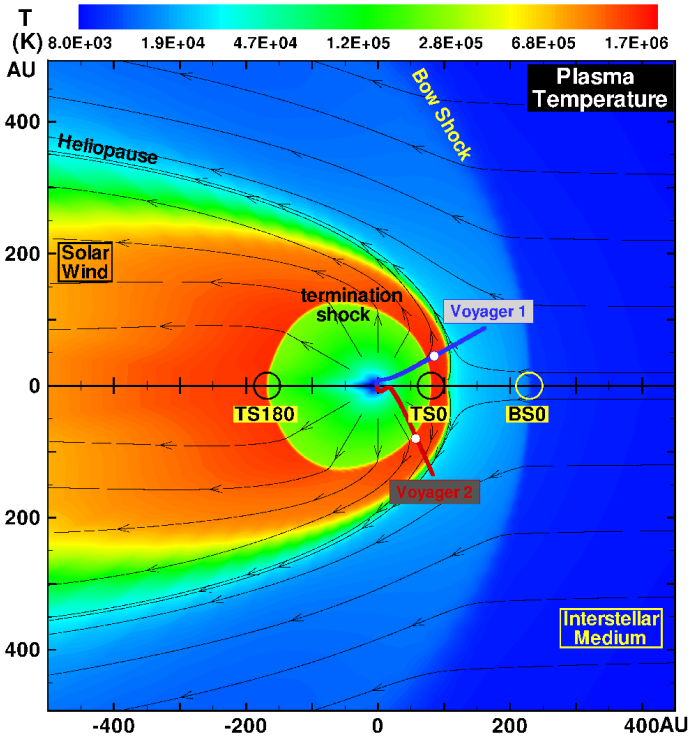

Figure 1.13: A magnetohydrodynamic simulation of the heliosphere indicating the plasma temperatures. The Voyager 1 and 2 spacecraft trajectories are indicated. Figure taken from http://www.dartmouth.edu/~heliosphere/R/heliosphere.html.

HELIOSPHERIC MAGNETIC FIELD

In the solar wind plasma as in many other astrophysical situations the particles mean free path is very long and the plasma can be considered collisionless with an infinite conductivity. In this limit it can be easily demonstrated that the magnetic flux through any loop inside the moving plasma is constant in time. Hence, the magnetic field lines move and change their shape as though they were frozen in the plasma. This phenomenon is known as flux freezing.

The outward flowing solar wind plasma carries the solar magnetic field out in the solar system creating the heliospheric magnetic field (HMF). The first description of the HMF was presented by Parker in 1958. Since the Sun rotates once every ~ 27 days on its axis[7] and since the solar wind is released radially outwards, the solar wind traces an Archimedean spiral as illustrated in Figure 1.14. Because of the flux

7 The 27.275 days rotation is usually referred to as a Carrington rotation. This chosen period roughly corresponds to rotation at a latitude of 26 deg, which is consistent with the typical latitude of sunspots.

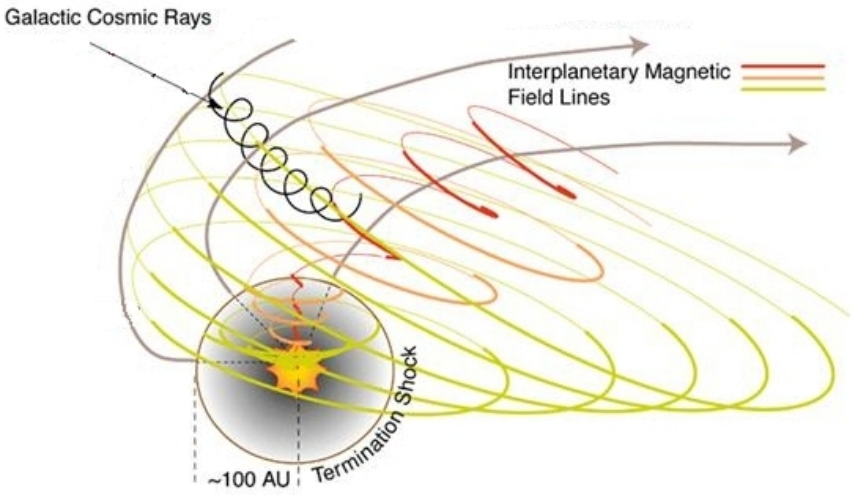

Figure 1.14: The Archimedean structure of the Parker magnetic field as seen from outside the TS [NASA]. Different colors represent the expanding magnetic field from different latitudes on the Sun. The field lines are stretched due to the Sun motion with respect to the Milky Way at a velocity of 25 km/s.

freezing the magnetic field in the solar wind takes up a spiral pattern first described by Parker [1958] and consequently modified by Jokipii and Kóta [1989] and can be expressed as:

$$\mathbf{B} = B_0(\frac{r_0}{r})^2(\mathbf{e}_r + \tan\psi\mathbf{e}_\phi)[1 - 2H(\theta - \theta')] \tag{1.10}$$

where $\mathbf{e}_\phi$ is a unit vector in the azimuthal direction, B_0 the HMF magnitude at $r_0 = 1$ AU, r is the radial distance from the Sun and

$$\tan\psi = \frac{\Omega(r - r_\odot)\sin\theta}{V_{sw}} \tag{1.11}$$

with $\Omega = 2.67 \times 10^{-6}$ rad s^{-1} the average angular rotation speed of the Sun, V_{sw} the SW speed, θ the heliographic latitude, and ψ the Parker spiral angle, defined to be the angle between the radial direction and the direction of the average HMF at a given position. The Heaviside step function H determines the polarity of the magnetic field. The magnetic field magnitude is given by:

$$B = B_0(\frac{r_0}{r})^2\sqrt{1 + (\tan\psi)^2} \tag{1.12}$$

The HMF plays a critical role in heliospheric modulation of CRs since their transport primarily depends on the HMF line configuration and its embedded turbulence.

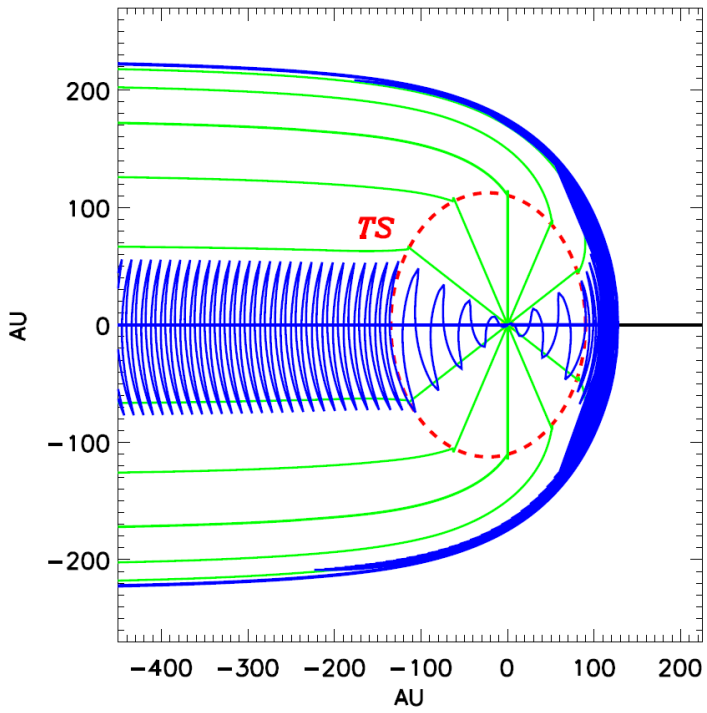

Figure 1.15: A schematic representation of the waviness of the heliospheric current sheet (solid line) during typical solar minimum condition. The x-axis corresponds to the solar ecliptic while the y-axis is the Sun rotation axis. A representation of how the waviness of the HCS could differ from the nose to the tail regions of the heliosphere is showed. Figure adapted from [Kóta, 2013].

THE HELIOSPHERIC CURRENT SHEET

As previously mentioned the magnetic field in the Northern and Southern hemispheres of the Sun are at opposite polarities. Between the two hemisphere lies a neutral current sheet which serves as the heliospheric magnetic equator where the open magnetic field lines from the poles meet. Since the Sun magnetic dipole axis is misaligned with respect to the solar rotation axis by an angle θ_t (the tilt angle), the solar magnetic equator does not coincide with the heliographic equator. As a consequence the heliospheric current sheet should best be thought of as a wavy sheet that corotates with the Sun as showed in Figure 1.15. A disadvantage is that it is not known how the waviness is preserved as it moves into the outer heliosphere, and especially what happens to it in the heliosheath. The waviness becomes compressed in the inner heliosheath as the outward flow decreases across the TS. It should also spread in latitudinal and azimuthal directions in the nose of the heliosphere. A schematic presentation of how the waviness of the HCS could differ from the nose to the tail regions of the heliosphere is shown

in Figure 1.15. Furthermore the tilt angle is correlated to the solar activity. At times of solar minimum, the tilt angle is small, often around $\theta_t = 5°$. At times of solar maximum the tilt angle grows to larger values becoming undetermined during times of extreme solar activity when the solar polarity flips and the new polarity is carried out to the heliopause by the solar wind. The tilt angle value as well as the SW velocity and the HMF magnitude have an impact on the propagation of charged particles through the heliosphere and each of them introduce a different contribution to the Solar modulation of the CRs. The next Section is devoted to the discussion of the Parker equation which describes the propagation of CRs through the interplanetary space.

1.6 THE PARKER TRANSPORT EQUATION

When Galactic CRs enter the heliosphere they are subjected to various modulation processes. These physical processes are responsible for altering the differential intensity and distribution of CRs. The CR intensity decreases with respect the local interstellar spectrum (LIS), which represent the CR intensity as measured outside the heliosphere. These effect is referred to as solar modulation of Galactic CR and becomes significant for energies below ~ 30 GeV.

The transport equation of CRs through heliosphere was derived by [Parker, 1965]. The Parker equation is formally similar to the Galactic transport Equation 1.2, however, because of the better knowledge of the interplanetary medium, the CR propagation is described with much more sophistication. Within a coordinate system that rotates with the Sun, the time-dependent transport equation is given by:

$$\underbrace{\frac{\partial f}{\partial t}}_{a} = -(\underbrace{\mathbf{V}_{sw}}_{b} + \underbrace{\langle \mathbf{v}_d \rangle}_{c}) \cdot \nabla f + \underbrace{\nabla \cdot (\mathbf{K}_s \cdot \nabla f)}_{d} + \underbrace{\frac{1}{3}(\nabla \cdot \mathbf{V}_{sw})\frac{\partial f}{\partial \ln p}}_{e} + \underbrace{Q}_{f} \tag{1.13}$$

The CRs omnidirectional distribution function $f(\mathbf{r}, p, t)$ is a function of position $\mathbf{r}$, particle momentum p, and time t. The quantity experimentally measured is the particle flux $J(\mathbf{r}, p, t)$ expressed in units of particles/area/time/energy/solid angle. The equation that relates the flux with the omnidirectional distribution is:

$$f(\mathbf{r}, p, t) = \frac{J(\mathbf{r}, p, t)}{p^2} \tag{1.14}$$

The terms on the right hand side of Equation 1.13 respectively represent:

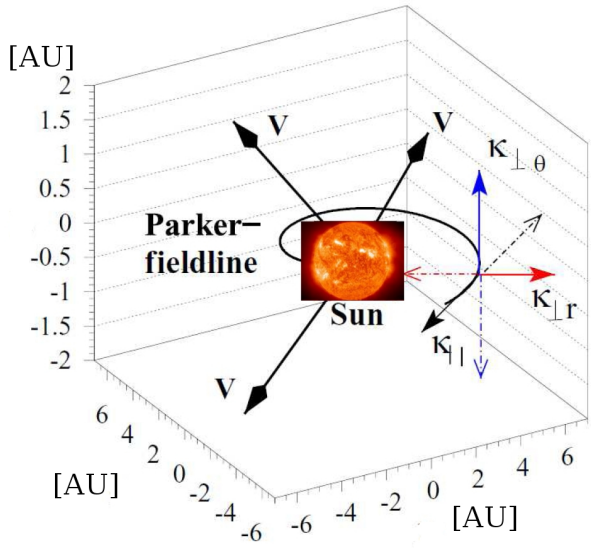

Figure 1.16: Illustration of the directions of the parallel and perpendicular diffusion coefficient components with respect to a magnetic field line in the equatorial plane. The radially expanding solar wind is indicated by the arrows emanating from the Sun. Adapted from [Kóta, 2013].

- b) outward convection with the solar wind velocity V_{sw};
- c) averaged particle drift velocity $\langle v_d \rangle$ caused by gradients and curvatures in the global HMF;
- d) diffusion caused by the irregular HMF with K_s the symmetrical diffusion tensor;
- e) adiabatic energy changes (deceleration or acceleration) determined by the SW divergence;
- f) possible additional sources of CRs within the heliosphere (for example, Jovian electrons).

The most relevant contributions to the solar modulation of electrons and positrons (diffusion and drift) are discussed in detail in the following paragraphs. As discussed in Section 1.7, the transport equation is solved in a coordinate system that rotates with the Sun. The solar wind speed $\mathbf{V}_{sw}$ in Equation 1.13 can be expressed as:

$$\mathbf{V}_{sw} = \mathbf{V}^*_{sw} - \boldsymbol{\Omega} \times \mathbf{r} \tag{1.15}$$

where $\mathbf{V}^*_{sw}$ is the stationary SW velocity given by Equation 1.9, $\boldsymbol{\Omega}$ is the rotational velocity of the Sun and $\mathbf{r}$ is the radial distance from the Sun. Concerning the local sources term, the Jovian magnetosphere is known to be a strong accelerator of electrons with energies up to ~ 30

MeV [Fichtner et al., 2000]. The analysis presented in this thesis regards particles with energies down to 70 MeV, and since no other local acceleration mechanism or sources of electrons or positrons within the heliospheric boundaries are known, this term (f) can be neglected. Moreover, even though the numerical model used for this study includes a termination shock, the effects of Fermi II acceleration that particles undergo at the termination shock are excluded for the purpose of this study (term e). For a transport equation which contains an additional term for the inclusion of Fermi II acceleration, derived from a more see e.g. [Schlickeiser, 2002]. The CR diffusion on the irregularities of the HMF is now discussed.

THE DIFFUSION TENSOR

In November of 1963, NASA launched the Explorer XVIII satellite, whose mission was to study charged particles and magnetic fields in heliosperic space [EXPLORER, 1963]. From these observations, Ness et al. [1964] were able to verify that the shape of the interplanetary magnetic force field was indeed a spiral. They also found that the magnetic field lines were not smooth, but rather had small irregularities with a scale size around 10^5-10^7 km. In 1964, Parker showed that the presence of magnetic irregularities in the turbulent HMF could cause CRs to scatter back and forth across the lines of force of the larger-scale field [Parker, 1964]. When viewed from a large-scale perspective, he hypothesized that the scattering process is equivalent for the CRs to undergoing a random-walk along and across the lines of force. Therefore, particle scatterings can be thought of as a diffusion process. Referring to the coordinate system showed in Figure 1.16 the diffusion tensor in Equation 1.13 takes the form:

$$\mathbf{K}_s = \begin{bmatrix} K_{\parallel} & 0 & 0 \\ 0 & K_{\perp\theta} & 0 \\ 0 & 0 & K_{\perp r} \end{bmatrix}$$

The diffusion coefficients in the symmetrical tensor describe particle diffusion parallel to the mean HMF ($K_{\parallel}$), as well as in the polar ($K_{\perp\theta}$) and radial ($K_{\perp r}$) directions perpendicular to it. Each diffusion coefficient (in units of area/time) can be related to a more tangible variable in terms of length, the mean free path λ [8]:

$$K = \frac{v}{3}\lambda \tag{1.16}$$

8 The mean free path is defined as the average distance traveled by a moving particle between two consecutive impacts which modify its direction, energy or other properties. In the case of diffusion it corresponds to the average distance traveled by a CR before being scattered by a magnetic irregularity.

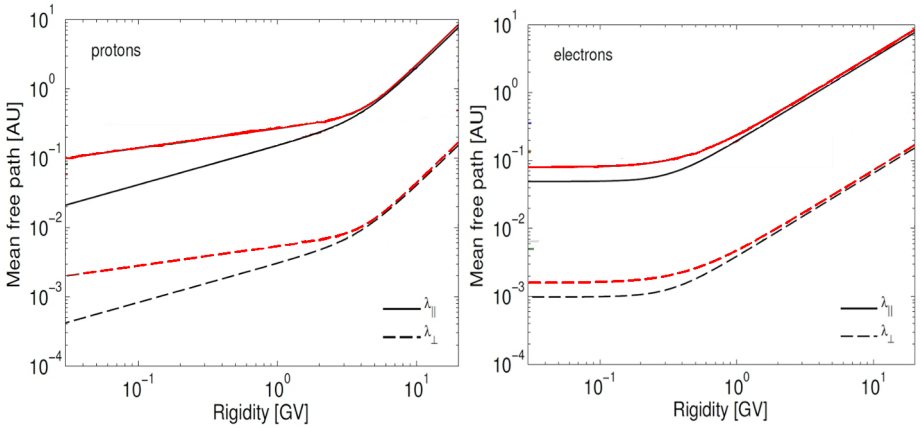

Figure 1.17: Typical rigidity dependence of the parallel (solid lines) and perpendicular (dashed lines) mean free path for Galactic protons and electrons at Earth [Etienne, 2011]. The difference between the two sets of colored lines shows the time dependence as a result of different average tilt angle and HMF values (2006-2009). The black lines represent the mean free path during a period of time with higher solar activity respect to the red lines.

where v is the velocity of the particle (CR). The weak turbulence quasi-linear theory, introduced by Jokipii [1966], allows us to derive expressions for both the parallel and perpendicular diffusion coefficients. The diffusion coefficient can be derived from the power spectrum of the magnetic field fluctuations that have been measured through magnetometer observations by space probes. A general expression for the diffusion coefficient parallel to the average HMF is given by [Etienne, 2011]:

$$K_\parallel = (K_\parallel)_0 \beta \left(\frac{B_0}{B}\right)\left(\frac{P}{P_0}\right)^a \left(\frac{\left(\frac{P}{P_0}\right)^c + \left(\frac{P_k}{P_0}\right)^c}{1+\left(\frac{P_k}{P_0}\right)^c}\right)^{\frac{(b-a)}{c}} \tag{1.17}$$

where $(K_\parallel)_0 = 6 \times 10^{20}$ cm^2 s^{-1}, $\rho_0 = 1$ GV and $B_0 = 1$ nT. Here a and b are dimensionless constants that respectively determine the slope of the rigidity dependence below and above a rigidity P_k, and c is another dimensionless constant which determines the smoothness of the transition between the two slopes. The perpendicular diffusion coefficient $K_\perp$ have a similar expression to Equation 1.17 and is supposed to scale as $K_\parallel$, an assumption that has been theoretically verified by Giacalone and Jokipii [1999], who found that the ratio $K_\perp / K_\parallel$ has a value between 0.02 and 0.04. The a,b and c coefficients change depending on the particle species. The rigidity dependence for the parallel and the perpendicular mean free path at Earth for electrons and protons are shown in Figure 5.16. For example the rigidity dependence of the parallel diffusion coefficient is essentially a combination of two power-

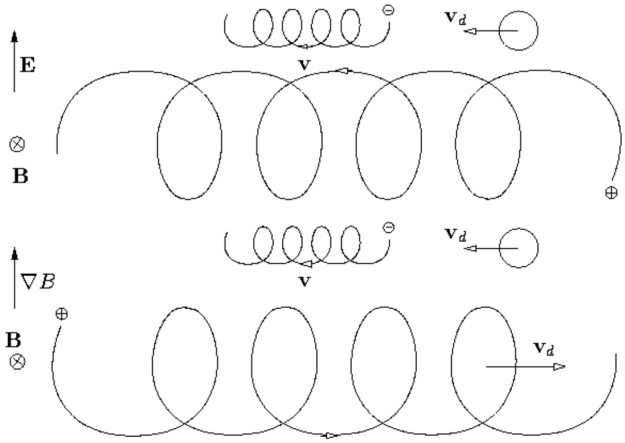

Figure 1.18: Top panel: the drift velocity for positively and negatively charged particles in the presence of perpendicular magnetic and electric field. Bottom panel: the drift velocity in the presence of a magnetic field gradient. The illustration of negatively and positively particle motion are not to scale. Figure adapted from http://silas.psfc.mit.edu/introplasma/chap2.html.

laws for protons while for electrons is predicted to become constant at rigidity below a few hundreds MV. Moreover the CR protons experience large adiabatic energy changes below 300 MeV thus the changes in K become unimportant and the proton propagation is dominated by the adiabatic energy losses. For the electrons the energy losses at low energies are negligible and, since the diffusion coefficient takes a constant value, the dominant process becomes diffusion. The energy value at which the electron diffusion coefficient should become constant can be generally predicted by the theory (see [Teufel, A. and Schlickeiser, R., 2003]), but the exact value needs to be verified empirically (see Section 5.5). On Figure 5.16 it is also shown the change in the mean free path as a result of the solar activity variation (see Section 5.5). Similarly to the diffusion coefficients, a drift coefficient is introduce to described the drift effects of CR solar modulation.

PARTICLE DRIFT

The drift motion due to the presence of gradients and curvatures in the HMF introduces a charge-sign dependent modulation. Because of the Lorentz force a charged particle in a uniform magnetic field undergoes a constant acceleration perpendicular to both the particle velocity and the magnetic field and its trajectory results in a circular motion at constant speed in the plane perpendicular to the magnetic field. If an external force **F** is introduced the particles will experience a

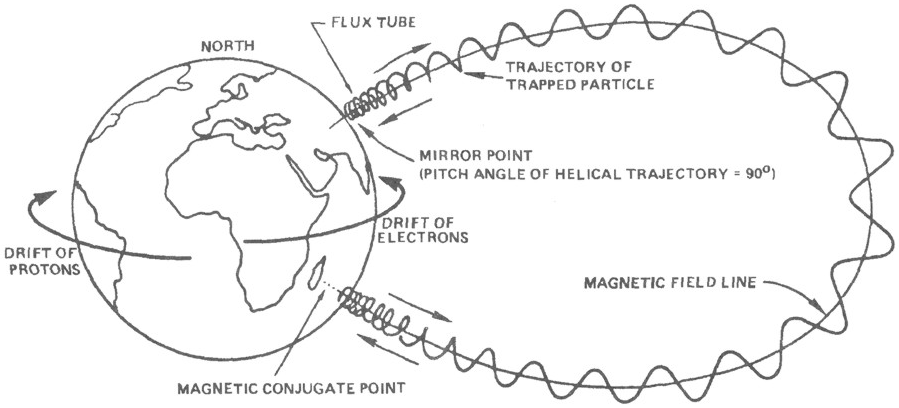

Figure 1.19: Drift velocity pattern for positively and negatively charged particles in a presence of a magnetic field curvature. The picture illustrates the dynamic of reentrant albedo particles inside the Earth radiation belts. A brief description of such phenomenon is presented in Section 3.2. Figure adapted from http://techdigest.jhuapl.edu/views/pdfs/V11_3-4_1990/V11_3-4_1990_Kinnison.pdf.

velocity drift in the direction perpendicular to both the external force and the magnetic field. The drift velocity is expressed as:

$$\mathbf{v}_{d(F)} = \frac{\mathbf{F} \times \mathbf{B}}{qB^2} \tag{1.18}$$

where q is the charge of the particles. A special case is the presence of an electric field, the drift velocity then becomes:

$$\mathbf{v}_{d(E)} = \frac{\mathbf{E} \times \mathbf{B}}{B^2} \tag{1.19}$$

Since the electric force on a particle depends on its charge, the drift velocity has the same direction for oppositely charged particles as shown on the top panel of Figure 1.18 which represents a schematic view of the drift motion introduced by the presence of an electric field. Charged particles experience a drift motion also in association with gradients in the magnetic field magnitude, the curvature of the field, and any sudden changes in the field direction such as those found in the heliospheric current sheet. In the case of a magnetic field gradient ∇B the drift velocity is:

$$\mathbf{v}_{d(\nabla B)} = \frac{v_\perp^2 m}{2qB^3} \nabla \mathbf{B} \times \mathbf{B} \tag{1.20}$$

where $v_\perp$ is the perpendicular component of the velocity. In the presence of a gradient the drift velocity depends explicitly on the particle

charge sign as can be seen on the lower panel of Figure 1.18. An inhomogeneous magnetic field may also have curvature associated with its $\nabla \times B \neq 0$. In this case the curvature of the field lines will create a centrifugal force on the particle:

$$\mathbf{F}_c = m v_{\parallel}^2 \frac{\mathbf{R_c}}{R_c^2} \tag{1.21}$$

where $\mathbf{R_c}$ is the radius of curvature, pointing outwards, of the circular arc which best approximates the curvature of the magnetic field at that point and $v_{\parallel}$ is the parallel component of the particle velocity. From Equation 1.18 the drift velocity associated with this centripetal external force is:

$$\mathbf{v}_{d(\nabla\times B)} = \frac{v_{\parallel}^2 m}{qB^2} \frac{\mathbf{R_c} \times \mathbf{B}}{R_c^2} \tag{1.22}$$

Also in this case the velocity direction depends on the particle charge. The drift velocity due to magnetic field curvature is illustrated in Figure 1.19 for trapped particles inside the Earth radiation belts (see Section 3.2).

The average drift velocity for CRs propagating inside the heliosphere can be computed from the interplanetary magnetic field, B, given in Equation 1.10. The pitch angle averaged guiding center drift velocity for a near isotropic cosmic ray distribution is given by:

$$v_d = \nabla \times (K_d \mathbf{e}_B) \qquad \text{with} \qquad K_d = \frac{pv}{3qB} \tag{1.23}$$

with $\mathbf{e}_B$ a unit vector pointing in the HMF direction. The drift coefficient is related to the so-called drift scale through:

$$\lambda_d = K_d \frac{3}{v} \tag{1.24}$$

Now, defining the asymmetric drift tensor as:

$$\mathbf{K}_d = \begin{bmatrix} 0 & 0 & 0 \\ 0 & 0 & K_d \\ 0 & -K_d & 0 \end{bmatrix}$$

and combining the diffusion tensor and the drift tensor in $\mathbf{K} = \mathbf{K}_s + \mathbf{K}_d$, it is possible to rewrite the transport equation in a more compact form as:

$$-\mathbf{V}_{sw} \cdot \nabla f + \nabla \cdot (\mathbf{K} \cdot \nabla f) + \frac{1}{3}(\nabla \cdot \mathbf{V}_{sw}) \frac{\partial f}{\partial \ln p} = 0 \tag{1.25}$$

where the average guiding center drift velocity $< v_d >$ is now included in the asymmetrical tensor $\mathbf{K}$. In Equation 1.25 both the source

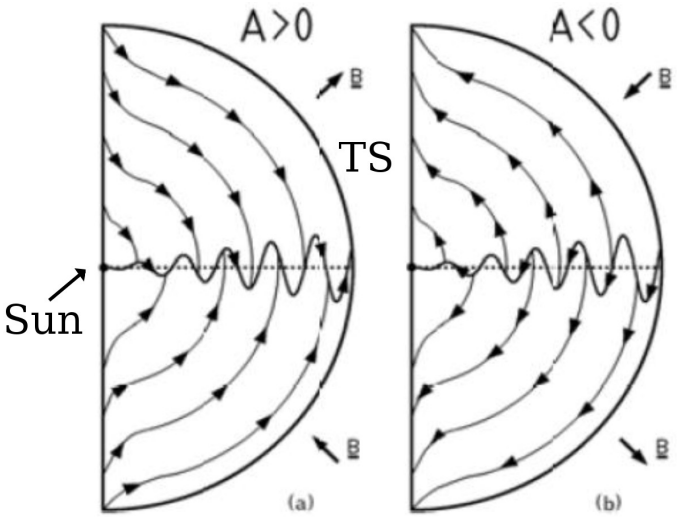

Figure 1.20: Idealistic global drift patterns of positively charged particles in an $A > 0$ and $A < 0$ magnetic polarity cycle. Adapted from [Heber and Potgieter, 2006].

term Q and the time-dependent changes $\partial f/\partial t$ in Equation 1.2 have now been reduced to zero. In fact as discussed in Section 5.5, the 3D model numerical solution is resolved in a steady-state configuration, thus $\partial f/\partial t = 0$.

Ideal global drift patterns of Galactic CRs in the heliosphere are illustrated in Figure 1.20 for positively charged particles in an $A > 0$ and $A < 0$ magnetic polarity cycle respectively, together with a wavy HCS as expected during solar minimum conditions. Since the HMF has opposite polarities in the regions separated by the HCS, particle drift motions are induced along the HCS. For an $A > 0$ cycle positively charged particles undergo drift motions from the polar regions toward the equatorial region, and outward along the HCS, negatively charged particles drift in opposite directions. During an $A < 0$ cycle the drift directions are reversed. The charge sign effects of the CR solar modulation can be experimentally quantified measuring simultaneously the behavior of negatively and positively charged CRs. Electrons could be compared with protons, the most abundant positive CRs. However, since electrons and protons have greatly different charge/mass ratios, the relation of velocity and magnetic rigidity is very different. On the other hand, considering positrons (which have an identical relationship between velocity and rigidity as electrons) allows a clear separation of the charge sign modulation from other possible effects. Thus, simultaneous measurements of CR electrons and positrons serve as a crucial test on the understanding of how large charge-sign dependent modulation in the heliosphere is. For some experimental evidence of the drift

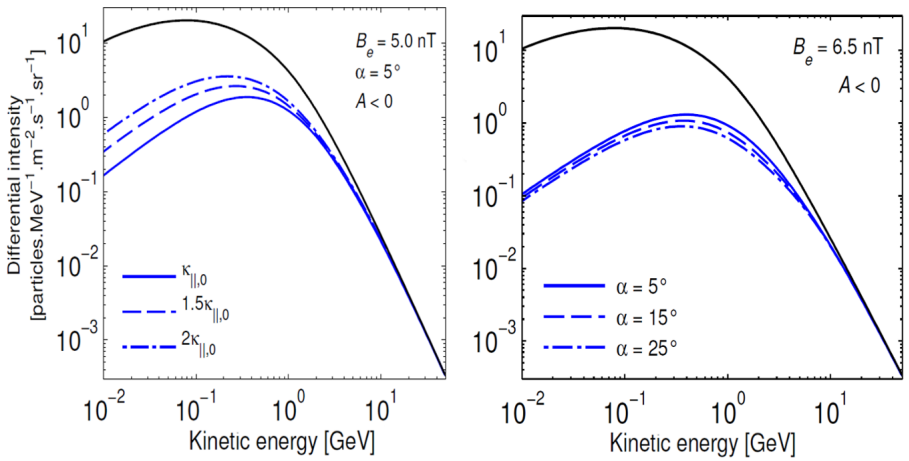

Figure 1.21: Left panel: the effect of the solar modulation on the CR proton spectrum. The black line represents the proton LIS used as input spectrum while the blue lines are the energy spectra computed at Earth using the numerical solution of the transport equation for various values of $k_{\|}$. As the value of $K_{\|}$, and thus the mean free path, increases, the intensity of CRs increases as well. Right panel: the energy spectra for protons during an $A < 0$ cycle for different current-sheet tilt angle values. Changing the tilt angle values correspond to change the drift contribution to the CR propagation. Figures adapted from [Etienne, 2011].

effects on the CRs propagation through the heliosphere see Sections 1.8 and 1.9 (Figures 1.22, 1.23 and 1.24). The drift motions do, however, only contribute significantly to CR modulation during solar minimum conditions, when the HMF exhibits a well-ordered structure [Ferreira and Potgieter, 2004]. How large drift effects are during solar maximum periods are still investigated, although some works indicate that they can be neglected (see the review by Potgieter [2013]).

1.7 NUMERICAL SOLUTION

In order to compute the intensity of CRs throughout the heliosphere, the CR transport equation is solved numerically as a three-dimensional steady-state modulation model. The approach adopted by e.g. Etienne [2011] is first to write the transport equation in terms of a heliocentric spherical coordinate system obtaining a parabolic differential equation which can be solved with a modified Crank-Nicholson finite difference method, called the Alternating Direction Implicit method [Peaceman and Rachford, 1955]. The LIS is taken as an input spectrum at the outer boundary of the heliosphere, located at 120 AU, and then is modulated in a steady state model in order to reproduce the CR fluxes at a cer-

tain location inside the heliosphere. A proper knowledge of the exact shape of the energy spectra in the local interstellar medium is of particular importance for the study of heliospheric modulation. Figure 1.21 shows the modulated proton spectrum at Earth (blue dotted and solid lines) for different values of the diffusion coefficient (left panel) and tilt angle values (right panel). Clearly visible is the intensity decrease of the proton spectrum after propagation with respect to the LIS (black line). Moreover, the left panel shows how as the parallel diffusion coefficient increases as a consequence of the solar activity decrease, the proton flux at Earth increases as well. On the contrary the right panel of Figure 1.21 shows the resulting effects on proton energy spectra produced by changes in tilt angle. Because of the huge difference between the electrons and protons mass at low energy different modulation processes become dominant. Adiabatic energy loss is the main modulation process for protons below a few hundreds of MeV thus the spectrum is expected to decrease as the energy decreases. Contrarily low energy electrons experience negligible energy losses and the modulation becomes diffusion dominated. Electron spectrum below a few hundreds of MeV have the same spectral index of the LIS. Models in principle can predict the energy at which the electron propagation becomes diffusion dominant. However the PAMELA results allow an experimental fine tuning of the numerical value for the diffusion coefficients and the drift scale. Section 5.5 explains how the numerical solution of the Parker equation is applied to reproduce the PAMELA results on the CR electron time-dependent fluxes.

1.8 TIME VARIATION OF CRS

In the previous sections the modulation mechanism responsible for the CR modulation inside the heliosphere has been discussed. In addition, long-term changes in the scattering properties, i.e. the 11-year solar cycle, are responsible for the long-term time variations in the near-Earth CR intensities. Figure 1.22 shows the neutron monitor (NM) counts measured by the Hermanus NM located in South Africa. When CRs reach the Earth they collide with molecules in the atmosphere producing air showers of secondary particles including neutrons. The neutron monitor count rate is thus proportional to the intensities of the CR flux at Earth. The CR intensity follows the 11-year solar activity. The comparison between Figure 1.22 and 1.8 reveals that the observed CR flux is anti-correlated with solar activity, thus higher CR fluxes are measured during solar minimum conditions.

Furthermore, the 22-year cycle, related to the HMF polarity reversal, can also be identified in Figure 1.22. During $A < 0$ polarity cy-

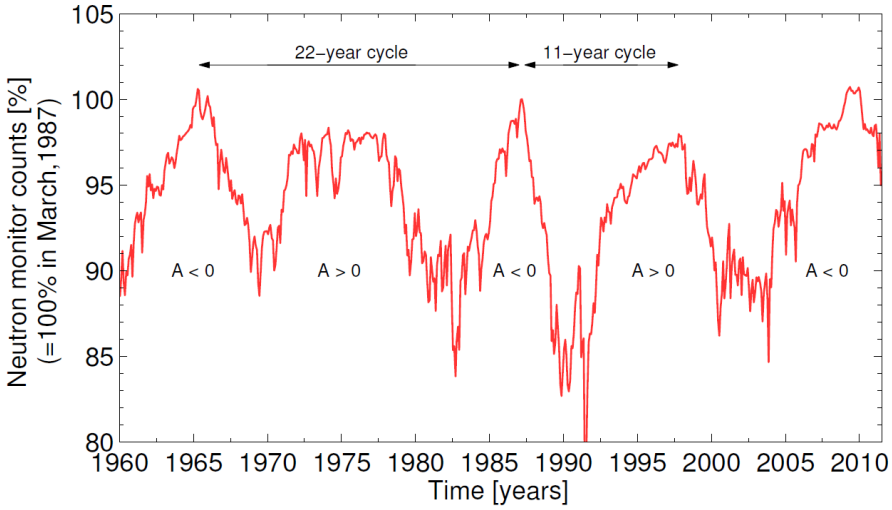

Figure 1.22: Neutron monitor counts as a function of time, as measured by the Hermanus neutron monitor. The 11-year and 22-year cycles are clearly noticeable. Data obtained from http://www.nwu.ac.za/content/neutron-monitor-data.

cles, peaks are formed by the heliospheric modulation, whereas for $A > 0$ polarity cycles the modulated flux has plateau shapes. Since most of the CRs are protons, these features can be ascribed to the drift motions. Indeed if CRs would be an equal mixture of negative and positive hadrons, drift motion would not be appreciable from neutron monitor measurements. The sudden decreases are ascribed to the Forbush decreases, related to violent transient solar events like coronal mass ejections that lead to the formation of propagating diffusion barriers (see Section 4.1). Long flight duration and detector capabilities make the PAMELA apparatus particularly suitable for measuring the time-dependent CR solar modulation.

1.9 PREVIOUS MEASUREMENTS

After De Shong et al. [1964] measurement, many experiments investigated the CR electrons and positrons at Earth during different periods of solar activity and solar magnetic field polarity. Clem and Evenson [2009] reported in Figure 1.23 a summary of the positron abundance measurements as a function of energy for different epochs of solar magnetic polarity. The solid symbols show data taken during a positive polarity solar cycles, while the open symbols represent data taken during negative polarity solar cycles. Table 1.1 summarizes the data shown in Figure 1.23 and indicates the type of experiment and the relative operational time. Except for AMS01, all the experiments cited in

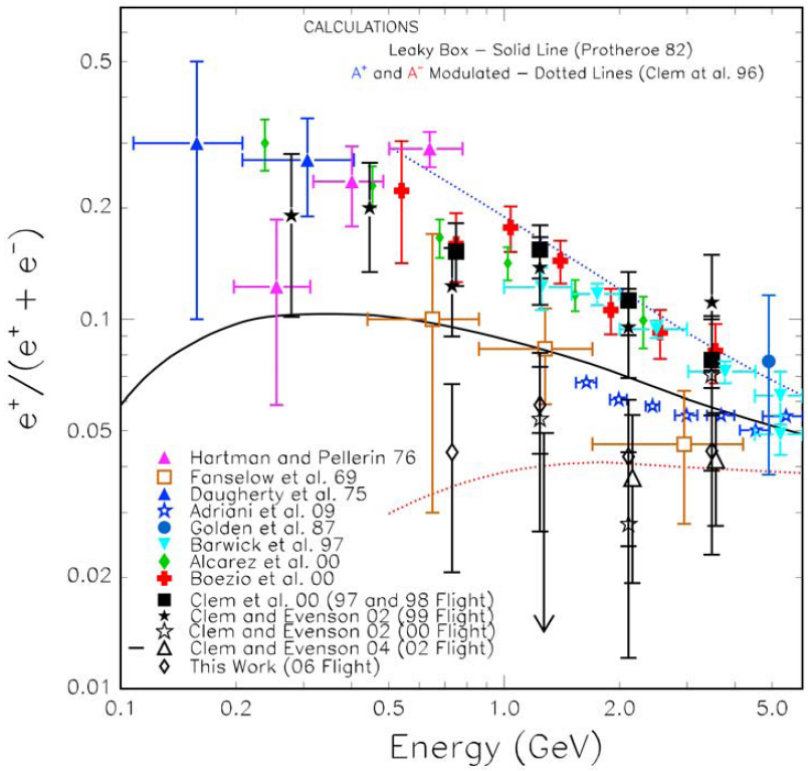

Figure 1.23: The world summary of the positron abundance and calculations of the positron abundance as a function of energy for different epochs of solar magnetic polarity [Clem and Evenson, 2009]. Solid symbols show data taken during a positive polarity cycle, while the open symbols represent data taken during a negative polarity cycle. The references to the data as well as the observational periods are summarized in Table 1.1. Dashed lines are abundance as calculated from Clem et al. [1996] for A positive (blue line) and A negative (red line) while the solid line is the prediction for no charge sign dependence of solar modulation.

Table 1.1 were balloon flight, thus were limited in time with respect to the PAMELA mission. For this reason their statistical uncertainties were much higher than the PAMELA results. Moreover the balloon flight measurements suffer from uncertainties due to secondary electrons and positrons[9] produced in the residual atmosphere above the instrument.

Beside their limitations, the balloon flight measurements show a time variation of the low energy positron fraction. This differences are due to the charge-sign dependence of the solar modulation (see Section 1.6). Moreover, during opposite polarity epochs of the HMF (the HMF

9 These electrons and positrons, as well as proton and pions, are produced in the air showers induced by high energy primary CRs, see Section 3.2

Table 1.1: Explanation of References for Figure 1.23.

Reference	Platform type	Observational period
[Fanselow et al., 1969]	Balloon	5 Jul, 5 Aug '65; 10, 15, 26 Jun '66.
[Daugherty et al., 1975]	Balloon	Two 1-day flights: Jul '72
[Hartman and Pellerin, 1976]	Balloon	15 Jul, 3 Aug '74
[Golden et al., 1987]	Balloon	20 May 1976
[Boezio et al., 2000]	Balloon	8-9 Aug '94
[Barwick et al., 1997]	Balloon	23– 24 Aug '95
[Alcaraz et al., 2000]	AMS01	2– 12 Jun '98
[Clem et al., 2000]	Balloon	1 Sept '97, 29 Aug '98
[Clem and Evenson, 2002]	Balloon	16 Aug '99, 25 Aug '00
[Clem and Evenson, 2004]	Balloon	13 – 14 Aug 2002
[Clem and Evenson, 2009]	Balloon	2 – 6 Jun 2006
[Adriani et al., 2009a]	PAMELA	Jul 2006 - Feb 2008

polarity reverses every ~ 11 years, see Section 1.5), the Galactic CRs of opposite charge will drift towards the Earth from different heliospheric directions since the drift patterns interchange (see Figure 1.20). For this reason a big difference is expected between the positron fraction measured in epochs with similar solar activity but different magnetic polarity. For example the blue and the red dotted lines in Figure 1.23, refer to a specific prediction of the expected positron abundance at the same phase of successive solar cycles (i.e. for both positive and negative polarity states) made by Clem et al. [1996]. In Figure 1.24 (right panel) is shown the prediction of the positron fraction at the rigidity of 1.2 GV made by Clem et al. [1996], where a sudden change (which last about one year) due to the magnetic polarity inversion is visible (see caption for more details). The various experimental observations seem to follow the pattern indicated by the prediction. The left panel of Figure 1.24 shows the ratio between electrons and helium measured between 1976 - 2000 (see Figure caption for more details) superimposed with a theoretical prediction. Also in this case a sudden change in the ratio values was observed in correspondence of the magnetic polarity reverse as for the positron fraction. However relatively large differences were found between the computed ratios and the observations for both the results in Figure 1.24. To fix this discrepancy more sophisticated refinement of the model and precise experimental measurements are needed.

The time variation of the positron fraction is observable, below ~ 2 GeV, also in Figure 1.4 where the AMS02 results, which refer to the

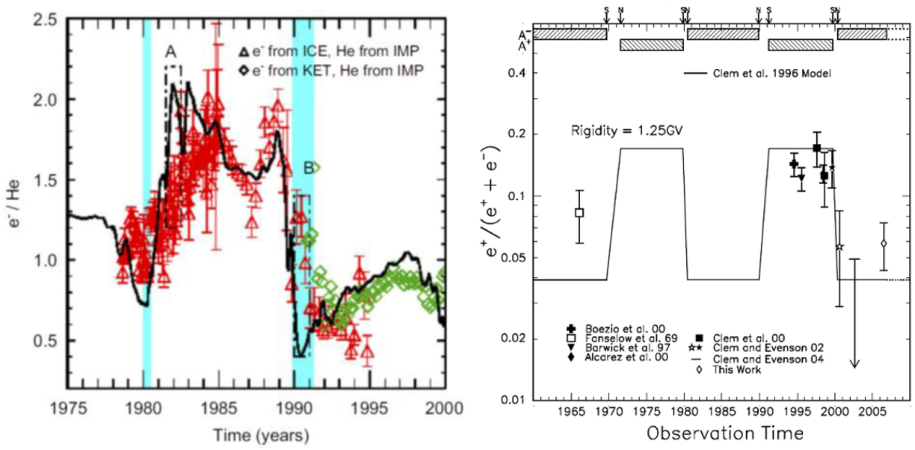

Figure 1.24: Left panel: computed 1.2 GV e^-/He ratio at Earth for 1976 - 2000 in comparison with the observed e^-/He obtained from electron measurements of ISEE3/ICE, He measurements from IMP and electron measurements from KET [Heber et al., 2003]. Right panel: time profile of the positron abundance observations with rigidities ~ 1.25 GV. Solid symbols show data taken in the $A > 0$ state, while the open symbols represent data taken in the $A < 0$ state. Shaded rectangles represent periods of well-defined magnetic polarity. The black line is a positron abundance prediction based on the analysis of Clem et al. [1996].

period from 19 May 2011 to 10 December 2012 (i.e. a period of high solar activity), are compared with the PAMELA results, which refers to a period of low solar activity and same HMF polarity (see Table 1.1). The statistical significance of these two experiments is much higher than the measurements shown in Figure 1.23 and thus the differences are more appreciable. The PAMELA results presented in this work have lower uncertainties with respect to the set of measurements showed in Figure 1.23, thus represent a significant improvement with respect to the previous experiments.

1.10 SOLAR MODULATION WITH PAMELA

The 23th solar minimum activity and the consequent minimum modulation conditions for CRs was unusual. It was expected that the new solar cycle would begin in early 2008. Instead solar minimum modulation conditions continued until the end of 2009 when the largest fluxes of Galactic proton CRs since the beginning of the space age were recorded. This period of prolonged solar minimum activity is well suited to study the modulation processes that affect the propagation

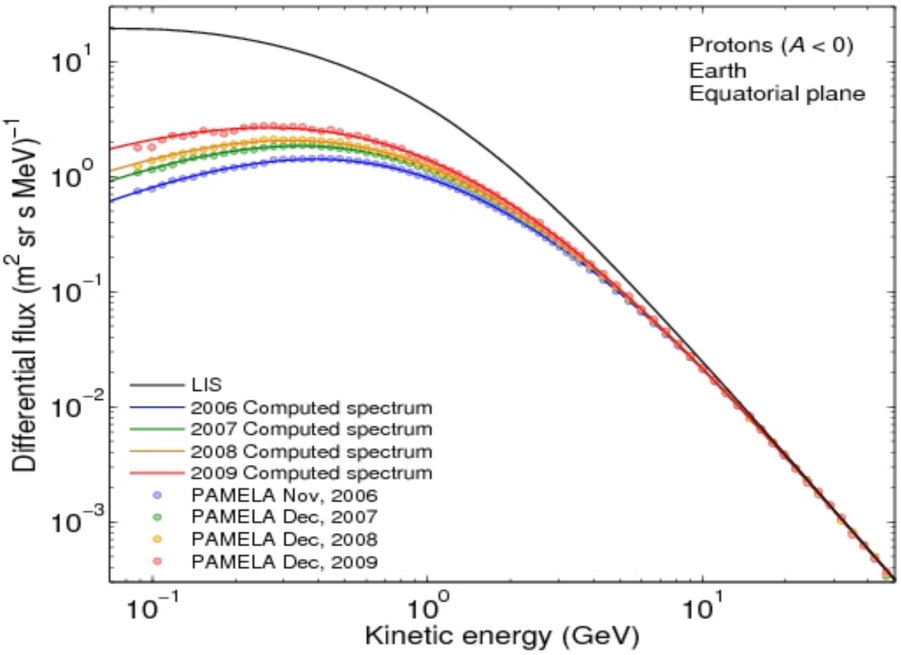

Figure 1.25: Time-dependent proton spectra measured by PAMELA from 2006 to 2009. Solid colored curves represent a solution of a numerical model tuned to reproduce the experimental data [Etienne, 2011]. The black line represents the proton LIS.

of galactic cosmic rays inside the heliosphere. In fact, as previously discussed, during solar minimum:

- the HMF is well ordered while, during period of intense solar activity, it becomes chaotic. Thus, from a modeling point of view is easier to reproduce the HMF during solar minimum;
- the solar activity is low and varies very little over time (several months). Again, from a modeling point of view, is easier to work with small and slow changes in the solar environment instead of the large and fast variation that occurs during solar maximum.

The PAMELA data analysis presented in this work is based on data collected from July 2006 until December 2009. Figure 1.25 shows published results on the time dependent CR proton spectra measured by PAMELA between 2006 and 2009 together with the proton LIS [Adriani et al., 2013b]. The time variation of the proton spectrum is clearly visible as well as the decrease with respect to the LIS. Above $\sim$ 30 GeV the measured spectrum is approximately identical to the LIS.

Precise measurements of the time-dependent CRs spectra are essential to understand the propagation of CRs in the heliosphere, thus allowing the LIS energy spectra of the various CR species to be deter-

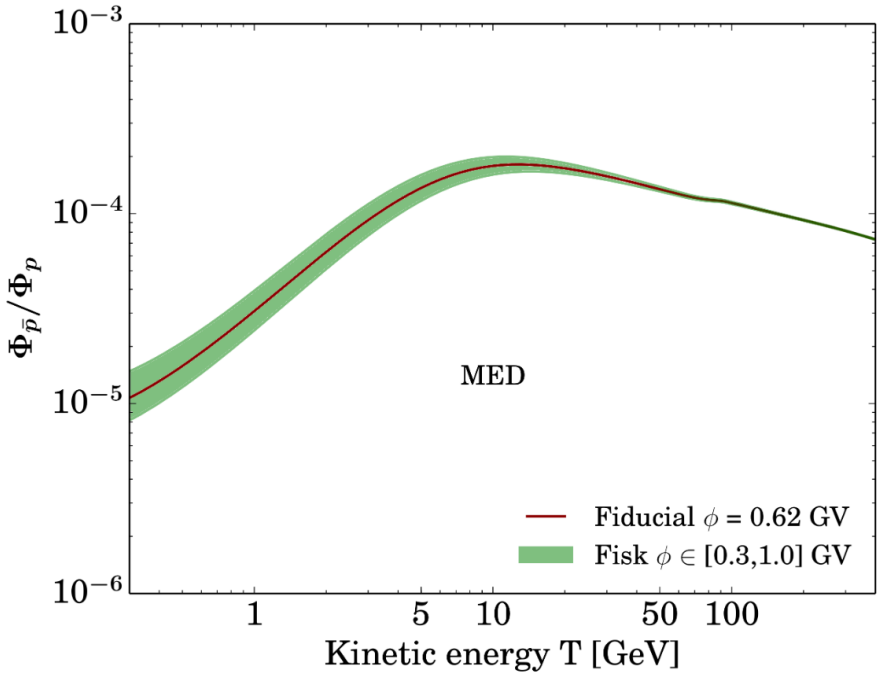

Figure 1.26: Illustration of the uncertainties for secondary anti-proton production model. The colored bands represent the uncertainties due to solar modulation parameters. Figure adapted from [Giesen et al., 2015].

mined. Furthermore, the experimental and theoretical investigation of this system provides information that can be easily applied to larger astrophysical systems. Hence very useful information for understanding the origin and propagation of CRs in the Galaxy can be derived. Then, understanding the effects and time dependence of solar modulation is significant also for space weather since the amount of CRs reaching the Earth can be predicted. Moreover, the physical processes governing the transport of CRs in the heliosphere to the Earth are the same ones affecting charged particles produced by solar events such flares (see Section 4.1). Understanding the sign charge dependence of solar modulation is essential to determine the low energy part of the interstellar spectra of antiparticles.

The energy spectra of the antiparticles CR are particularly relevant for the indirect search of dark matter annihilation or decay. However the uncertainties on the solar modulation parameters affects the study of possible contribution of DM annihilation or decay to the antiparticle component. The uncertainties on these parameters can be significantly reduced by studying the propagation of ordinary CRs, which are known to have a non-exotic origin, inside the heliosphere. Figure 1.26 illustrates the uncertainties due to the solar modulation parameter

for the secondary anti-protons prediction [Giesen et al., 2015]. However the model considered by Giesen et al. [2015] does not contain any charge-sign dependence due to drift effects. A more realistic picture should consider the uncertainties due to the polarity change of the HMF (see Section 1.6). Hence an additional band, e.g. see the calculation of Clem et al. [1996] for the positron abundance during opposite polarity states presented in Figure 1.23, should be added to the uncertainty band of Figure 1.26.

The results presented in this work provide for the first time the opportunity to study in detail the Galactic electron and positron time-dependent spectra down to 70 MeV. These data are essential to test the numerical model developed to describe the CR modulation inside the heliosphere and reduce the uncertainties on the propagation parameters. Moreover the combined measure of electrons and positrons make possible to investigate the charge-dependent solar modulation.

2 THE PAMELA INSTRUMENT

INDEX

The PAMELA (Payload for Antimatter Matter Exploration and Light-nuclei Astrophysics) mission is the culmination of the scientific activity of the WiZard collaboration, created in the late 1980's to develop a program of direct measurements of cosmic rays, with a particular focus on antimatter. This collaboration included universities and research institutes from Italy, Germany, Sweden, Russia and USA. The PAMELA collaboration was formed in the late 1990's with the goal to make a satellite-borne experiment with very high sensitivity and excellent particle identification capability. The 470 kg PAMELA instrument has a power budget of 355 W and is mounted in a pressurized container on-board the 6.7 ton Russian Resurs DK1 satellite that provides multi-spectral Earth images. It was launched from the Baikonur cosmodrome in Kazakhstan on 15 June 2006 and since then it has been almost continuously taking data. The quasi-polar elliptical satellite orbit has an altitude varying from 350 to 600 km. About 15 GB of PAMELA data are transmitted each day to Moscow for further distribution within the collaboration. Section 2.1 of this Chapter intends to give a general overview on the PAMELA instrument and its scientific objectives. In Section 2.2 the Resurs DK1 satellite and its orbital features are discussed. In Section 2.3 the PAMELA sub-detectors are discussed with particular focus on their features relevant to the measurement discussed in this thesis. For a complete review about the instrument and the results published by the PAMELA collaboration see [Adriani et al., 2014b].

2.1 SCIENTIFIC OBJECTIVES

The PAMELA instrument was conceived for the direct detection of the cosmic radiation outside the atmosphere. Since the launch in June 2006

PAMELA has been almost continuously taking data to achieve its scientific objectives which are to measure the:

- Antiproton spectrum up to 150 GeV
- Positron spectrum up to 200 GeV
- Electron spectrum up to 1 TeV
- Nuclei spectra (Li to O) up to 200 GeV/n

To search for:

- Antinuclei with a anti-He/He sensitivity of 10^{-7}
- New forms of matter, e.g. strangelets
- Structures in cosmic ray spectra from e.g. dark matter or new astrophysical sources

To study:

- Cosmic-ray acceleration and propagation mechanisms
- Solar flare emissions
- Particles in the Earth's magnetosphere
- **Solar modulation effects**

The long flight duration (in June 2017 the satellite will have covered an entire 11 year solar cycle) make the PAMELA instrument particularly suitable for CR solar modulation studies. The long-term time-variation of the CR intensity due to the changing in solar activity can be accurately measured by PAMELA at a distance of 1 astronomical unit[1] (AU) from the Sun. The orbital features of PAMELA make it possible to investigate CRs down to a low energy region (~ 70 MeV for electrons and positrons) where solar modulation effects on CR propagation inside the heliosphere are particularly important. The next Section is devoted to a general overview of the PAMELA orbital features and the Resurs DK1 satellite.

2.2 SATELLITE, ORBIT, DATA TRANSFER

RESURS DK1 SATELLITE

PAMELA was launched on-board the Resurs-DK1 Russian satellite by a Soyuz rocket, on the 15th of June 2006, from the Baikonur cosmodrome.

1 One astronomical unit corresponds to the distance between the Sun and the Earth and is approximatively 150 millions of kilometers.

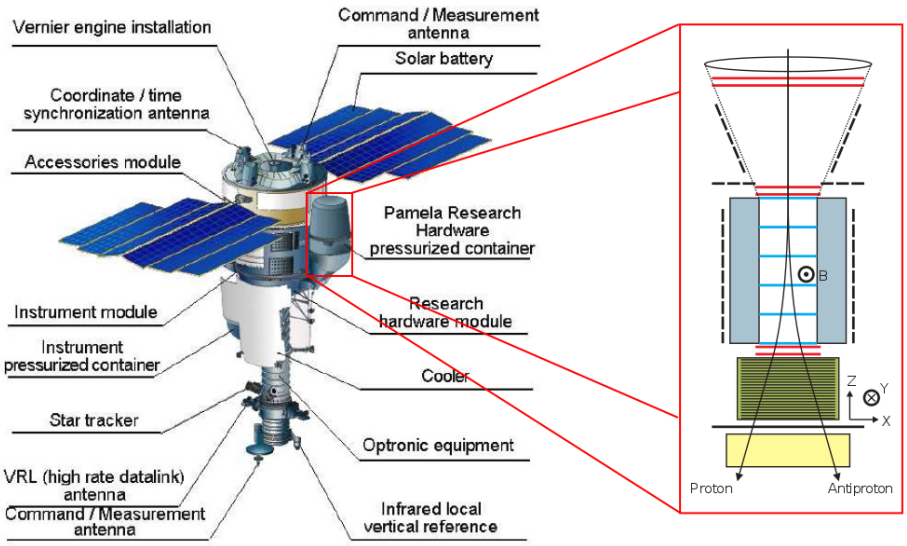

Figure 2.1: A sketch of the Resurs DK1 satellite which hosts the PAMELA experiment (red panel) in a pressurized container (shown in the data-taking position). The satellite has a height of 7.4 m.

The Resurs DK1 satellite was manufactured by the Russian space company TsSKB Progress. This class of spacecrafts performs multi-spectral remote sensing of the Earth's surface and acquires high-quality images in near real-time. Data delivery to the ground is realized via a high-speed radio link. The satellite has a mass of ~ 6.7 tonnes and a height of 7.4 m (see Figure 2.1). The solar array span is ~ 14 m. The satellite is three-axis stabilized with an axis orientation accuracy of 0.2 arcmin and an angular velocity stabilization accuracy of 0.005 /s.

PAMELA is mounted in a dedicated pressurized container (PC) attached to the Resurs DK1 satellite. The container is cylindrical in shape and has an inside diameter of about 105 cm, a semi-spherical bottom and a truncated conical top. It is made of an aluminum alloy, with a thickness of 2 mm in the acceptance of PAMELA. Proton and heavier nuclei interacting with the aluminum foil can produce multi-particle events which results in a secondary background. The analysis of low energies positrons and electrons is particularly affected by secondary pions which constitute a significant contamination below ~ 1 GeV (see Section 3.2).

ORBITAL FEATURES

The satellite orbital altitude varied between 350 km and 600 km at an inclination of 70 degrees. In September 2010 the orbit was changed to a nearly circular one at an altitude of ~ 570 km. The quasi-polar orbit al-

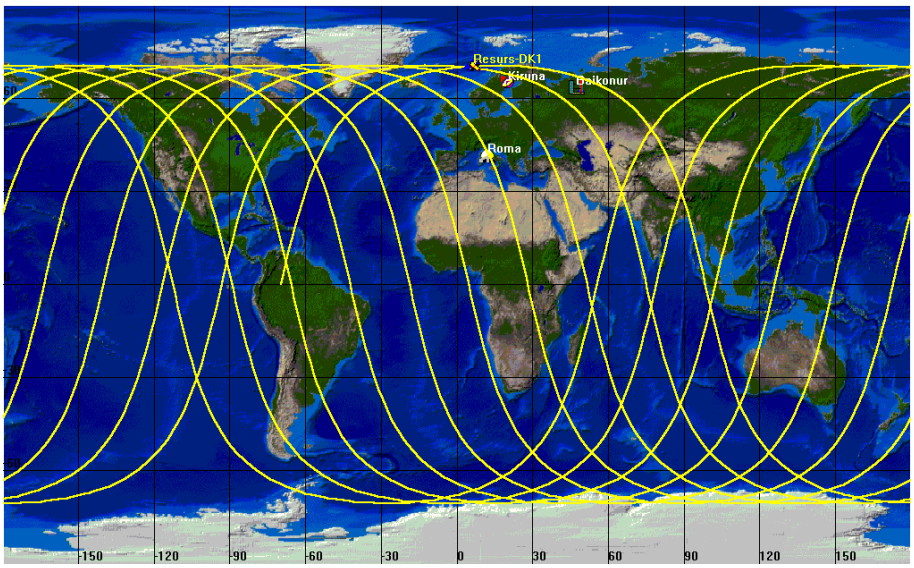

Figure 2.2: The projection on the Earth surface of the trajectory of satellite Resurs DK1.

lows PAMELA to sample very high geomagnetic latitudes. Below ~ 20 GV the magnetic field of the Earth deflects the CR trajectories introducing a cutoff which prevent low rigidity (see Equation 2.1) CRs to reach all the geomagnetic latitudes. Specifically, CRs below few hundreds of MV, could be sampled only in proximity of the geomagnetic pole (see Section 3.2 for detail). The PAMELA orbit allows to measure CRs down to few tens of MeV giving access to rigidities at which the solar modulation of CRs is particularly important.

DATA TRANSFER

The ground segment of the Resurs DK1 system is located at the Research Center for Earth Operative Monitoring (NTs OMZ) in Moscow, Russia. This center is part of the Russian Space Agency (Roskosmos) ground segment designed for acquiring, recording, processing and distributing data from remote sensing systems in space. The Resurs DK1 radio link towards NTs OMZ is active 2-3 times a day. The average volume of data transmitted during a single downlink is currently ~ 6 GBytes, giving a total of 15 GBytes/day. Data received from PAMELA are collected by a data-set archive server. The downlinked data are transmitted to a server dedicated to data processing for instrument monitoring and control, and are also written to magnetic tape for long-term storage. After this first level of data analysis, both raw and preliminary processed data are moved through a normal Internet line to the main storage center in Eastern Europe, which is located at MEPHI

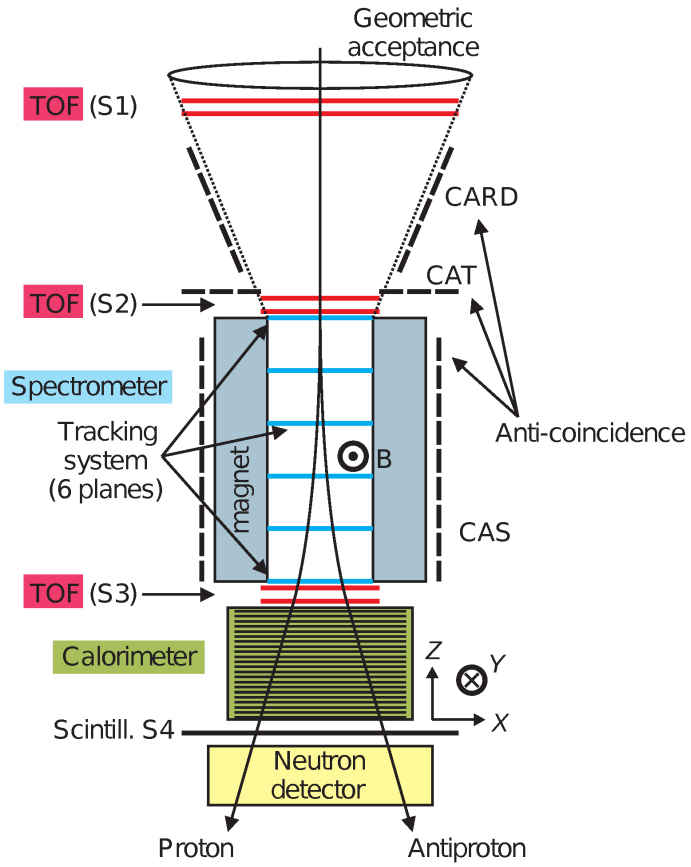

Figure 2.3: A schematic overview of the 1.3 m high PAMELA instrument. All subdetectors are visible: the time of flight system (ToF) , the magnetic spectrometer, the electromagnetic calorimeter, the anticoincidence system (CAS, CAT, CARD), the additional bottom scintillator (S4) and the neutron detector.

(Moscow, Russia). From here, GRID infrastructure is used to transfer raw data to the main storage and analysis center of the PAMELA collaboration, located at CNAF (Bologna, Italy), a specialized computing center of the Italian National Institute of Nuclear Physics (INFN). Here data are accessible to all institutions within the PAMELA collaboration.

The next section is devoted to discuss each PAMELA sub-detector. The basic instrumental features of each device will be discussed together with the key aspects and the detection techniques relevant to the measurement discussed in this work.

2.3 THE PAMELA INSTRUMENT

The PAMELA instrument was designed to optimize the study of the matter and antimatter component in the cosmic radiation. For this

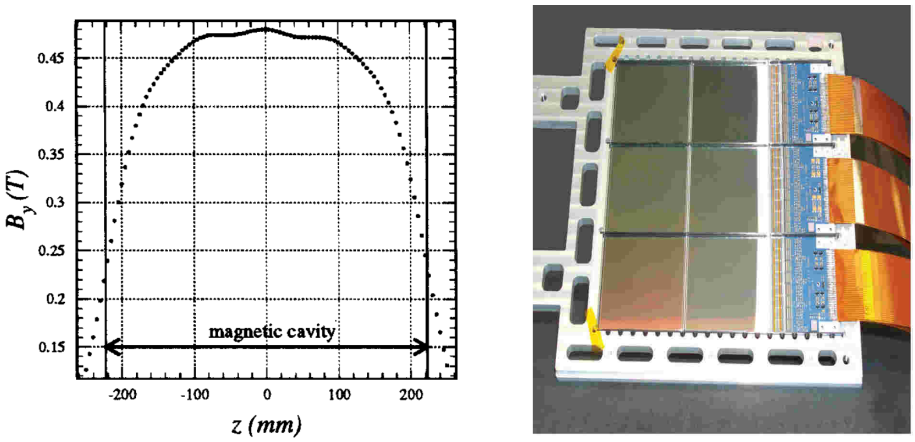

Figure 2.4: Left panel: main component of the magnetic field (B_y) plotted as a function of the z coordinate along the central axis coordinate of the cavity (see Figure 2.3). Right panel: a silicon plane comprising six silicon strip detectors and front-end electronics.

type of investigation, it is necessary to have information about the particle charge, energy and type of interaction from several redundant subdetectors, in order to uniquely identify rare particles from backgrounds as in the case of the positron components which represent only a small fraction of the total CR budget (see Figure 1.1). The PAMELA apparatus, as shown in Figure 2.3, comprises the following subdetectors: a time of flight system (ToF), a magnetic spectrometer, an electromagnetic calorimeter, an anticoincidence system (CAS, CAT, CARD), an additional bottom scintillator (S4) and a neutron detector. The apparatus is $\sim$ 1.3 m high, has a mass of 470 kg and an average power consumption of 355W. The core of the apparatus is the magnetic spectrometer.

THE MAGNETIC SPECTROMETER

The central part of the PAMELA apparatus is a magnetic spectrometer [Straulino et al., 2006] consisting of a permanent magnet and a silicon tracker. The permanent magnet is composed of five modules forming a tower 44.5 cm high. Each module comprises twelve magnetic blocks, made of a Nd-Fe-B alloy with a residual magnetisation of 1.3 T. The blocks are configured to provide an almost uniform magnetic field oriented along the y-direction inside a cavity of dimensions 13.1 $\times$ 16.1 cm^2. The magnetic field has been mapped by means of an FW-Bell9950 gaussmeter equipped with a three-axis Hall probe mounted on an automatic positioning device, see Figure 2.4 (left panel). The dimensions of the permanent magnet define the maximum geometrical factor of the PAMELA experiment to be 21.6 $cm^2 sr$.

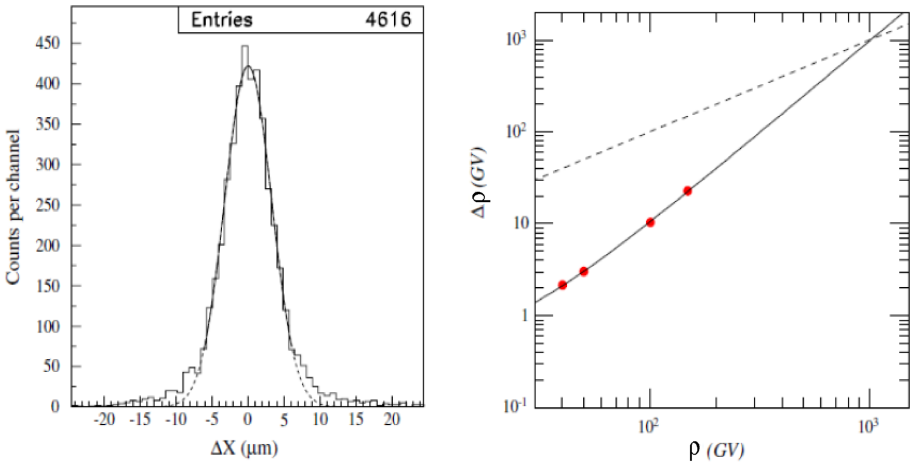

Figure 2.5: Left panel: spatial resolution of the tracking silicon sensors in the bending view. Right panel: reconstructed rigidity versus rigidity uncertainty (solid line). The MDR (see text) is defined as a 100% uncertainty in the rigidity determination corresponding to the interception of the solid line with the bisector (dotted line) at ~ 1 TV.

The five magnetic modules interleave six equidistant 300μm thick silicon detector planes inserted inside the magnetic cavity. The double-sided silicon sensors provide two independent impact coordinates on each plane. The basic detecting unit is the ladder that comprises two sensors, 5.33×7.00 cm^2, assembled with a front-end hybrid circuit, as shown in Figure 2.4 (right panel). Each plane is built from three ladders that are inserted inside an aluminum frame that connects to the magnet canister. Each side is equipped with eight VA1 chips. The VA1 consists of 128 charge sensitive preamplifiers, each connected to a CR-RC shaper and followed by a sample and hold circuitry. The progressive failure of the VA1 chips is reducing the efficiency of track reconstruction as discussed in Section 4.3.

In order to limit multiple scattering in dead layers, no additional supporting structure is present above or below the planes. Each high resistivity n-type silicon detector is segmented into micro-strips on both sides with p+ strips implanted on the junction side (bending, x-view) and n+ strips on the Ohmic side (non-bending, y-view) with the strips orthogonal to those in the x-view. In the x-view, the implantation pitch is 25 μm, 67 μm in the y-view and the read-out pitch is 50 μm for both the views.

The main task of the spectrometer is to measure the magnetic deflection η of charged particles as they pass through a region where a magnetic field is present. The magnetic deflection is defined as the in-

verse of the particle rigidity R. If the rigidity of a charged particle is known, its momentum and charge-sign are derived from:

$$R = \frac{1}{\eta} = \frac{|\mathbf{p}|}{Ze} \tag{2.1}$$

where $|\mathbf{p}|$ and $q = Ze$ are the momentum and charge of the particle, respectively, and c the speed of light. The rigidity is the parameter that unequivocally determines the dynamics of a charged particle in a magnetic field $\mathbf{B}$: charged-particles having different momentum and charge but same rigidity have identical trajectories under the action of the Lorentz force which is expressed as:

$$\mathbf{F} = q\mathbf{v} \times \mathbf{B} \tag{2.2}$$

where $\mathbf{v}$ is the particle velocity. In case of a uniform magnetic field, from Equation 2.2 it can be seen that for a particle with charge q, the projection of the track on the plane perpendicular to $\mathbf{B}$ (the bending plane) is a circle whose radius r is approximately related to the momentum intensity p (expressed in GeV/c) by:

$$p \cdot \cos\lambda \simeq 0.3 \cdot Z \cdot B \cdot r; \tag{2.3}$$

where λ is the angle between p and the plane. However, if the magnetic field is not constant (as in the PAMELA case), in order to obtain the trajectory of a particle with mass m, the relativistic equation of motion has to be solved:

$$m\gamma \frac{d^2\mathbf{r}}{dt^2} = q\left(\frac{d\mathbf{r}}{dt} \times \mathbf{B}\right) \tag{2.4}$$

Where $\gamma = 1/\sqrt{1-\beta^2}$ is the Lorentz factor with $\beta = v/c$ the ratio between the particle velocity and the speed of light. Introducing the path length $l = \beta ct$ and using $p = m\gamma\beta c$, from Equation 2.1 this equation can be rewritten as:

$$\frac{d^2\mathbf{r}}{dl^2} = \frac{q}{m\gamma\beta c}\left(\frac{d\mathbf{r}}{dl} \times \mathbf{B}\right) = \eta\left(\frac{d\mathbf{r}}{dl} \times \mathbf{B}\right) \tag{2.5}$$

Generally, Equation 2.5 can be solved by numerical methods for a certain set of initial conditions, provided that the magnetic field along the trajectory of the particle is known. The deflection η of the particle is calculated by looking for the set of initial conditions which results in the curve that best reproduces the track. More details about the algorithm for deflection determination with PAMELA can be found in [Bongi, 2005]. The resolution in the deflection measurement depends on the geometrical configuration of the spectrometer, on the intensity

of the magnetic field and on the spatial resolution of the silicon sensors. This spatial resolution depends on the particle incidence angle. For normally incident tracks, tests with particle beams showed a spatial resolution of (3.0 ± 0.1) μm and (11.5 ± 0.6) μm in the bending and non-bending views, respectively (see Figure 2.5 left panel). The maximum detectable rigidity (MDR, defined as a 100% uncertainty in the rigidity determination) is ~ 1 TV (see Figure 2.5 right panel). In flight, the deflection measurement of the tracking system was cross-checked with the energy measurement from the calorimeter for high-energy electrons. Finally, ionization loss measurements are also made in the silicon planes, allowing absolute particle charge to be determined up to $Z = 6$.

Since an up-going positive particle is bended as a down-going negative particle inside the same magnetic field, to determine the electric charge-sign the direction of motion has to be measured. Moreover, when the absolute value of the charge is determined, the momentum can be calculated from Equation 2.1. The Time of Flight (ToF) system measures the velocity, the direction and the absolute charge of incoming CRs.

TIME OF FLIGHT

The ToF system [Osteria et al., 2004] comprises of six layers of fast plastic scintillators arranged in three double planes (S1, S2 and S3), with alternate layers placed orthogonal to each other as shown in Figure 2.6. The distance between S1 and S3 is 77.3 cm. The sensitive area of each of the two S1 layers is 33 cm $\times$40.8 cm with the first layer divided into 8 bars and the second layer divided into 6 bars. The total sensitive area of the S2 and S3 planes is 15 cm $\times$18 cm segmented into 2×2 and 3×3 orthogonal bars, respectively. The S1 and S3 layers are 7 mm thick while the S2 layers are 5 mm thick. There are 24 scintillator bars in total. Both ends of each scintillator bar are glued to a plastic light guide which is mechanically coupled to a photomultiplier by means of silicone pads. The ToF electronics system converts the 48 photomultiplier (PMT) pulses into time- and charge-based measurements. The intrinsic time resolution of each ToF paddle was measured in different experimental situations to be about 120 ps. A typical time resolution plot is shown in Figure 2.7. The experimental points are well reproduced by a Gaussian distribution.

The ToF system measures the flight time of particles crossing its planes. Once flight time is combined with the measurement of the particle trajectory length, the CR velocity can be derived. The multi-

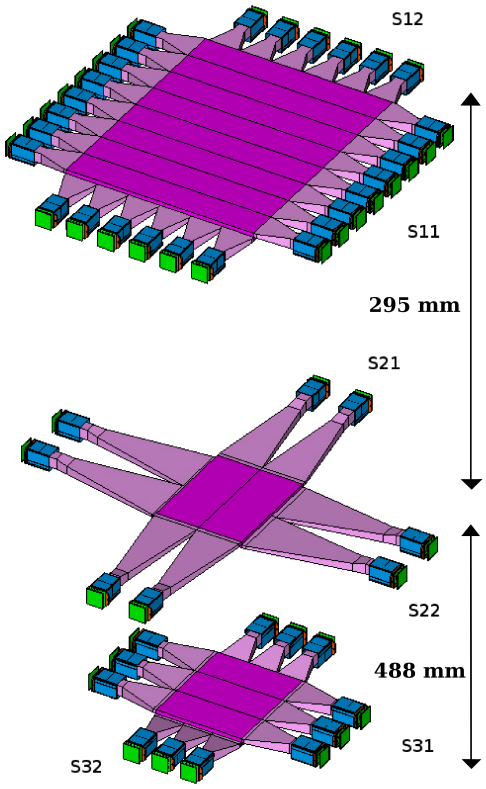

Figure 2.6: Isometric view of the ToF telescope.

ple measurement of the energy loss dE/dx in the scintillator counters allow the particle charge (Z) to be determined up to $Z = 8$.

The ToF system acts as the main PAMELA trigger [Osteria et al., 2004] by identifying coincidental energy deposits in the scintillators (S1&S2&S3). Other trigger configurations (e.g. S2&S3) are activated in regions with high particle fluxes (polar regions and radiation belts, see Section 3.2 and Figure 4.1), where the S1 scintillators would be continuously saturated. The segmentation of each plane allows redundant studies of the trigger efficiency. Once the rigidity and the charge-sign are determined, leptons are separated from hadrons by analyzing the shower development originating by the incoming particle inside the calorimeter.

ELECTROMAGNETIC CALORIMETER

Figure 2.8 shows the PAMELA imaging calorimeter. This detector is a sampling calorimeter made of silicon sensor planes interleaved with plates of tungsten absorber. The application of silicon detectors as active layers for sampling calorimeters is a well established technique in

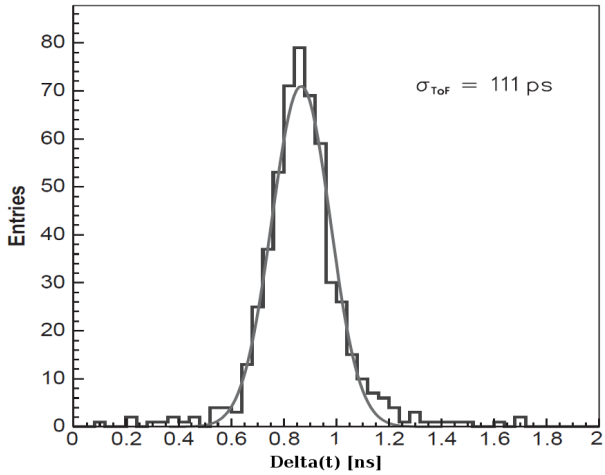

Figure 2.7: Time resolution of a time of flight paddle.

experimental high-energy physics. Among the advantages of these detectors are excellent stability, linearity, efficiency, and low-voltage operation. These features allow their use in cosmic-ray experiments on satellites.

The instrument was designed to have a high segmentation, both in the longitudinal (Z) and in the transversal (X and Y) directions. In the Z direction, the granularity is determined by the thickness of the layers of absorbing material. Each tungsten layer has a thickness of 0.26 cm, which corresponds to 0.74 X_0 (radiation lengths, see Equation A.3). Since there are 22 tungsten layers, the total depth is 16.3 X_0 (i.e. about 0.6 interaction lengths, see A.11). The depth of the instrument is not sufficient to fully contain high-energy electromagnetic showers. However, the granularity, along with the energy resolution of the silicon detectors, allows an accurate topological reconstruction of the shower development, making the calorimeter a powerful particle identifier. The transverse granularity is given by the segmentation of the silicon detectors into strips. The silicon detectors for the PAMELA calorimeter are large area devices (8×8 cm^2 each), 380 μm thick and segmented into 32 large strips with a pitch of 2.4 mm.

Each tungsten plane is sandwiched between two layers of silicon detectors, i.e. the layout of a single plane is Si-X/W/Si-Y. Either type of view (X or Y) is made by nine silicon detectors, arranged in a square matrix of 3×3 detectors. The total sensitive area is about 24 cm $\times$24 cm. Each of the 32 strips of a detector is connected to those belonging to the other two detectors of the same row (or column) forming 24 cm long strips. The number of electronics channels per plane is $32 \times 3 \times 2 = 192$ and the total number of channels is $192 \times 22 = 4224$.

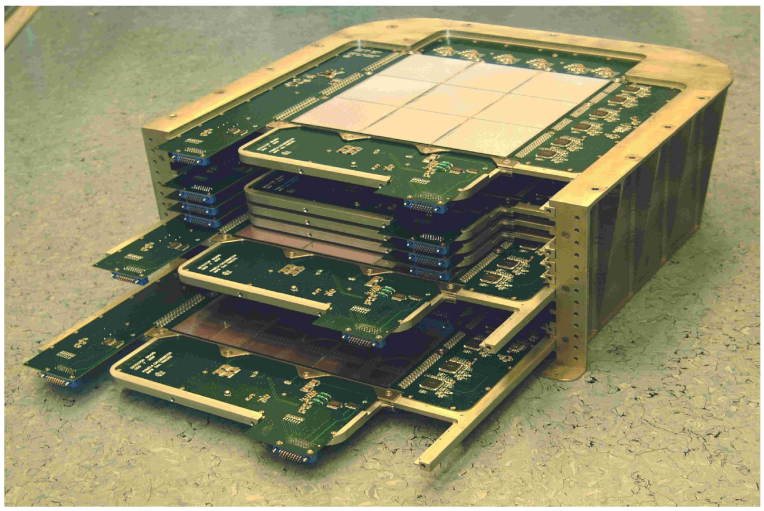

Figure 2.8: The PAMELA calorimeter. The device is ~ 20 cm tall and the active silicon layer is ~ 24 cm ×24 cm in cross-section. The silicon detectors arranged in a square matrix of 3×3 detectors are visible. Each of the visible module module comprised two tungsten layers each sandwiched between two silicon detector planes.

The longitudinal and transverse segmentation of the calorimeter combined with the measurement of the energy lost by the particle in each silicon strip results in a high identification power for electromagnetic showers. Appendix A summarizes the basic features of the electromagnetic and hadronic shower development in matter. Many specific features related to the shower development inside tungsten (see Table A.1) and to the PAMELA calorimeter (see Table A.2) are also introduced. In Section 3.3 several quantities based on the hadronic and electromagnetic shower development are defined in order to achieve enough identification power to extract a clean sample of electrons and positrons. The hadron background (especially secondary pions, see Section 3.2) can be reduced also applying a selection on the anti-coincidence system.

ANTI-COINCIDENCE

Simulations have shown that the majority (~ 75%) of triggers in orbit are "false" triggers, i.e. where coincidental energy deposits in the time of flight scintillators are generated by the passage of primary CRs (see South Atlantic Anomaly, Section 4.1) or by secondary particles produced in the mechanical structure of the experiment as illustrated in Figure 2.9 (second panel). The anti-coincidence systems can be used to identify these events in the off-line data analysis. The PAMELA instrument contains two anticoincidence (AC) systems. The primary

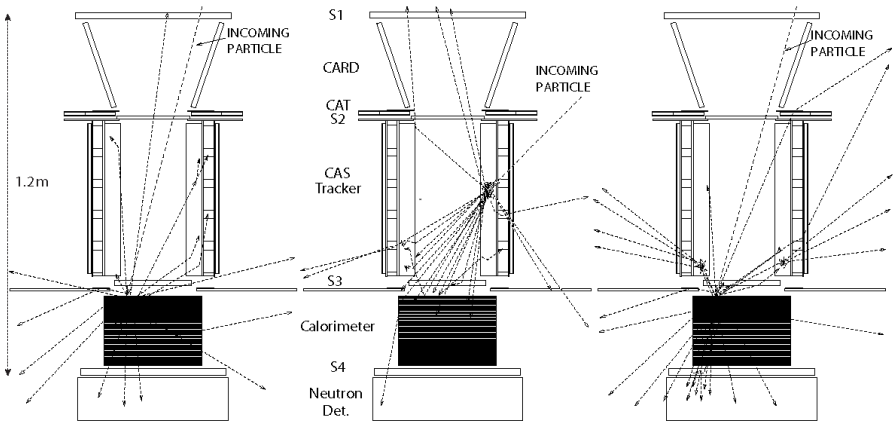

Figure 2.9: Visual representation of simulated proton interactions in the experiment. Left: good trigger event. A particle entering the tracker cavity from the sides may give rise to particle showers that trigger the experiment (false trigger, center). False trigger events are often characterized by activity in the AC detectors, as are good trigger events with backscattering from the calorimeter (right).

system consists of 4 plastic scintillators (CAS) surrounding the sides of the magnet and one covering the top (CAT), as shown in Figure 2.3. A secondary AC system consists of 4 plastic scintillators (CARD) that surrounds the volume between the first two time-of-flight planes. The CARD detectors are scaled-down versions of CAS. The AC systems use 8 mm thick plastic scintillators read out by photomultipliers. Each scintillator is covered in reflective material and coupled via a 7 mm thick silicone pad to the PMTs. Each CAS and CARD detector is read out by two identical PMTs in order to decrease the possibility of single point failure. For this reason, and to cover the irregularly shaped area, the CAT detector is read out by 8 PMTs. The AC system is extensively used in this analysis to reject multi-particle events produced from the interaction of primary hadron with the material above the instrument (see Section 3.3).

S4 and NEUTRON DETECTOR

The shower tail catcher scintillator (S4) improves the PAMELA electron-hadron separation performance by measuring shower leakage from the calorimeter. This scintillator is placed directly beneath the calorimeter. It consists of a single square piece of 1 cm thick scintillator of dimensions 48 cm $\times$48 cm which is read out by six PMTs (Figure 2.10, left panel).

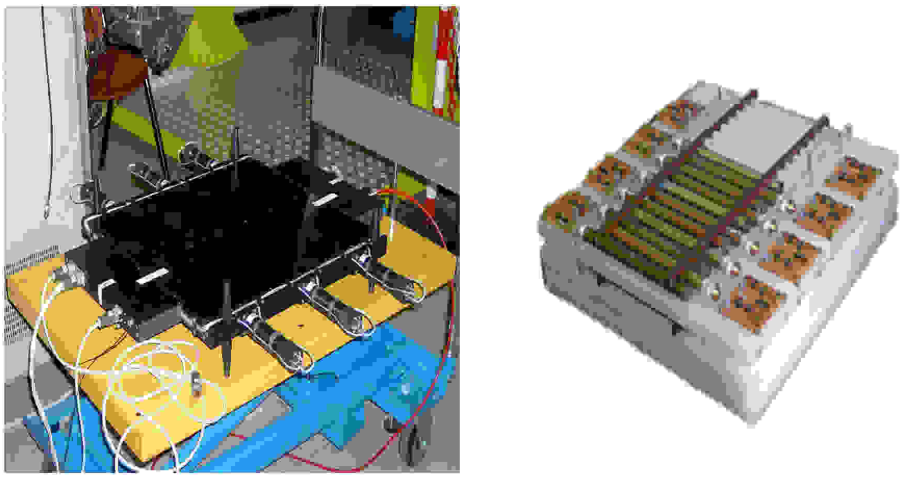

Figure 2.10: Left panel: the shower tail catcher scintillator S4. The scintillator has dimensions 48×48 cm^2. Right: The neutron detector partially equipped with 3He proportional counters. The neutron detector covers an area of 60×55 cm^2.

The neutron detector (Figure 2.10, right panel) is located below the S4 scintillator and consists of 36 proportional counters, filled with 3He and surrounded by a polyethylene moderator enveloped in a thin cadmium layer to prevent thermal neutrons entering the detector from the sides and from below. The counters are stacked in two planes of 18 counters, oriented along the y-axis of the instrument. The size of the neutron detector is $60 \times 55 \times 15$ cm^3. The neutron detector complements the electron-proton discrimination capabilities of the calorimeter. However in this analysis the neutron monitor was not used.

The information provided by each PAMELA subdetectors can be combined to select a specific component of the cosmic radiation. The next chapter is devoted to describe the selection Criteria based on each PAMELA subdetectors for the positron and electron identification.

3 ELECTRON AND POSITRON SELECTIONS

INDEX

Since June 2006 PAMELA has been almost continuously taking data. As discussed in the previous chapter the magnetic spectrometer is the core of the PAMELA apparatus and allows to discriminate positively from negatively charged particles and to precisely measure the rigidity of CRs up to oxygen nuclei. As discussed in the first chapter approximately 90% of the CR are protons. Electrons account only for a small fraction of the CR budget (~ 1%) and the positron to proton ratio is between 10^{-3} and 10^{-4} depending on the energy. In order to select positrons among the vast hadron background an extremely good rejection power was needed. The selection of electron and positron was performed exploiting the informations coming from the PAMELA sub-detectors. In this chapter the entire set of electron and positron selections will be discussed. The background sources will be described together with the estimation of any residual contamination.

3.1 PRIMARY BACKGROUND

Positrons and electrons represent only a small fraction of the data collected by PAMELA. In order to obtain reliable fluxes, all the sources of contamination were carefully studied.

- **Antiprotons**: are a small but not negligible component of the cosmic radiation. As positrons they can be produced by CR nuclei interacting with the interstellar matter. Exotic sources of primary antiprotons such as the annihilation of dark matter particles [Delahaye et al., 2012] and the evaporation of primordial black holes could also contribute to the antiproton signal. The Galactic antiproton component represents a contamination for the electron

signal of a few percent over the entire rigidity range. The contamination coming from secondary production of antimatter with an absolute charge $Z > 1$, is negligible. For example Chardonnet et al. [1997] predicted, for the ratio between secondary antideuterium nuclei and primary protons, a value of the order of 10^{-9}. In the case of antihelium nuclei the ratio was predicted to be of the order of 10^{-13}.

- **Protons**: represent the major contamination for positrons. Since the positron to proton ratio was about 10^{-3} - 10^{-4} (e.g. see Figure 1.1) a robust identification power was needed to extract a clean positron signal. The PAMELA calorimeter allows for an extremely good separation between leptons and hadrons.
- **Helium, nuclei**: helium and heavier nuclei contaminate the positron signal. They account for approximatively the 8% of the total CR budget. However the tracker and the ToF system allow an excellent charge separation using the information on the ionization energy release.

Primary CRs are only one component of the total contamination. A large quantity of secondary particles are produced locally in the atmosphere by the primary CRs which interacts with the atmosphere. These interactions produce particle showers in the atmosphere, including positrons and electrons. Using the PAMELA orbital informations it was possible to separate the Galactic from the atmospheric lepton component.

3.2 SECONDARY BACKGROUND

Primary CRs produce secondary particles interacting with the atmosphere and, locally, with the dome above the PAMELA instrument. Secondary particles comprise protons, antiprotons, pions, heavy nuclei, electrons and positrons. The propagation of secondary particles close to the Earth, as well as that of the primary CRs, is profoundly influenced by the Earth's magnetic field.

GEOMAGNETIC CUTOFF

Charged particles traversing a magnetic field undergo a vector force that results in a curved path. CRs originating from outer space tend to be deflected away via the Lorentz force when they approach the Earth's magnetic field. Essentially the Earth's magnetic field acts as a shield against Galactic CRs. However, the tendency to be deflected is

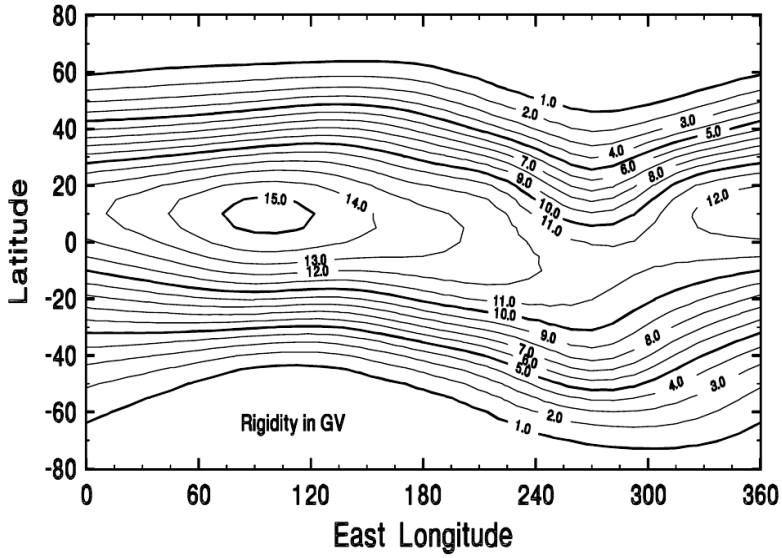

Figure 3.1: Contour maps of universal time averaged computed vertical cutoff rigidities for a 450-km orbiting spacecraft. Picture taken from [Smart and Shea, 2004].

opposed to some extent by the particle's momentum. More precisely the ability of a particle to penetrate into the geomagnetic field depends upon its rigidity (see Equation 3.1). Geomagnetic cutoff rigidities are a quantitative measure of the shielding provided by the Earth's magnetic field and correspond to the minimum rigidity required to reach a certain point in the magnetosphere. Particles with less rigidity than the geomagnetic cutoff will be deflected before reaching that location and cannot be detected.

Approximating the Earth magnetic field as a geocentric dipole field and assuming a vertical direction for the incoming particles, the (vertical) geomagnetic cutoff rigidity in the Störmer theory is given by:

$$R_{\perp} = \frac{M \cos^4 \lambda}{4r^2} \tag{3.1}$$

where M represents the Earth magnetic dipole moment, r the distance from the dipole center (in units of Earth radii) and λ the magnetic latitude. Figure 3.1 shows the vertical geomagnetic cutoff for an altitude of 450 km computed using the International Geomagnetic Reference Field (IGRF) model for the Earth magnetic field [IGRF]. The IGRF is a spherical harmonic model with coefficients derived from satellites and ground-based instruments for which every five years a new set of parameters is released by the International Association of Geomagnetism and Aeronomy (IAGA).

Detection of CRs in the Earth proximity is largely influenced by the presence of the geomagnetic cutoff. Figure 3.1 shows that low rigid-

ity CRs (< 1GV) can be detected only at high terrestrial latitudes near the poles. PAMELA spends only a small fraction of its total lifetime at these latitudes and consequently the low energy CR statistics were proportionally lower. A vertical cutoff rigidity is associated at each PAMELA position. The accuracy of this value depend on the model used for the Earth's magnetic field and the precision of the orbital information.

The Earth's magnetic field affects also the propagation of the atmospheric secondary particles.

ALBEDO COSMIC RAY

The term albedo cosmic rays is used for those particles produced by interactions of primary CRs in the Earth atmosphere and escaping from it. Albedo particles are classified depending on the type of trajectories followed from the production site:

- **Splash albedo**: are particles leaving the atmosphere and moving upwards. If splash albedo are produced with an energy greater than the local geomagnetic cutoff rigidity they are able to escape from the magnetosphere. If their energy is lower than $R_\perp$ they become re-entrant albedo particles. Splash albedo were reconstructed by PAMELA ToF system as particles with a $\beta < 0$, see Figure 3.2, and were easily rejected requiring $\beta > 0$.

- **Re-entrant albedo**: this term is used for downward moving particles with rigidities lower than the corresponding geomagnetic cutoff. This population consists of splash albedo particles produced with rigidities below the local geomagnetic cutoff which are able to spiral along the magnetic field lines and reenter the atmosphere in the opposite hemisphere of the Earth at about the same magnetic latitude. The intensity of splash and re-entrant albedos are expected to be of the same order. The re-entrant albedo particles concentrate in the near equatorial region, inside and below the inner Van Allen belt[1]. Re-entrant albedo can be rejected selecting CRs with a rigidity greater than the local geomagnetic cutoff. However in the present analysis the Galactic CR selection was not performed here, but after the flux estimation and will be described in Section 4.5.

1 A radiation belt corresponds to a layer of energetic charged particles that is held in place around the Earth by the planet's magnetic field. The Earth has two belts: the inner belt consists largely of high energy (> 80 MeV) secondary atmospheric protons and electrons while the outer belt consists mainly of electrons. The inner region is centered approximately 3000 km above the terrestrial surface while the outer region is centered at an altitude of about 15000 km.

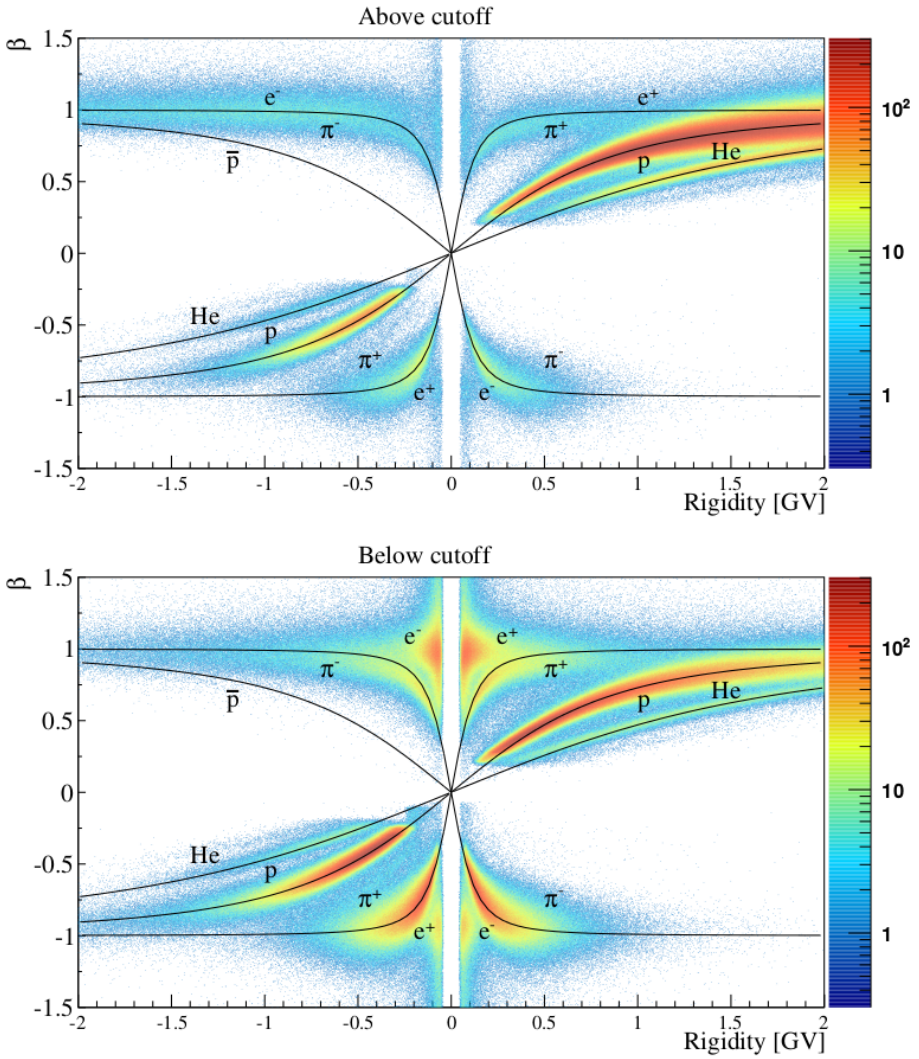

Figure 3.2: Top panel: beta (v/c) versus rigidity distribution for particles with rigidities above the geomagnetic vertical cutoff selected from flight data collected from July 2006 to December 2009. Down-going (positive beta) protons, electrons, positrons, helium and antiprotons represent the Galactic CR component. Up-going particles (negative beta), which are reconstructed with the opposite rigidity sign, correspond to splash albedo. Spectral features, composition and intensity of the splash albedo particles are significantly affected by the passage through the calorimeter. Most of the up-going particles are secondary products coming from electromagnetic or hadronic showers. The lepton component is almost completely suppressed while hadrons are still present. Down-going pions are produced by primary protons interacting with the aluminum dome above the apparatus while up-going pions come from the calorimeter.
Bottom panel: sub-cutoff beta distribution (flight data). Down-going particles correspond to re-entrant albedo CRs. A slight excess of positrons can be noticed. Splash albedo intensity of electrons, positrons and protons, as in the top panel, is strongly suppressed because of the calorimeter.

Albedo electrons and positrons are produced from the interactions of protons and nuclei with residual atmospheric nuclei through the decay chains $\pi^{\pm} \rightarrow \mu^{\pm} \rightarrow e^{\pm}$ and $K^{\pm} \rightarrow \mu^{\pm} \rightarrow e^{\pm}$. Depending on the primary proton energy, the cross section for π^{+} production is 1–2 times greater than for π^{-}, and so positrons are expected to dominate. A slight excess of positrons can be noticed in Figure 3.1 (bottom panel). Also albedo protons, antiprotons and helium are produced. PAMELA measurements on re-entrant albedo reveal an intensity one order of magnitude greater than the Galactic component for the electrons and two order of magnitude for positrons [Adriani et al., 2009b]. In order to derive reliable fluxes rigorous separation of the albedo component is thus necessary.

PION CONTAMINATION

Before being detected, Galactic CRs traverse the mechanical structures of the upper part of the PAMELA apparatus, in particular the aluminum pressurized top container. A small fraction of protons and heavier nuclei undergo nuclear interactions and secondary charged particles are created, see Figure 3.3. Because of the abundant proton flux the amount of secondary particles represent a non-negligible contamination. High energy interacting protons and heavier nuclei produce multi-particle shower with many pions and because of charge conservation an excess of π^{+} is expected, see Figure 3.4. Also electrons and positrons are created, however simulations show that the contamination from these secondary particles was about three orders of magnitude less than secondary pions, being negligible over the entire energy range, see Figure 3.4. A first selection was made on the number of the reconstructed tracks in the track system selecting only single-track events. This selection reduced significantly the pion contamination. However very tilted protons can produce a single pion traversing the tracking system with high transverse momentum, as illustrated in Figure 3.3. In this case the single track selection was not sufficient and additional selections on the anti-coincidence system and the calorimeter were needed, see next section.

Contamination from secondary pions was already studied in previous work [Bruno, 2009] using PamVMC, the official PAMELA collaboration simulation tool based on the GEANT package 4 [GEANT4]. PamVMC precisely reproduces the entire geometry and material composition of the PAMELA sub-detectors. The proton flux measured by PAMELA was used to generate events impinging on the aluminum top container and the resulting energy spectrum of secondary pions was estimated. The simulation was validated by selecting a sample of π^{-}

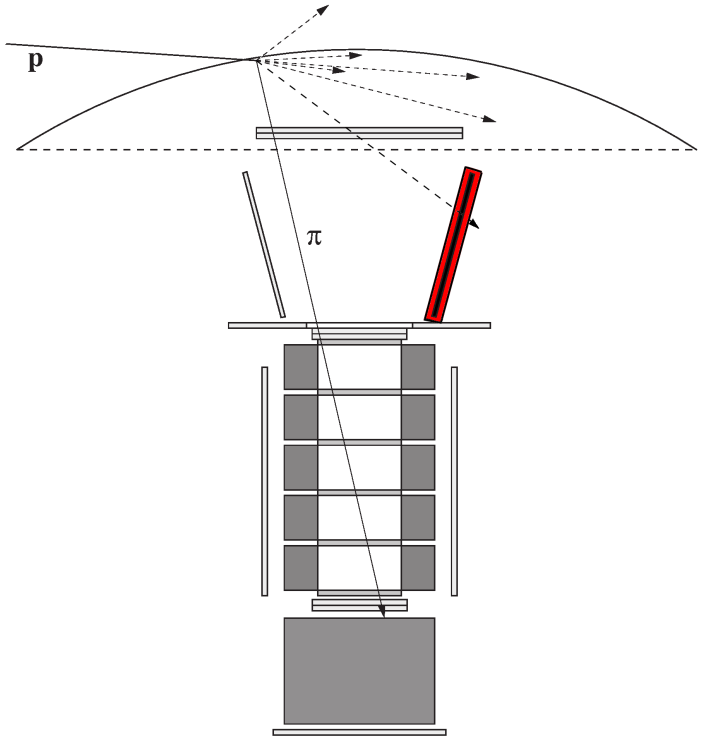

Figure 3.3: Illustration of a proton CR interacting with the PAMELA pressurized container and originating a shower of secondary particles. A single pion with high transverse momentum is produced inside the PAMELA acceptance.

from flight data below 1 GV. Figure 3.4 shows the rigidity spectrum for locally produced positive and negative pions originating from a very large statistic of Monte Carlo protons. Only events with a single track in the tracking system were selected. More than $3.5 \cdot 10^{11}$ events, corresponding to 7 years of data taking, were simulated. The pion spectrum peaks around 1 GV and decreases as the energy increases. Moreover, as the energy of the primary particle increases, the transverse momentum $p_\perp$ of the secondaries increases as well. However the ratio between the transverse and the total momentum $p_\perp/p$ decreases as the energy increases and particles are boosted in the forward direction. As a consequence the probability to produce particles inside the instrumental acceptance decreases as the energy increases. For this reason the secondary pion intensity was expected to decrease faster than the primary proton intensity and above few GV pion contamination becomes negligible for both positive and negative rigidities. Finally, since the electron flux was approximatively ten time smaller than the positron one, and since an excess of positive pions was expected, the ratio between positrons and positive pions will be at least ten times higher than elec-

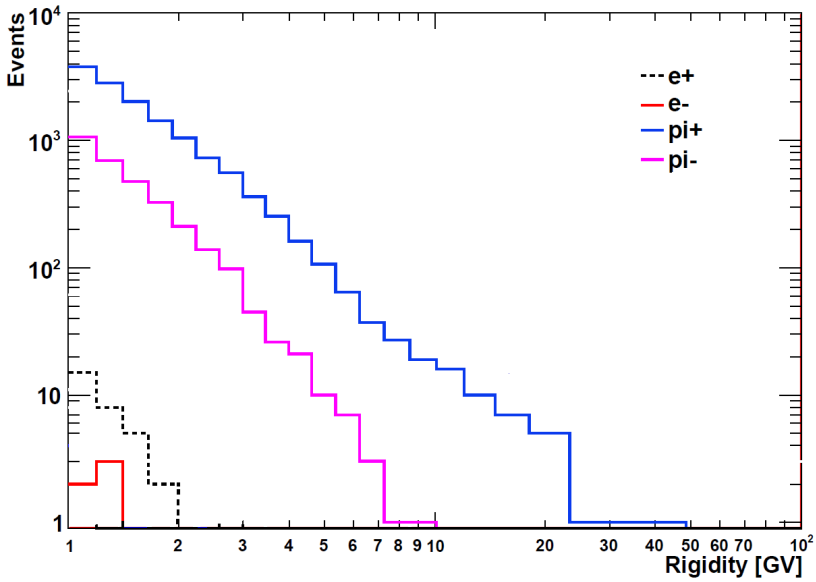

Figure 3.4: The rigidity distribution of locally produced positive (blue line) and negative (magenta line) pions between 1 and 100 GV from Monte Carlo data. These distributions are obtained after having applied the single track selection. Secondary positrons (black dotted line) and electrons (red line) are also shown. Since secondary particles are mainly produced by primary protons and helium nuclei, due to charge conservation, more positive pions (about a factor four) respect to negative pions are produced, as well as more positrons respect to the electrons. Figure adapted from [Bruno, 2008]

trons and negative pions. For these reasons, as will be explained in Section 3.3, more stringent calorimeter selections were needed for the positron selection.

SPILLOVER PROTONS

These events included high energy protons to which the wrong sign of the curvature was assigned due to the intrinsic deflection uncertainty in the spectrometer measurements; protons that scattered in the material of the tracking system mimicking the trajectory of negatively charged particles and events with spurious hits in the tracker planes causing a wrong reconstruction of the curvature. The last two effects were the dominant causes for protons reconstructed with low negative rigidities. This contamination comprises two categories of events:

- **"Positive" protons**: are mostly relativistic events with a correct determination of the charge sign and an incorrect assignment of the energy. Most of these events are high energy (> few GV) non-

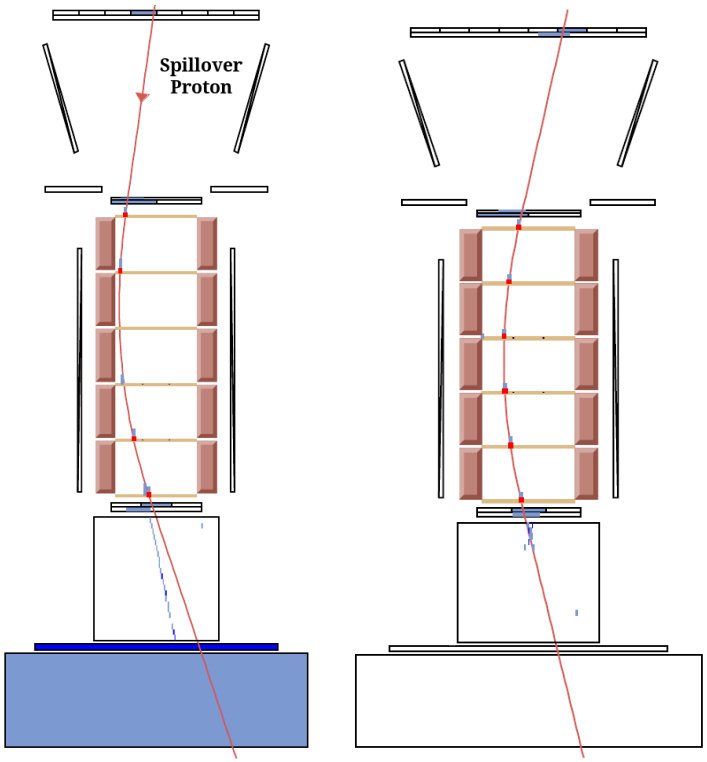

Figure 3.5: Left panel: a 100 MeV event selected as a spillover proton from flight data. The bending (x) views is shown. A plan view of PAMELA is shown in the center. The signals as detected by the PAMELA detectors are shown along with the particle trajectory (red solid line) reconstructed by the fitting procedure of the tracking system. The energy release pattern in the calorimeter suggests that this particle is an high energy (> few GeV) proton. However, due to spurious hits in the tracker plane, this relativistic p was reconstructed as a low energy particle with negative rigidity. Right panel: the event display of an ~ 120 MV event selected as electron from flight data.

interacting protons reconstructed as low energy (< few hundreds MV) events.

- **"Negative" protons**: are mostly relativistic events with incorrect determination of both the charge sign and energy. Protons that scattered in the material of the tracking system can mimic the trajectory of negatively charged particles. For example Figure 3.5 shows a relativistic proton which was reconstructed as a negatively charged particle of 100 MV.

Spillover protons were significant at low rigidities below 600 MV and above ~ 20 GV. The amount of contamination highly depends on the quality of the reconstructed track. The less the number of hits on the

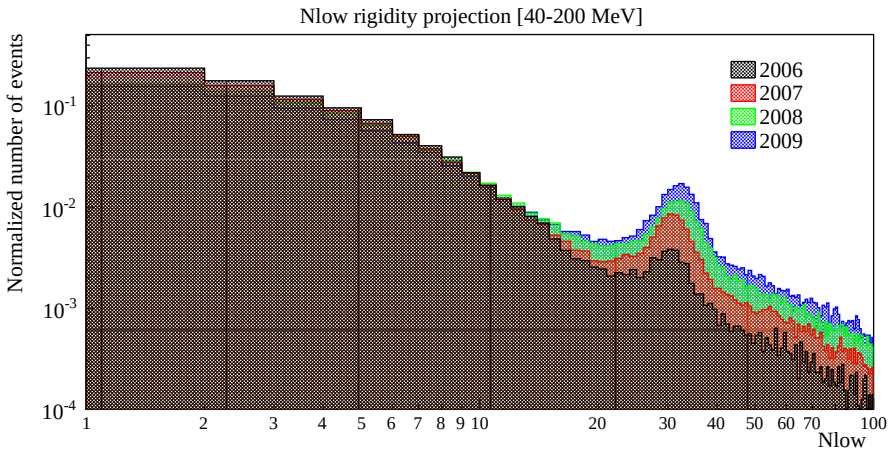

Figure 3.6: Normalized distribution for the Nlow rigidity projection for events selected between 40 and 200 MV from flight data collected from July 2006 to December 2009. The distribution refers to flight data which survived selection Criteria 1-11. Colors represent data collected during different time periods. It follows from the definition of Nlow (see Section 3.3) that the spillover proton contamination peak around Nlow $30-35$ and increases with time as explained in the text.

x-view the higher the probability that noisy strips could be taken as good points for the fit of a highly bended track. Spillover protons represent a contamination of $\sim$ 5% in 2006 increasing to more than 30% in 2009. This can be ascribed to the deterioration of the tracker performance due to the progressive failure of the read-out chips with time. In 2006 most of the events have 5 or 6 hits in the x-bending view thus the probability to reconstruct a fake track due to spurious hits was very low. In 2009 the majority of the events had only 3 or 4 hits on the x-bending view hence the probability to use a spurious hit in the track reconstruction was higher. Figure 3.6 represents the flight data rigidity projection of a calorimeter variable called Nlow during different time periods. This variable was created to discriminate the spillover proton from the lepton component (see next Section for a detailed description of Nlow). The Nlow projection clearly shows a peaked structure due to the spillover protons as well as the increase with time of the contamination. Spillover protons are rejected combining several calorimeter selections.

Once all the contamination sources were well understood the information coming from each sub-detector was combined to reject the background and select a clean sample of positrons and electrons.

3.3 PARTICLE SELECTIONS

PAMELA sub-detectors allow to select electrons and positrons from the vast hadron background with a negligible residual contamination. Electrons and positrons are fully relativistic over the entire energy range (70 MeV - 50 GeV) contrarily to the protons and pions which become relativistic above ~ 1 GV and ~ 200 MV respectively. Below these energies leptons were selected using the ToF beta velocity and the ionizing energy released in the tracker plane. However when protons and pions become relativistic these selections were not sufficient anymore. Exploiting their different interactions in the calorimeter was used to discriminate relativistic hadrons from leptons with high precision. The PAMELA calorimeter measures with great accuracy the shower profile of secondary particles originating from primary CRs interacting with the tungsten planes. A large class of variables based on the shower topological development and the energy deposit pattern were created. Appropriate selections on these quantities permitted the separation of the electromagnetic from the hadronic showers. In this section the role of each sub-detector for particle identification is described.

TRACKING SYSTEM

The tracking system is the core of the PAMELA apparatus. The silicon micro-strips measure with high resolution the impact points of the incoming particles and make possible a precise determination of the particle curvature which, combined with the knowledge of the magnetic field inside the cavity, allows the determination of the particle rigidity. If the incoming direction of the particles is known (ToF system), the sign of the charge is thus determined. A set of basic criteria are applied in order to have events with reliable measurements of the sign and absolute value of the particle rigidity.

- 1) **Single track**: a single track fitted within the spectrometer fiducial volume where the reconstructed track was at least 1.5 mm away from the magnet wall was required. Multi-tracks events were significantly reduced with this selection. The track containment at 1.5 mm was intended to reject events that eventually hit the magnetic wall for which the measured curvature was not a reliable estimation of the real rigidity. For example high energy CRs initially outside the instrumental acceptance can hit the magnetic wall, change their direction and be reconstructed as highly bended (low energy) particles. A fraction of the spillover protons belonged to this category of events and were reduced with the containment requirement.

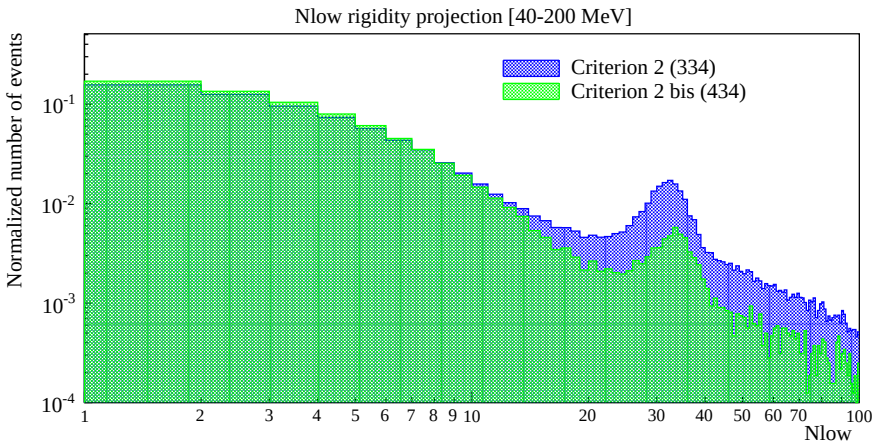

Figure 3.7: Comparison between the normalized Nlow rigidity distribution for events selected with either Criterion 2 or 2bis from flight data collected from January 2009 to December 2009. The more stringent Criterion (2bis) reduces significantly the spillover proton contamination.

- 2) **Impact points**: at least three points were needed to reconstruct the curvature of a charged particle inside the magnetic field. The less restrictive request adopted in this analysis was to select tracks with at least three hits on the bending x-view, at least three hits on the non-bending y-view and a track lever-arm of at least four silicon planes. For simplicity this selection will be referred to as 334. This selection ensures the maximal efficiency but increases the probability that noisy strips could be taken by the fit procedure as good points of a highly bended track (spillover protons). In order to decrease the low energy spillover proton contamination a different selection was performed.

- 2 bis) A more stringent Criterion requires at least four hits on the bending x-view, at least three hits on the non-bending y-view and a track lever-arm of at least four silicon planes (434 selection). The efficiency of this selection is lower with respect to Criterion 2, especially in 2008 and 2009. However 2 bis allows to reduce significantly the spillover proton contamination. Figure 3.7 shows the comparison between the Nlow projection for flight events surviving either Criterion 2 (blue shaded area) or Criterion 2bis (green shaded area). From this figure is clear how the spillover proton component is significantly reduced with Criterion 2bis. Criterion 2bis was used to estimate the electron and positron fluxes up to 600 MeV while Criterion 2 was used elsewhere.

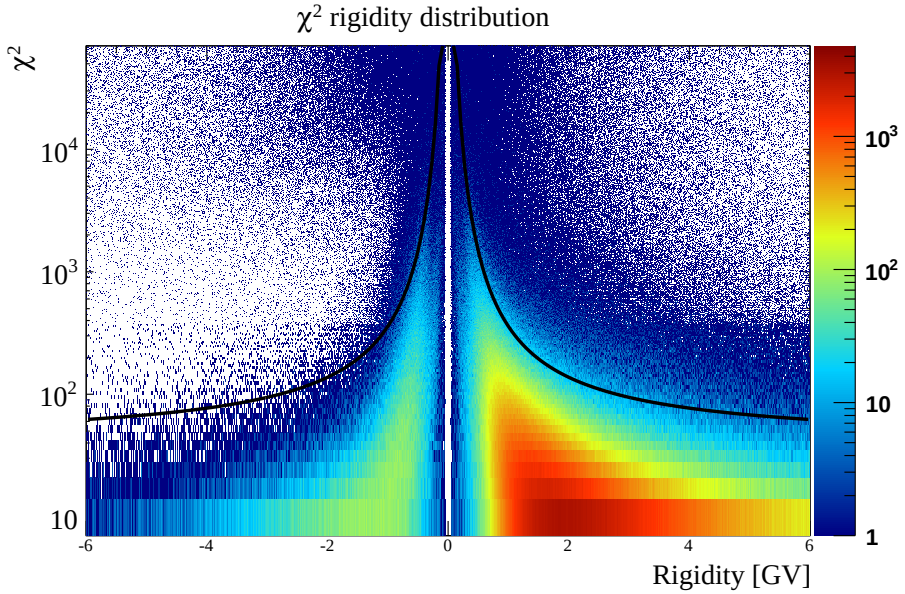

Figure 3.8: Rigidity dependence of the χ^2 distribution for flight data collected from July 2006 to December 2009. The χ^2 increases with decreasing rigidity because of the effect of multiple scattering. The black lines represent the upper limits of the constant efficiency cut performed to select good reconstructed tracks.

- 3) **Quality track**: the goodness of the track is expressed in terms of the χ^2 of the fitting algorithm. Figure 3.8 represents the χ^2 versus rigidity distribution for flight data. The black lines represent the upper limit for the selection performed to exclude tracks which were not well reconstructed. The chosen threshold is not constant but it depends on rigidity to account for increases of χ^2 due to the effect of multiple scattering at low energy, see Equation A.8. Above a few GV the multiple scattering becomes negligible and the χ^2 decreases to values less than one. The selection is defined to have constant efficiency over the entire energy range.

- 4) **Tracker dE/dx selection**: each tracker plane is able to measure independently the mean ionization energy losses (dE/dx). A constant selection on the mean value of dE/dx is performed in order to select relativistic particles. In terms of minimum ionizing particle units only CRs with dE/dx < 1.8 MIP[2] were selected. Figure 3.9 shows the dE/dx selection for experimental data passing selection Criteria 1-2-3. This selection rejects the $Z > 1$ particles as illustrated by the dE/dx distribution. The dE/dx cut allows

2 Energy loss is expressed in terms of MIP that is the energy released by a particle which mean energy loss rate in matter is minimum (see Appendix A).

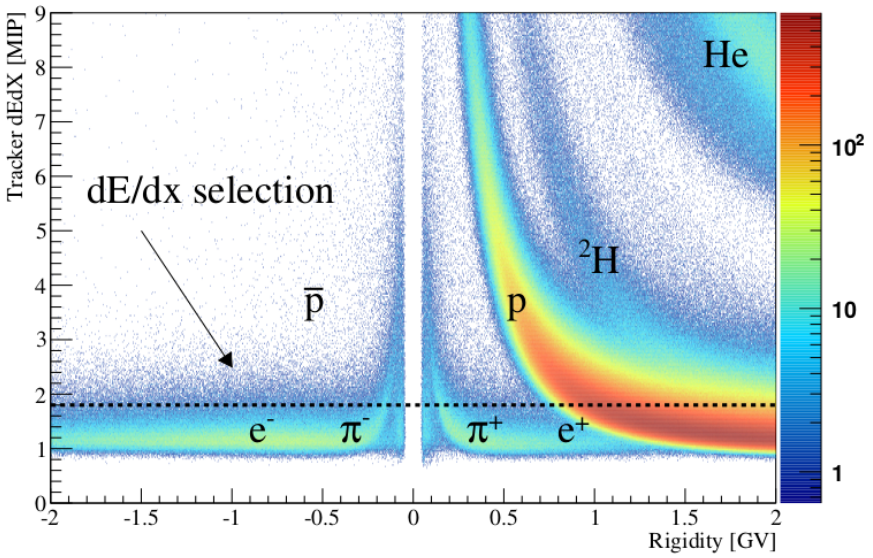

Figure 3.9: Rigidity dependence of the mean ionization energy losses in the tracker plane for flight data collected from July 2006 to December 2009. The various particles species are clearly visible. The selection is indicated by the black dotted line and it rejects the $Z > 1$ particles in the whole energy range, protons and pions up to ~ 800 MV and ~ 200 MV respectively.

to reject pions up to ~ 200 MV and proton up to 800 MV. Above this energy protons and pions become relativistic and the dE/dx selection was not sufficient. Spillover protons were unaffected by the energy selection since they are relativistic in the whole rigidity range.

Figure 3.10 (second panel) shows the beta versus rigidity distribution after the selection Criteria 1-4. The helium component entirely disappeared while protons are rejected only below 800 MV. A residual pion contamination below 200 MV is still present. Anti-coincidence and ToF system selections reduce this residual contamination to a negligible amount. Pions above 200 MV, protons and antiprotons above 800 MV are handled with the calorimeter selections.

ANTI-COINCIDENCE SELECTIONS

The main purpose of the anticoincidence system was to reject spurious events in the off-line phase. Two different selections were applied depending on the energy:

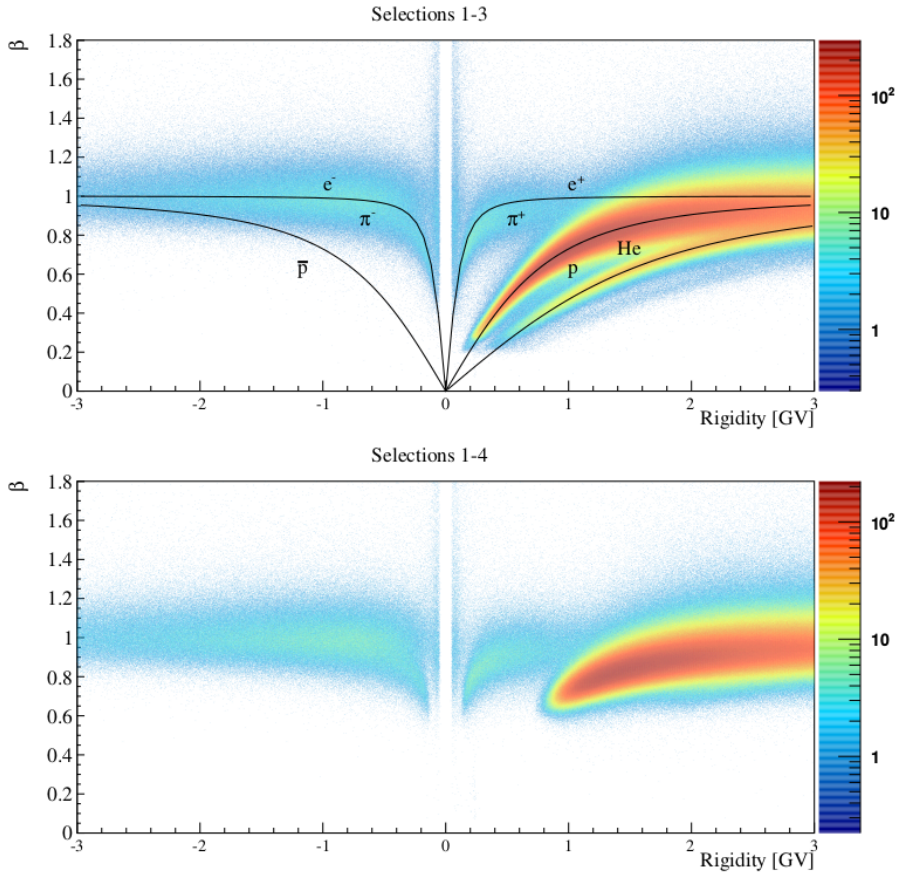

Figure 3.10: Rigidity versus beta distributions for flight data collected between July 2006 and December 2009. First panel: flight data after the single and quality track selections (1-3). Second panel: flight data after the tracker dE/dx selection (4).

- 5) **CARD, CAT**: no activity in the CARD and CAT scintillators below 10 GV was required. This selection as Criterion 1 reduces the multi-tracks events. Anti-coincidence selection reduces significantly the pion events that had hits in the AC scintillators like the one illustrated in Figure 3.3. The anti-coincidence selection had a constant efficiency up to 10 GV while above this energy it starts to decrease because of particle back-scattering from the calorimeter (see CAS selection). Since pion contamination is negligible above 10 GV the CARD and CAT selection is performed only up to this rigidity in order to increase the efficiency.

- 6) **CAS**: no activity in the CAS scintillators below 300 MV was required. The different rigidity limit for CARD and CAT respect to CAS is due to the different location of the scintillators respect to the calorimeter. As the electron energy increases, back-scattering

from the electromagnetic shower in the calorimeter increases resulting in an increasing activity in the anti-coincidence scintillators. Since CAS is very close to the calorimeter its efficiency starts do decrease very rapidly above 300 MV (50% at few GV). However comparison between simulation and flight data reveals that without CAS selection below 300 MV a large residual pion contamination would be present.

The rigidity ranges for the anti-counter selections were then a compromise between residual pion contamination and electron selection efficiencies. Comparing the second panel of Figure 3.10 and the first panel of Figure 3.11 the effect of selection Criteria 5-6 is visible.

TOF SYSTEM SELECTIONS

The time of Flight system provides information about the particles velocity and the ionization energy losses. ToF selections contribute to reject non relativistic hadrons.

- 7) **ToF dE/dx selection**: mean $dE/dx < 3$ MIP in both ToF S1 and S2 scintillators. This cut rejects pions up to 200 MV and protons up to 800 MV similarly to selection 4.
- 8) **Velocity selection**: relativistic particles were selected requiring $\beta > 0.9$. The six planes of scintillators which compose the ToF system provide 12 velocity measurements. In this analysis the mean value of the 12 measurements was used to perform the selection. As shown in Figure 3.11 (second panel) the velocity selections reduce the residual pion contamination up to 250 MV and the proton contamination up to 1 GV.

The remaining pion, antiproton, proton and spillover proton contaminations were removed using the calorimeter information.

CALORIMETER SELECTIONS

PAMELA calorimeter was the main sub-detector employed for lepton identification. The calorimeter selections were developed using PamVMC. To calibrate the selections more than 10^7 electrons and positrons were simulated. Moreover, in order to test the hadron rejection power, more than 10^7 protons and pions were simulated as well. The calorimeter selections were based on the different topological development of the hadronic and electromagnetic showers as well as the different energy deposition. For more details about the physics of electro-

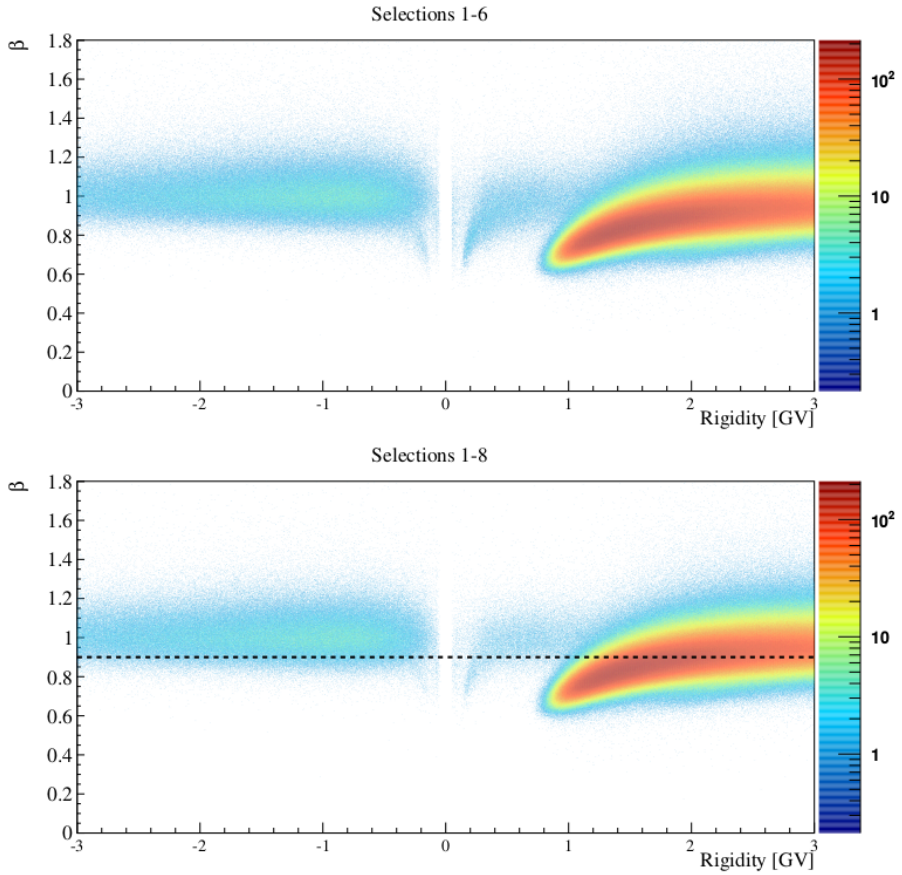

Figure 3.11: Rigidity versus beta distributions for flight data collected between July 2006 and December 2009. Firs panel: flight data after the AC selections (5-6). Second panel: flight data after ToF selections (7). Black dotted line represents the lower limit of Criterion 8.

magnetic and hadronic showers in matter see Appendix A. The longitudinal and transverse segmentation of the calorimeter allowed leptonic showers to be selected with high efficiency and small contamination above 300 MV. Below this rigidity more stringent selections were required and, consequently, the overall efficiency decreased. In order to achieve a good hadron rejection power several variables were combined.

- 9) **Ncore**: this quantity emphasizes the shower multiplication with increasing calorimeter depth and the collimation of the electromagnetic cascade along the shower axis. To better understand this property, Figure 3.12 (left panel) illustrates the electromagnetic cascade produced by an electron of 8 GeV. About 90% of the secondary particles are contained in a small radius around the shower axis called the Moliere radius R_M (see Equation A.9)

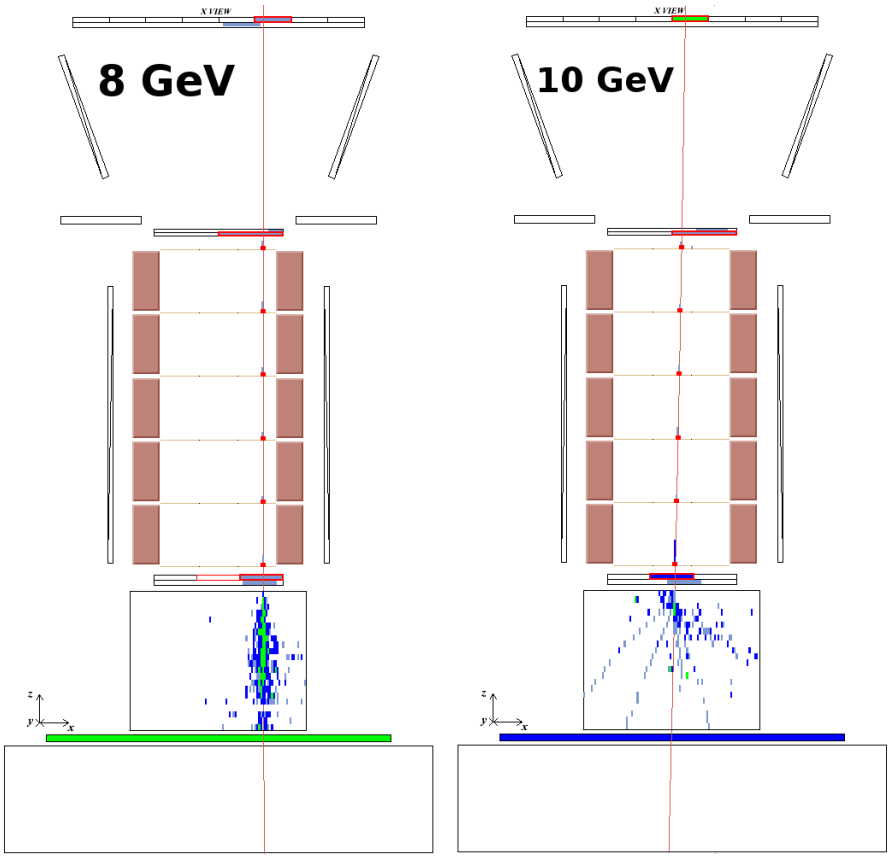

Figure 3.12: A schematic view of the PAMELA instrument (see Figure 3.5) is presented. Left panel: event display of a flight data electron of ~ 8 GV. The electromagnetic shower inside the calorimeter is very collimated along the cascade axis. Right panel: event display of a flight data interacting proton of ~ 10 GV. Because of nuclear interaction the shower of secondary particles is broader and the energy deposit pattern differs significantly from the electromagnetic cascade.

which for the PAMELA calorimeter is equivalent to the pitch of four silicon strips (~ 1 cm). On the contrary the right panel of Figure 3.12 represents an interacting proton of 10 GV. Different from the electromagnetic cascade, because of the nuclear interaction (see Section A.3), the hadronic shower is broader (about ten times more than the electromagnetic cascade) and the energy deposit can extend quite far from the shower axis (see Equation A.11). Considering these features Ncore was defined as:

$$\mathrm{Ncore} = \sum_{j=1}^{2} \sum_{i=1}^{i_{max}} N_{hit}(i,j) \cdot i \tag{3.2}$$

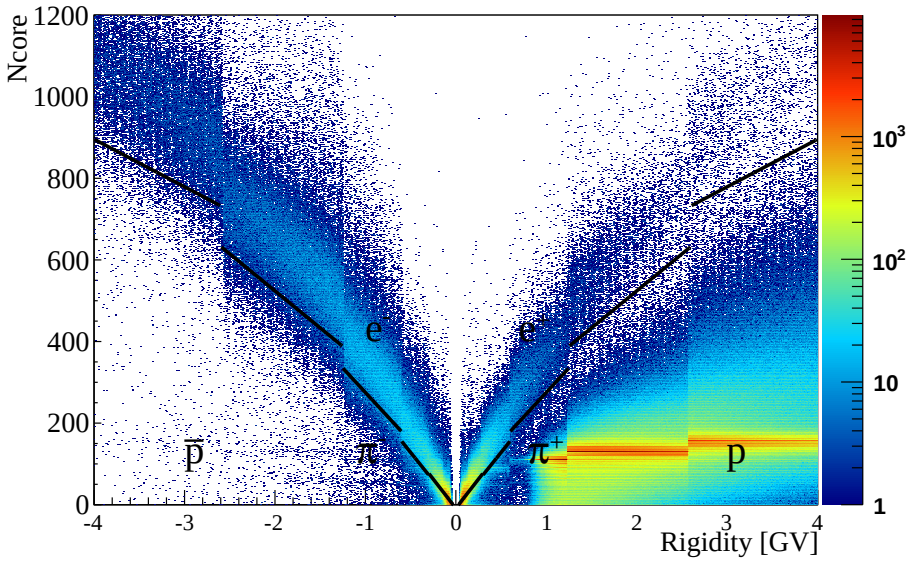

Figure 3.13: Ncore rigidity distribution for flight events collected from July 2006 to December 2009 surviving Criteria 1-8. The solid black lines indicate the limits for electron and positron selection.

where $N_{hit}(i,j)$ was the number of hits in a cylinder of radius 2 R_M around the track in the i-th calorimeter plane. The j index refers to the view and runs from $j = 1$ (x bending view) to $j = 2$ (y non bending view). The second sum runs from the top plane (number $i = 1$) up to plane number i_{max}, the closest to the calculated electromagnetic shower maximum of the j-th view (see Equation A.7). The track used to perform the sums was the projected track inside the calorimeter given by the fitting algorithm (red lines on Figure 3.5 and 3.12). Figure 3.13 represent the rigidity versus Ncore distribution for flight events surviving Criteria 1-8. This quantity has large values for leptons, small for non interacting and late interacting hadrons as follows from Equation 3.2. The solid lines in Figure 3.13 indicate the lower limits for electron and positron selection based on this quantity. Ncore selection was calibrated to have constant efficiency over the whole range of rigidities. Most of the high energy protons and pions were rejected by this criterion. However simulation showed that most of the low rigidity pions, between 200 and 400 MV, were unaffected by the Ncore selection. Another variable was defined to reduce the pion contamination at low energy.

- 10) **Calostrip**: this variable rejects pions below few hundreds of MV. Both flight and simulated pions were studied to define

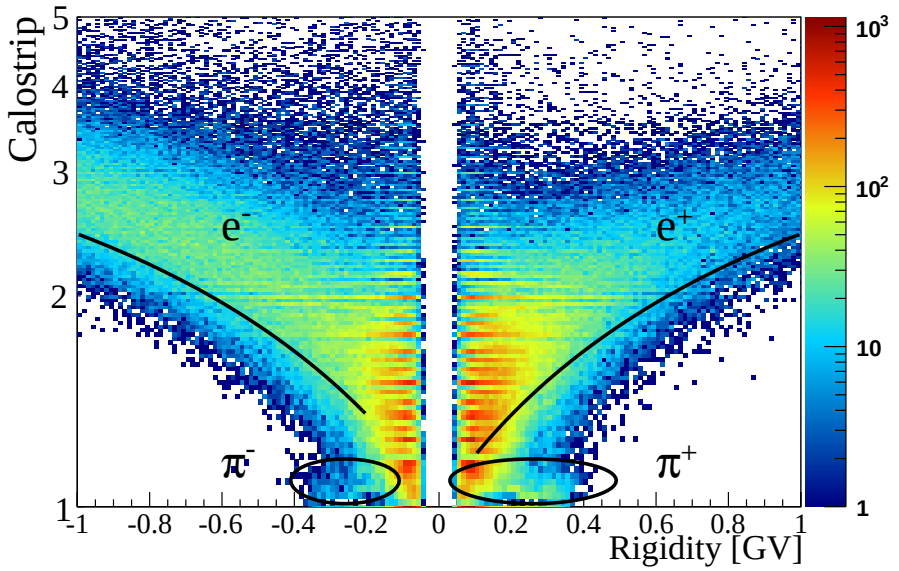

Figure 3.14: Calostrip versus rigidity distribution for flight events collected from July 2006 to December 2009 surviving Criteria 1-9. The solid black line indicate the limits for electrons and positrons selection. The residual pion contamination between 200 and 400 MV is visible.

this quantity. Calostrip was extensively discussed in [Munini, 2011], chapter three. Low energy pions assume small values of Calostrip, around one, while electrons and positrons usually have values greater than one. Figure 3.14 shows the rigidity distribution of Calostrip for flight events surviving selection Criteria 1-9. Below 400 MV the residual pion contamination is visible with a slight excess for positive rigidities. The black lines represent the constant efficiency electron and positron selection. It was noticed that Calostrip and Ncore selection efficiencies decrease sharply below few hundreds of MV (see Section 4.3). Since below 200 MV the energy and velocity selections (7-8) were sufficient to eliminate for the negative pion contamination, Criteria 9-10 were used only above 200 MV in order to increase the electron statistics. On the other hand, since contamination in the positron sample was proportionally much larger, Criteria 7-8 were not sufficient to reduce the pion contamination to a negligible amount between 100-200 MV. Therefore Calostrip and Ncore selections were applied down to 100 MV. After Ncore and Calostrip selections the negative pion contamination becomes negligible over the entire energy range while positive pions residual contamination was about 1-2% between 200 and 400 MV (see Section 3.4).

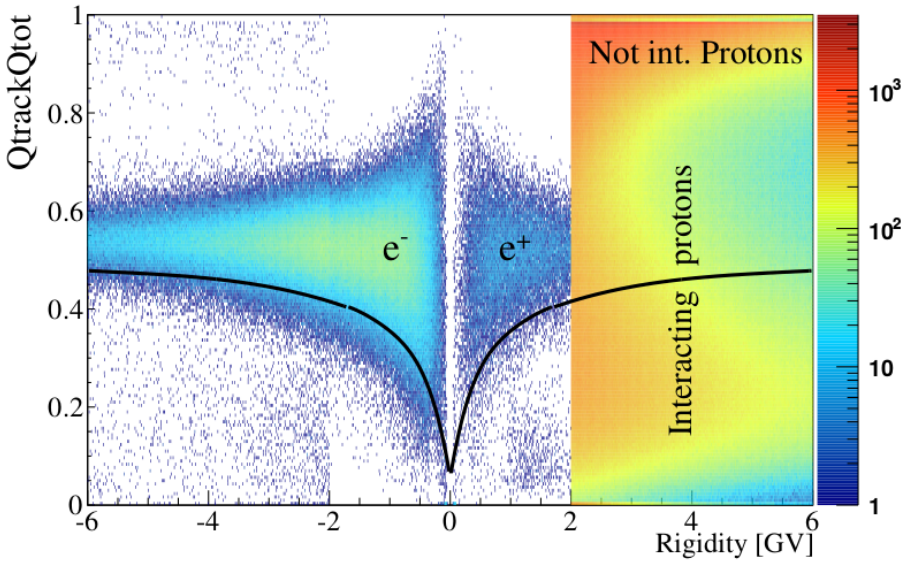

Figure 3.15: QtrackQtot versus rigidity distribution for flight events collected from July 2006 from December 2009 surviving Criteria 1-10 below 2 GeV, and 1-8 above 2 GV. Due to the presence of Ncore and Calostrip selections, below 2 GV events were mainly electrons and positrons and they distribute around 0.5-0.6. Above 2 GV QtrackQtot distribution is presented without any calorimeter selections to show how protons and antiprotons distribute. Events around QtrackQtot = 1 represents non interacting protons and antiprotons, while interacting hadrons spread between 0 and 1. The black lines indicate the lower limit for the positron and electron selection.

- 11 **QtrackQtot**: this quantity was defined as the ratio between the energy deposited in the two strips (about 3/4 R_M, see Table A.2) closest to the track (the projected track reconstructed by the fitting algorithm) and the total energy released in the calorimeter. The sum along the track runs over all the calorimeter planes. Figure 3.15 shows the QtrackQtot versus rigidity distribution obtained from experimental data collected from July 2006 from December 2009. Flight data were selected with all the previous criteria below 2 GV while above this rigidity the calorimeter selections (9-10) were not used. Below 2 GV for negative rigidities almost all the events were electrons. These events show that typical QtrackQtot values for the electromagnetic shower (above few hundreds of MV, i.e. when the profile of the electromagnetic shower was well defined) were between 0.5-0.6, meaning that, on average, half of the total energy was released very close to the shower axis. Above 2 GV (positive rigidities) on Figure 3.15 most of the events were

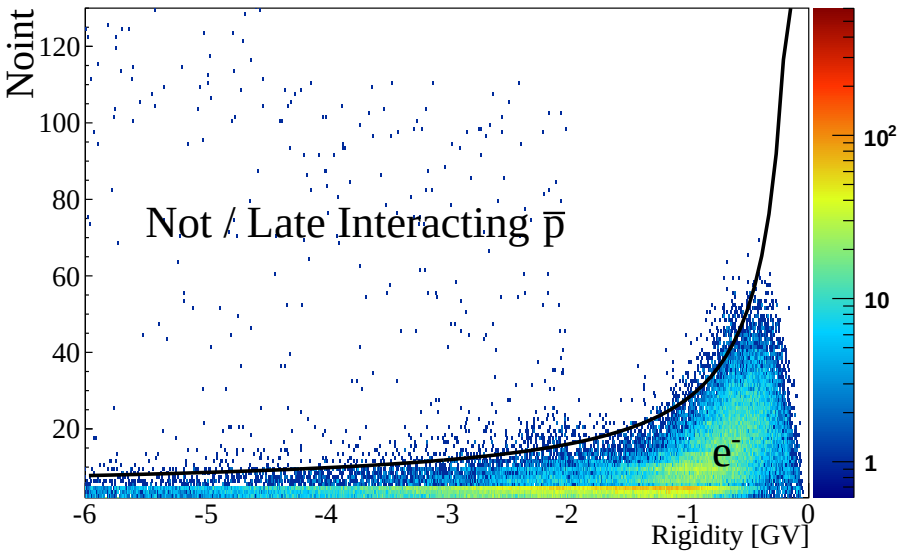

Figure 3.16: Noint versus rigidity distribution for flight electrons collected from July 2006 to December 2009 surviving selection Criteria 1-11 below 2 GV, and 1-8 above 2 GV. Below 2 GV the contamination of interacting antiprotons is visible for values of Noint greater than 20. The solid black line indicates the lower limit for electron selection.

protons. Since non-interacting protons release most of their energy along the track they distribute around QtrackQtot = 1. On the other hand, because of the hadronic shower dispersion, interacting protons were represented by the population of events which spread between 0 and 1 above 2 GV. The black lines represent the lower limit for electron and positron selection. The QtrackQtot variable was effective in rejecting protons above a few GeV.

Since antiproton contamination was proportionally lower with respect to proton, above 2 GV, less restrictive criteria (with respect to selections 9-11) were sufficient to select a clean sample of electrons. Hence, to keep the electron statistics higher, more efficient calorimeter cuts were defined above 2 GV. Below 2 GV selections Criteria 9-11 were needed to reject negative pions and spillover protons.

- 12) **Additional selections**: above 2 GV different calorimeter selection criteria were defined to reject the antiprotons and keep the efficiency high with respect to Criteria 9-11. The additional calorimeter selections were needed to reject antiprotons and high energy spillover protons (see Figure 4.19). These selections were

already used and discussed in previous works (for more detail see [Adriani et al., 2011a]). These variables intend to emphasize the different longitudinal profile and energy deposition pattern of electromagnetic and hadronic showers. Both simulation and flight data were used to calibrate these selections. These selections were defined to have a constant efficiency over the whole rigidity range. One of these variables was called Noint and was defined as:

$$\text{Noint} = \sum_{j=1}^{2} \sum_{i=1}^{22} T_{hit}(i,j) \cdot i \tag{3.3}$$

where $T_{hit}(i,j) = 1$ if the i-th plane of the j-th view has a cluster along (less than 4 mm away) the track with a deposited energy typical of a proton (order of one MIP), otherwise $T_{hit}(i,j) = 0$. Most of the electrons interact in the first or the second plane of the calorimeter while, on average, hadrons interact after having traversed several calorimeter planes. Since Noint emphasizes the deposit of non-interacting particles it had higher values for interacting and late interacting hadrons, lower for interacting electrons. Figure 3.16 shows the Noint versus rigidity distribution for flight data survived to selections Criteria 1-11 above 2 GV and Criteria 1-8 below 2 GV. Electrons above 2 GV lie below Noint = 20 while the population of non interacting and late interacting antiprotons and spillover protons spreads over values up to Noint = 120. The black line represents the upper limit of the electron selection which has a constant efficiency of $\sim$ 98%. Combining several selections it was possible to reject antiprotons and spillover protons above 2 GV with a negligible residual contamination maintaining the overall selection efficiency higher than selections 9-11.

Selection Criteria 9-11 where applied to select positrons and electrons down to 100 MV and 200 MV respectively (see Table 3.1 which summarizes the rigidity range of the selection Criteria). However the efficiency of the selection Criteria 9-11 sharply decreases below 100 MV (15% at 80 MV, see Section 4.3). While below 200 MV the dE/dx tracker and velocity selections ensure a good proton rejection, the spillover protons, being relativistic, remain unaffected by these cuts. In order to reject the low energy spillover protons and keep the statistics high, at low energies other calorimeter selections with higher efficiencies were studied. Indeed it was possible to exploit the peculiar features of the spillover protons to define a set of selections which left unaffected the electron and positron components.

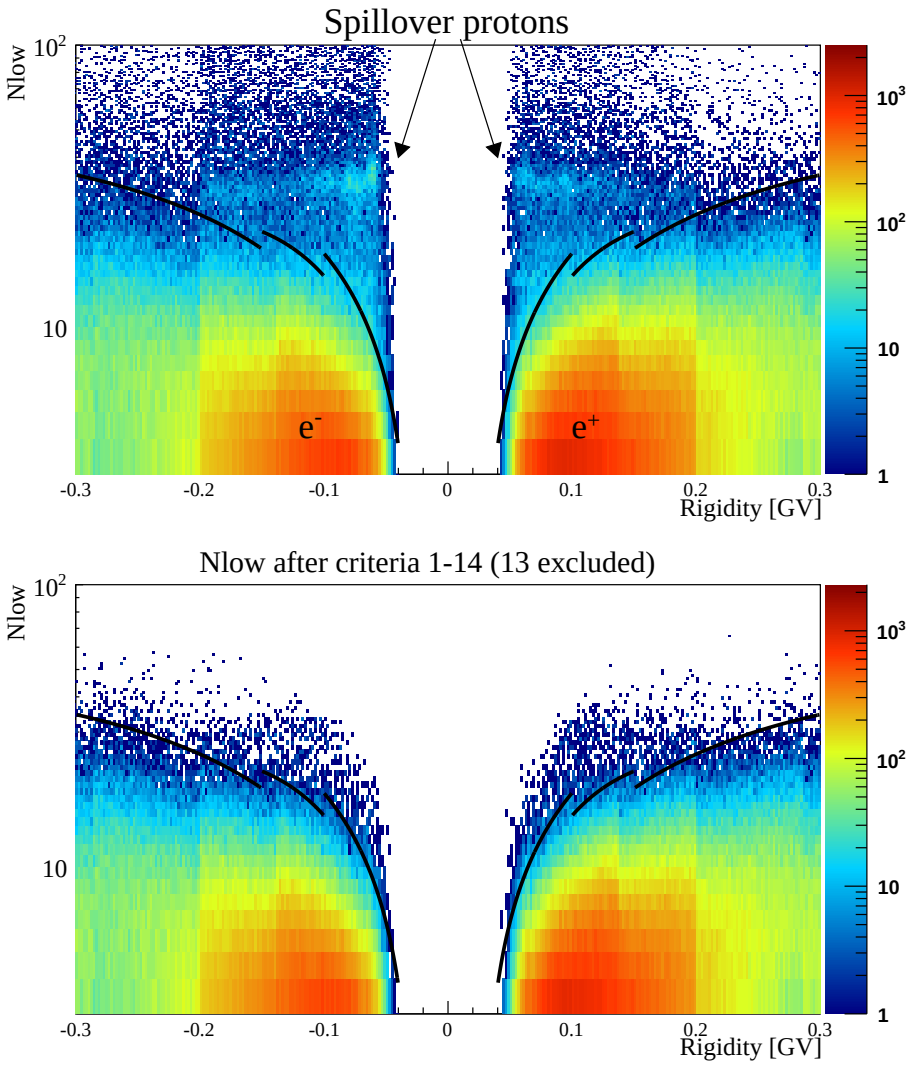

Figure 3.17: Top panel: Nlow versus rigidity distribution for flight events collected from July 2006 to December 2009 surviving selection Criteria 1-12. Contamination of spillover protons is visible for both positive and negative rigidities with a slightly excess of the latter. The solid black lines indicate the upper limits for electron and positron selection. Bottom panel: Nlow versus rigidity distribution for flight events surviving selection Criteria 1-14 (13 excluded). Spillover proton contamination is significantly reduced with respect to the top panel distribution. Residual contamination was rejected by the selection on Nlow.

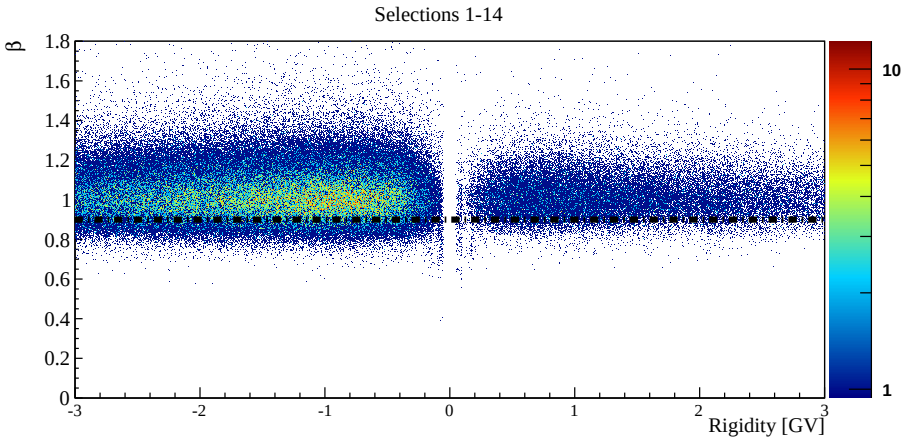

Figure 3.18: Rigidity beta distributions for flight events collected from July 2006 to December 2009 after all selection Criteria 1-14. The dotted black line represent the beta selection.

- 13) **Nlow**: at the lowest rigidities (below 300 MV) spillover protons accounted for the residual contamination after selection with Criteria 1-12, see Figure 3.17. Low energy spillover protons are mostly high energy hadrons reconstructed with rigidities below few hundreds of MV and most of them traverse the entire calorimeter volume. On the other hand electromagnetic showers below 500 MV mostly develop in the first planes of the calorimeter, see Figure 3.5. Exploiting these features it was possible to define several selections which did not affect significantly the electron signal hence keeping the selections efficiency higher than 95%. Nlow was defined as the number of the strip hit in the calorimeter planes after i_{max}, the closest plane to the calculated electromagnetic shower maximum of the j-th view (see Equation A.7). Below few hundreds of MV i_{max} coincides to the first 4-5 calorimeter planes. For this reason Nlow is expected to have low values for low rigidity interacting leptons (see Figure 3.5 right panel) and to peak around $\approx$ 30-35 for non interacting spillover protons (approximatively one hit for each plane after i_{max}). Figure 3.17 (top panel) shows the Nlow rigidity distribution for flight data selected after the Criteria 1-12. The electron and positron components are well separated from the spillover protons. Above 200 MV is visible the effect produced by the selections on Ncore and Calostrip which reduce significantly the contamination. The solid black lines indicate the upper limit for electron and positron selection which was calibrated with simulation to have high efficiency ($>$ 97%). This selection was used below 350 MV since above this energies spillover protons after the previous selections were neg-

Table 3.1: Summary of the selections Criteria 1-14. For each criterion the rigidity ranges for both the electron and positron selection are indicated.

	Electron selections	Positron selections
1) Single track	• 70 MV - 50 GV	• 70 MV - 50 GV
2) Impact points (434)	• 70 MV - 600 MV	• 70 MV - 600 MV
2bis) Impact points (334)	• 600 MV - 50 GV	• 600 MV - 50 GV
3) Quality track χ^2	• 70 MV - 50 GV	• 70 MV - 50 GV
4) Tracker dE/dx	• 70 MV - 50 GV	• 70 MV - 50 GV
5) Anti (CARD, CAT)	• 70 MV - 10 GV	• 70 MV - 10 GV
6) Anti (CAS)	• 70 MV - 300 MV	• 70 MV - 300 MV
7) ToF systema dE/dx	• 70 MV - 50 GV	• 70 MV - 50 GV
8) Velocity selections (β)	• 70 MV - 50 GV	• 70 MV - 50 GV
9) Ncore	• 200 MV - 2 GV	• 100 MV - 50 GV
10) Calostrip	• 200 MV - 2 GV	• 100 MV - 50 GV
11) QtrackQtot	• 200 MV - 2 GV	• 100 MV - 50 GV
12) Additional calo cuts	• 2 GV - 50 GV	×
13) Nlow	• 70 MV - 350 MV	• 70 MV - 350 MV
14) Qtot, Nstrip	• 70 MV - 350 MV	• 70 MV - 350 MV

ligible. Nlow was combined with other variables to reduce the spillover proton to a negligible amount.

- 14) **Nstrip, Qtot**: both the total number of strips hit (Nstrip) and the total energy (Qtot) were used to reduce the proton spillover. Low energy electrons and positrons release significantly less energy with respect to high energy protons as well as they hit less strips in the calorimeter planes. The selections were calibrated using the simulation to have constant efficiency greater than 98%. Bottom panel of Figure 3.17 shows how the proton spillover contamination was reduced after the Qtot and Nstrip selections. As with Nlow these selections were used only below 350 MV.

Combining the calorimeter selections an excellent hadron rejection power was achieved. Figure 3.18 shows the rigidity versus beta distribution after selection Criteria 1-13. The beta selection was represented by the black dotted line. Comparing this distribution with the second panel of Figure 3.11 it can be noticed how the huge proton background, as well as the pion contamination, disappeared. However it was essential to quantitatively estimate any residual contamination. Both simulation and flight data was used to estimate the residual amount of protons and pions in the final sample of particles.

3.4 RESIDUAL CONTAMINATION

The residual hadron contamination was estimated using both Monte Carlo and flight data. Since the Galactic CR proton to positron ratio was about 10^4, even a small fraction of protons surviving the selection criteria could lead to a significant overestimation of the positron fluxes. For this reasons strong calorimeter selections were used over the whole energy range to select positrons. On the contrary, since the antiproton to electron ratio was significantly lower (see Figure 1.1), above 2 GV, less stringent calorimeter selections (see Table 3.1) were sufficient to reduce the antiproton contamination to a negligible amount. However, the low energy residual contamination from spillover protons needs to be carefully estimated.

Residual pion contamination was measured with particular attention in the rigidity range between 150-400 MV. Indeed in this rigidity range the secondary pion production reaches its maximum and the calorimeter selections were less efficient in rejecting pions.

RESIDUAL PROTON CONTAMINATION

The residual (spillover) proton contamination was evaluated by means of the Monte Carlo data. The simulated[3] (spillover)[4] proton, positron and electron spectra were normalized to the high energy (between 20 and 30 GV) Galactic CR fluxes measured by PAMELA (see Figure 1.1). In this way, the number of simulated events, was converted into flux units $[(\mathrm{m^2 s\ sr\ GV})^{-1}]$, preserving the magnitude differences between the Galactic fluxes of the various particle species. All the selection criteria were then applied to the Monte Carlo data obtaining the residual flux of (spillover) protons, electrons and positrons. Figure 3.19 (top panel) shows the residual electron flux (red points) and the residual spillover proton flux (black points), while Figure 3.20 (top panel) shows the residual positron flux (red points) and the residual proton flux (black points). The ratio between the residual (spillover) protons and the (electrons) positrons gives an estimation of the residual hadron contamination in the final particle sample (lower panels of Figures 3.19 and 3.20)fraction of spillover protons and protons. As can be seen from these results, the residual proton contamination in the positron sample was negligible over the hole energy range except between 200 and 500

3 As already discussed, a set of Monte Carlo electrons and positrons was simulated reproducing the shape of the Galactic spectrum of the electron CRs. Similarly, for the protons, approximatively 10^8 events were isotropically simulated following the shape of the Galactic spectrum of the proton CRs (see Figure 1.1).

4 The Monte Carlo spillover protons were defined as those protons reconstructed in the simulation with negative rigidities.

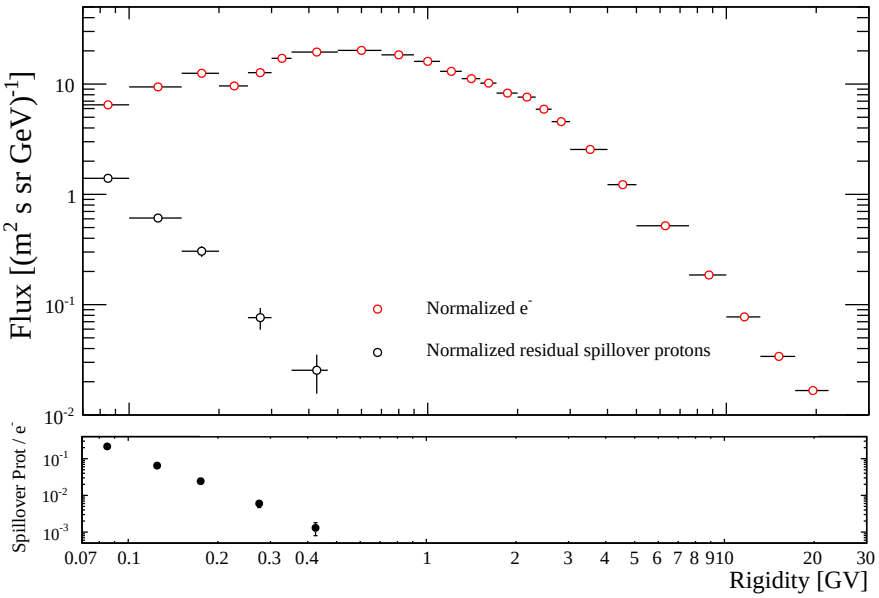

Figure 3.19: Top panel: the red points represent the normalized Monte Carlo electron flux after the whole set of selection criteria (the electron selections of Table 3.1) while the open black points represent the residual Monte Carlo spillover protons after the same set of selections. Bottom panel: residual fraction of spillover protons measured as the ratio between the open black and red points shown on the upper panel.

MeV where it varied from 10% to 2% [5] For the electrons, Monte Carlo data suggested the presence of a residual spillover proton contamination of the order of 20% at 70 MV. This contamination decreased as the energy increased and became negligible above 200 MV. Simulation showed that if Criteria 9-11 were applied below 200 MV, the residual spillover proton contamination was rejected. In order to verify with flight data the presence of this residual contamination, electrons were selected below 200 MV with and without selection Criteria 9-11. The sample of particles selected with Criteria 9-11 only below 200 MV were thus divided by the calorimeter selection efficiencies evaluated from Monte Carlo data, in order to not introduce possible biases due to residual contamination in the experimental efficiency sample. The two set of electrons were thus compared and, below 200 MV, were found to be compatible inside the statistical errors. Ultimately, no clear indication of spillover proton contamination of the magnitude predicted by Monte Carlo data in Figure 3.19 (bottom panel) were found. For this

5 It can be noticed, however, that the error bars of the points in Figure 3.20 (lower panels) are compatible with a contamination of the order of less than one percent.

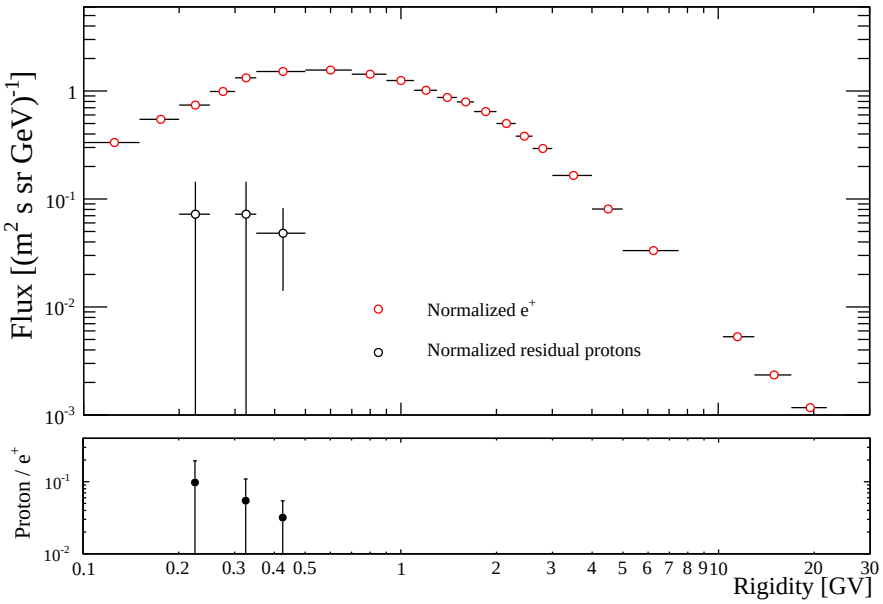

Figure 3.20: Top panel: the red points represent the normalized Monte Carlo positron flux after the whole set of selection Criteria (the positron selections of Table 3.1) while the open black points represent the residual Monte Carlo proton flux after the same set of selections. Bottom panel: residual fraction of protons measured as the ratio between the open black and red points shown on the upper panel.

reason the electrons were selected by means of the Criteria 9-11 down to 200 MV, in order to increase the statistics. However an uncertainty corresponding to the estimated residual contamination of the spillover protons of Figure 3.19 (bottom panel) was added to the electron systematics. Below 200 MV positrons had to be selected by means of selection Criteria 9-11 since without these additional selections the residual proton contamination turned out to be one order of magnitude greater than the positron signal itself. As for the electron case, the estimated residual contamination of Figure 3.20 was added to the positron systematics.

RESIDUAL PION CONTAMINATION

As discussed in Section 3.2 pion contamination was significant below 1 GV and became negligible above a few GV . Electrons and positrons were relativistic over the whole energy range while pions below 200 MV, because of their higher mass ($m_\pi \sim 120$ MeV/c^2), were not relativistic and the velocity measurement allowed to select them from flight

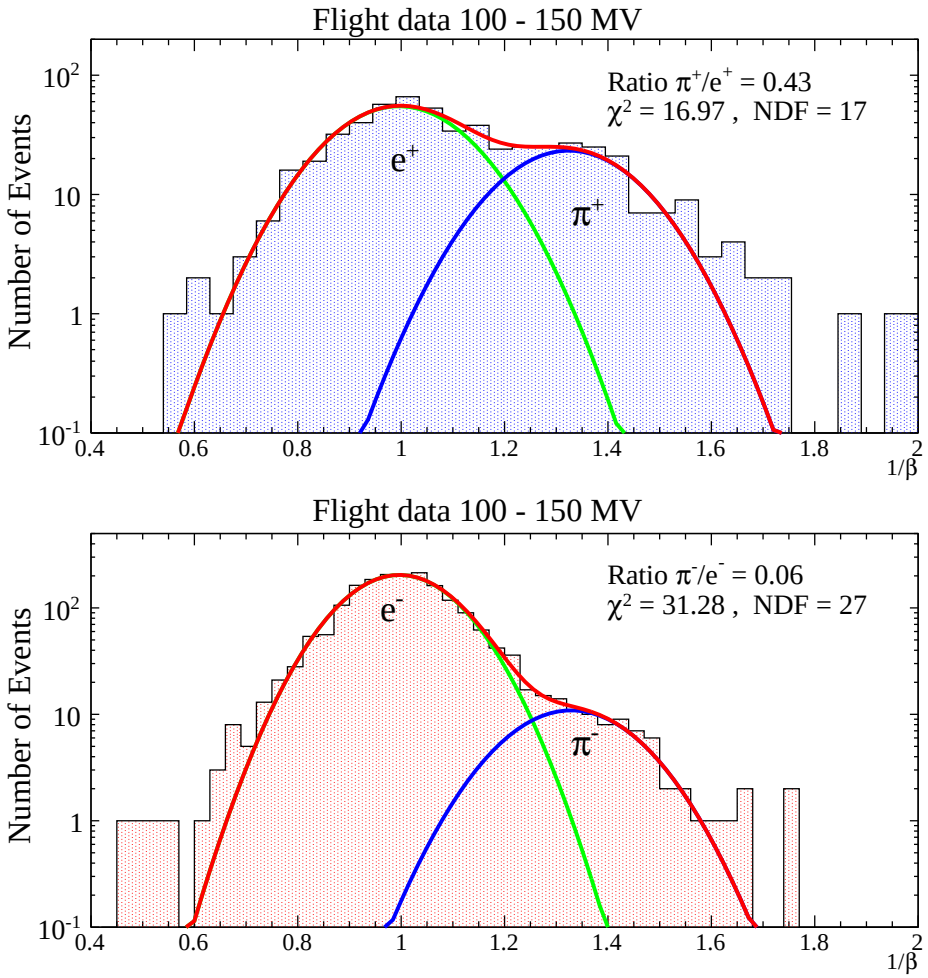

Figure 3.21: Top panel: one over beta distribution for positive rigidity flight events collected from July 2006 to December 2009 between 100-150 MV before the calorimeter selections. The red line represents the double Gaussian fit which allows to estimate the fraction of positive pions with respect to the positron signal. The green and blue curves represent respectively the pion and positron components. The value of the positive pion fraction in the positron sample is reported in the legend. Bottom panel: same distribution for negative rigidities events. As expected the fraction of negative pions was about ten times smaller with respect to the positive pions.

data. In order to evaluate the number of pions and electrons the $1/\beta$ distribution was studied. As showed in Figure 2.7, the resolution on the particle time-of-flight is approximated with a Gaussian. Thus, being proportional to the particle time-of-flight inside the apparatus,the $1/\beta$ distribution at a given rigidity, is well described by a Gaussian distribution. By means of a double Gaussian fit it was possible to evaluate the number of leptons and pions. The procedure is summarized in Figure 3.21 which represents the flight data selected between 100 - 150 MV for positive (top panel) and negative (bottom panel) rigidities. Electrons and positrons were distributed around one while pions were peaked at values greater than one. The distribution represents events before the calorimeter selections and the red line is the double Gaussian fit.

The residual fraction of pions (the ratio between the number of pions and electrons) was estimated from the $1/\beta$ distribution after the whole set of selection criteria (ecxept the velocity selection). The fit was performed fixing the mean value and the sigma of the pion distribution to the values obtained by fitting the corresponding $1/\beta$ distribution for up-going pions (negative β). Indeed negative up-going particles were mainly (positive) pions with a small component of positrons below 100 MV. As can be noticed from Figure 3.2 (both panels) negative up-going pions were significantly more abundant ($\sim$ 10 times) to down-going pions. The final fraction of pions was obtained calculating the integral of the two Gaussian distributions below $1/\beta \simeq 1.1$ in order to take into account the velocity selection $\beta > 0.9$. The first four points of the graph reported on Figure 3.22 show the values obtained from the fitting procedure for both electrons and positrons.

Above 200 MV pions become relativistic and it was not possible to use flight data since the Gaussian distributions were non distinguishable. However combining the experimental with the simulated data it was possible to extrapolate the residual pion contamination above 150 MV. The first step was to define the fraction of pions before the calorimeter selections as $F^i_\pi = N^i_\pi / N^i_{e^\pm}$. Since pion contamination reaches its maximum around a few hundred MV and decreases with increasing energy (see Section 3.2), the experimental values of F^i_π between 100 - 150 MV was considered as an upper value over the entire energy range. The second step was to estimate with the simulation the rigidity dependence of the calorimeter selection efficiencies for both electrons (positrons) $Eff_{e^\pm}(R) = N_{e^\pm}(R)^f / N^i_{e^\pm}(R)$ and pions $Eff_\pi(R) = N^f_\pi(R)/N^i_\pi(R)$. Finally an upper limit for the residual pion fraction above 150 MV was obtained combining the previous quantity:

$$F^f_\pi(R) = F^i_\pi(100\text{-}150\ \text{MV}) \frac{Eff_{e^\pm}(R)}{Eff_\pi(R)} \tag{3.4}$$

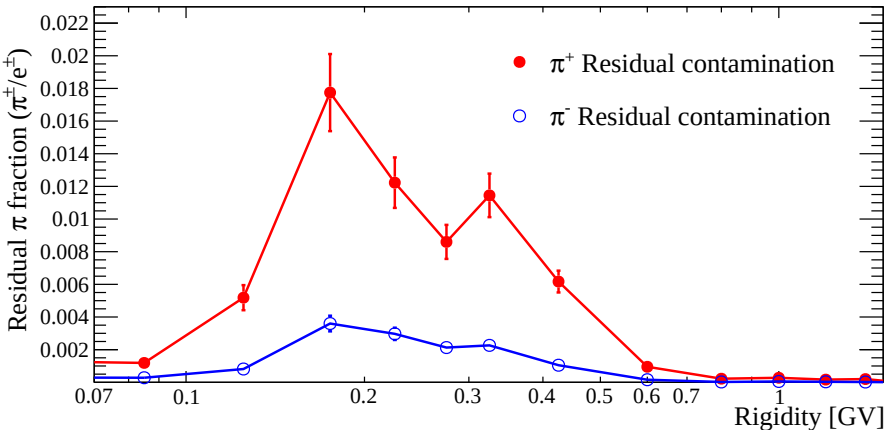

Figure 3.22: The estimated residual pion contamination. Blue points represent the fraction of the residual negative pion while the red points represent the fraction of the residual positive pion. The estimated residual pion contamination was not subtracted but treated as a systematic error.

On Figure 3.22 the numerical values for the residual pion contamination are shown. Positive pion contamination reaches a maximum of $1-2\%$ between 100 and 400 MV while the negative pion contamination was lower than $\sim 0.4\%$ over the whole rigidity range. Residual pion contamination was not subtracted but treated as a systematic error.

4 FLUX ESTIMATION

INDEX

The results of this work were based on data collected by the PAMELA instrument between July 2006 and December 2009. Data are presented in six-month time periods, a compromise between statistically significant results and detailed analysis of the time variation of the fluxes. This chapter is devoted to discuss the main steps necessary to evaluate the positron and electron time-dependent fluxes. First, the selection of electrons and positrons over the PAMELA orbit is discussed in Section 4.1. Then the selection efficiencies and their dependence on time, energy and charge-sign are presented in Section 4.3. A fundamental step, the spectra unfolding, for which a statistical procedure based on Bayesian inference was adopted, is discussed in detail in Section 4.4. The unfolding allows to account for both the response of the spectrometer and the energy losses suffered by the electrons and positrons prior entering the tracking system and allows to reconstruct the CR flux as a function of the particle energy at the top of the payload (i.e. before interacting with PAMELA material). The selection of Galactic electrons and positrons is discussed in Section 4.5. The live-time and the geometrical factor estimation are described in Section 4.6 and Section 4.7 respectively. Finally, in Section 4.8, a brief summary of the flux evaluation procedure is presented. The results on the time-dependent electron and positron fluxes are shown and discussed in Chapter 5.

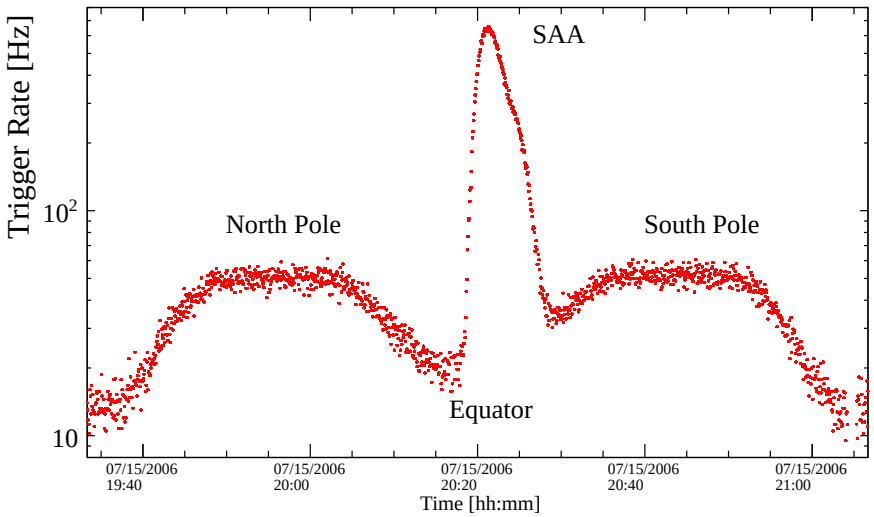

Figure 4.1: The trigger rate during one PAMELA orbit. The trigger rate increases during the polar passage since the vertical cutoff decreases and low energy CRs can be detected. The trigger rate increases about one order of magnitude with respect to the polar passage corresponding to the Van Allen radiation belts.

4.1 EVENT SELECTION

The electron and positron time-dependent fluxes presented in this work were based on data collected by the PAMELA apparatus during the 23th solar minimum, i.e. between July 2006 and December 2009. Electrons and positrons were selected according to the criteria discussed in Chapter 3. However data acquired during particular periods of time or PAMELA orbital positions were excluded from the analysis:

- **South Atlantic Anomaly** (SAA): the SAA is the region where the inner Van Allen radiation belt makes its closest approach to the Earth's surface. The SAA is mainly localized above the coast of Brazil and extends over much of South America. In fact, the radiation belts are asymmetric respect to the Earth rotation axis, as a consequence of the tilt ($\sim 11.3°$ with respect to the rotational axis) and of the offset of the magnetic dipole of the Earth which is not centered on the Earth core, but instead is displaced by about 450 km towards the direction of southeastern Asia. The SAA dips down to about 200 km from the Earth surface.

  Because of the presence of trapped particles (albedo particles), the PAMELA trigger rate in this region was significantly higher. It has already been introduced in Section 2.3 that a significant fraction of the total trigger rate is due to random coincidence

Table 4.1: Rigidity range for the sixteen geomagnetic cutoff intervals used to select electrons and positrons.

Geomagnetic cutoff intervals [GV]		
1) 0-0.05	2) 0.05-0.071	3) 0.071-0.107
4) 0.107-0.178	5) 0.178-0.250	6) 0.250-0.5
7) 0.5-0.93	8) 0.93-1.21	9) 1.21-1.64
10) 1.64-2.14	11) 2.14-3.57	12) 3.57-7.15
13) 7.15-9.3	14) 9.3-12.1	15) 12.1-15.7
16) 15.7-20		

from spurious hits in the ToF planes (e.g. CRs which enter sidewards, see Figure 2.9). During the passage inside the SAA the intensity of particles (low energy protons with a small electron component) hitting the PAMELA apparatus increases by orders of magnitude. As a consequence the frequency of random coincidences increases and thus the trigger rate. Figure 4.1 shows the trigger rate during one PAMELA orbit as a function of time. The PAMELA passage over the SAA at 20:20 is clearly visible and corresponds to the sharp increase in the trigger rate which becomes about one order of magnitude higher with respect to the polar passages. The consecutive increase and decrease of the trigger rate respectively over the poles and the equator reflects the effect of the geomagnetic vertical cutoff. Data acquired during the passages over the SAA, where the trigger saturated, was excluded in the off-line phase. Moreover in this way the quantity of sub-cutoff particles were also reduced.

- **Solar flares**[1]: significant solar activities were excluded from the data in the off-line phase. Solar flares are often accompanied by coronal mass ejection (CME) which can produce shock waves and accelerate particles (solar energetic particles SEPs) up to a few GeV. The PAMELA collaboration studied the intense solar flare that occurred on 2006 December 13 and 14 [Adriani et al., 2011b] and measured an increase of the proton flux below 2 GeV up to three orders of magnitude with respect to the Galactic spectrum. However no electrons or positrons of solar origin were found by PAMELA above 50 MeV. Nevertheless when the forward shock

1 A solar flare is defined as a sudden, rapid, and intense variation in the brightness of the Sun. A solar flare occurs when magnetic energy that has built up in the solar atmosphere is suddenly released. Radiation is emitted across the entire electromagnetic spectrum, from radio waves at the long wavelength end, through optical emission to x-rays and gamma rays at the short wavelength end.

Table 4.2: Energy bin divisions of the electron and positron fluxes.

Flux energy bin [GeV]			
1) 0.04-0.07	2) 0.07-0.1	3) 0.1-0.15	4) 0.15-0.2
5) 0.2-0.25	6) 0.3-0.35	7) 0.35-0.5	8) 0.5-0.7
9) 0.7-0.9	10) 0.9-1.1	11) 1.1-1.3	12) 1.3-1.5
13) 1.5-1.7	14) 1.7-2.0	15) 2.-2.3	16) 2.3-2.6
14) 2.6-3.0	15) 3.0-4.0	16) 4.0-5.0	17) 5.0-7.5
18) 7.5-10	19) 10-13	15) 13-17	16) 17-22
19) 22-30	20) 30-50	21) 50-100	

of the CME reached Earth it caused a Forbush decrease[2] of the Galactic CR intensities, including electrons and positrons up to several GeV, that lasted for several days . In order to exclude short-term temporal flux variation which are not correlated to the usual solar activity, data collected on December 2006 were excluded from the analysis.

Because of the wide geomagnetic region spanned by the satellite over its orbit, electrons and positrons were selected for various, sixteen, vertical geomagnetic cutoff intervals showed in Table 4.1, estimated using the satellite position and the Stormer approximation. The energy (rigidity) bin division of the fluxes is presented in Table 4.2. As previously discussed the time-variation of CR fluxes are presented over six-month time periods, thus a total of $16 \times 7 = 142$ rigidity count distributions were obtained for electrons and positrons respectively. These count distributions were then analyzed in order to evaluate the fluxes. The next section is devoted to a brief overview of the key passages of the analysis chain.

4.2 ANALYSIS CHAIN

After having selected electrons and positrons by means of the criteria discussed in the previous chapter, each of the 142 count distributions were processed to estimate the time-dependent spectra over the 23th solar minimum. The rigidity count distribution, which is referred to as the folded distribution, were divided for those efficiencies estimated as a function of rigidity and then unfolded by means of the procedure explained in detail in Section 4.4. The unfolding reconstructed the count distribution as a function of the real energy, also referred to as unfolded

2 Forbush decreases are short term decreases in the CR intensity, which are due to the interactions of the CRs and the magnetic clouds carried out by the CMEs from the Sun.

distributions. The unfolded distributions were then corrected for the remaining efficiencies which were estimated as a function of the real energy. At this point the distributions comprised two components, at energies higher than the corresponding geomagnetic cutoff the Galactic component and at lower energies the re-entrant albedo one, with a transition region where the two components mixed. The Galactic CR selection was performed on each of these spectra where the fluxes were assumed to be of Galactic origin and unaffected by the Earth magnetosphere, see Section 4.5. Then, the final electron and positron spectra were determined by combining the spectra of each geomagnetic cutoff interval weighted for its fractional live-time. Each passage of the analysis chain is discussed in detail in the following sections starting from the selection efficiency evaluation.

4.3 EFFICIENCIES

The redundant information provided by the PAMELA sub-detectors allowed the study of the electron selection efficiencies to be conducted using flight data. On the contrary, because of the huge proton background, it was not possible to evaluate the positron efficiency with the experimental data. The efficiencies study was complemented by an analysis of simulated data. With the Monte Carlo data it was possible to validate the results obtained from flight data and detect any source of bias like contamination of the efficiency samples. The efficiencies were evaluated having special attention to the following aspects:

- **Energy-dependence**: most of the selection efficiencies were found to be constant above 1 GV. On the contrary, as the rigidity approaches the instrumental limit (48 MV[3] for electrons and positrons), many efficiencies were found to decrease. For each efficiency, the energy (rigidity) dependence was carefully studied using both flight and simulated data selecting events using the bin division of Table 4.2. The experimental and Monte Carlo results were then compared to find possible discrepancy. Most of the efficiencies were fitted with functions which reproduced their energy dependence. In order to reduce the statistical fluctuations, instead of using the efficiencies evaluated in each energy (rigidity) bins, the fitted functions were used in the flux evaluation. The errors associated to the fits were quadratically summed to the systematic errors (see Section 5.2).

3 For electrons and positrons the minimum detectable rigidity is about 48 MeV. Below this rigidity the particle curvature inside the magnetic cavity prevents the instrumental trigger to be activated (e.g see Figure 4.5).

- **Temporal-dependence**: a crucial point in the time-dependent flux analysis was the correct estimation of the temporal variation of the selection efficiencies . Many efficiencies like the calorimeter and anti-coincidence ones were constant with time. Velocity and energy selection efficiencies exhibited a small variation with time while the tracker efficiency had large temporal variation. Sufficiently large statistics were collected in order to allow the time dependence of the electron efficiencies to be monitored over a six-months time scale. However in some cases it was not possible to evaluate efficiencies from data collected in space (e.g. the tracking system) and thus the Monte Carlo data were used. For this reason, to correctly reproduce the time-dependent efficiencies, the simulation had to account for any electronic or mechanical temporal variation of PAMELA sub-detectors.

- **Charge-dependence**: Positrons through matter, contrarily to electrons, can interact via positron-annihilation or via Bhabha scattering. However, at energies greater than few hundreds of MeV, the dominant process is bremsstrahlung energy losses, while positron annihilation and Bhabha scattering become negligible (see Figure A.1). For this reason, above a few hundreds of MeV, electrons and positrons interact through matter with the same physical processes and the selection efficiencies were expected to be independent on the charge-sign of the particle. On the contrary below a few hundreds of MeV, a small charge dependence of the selections efficiencies could exist (e.g. the calorimeter selection efficiencies).

  A large dependence on the charge-sign was present in the low energy tracker efficiency (< 1 GeV). At these low energies the bending of charged particles in the tracker system is significant (e.g. see Figure 4.6). Hence, particles with opposite charge-sign illuminate different areas of the tracker planes. Since the tracker plane surface was not homogeneously active because of the progressive failure of several front-end chips a charge-sign dependence was introduced.

- **Correlations**: to prevent any bias in the flux estimation the simulated efficiency samples were selected in the same order as in the experimental analysis. First the tracking system efficiency, e.g. the Criteria 1 and 2(bis) presented in Section 3.3, was evaluated by means of the Monte Carlo data. The sample of electrons selected with the tracking system information was then used to evaluate the χ^2 efficiency. All the other efficiencies were measured selecting the electron sample by progressively adding the remaining criteria in the order presented in Section 3.3. Experimentally this

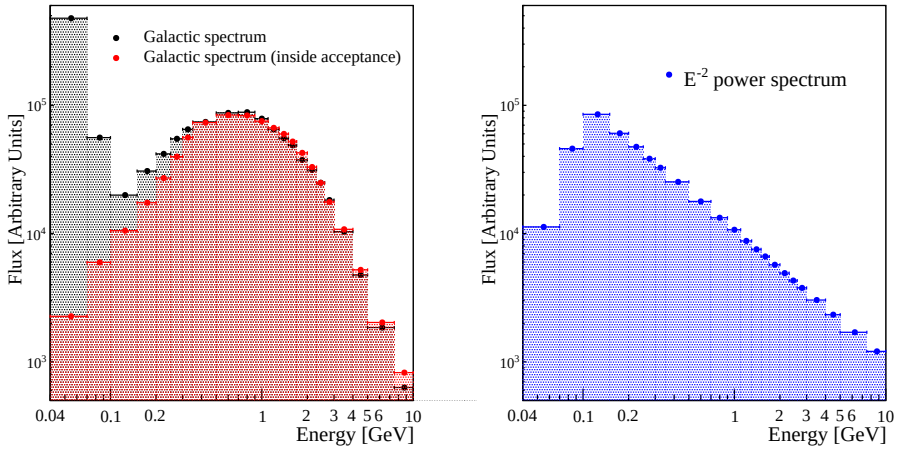

Figure 4.2: Left panel: black points represent the spectral shape used to generate simulated electrons which correspond to the Galactic electron spectrum measured in [Munini, 2011]. Red points represent the corresponding spectrum reconstructed inside the PAMELA acceptance. The sharp decrease below 400 MeV was due to the fast decrease of the geometrical factor. Right panel: simulated electrons generated with a E^{-2} power law reconstructed inside the PAMELA acceptance. In this case there would be an overabundance of low energy events with respect to the previous case.

procedure cannot be realized. Indeed it was not possible to select a clean electron sample just using the tracking system selection since several of the other selections were also needed. Therefore the simulated and experimental efficiencies were compared to estimate possible correlations among the selection Criteria.

The PamVMC toolkit was used to simulate about 10^7 electrons and positrons between 50 MeV and 100 GeV. In order to reproduce the experimental environment the simulated events were generated following the Galactic electron spectrum measured in [Munini, 2011]. Figure 4.2 shows the generated Monte Carlo electrons (left panel, black points) together with the particle spectral shape for the events inside the PAMELA acceptance (left panel, red points). Below 400 MeV the simulated electron rigidity distribution drops as a result of a sharply decreases geometrical factor (see Section 4.7). The spectral shape of simulated events had to be as much as possible similar to the experimental spectrum in order to correctly reproduce effects such as the event migration. As will be explained in Section 4.4, the reconstructed rigidity does not always coincide with the particle energy (E_0) at the top of the payload (tracker resolution, energy losses). A fraction of electrons and positrons were thus reconstructed with a rigidity which did

not correspond to their E_0. This phenomena was referred as to "migration" and had to be carefully reproduced in the simulation since it had a great impact on the unfolding procedure (see 4.4) and the rigidity efficiency estimation. Figure 4.2 (right panel) shows a set of Monte Carlo electrons reconstructed inside the PAMELA acceptance generated with a power law $E^{-\gamma}$ with $\gamma = 2$. With respect to the Galactic spectrum the amount of events below 500 MeV was significantly larger. Consequently also the fraction of migrating events in the low energy bins was different affecting both the unfolding and the rigidity efficiency estimation as will be discussed later. For this reason the spectral shape of Monte Carlo events was tuned on the experimental electron Galactic spectrum. The efficiencies of the selection criteria presented in Chapter 3 will be discussed in detail starting from the tracking system.

TRACKER EFFICIENCY

Similarly to the case of the analysis of the proton flux [Adriani et al., 2011c], the efficiency of the tracking system selection (Criteria 1, 2 and 2 bis) and, especially, its top of the payload energy (E_0) dependence were obtained by Monte Carlo data. Since to determine the particle rigidity a track has to be reconstructed, the rigidity dependence of the tracking system selections could not be evaluated either with experimental or simulated data. Figure 4.3 shows the time evolution of the selection efficiency for Criteria 1 and 2 evaluated with simulated data for both electrons (filled points) and positrons (open points). This picture illustrates two important features of the tracker efficiency:

- **Time-dependence**: the tracking system selection efficiency was found to decrease over the years. As can be seen from Figure 4.3 the tracker efficiency goes from a maximum of 90% in 2006 to the 20% of 2009 when Criterion 2 (334), the less restrictive in terms of track quality, was used. With Criterion 2bis (434) the decrease in the efficiency was sharper, down to 10% at the end of 2009. Figure 4.4 shows the efficiency ratio between Criteria 334 and 434 together with its time evolution. In 2006 the ratio was almost one. Then it constantly decreased with time till late 2009 when the efficiencies of Criterion 2bis was 50% of Criterion 2.

  This significant time dependence was due to the sudden, random failure of a few front-end chips in the tracking system. This resulted in a progressive reduction of the tracking efficiency, since the number of hits available for track reconstruction decreased. In 2006 almost all the front-end chips were active thus the efficiency was nearly one. Furthermore there was no difference in terms of efficiency between Criterion 334 or 434 since the parti-

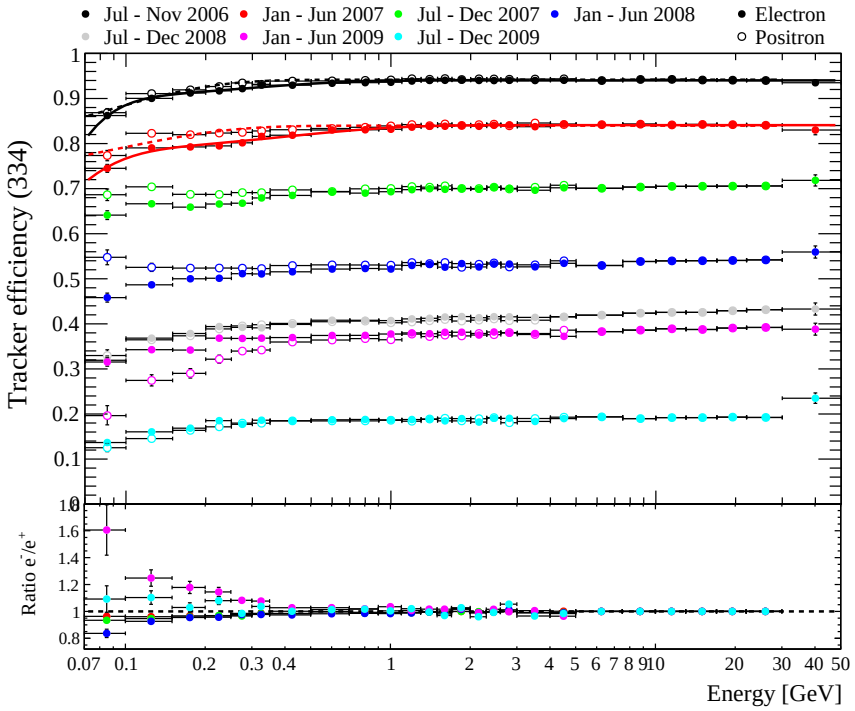

Figure 4.3: Top panel: energy dependence for th tracking system efficiency (Criteria 1-2) evaluated with Monte Carlo data. Filled and open points correspond to electron and positron efficiencies respectively. A progressive reduction of the efficiency with time was measured since the active area of the silicon planes decreased with time. Solid and dotted lines represent fits to the electron and positron efficiencies respectively. Bottom panel: ratio between electron and positron efficiency. Colors pattern correspond to the top panel. The discrepancy at low energy between electron and positron was ascribed to different illumination of the tracker plane area.

cles had (on average) one hit each silicon plane. As the effective area of the tracker planes decreased with time the probability to reconstruct tracks with a number of impact points greater than three decreased as well. As a consequence, especially in 2008 and 2009 when a sizable fraction of front-end chips were not working, the efficiency increased significantly going from Criterion 434 to Criterion 334 as showed in Figure 4.4.

Despite of the front-end chip failures, no degradation in the signal-to-noise ratio and spatial resolution was observed. The front-end chip failures were treated in the simulation with the inclusion of a time-dependent map of dead channels to correctly reproduce the efficiency variations.

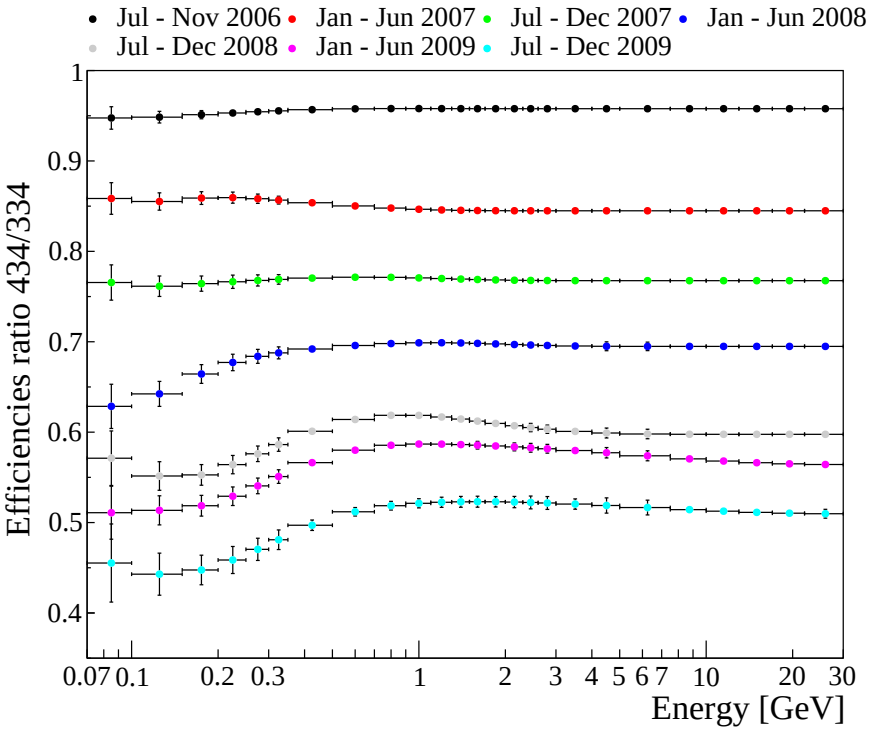

Figure 4.4: Time evolution of the ratio between the efficiency of Criterion 2 and Criterion 2bis. In 2006 the ratio was almost one and it constantly decreased with time till late 2009 when the efficiency of Criterion 2bis was 50% of Criterion 2.

- **Charge-sign dependence**: below 500 MeV the tracking efficiency was found to depend on the rigidity sign. The bottom panel of Figure 4.3 shows the ratio between electron and positron efficiency for Criterion 2. During January-June of 2009 electron and positron efficiency differed more than 60% at 70 MeV but during July-December 2008 the difference was negligible over the whole energy range. Moreover during 2009 the electron efficiency was higher than the positron one but the situation reversed in 2007 and 2008.

  This charge-sign dependence was a consequence of the front-end chip failures combined with the asymmetric illumination of the silicon planes. The latter effect was due to the increasing bending of low energy particles inside the magnetic cavity. As the track bending increases the particle incoming direction became limited to very tilted trajectories with respect to the PAMELA zenith. The situation is illustrated in Figure 4.5 which shows a schematic view of the PAMELA detector (not in scale) together with the trajectories of a low energy positron and electron inside the instrument acceptance. As can be noticed, since they were

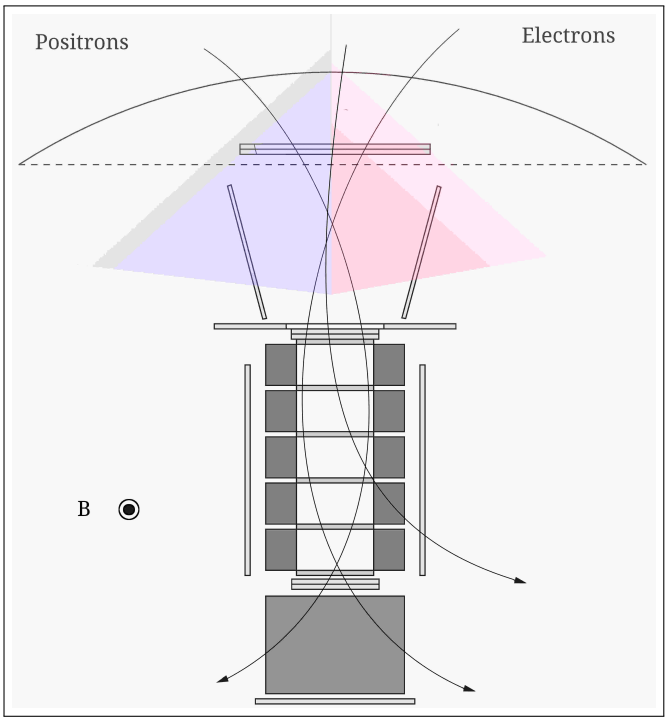

Figure 4.5: Schematic picture of the PAMELA apparatus (not to scale) together with the preferential incoming direction of low energy positrons and electrons. At low energies only particles very tilted with respect to the PAMELA zenith were reconstructed. Since electrons and positrons were oppositely bended the first come preferentially from the right the latter from the left with respect to the coordinate system of the figure.

oppositely bended, positrons came preferentially from the right-side and positrons from the left-side. As a consequence they hit different areas of the tracker planes. Figure 4.6 shows the spatial distribution of the reconstructed impact point on the third tracker plane for 10^6 Monte Carlo electrons and positrons isotropically simulated. Positively charged particles (red line) hit preferentially the right border of the silicon plane while negatively charged particles (black line) hit the left border. This effect was particularly visible at the lowest rigidities (first two panels of Figure 4.6). As the rigidity increases particle trajectory approaches a straight line thus electrons and positrons tend to illuminate the silicon planes with the same spatial distribution (last two panels of Figure 4.6). The tracker efficiency strongly depends on the dead areas over the silicon planes and since below 500 MeV positrons and electrons illuminate different tracker plane areas the resulting efficiencies were expected to be charge-sign dependent.

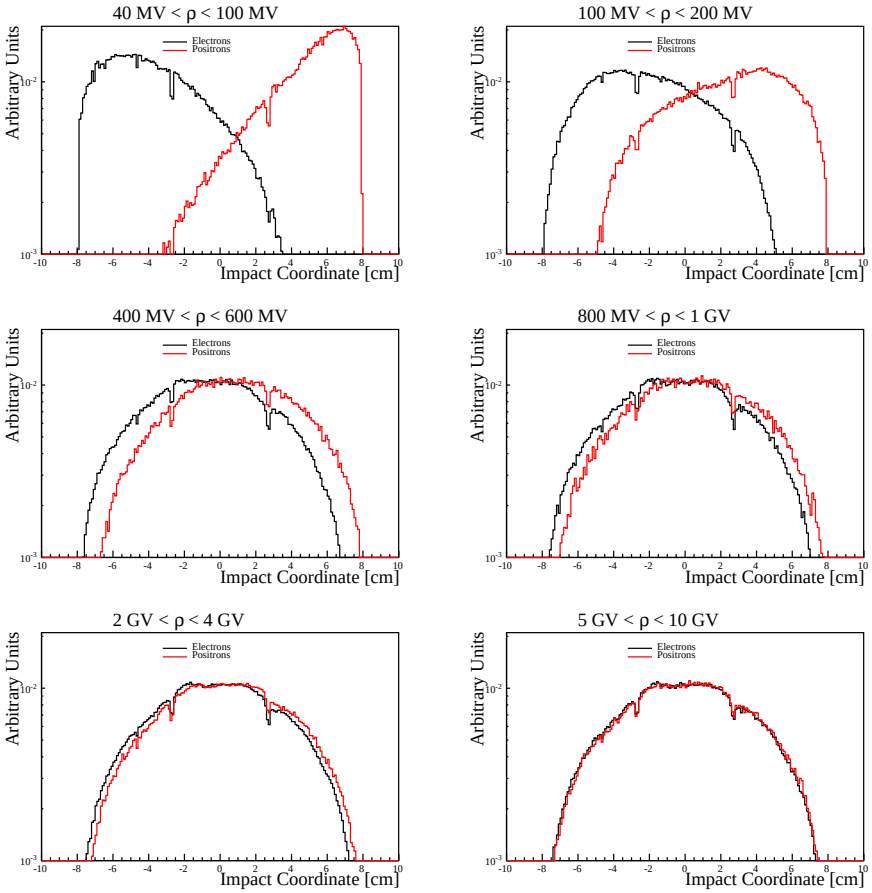

Figure 4.6: Impact point distribution over the third tracker plane for simulated positrons and electrons. The system of reference was centered in the middle of the plane. Each panel displays simulated events in progressively higher rigidity intervals. As the energy increases the asymmetric illumination due to the highly bending of the tracks tends to disappear. Above 5 GeV electrons and positrons have the same distribution.

By definition, the rigidity dependence of the tracking efficiency cannot be evaluated, thus to compare the Monte Carlo with flight data a different approach was adopted. A check on the tracking efficiency was done selecting a sample of electrons with the calorimeter. Indeed at high energy (above few GeV) it was possible to estimate the electron energy measuring the energy released by the electromagnetic shower. Moreover above a few GeV the ionization energy losses above the calorimeter were negligible. At low energies this was not possible since the electron shower was not sufficiently developed to provide a reliable energy estimation (see Figure 3.5). A sample of experimental electrons between 5 and 30 GeV was selected for each six-month interval and the efficiencies of Criteria 2 and 2bis evaluated. A set of Monte

Carlo electrons was selected with the same criteria and the corresponding efficiencies were evaluated. The experimental and simulated results were then compared finding a maximum discrepancy of the order of 5%.

A fit to the tracking efficiency was done with the following function:

$$f(x) = a \cdot (1 - b \cdot e^{-c \cdot x}) \tag{4.1}$$

where a, b and c are three free parameters and x corresponds to E_0. This function was used in order to reproduce the energy dependence of the tracking efficiency observed from the Monte Carlo simulation. As $c \cdot x$ (thus the energy) increases, the exponential terms tend to zero and the function became constant with $f(x) \simeq a$. On the contrary at low values of $c \cdot x$, the exponential term increases reproducing the efficiency decrease, when present. In Figure 4.3 the fits to the electron and positron efficiencies are showed. Tracker efficiency was applied to the unfolded event distribution. Once the track was reconstructed the rigidity dependence of the other selection efficiencies could be evaluated.

Depending on the tracker selection (2 or 2 bis) used to select the efficiency sample, a bias in the efficiency estimation of the other selection criteria could be introduced. Indeed the Criterion 2 bis implies, on average, a better quality of the reconstructed track with respect to Criterion 2, and thus, any efficiencies which depend on the quality of the track as the χ^2 and the velocity selection as well as some calorimeter variables (Ncore), could depend on the tracker selection. For these reason the efficiencies discussed in next sections were evaluated starting from samples of particles selected with both Criteria 2 and 2 bis. It can be anticipated that overall, the differences obtained between the two sets of efficiencies, were less than 2% in 2009 and smaller for the previous time periods. In the following the discussion and the figures refer only to the efficiencies evaluated starting from events selected with the Criterion 2 bis. A final check on the consistency between the efficiency evaluated with Criterion 2 and 2 bis is discussed in Section 5.3.

QUALITY TRACK EFFICIENCY

The rigidity dependence of the χ^2 efficiency was found to depend on the spectral shape of the simulated events. Figure 4.7 shows the rigidity dependence of the χ^2 efficiency resulting from Monte Carlo electrons generated with the Galactic spectrum (filled points) and with the E^{-2} power law (open points). Below 400 MV a large discrepancy was observed: the efficiency evaluated with the Galactic spectrum was significantly lower. This sharp decrease below 400 MV was due to the

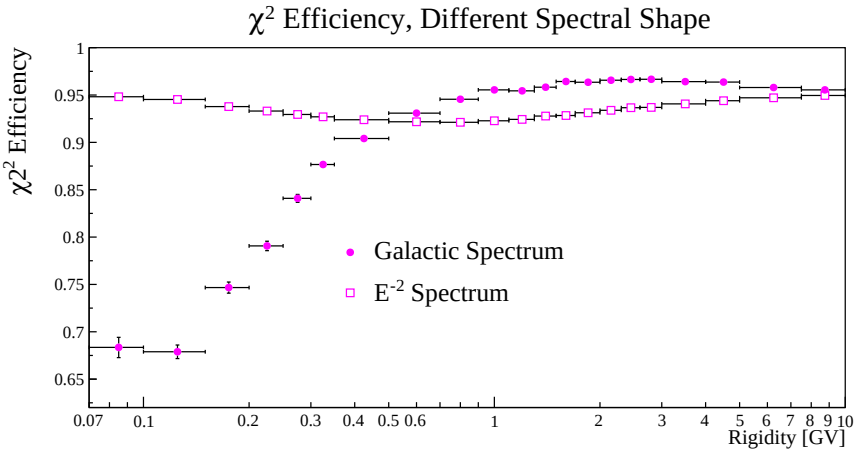

Figure 4.7: Comparison between the rigidity dependence of the quality track efficiencies obtained with simulated events generated with different spectral shape. Filled points represents event generated following the electron Galactic spectrum while open points represent events generated using a power law E^{-2}.

migration of high energy electrons towards lower rigidity. On average those events had higher χ^2 caused by the wrong reconstruction of the track. In the first case (Galactic spectrum), below 500 MV, the quantity of the wrong reconstructed events was a measurable amount of the electron sample causing a decrease in the overall efficiency. On the contrary in the case of the single power law spectrum they was a negligible amount of the total electrons causing a significantly smaller decrease in the efficiency. On the other hand the efficiency dependence on E_0 was not affected by the spectral shape of the input electrons and consequently was used for the determination of the efficiency. Hence the selection efficiency of Criterion 3 was applied to the unfolded event distribution.

Figure 4.8 shows the time evolution of the χ^2 efficiency evaluated with the simulated electrons as a function of E_0. The efficiency sample was selected with Criteria 1 and 2. The χ^2 efficiency was found to decrease over time because of the decreasing number of the points used by the fitting procedure. The solid lines in Figure 4.8 represent the fit performed to the χ^2 efficiency. The energy dependence was more complicated with respect to the tracking efficiency. However it was found that the product of two functions like Equation 4.1 (six free parameters) reproduced well the energy dependence of the χ^2 efficiency. The efficiency shown in Figure 4.8 includes also that of Criterion 4 (dE/dx $<$ 1.8 MIP). The dE/dx selection alone had an efficiencies of the order of 99% and was constant over time.

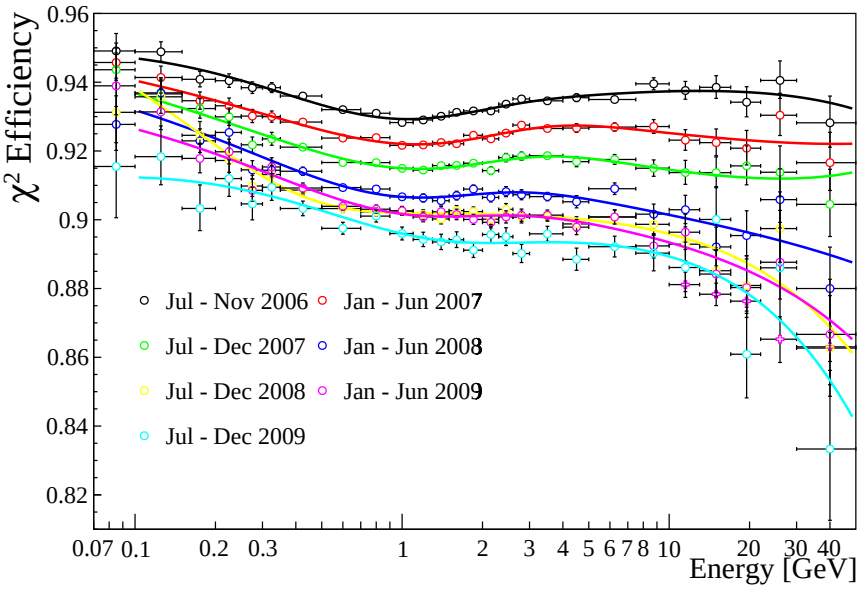

Figure 4.8: Time evolution of the energy dependence of the χ^2 selection efficiency (Criterion 3-4) evaluated with Monte Carlo data. The solid lines represent a fit to the data.

The χ^2 Monte Carlo efficiency was checked with the experimental data. Because of the background sources, flight electrons were selected by means of the calorimeter and velocity selections. Hence, to compare the simulated and the experimental efficiencies, a set of Monte Carlo events was selected using the same selections. The ratio between simulated and experimental efficiencies is illustrated in Figure 4.9 (top panel). Only the first and the last semester were displayed, the other time periods had similar values and energy dependence. Monte Carlo and experimental efficiencies were consistent within 2% in 2006 and 4% in 2009. This ratio was introduced as a systematic error (a fit to the data was done and is shown on Figure 4.9 with the black and red solid lines).

Finally the simulated electron and positron efficiencies were compared to find possible charge-sign dependence. Figure 4.9 (bottom panel) shows the comparison between the 2006 Monte Carlo electron and positron efficiencies. A small discrepancy within 3% was found below 400 MeV. As in the case of the tracking efficiency this difference was due to different illumination of the tracker planes. In fact, since the quality of the fit depended on the dead areas traversed by the particles, and since these areas were not equally distributed over the tracker planes, on average, a different number of points were used to recon-

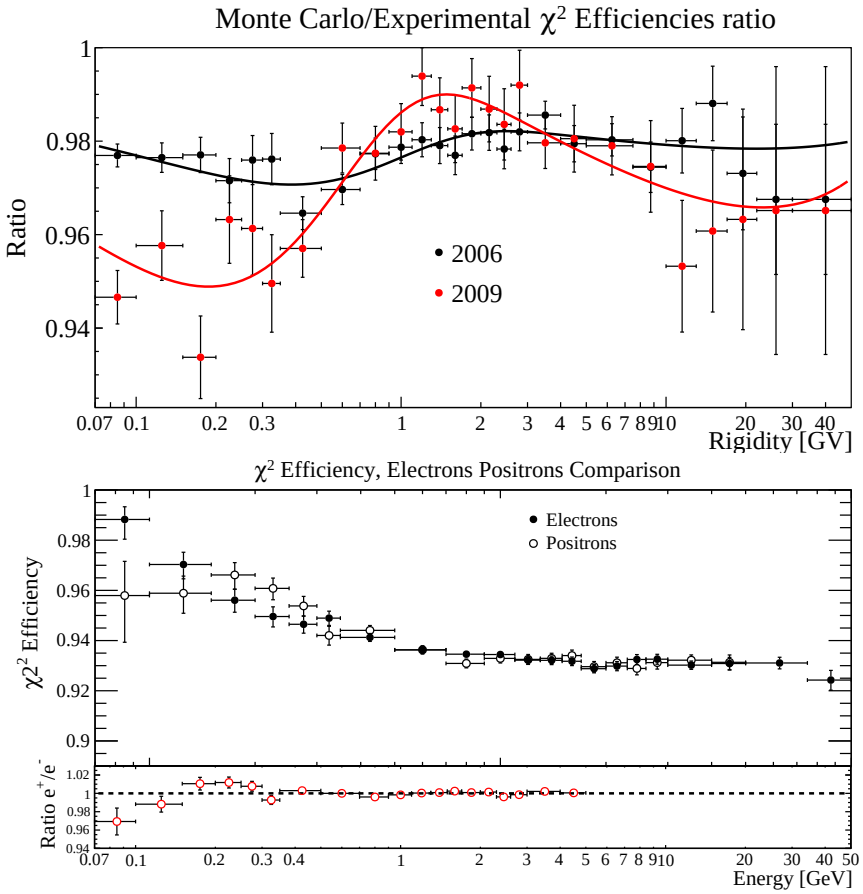

Figure 4.9: Top panel: ratio between the simulated and experimental χ^2 efficiencies for the first and the last semester. The black and the red solid lines correspond to a fit done on the 2006 and 2009 data respectively. Bottom panel: comparison between the 2006 simulated χ^2 efficiency for electrons and positrons together with their ratio.

struct the tracks of low energy electrons and positrons resulting in a slightly different quality of the track.

ANTI-COINCIDENCE EFFICIENCY

As for the χ^2 selection, the rigidity dependence of the anti-coincidence efficiency was found to depend on the spectral shape of the simulated events. Figure 4.10 shows the AC selection efficiency measured with electrons simulated with both the Galactic spectral shape (black open points) and the single power law spectrum (black filled points). The efficiency sample was selected by means of Criteria 1-3. Below $\sim$ 300 MV the AC efficiency evaluated with the Galactic spectrum decreases significantly faster because of the selection on the CAS system (see Fig-

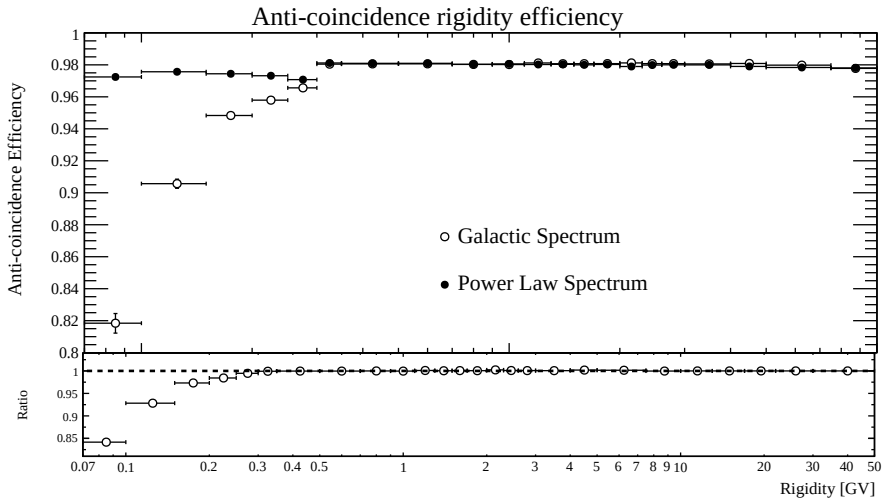

Figure 4.10: The rigidity dependence of the AC efficiency estimated with Monte Carlo electrons. Black filled points represent the efficiency obtained with electrons simulated with a single power law spectrum, black open points the one obtained with electrons simulated with the shape of the Galactic spectrum. The lower panel represents the ratio between the two efficiencies.

ure 4.10, lower panel). In fact, since the migrating events had a greater energy with respect to their reconstructed rigidity, on average they produce much more backscattering particles (with respect to the low energy events) from the calorimeter activating the CAS system. As for the χ^2 efficiency, in the case of the electrons simulated with the Galactic spectrum shape the quantity of migrating events was a measurable amount of the electron sample, causing a decrease of the overall efficiency. On the contrary in the case of the single power law spectrum they were a negligible amount of the total electrons, consequently the efficiency decreased significantly less. The E_0 AC efficiency was not affected by the spectral shape of the input electrons. For this reason the AC efficiency was applied to the unfolded distribution and its energy dependence was estimated from Monte Carlo data. Figure 4.11 shows the anti-coincidence energy dependence for both Monte Carlo electrons and positrons (top panel) together with their ratio (lower panel). Except between 100-150 MeV, where a little discrepancy of $\sim$ 1% was found, the electron and positron efficiencies were compatible and no charge-dependence was found.

The experimental data were used to evaluate possible time dependence of the anti-coincidence efficiency. A clean sample of experimental electrons was selected by means of the tracker (Criteria 1-3), the calorimeter and the velocity selections. This efficiency was found to be constant with time as illustrated in Figure 4.12 where the rigidity

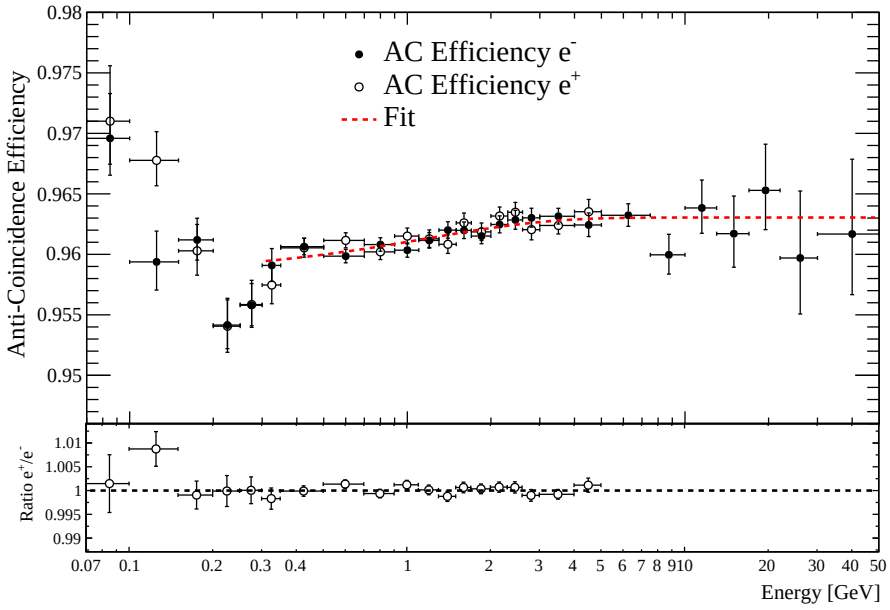

Figure 4.11: Energy dependence of the simulated anti-coincidence efficiency normalized to the experimental data. Filled black points represent the simulated electrons while open black points the positrons. The red dotted line represents a fit to the Monte Carlo electron data.

dependence of the 2006 (filled black points) and 2009 (filled magenta points) experimental efficiency were shown. These efficiencies were compatible inside the statistical errors showing no appreciable variation over time. Monte Carlo data were used to find possible correlations between the anti-coincidence, the calorimeter and the velocity selections but no evidence of bias was found.

A consistency check was done comparing the Monte Carlo and the experimental efficiencies. Figure 4.12 shows the rigidity distribution of the 2006 Monte Carlo (open black points) and experimental efficiency (filled black points). A constant value for the anti-coincidence efficiency was observed between 300 MV and 10 GV. Below 300 MV the presence of CAS in the selection causes the efficiency to decrease due to backscattering particles from the calorimeter as already explained before. As can be seen from the lower panel of Figure 4.12, which shows the ratio between the simulated and the experimental (2009) AC efficiency, the latter, below 200 MV, has a sharper decrease with respect to the simulated one because of the residual contamination of multi-track events. The ratio shows also that above 300 MV a constant discrepancy was found between the simulation and the flight data. A normalization factor F_{Norm} was obtained by means of a constant fit between 300

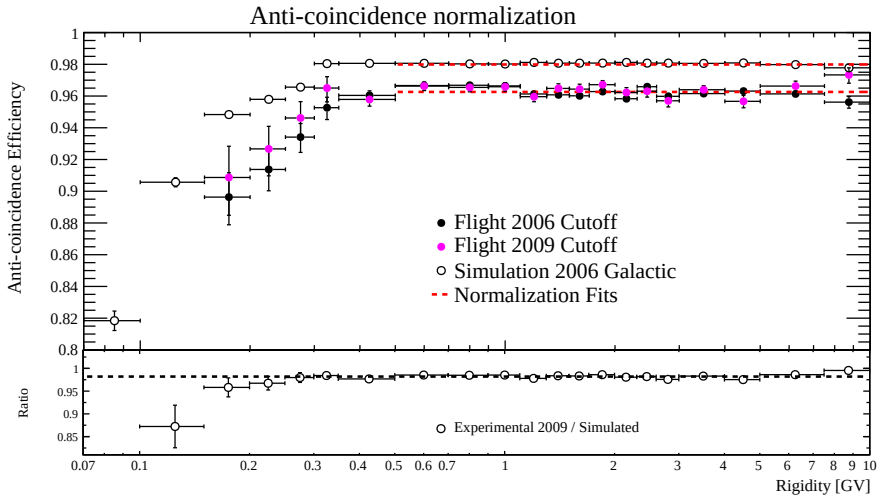

Figure 4.12: Black and magenta filled points represent the experimental anti-coincidence efficiency measured in 2006 and 2009 as a function of the rigidity. The results showed no time-dependence for this efficiency. The open black points represent the Monte Carlo efficiency for 2006. The red dotted lines represent constant value fits used to determine the normalization factor between simulation and experimental data reported in the legend. The lower panel represents the ratio between the simulated and the experimental (2009) AC efficiency.

MV and 10 GV on both the experimental and the simulated efficiency (red dotted lines on Figure 4.12). The normalization factor was derived from the ratio between the two fits and was found to be $F_{Norm} \simeq 1.018$. This value was used to normalize the E_0 Monte Carlo efficiency (the E_0 efficiency in Figure 4.11 was already corrected for F_{Norm}).

The E_0 efficiency was nearly constant between 300 MeV and 10 GeV while it was slightly higher with respect to the rigidity efficiency below 300 MeV because in this case low energy migrating events did not affect the distribution. Above 300 MeV a fit was done to the E_0 efficiency obtaining a nearly constant value of 96% (red dotted line of 4.11) while below this energy the efficiencies estimated in each energy bin were used.

ToF VELOCITY EFFICIENCY

Since the simulation was not fully calibrated to reproduce the velocity information, the ToF velocity ($\beta > 0.9$) selection efficiency was evaluated with the experimental data and thus applied to the folded event distribution.

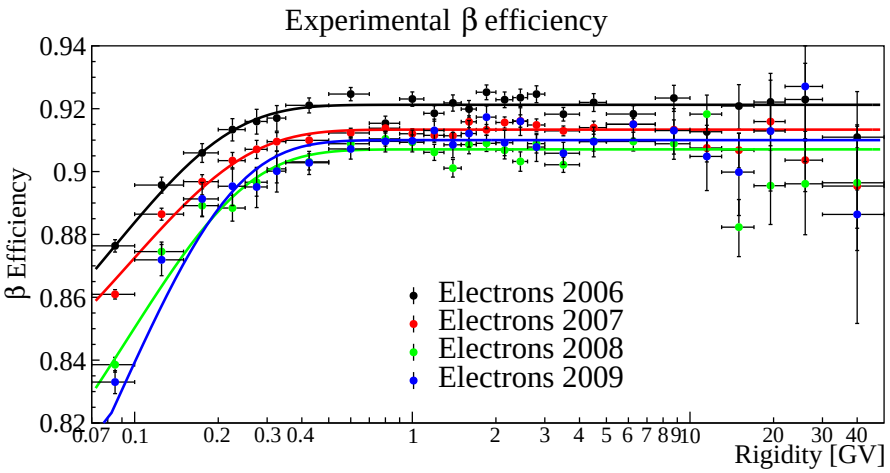

Figure 4.13: Time dependence of the velocity selection efficiency ($\beta > 0.9$) estimated with flight electrons. A small decrease was observed over time ($\sim$ 2%). The colored lines represent a fit performed on the data with Equation 4.1. The small efficiency decrease with time is due to the deterioration of the tracking system and then of the resolution of the measured trajectory. Consequently, the resolution on the beta measurement, decreases. Since the velocity selection was constant with time, this resulted in a lower efficiency.

Figure 4.13 shows the time evolution for the rigidity distribution of the β efficiency. The efficiency sample was selected with the whole set of cuts except of the β selection. The selection efficiency was constant over rigidity and decreases below 300 MV. Indeed, since at low energies the multiple-scattering inside the tracker planes (see Equation A.8) increases, the resolution of the measured trajectory, and consequently of the beta measurement, decreases. Since the velocity selection was constant with the rigidity this resulted in a lower efficiency. The experimental data were also used to evaluate the time-dependence of the β efficiency. A slight variation with time was found. The efficiency decreased by about 2% from 2006 to 2009, as can be seen in Figure 4.13. This small decrease with time is due to the deterioration of the tracking system and then of the resolution of the measured trajectory. As a consequence, the resolution on the beta measurement, decreases. Since the velocity selection was constant with time, a decrease with time of the efficiency was measured. A fit to the experimental velocity efficiency was performed with the function presented in Equation 4.1. The colored lines on Figure 4.13 represent the result of the fit on the flight electron and indicate the efficiency used in the data analysis.

Above few GV the velocity selection efficiency was not expected to depend on the sign of the charge. At low rigidities the Monte Carlo

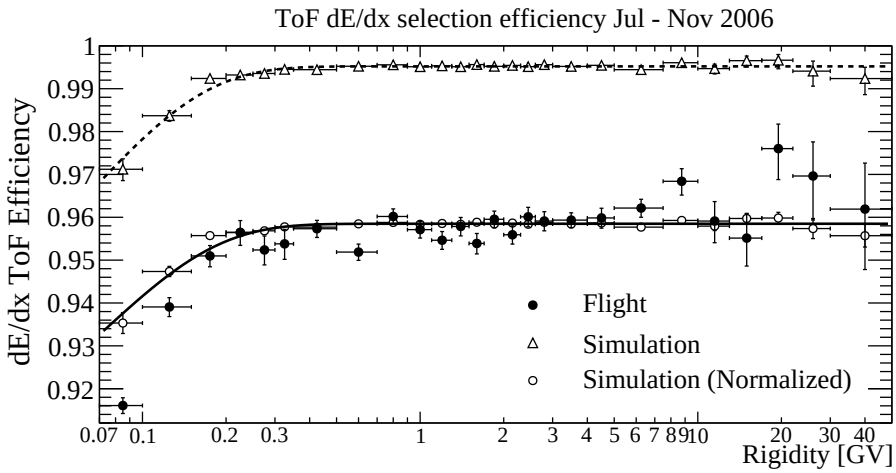

Figure 4.14: Efficiency of the ToF dE/dx selection as a function of rigidity for the first time interval (July-November 2006) for flight (full circles) and simulated (open triangles) data. Open circles indicate the simulated efficiency normalized to reproduce the experimental data between 1 and 10 GV. The dashed line is a fit to the simulated data while the solid line is a fit to the normalized data and indicate the efficiency used in the data analysis.

electrons and positrons were used to check for the charge-dependence of the velocity selection. No evidence for charge-sign dependence was found.

ToF dE/dX SELECTION EFFICIENCY

The ToF dE/dx selection efficiency was applied to the rigidity distribution. Its rigidity dependence was measured starting from the Monte Carlo data normalized to the experimental efficiency at high energy. The experimental efficiency was measured selecting an electron sample using all the selections (including calorimeter) except for the ToF dE/dx cut. Possible correlations between the ToF dE/dX and the calorimeter selections were checked with simulations but no evidence of their presence was found. Figure 4.14 shows the simulated (open triangles) and experimental (filled black circles) dE/dx selection efficiency for 2006. A constant offset was present at energies above 1 GV. Both the Monte Carlo and experimental efficiencies were fitted with a constant value between 1 and 10 GV. The ratio between the fit outputs was found to be $F_{norm} = 1.04$ and was used as a normalization factor between the experimental and simulated data. The simulated efficiency was normalized to the high energy experimental data and is represented by the open circle points on Figure 4.14. It should be noted that the shape of the flight data is well reproduced by simulation except at very low

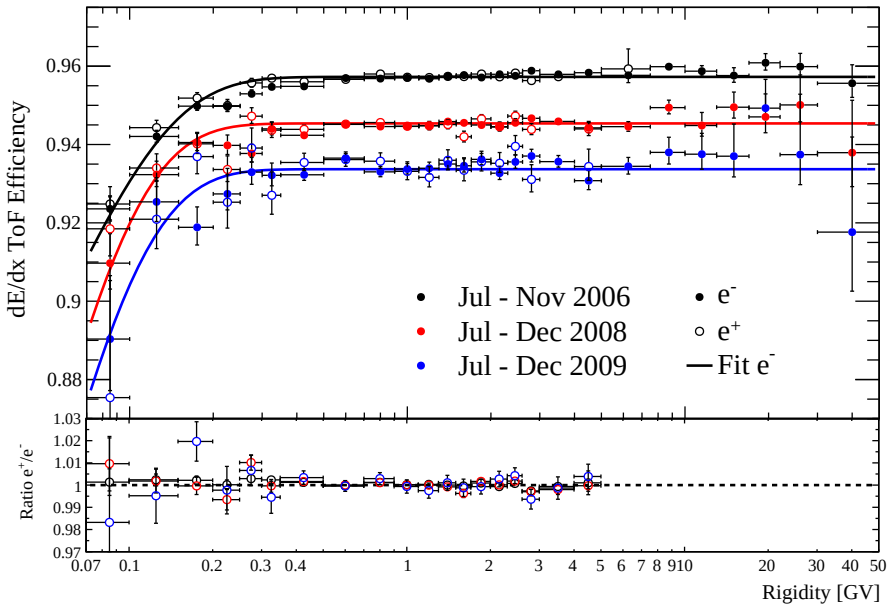

Figure 4.15: Top panel: temporal evolution of the ToF dE/dx selection efficiency. Filled points represent the normalized electron simulated efficiency while the open points are the same efficiency estimated with simulated positrons. Solid and dotted lines represent the fits to the data and indicates the efficiency used in the data analysis. Bottom panel: ratio between the simulated positron and electron efficiency. No indication for a charge sign dependence was found.

rigidities, below about 150 MV. The difference between experimental and simulated efficiencies are about 2% at 70 MV. This difference was due to a residual contamination in the experimental efficiency sample, as shown by a visual inspection of a random sample of events. In fact, it was noticed that only a combination of selections based on all PAMELA detectors was able to produce a clean electron sample at the lowest rigidities. Because of this residual contamination the ToF dE/dx selection efficiency was obtained fitting the simulated data (black line in Figure 4.14) with Equation 4.1.

The ToF dE/dx selection efficiency was constant above 300 MV and slightly decreased below this rigidity. Indeed at low energies the track bending increases and the particles have a larger path length inside the scintillating material (see Figure 4.5), losing more energy through ionization with respect to higher energy particles. Since the dE/dx selection was constant over the energy the efficiency decreased at low rigidities.

Flight data show a small time dependence (about 2% over four years) of the ToF dE/dx efficiency. This variation was due to a slight change in the output of the read-out signals over the years. The simulations were not able to reproduce the efficiency time variation thus normalization factors between experimental and Monte Carlo data were measured. Figure 4.15 (top panel) shows the normalized electron simulated efficiency (filled points) at the beginning, in the middle and at the end of the data taking, together with the fits used in data analysis (solid lines). Moreover Figure 4.15 (top panel) shows the normalized positron simulated efficiency (open points) together with the fit to the data (dotted lines). Bottom panel of Figure 4.15 shows the ratio between simulated positron and electron efficiencies, no indication of charge-sign dependence was found.

CALORIMETER EFFICIENCIES

The PamVMC toolkit was used to simulate the hadronic and leptonic showers inside the PAMELA calorimeter. Indeed, as discussed in Section 3.3, the calorimeter selection criteria were calibrated on the simulated electrons. However particle shower simulation is a delicate work and many elements concur to introduce uncertainties. The longitudinal and latitudinal profiles of the shower, as well as the energy deposition pattern, depend on the models and the physical parameters chosen to simulate the shower development.

In order to better reproduce the passage of radiation through matter the GEANT package is constantly updated with the latest measurements of such parameters as the interaction cross sections. Depending on the GEANT version some physical outputs could be different. As an example Figure 4.16 (top panel) shows the Ncore projection for Monte Carlo electrons with rigidities between 500 MV and 1 GV. The black area represents the Ncore distribution results from the electrons simulated with GEANT4 version while the red area refers to a set of electrons simulated with GEANT3. The distributions differ from each others and a Kolmogorov test[4] excludes the compatibility between the two histograms. The bottom panel of Figure 4.16 represents the comparison between the Monte Carlo electrons and the experimental electrons selected in 2006 with all the selection criteria except for the calorimeter which ensures a negligible residual hadron contamination at these rigidities. Monte Carlo electrons were selected as in the experimental case in order to not introduce any bias. As can be seen also in this case the distributions were not compatible. Part of the disagreement was due to the intrinsic limitation of the simulation toolkit as

4 A statistical test of compatibility in shape between two histograms.

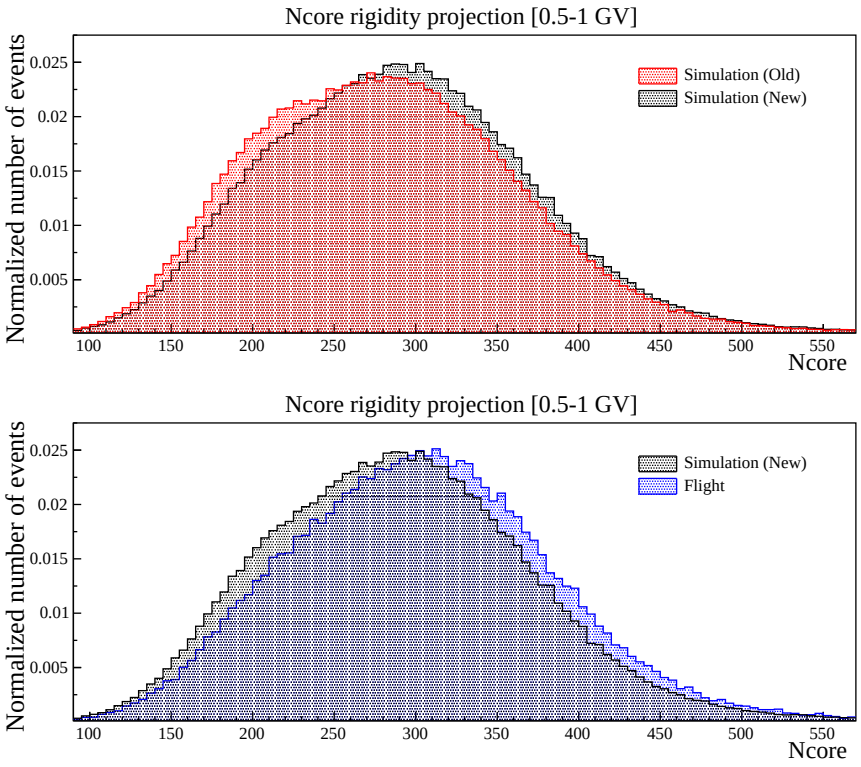

Figure 4.16: Top panel: Ncore projection for electrons between 500 MV and 1 GV. The shaded red area represents the Monte Carlo electrons simulated with the old GEANT configuration while the blue area represents simulated events with the latest GEANT version. Lower panel: Ncore projection for electrons between 500 MV and 1 GV. The shaded blue represents the Monte Carlo electrons simulated with the new GEANT configuration while the black area represents eperimental data selected with all the selection Criteria but the calorimeter.

discussed above. Moreover it should be mentioned that effects such as electronics noise were not fully simulated. For both these reasons the efficiencies of selection Criteria 9-12 were evaluated from flight data and thus applied to the folded event distribution.

The experimental efficiency sample was selected by means of the Criteria 1 - 8 plus an additional cut called ToF-Pattern. This additional selection was used to reduce the spillover protons from the efficiency sample below 1 GV. ToF-Pattern Criterion requires a consistency between the paddles hit in the ToF planes and the projection of the fitted track. Since the curvatures of the spillover proton were wrongly reconstructed, the projected tracks were not associated to hit in the ToF paddles. ToF-Pattern ensures the reduction of the spillover protons to a negligible amount but turns out to have a very low efficiencies be-

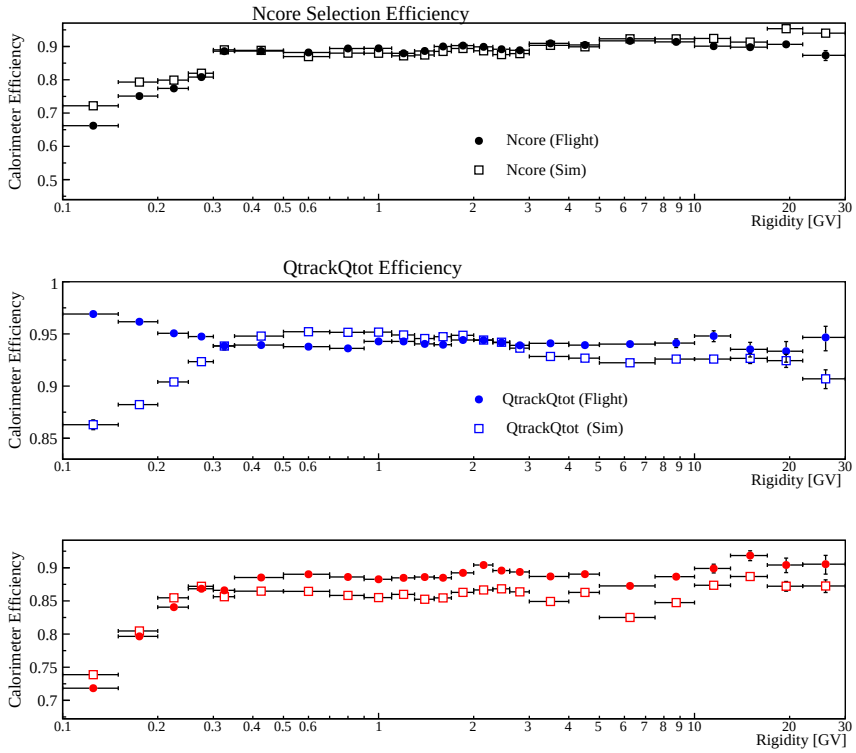

Figure 4.17: Top panel: comparison between experimental and simulated electron Ncore efficiency. Middle panel: QtrackQtot efficiency estimated in cascade after the Ncore efficiency. Bottom panel: Calostrip efficiency evaluated after the Ncore and QtrackQtot selection.

low few hundreds of MV (10% at 100 MV) and hence was not used for particle selection. The simulation shows no correlations between ToF-Pattern and the calorimeter selections. The three panels of Figure 4.17 shows the efficiencies of Ncore, Calostrip and QtrackQtot selections respectively. Filled points represent the experimental data while the open circles are the simulated efficiencies. The Ncore efficiency was evaluated from a sample selected with Criteria 1 - 8 plus ToF-Pattern while Calostrip and QtrackQtot efficiencies were measured after Ncore.

Above 10 GV the Ncore experimental efficiency decreases and becomes lower than the simulated data. This was due to the increasing residual anti-proton contamination in the efficiency sample together with the high energy spillover protons. Up to 10 GV the anti-proton contamination was less than 1% but increased above 10 GV up to 10% (see Figure 1.1). For this reason above this rigidity the shape of the Monte Carlo efficiency normalized to the experimental data at 10 GV was used. The efficiency of Ncore, QtrackQtot and Calostrip selections was found to be constant with time. Figure 4.18 (top panel) shows the

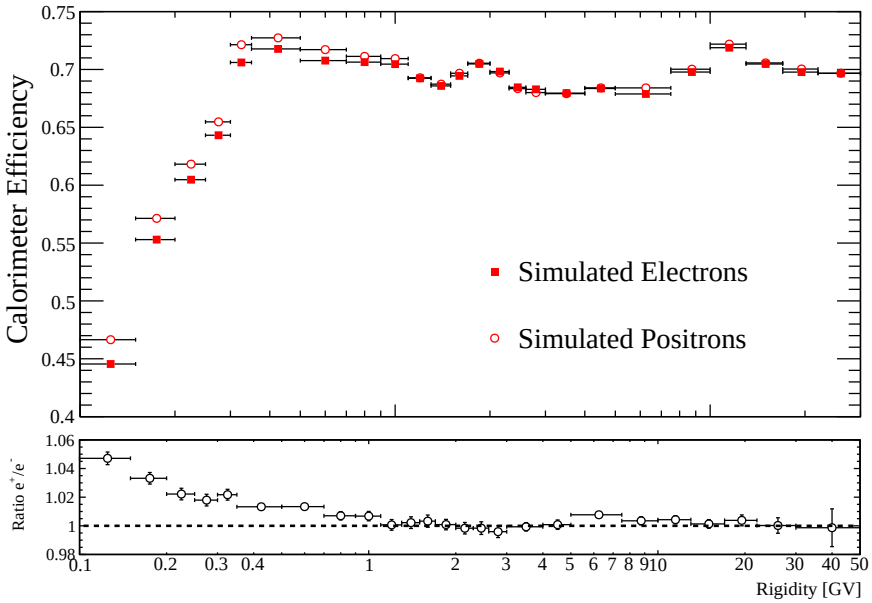

Figure 4.18: Top panel: overall calorimeter selection efficiency for Criteria 9 - 11. Open red points represent electron Monte Carlo efficiencies while the open points are the simulated positron efficiency. Bottom panel: ratio between the simulated positron and electron efficiency. An offset of less than 1% was found between positive and negative particles.

comparison between positron and electron simulated efficiencies of selection Criteria 9 - 11 together with their ratio (lower panel) Below ~ 1 GV the calorimeter efficiency was found to depend on the charge-sign. The difference between electron and positron efficiencies increases as the energy decreases up to 4% below 150 MeV.

The efficiency of selection Criteria 12 was evaluated from an experimental electron sample selected with Criteria 1-8 and ToF-pattern. No temporal dependence was found for this efficiency and the comparison between the experimental and Monte Carlo simulation is shown in Figure 4.19. Since selection Criteria 12 were used to select electrons above 2 GV (see Table 3.1) its charge sign dependence was not evaluated. Above 8-9 GV the experimental efficiency decreases due to the anti-proton and spillover proton contamination. Since the Monte Carlo efficiency was constant above 2 GeV a constant fit to the experimental efficiency between 2 and 7 GV was performed. The value obtained from the fit (~ 85%) was then used in the data analysis.

The dependence on the spectral shape of the efficiencies of selection Criteria 9-11 was studied with Monte Carlo electrons and no significant dependence was found. On the contrary, as shown in Figure

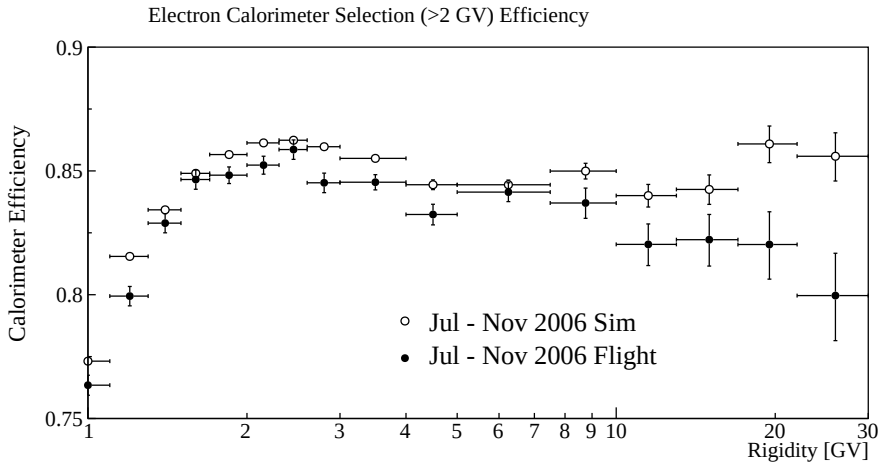

Figure 4.19: Comparison between the experimental (filled points) and simulated (open points) additional calorimeter selection (Criterion 13) efficiency.

4.20, the efficiency of selection Criteria 13 and 14 strongly depended on the input spectral shape. The red filled points represent the rigidity efficiency dependence evaluated with the Galactic spectrum while the red open points results from the single power law spectrum. The latter efficiency was higher of about 3-7% below 300 MV. This difference arose because Nlow, Qtot and Nstrip selections rejected also electrons (positrons) which produced a bremsstrahlung photon. As already discussed these events were reconstructed with a rigidity significantly lower with respect to their real energy (E_0) because of the photon emission. However, because of the emitted photons converted inside the calorimeter (see Figure 4.21), the energy deposition corresponded to the one expected from a particle with rigidity higher than the reconstructed one. As a consequence the calorimeter cuts were more inefficient for this type of event and the efficiency decreased. In the case of Monte Carlo electrons simulated with the single power law the fraction of migrating events was underestimated, and the resulting efficiency overestimated with respect to the experimental situation. In order to disentangle the efficiency estimation from the simulated spectral shape, this efficiency was as a function of E_0 and then applied to the unfolded distribution. On Figure 4.20 the black points represent the E_0 efficiency dependence. The low energy efficiency is considerably higher than the rigidity efficiency. This result reflects the fact that below 350 MV the rejected events were mostly migrating events coming from higher rigidity intervals.

As extensively discussed in this section the presence of migrating events had a fundamental role in the correct estimation of the low energy ($<$ 500 MeV) efficiencies and thus of the electron and positron

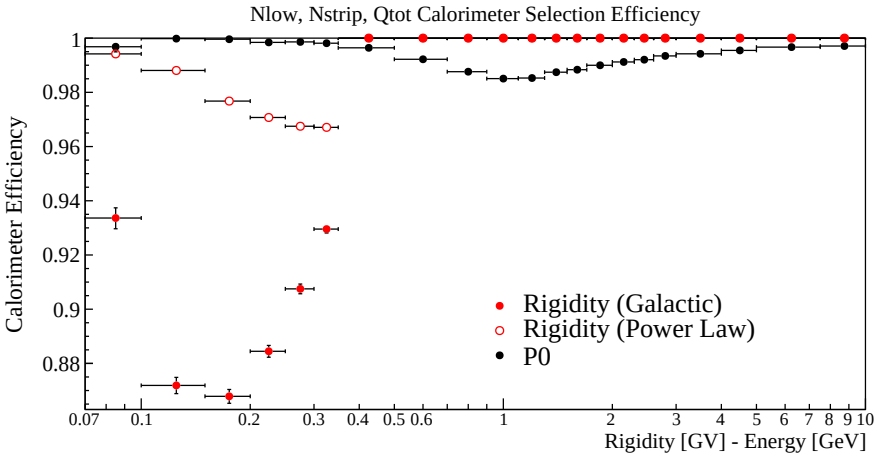

Figure 4.20: Simulated efficiencies for the calorimeter selection Criteria 13-14. The black points represent the E_0 dependence of the electron efficiency. Red filled points are the rigidity dependence of the efficiency obtained with Monte Carlo electrons simulated with the Galactic spectral shape. The open red points represent the rigidity efficiency evaluated from the Monte Carlo data simulated with the single power law spectrum.

fluxes. Indeed the spectral shapes of Galactic CRs were significantly distorted by the interaction with the PAMELA instrument. A statistical unfolding procedure to reconstruct the spectral shape of the Galactic flux at the top of the payload was adopted.

4.4 UNFOLDING

Since in this analysis the electron energies were obtained by measuring the deflections, hence the rigidities, of the particles in the magnet, both the response of the spectrometer and the energy losses suffered by the electrons prior entering the tracking system had to be properly accounted for. Particularly significant were the energy losses due to bremsstrahlung of electrons while traversing the pressurized container and parts of the apparatus on top of the tracking system (equivalent to about 0.1 radiation lengths), since the resulting photons were able to traverse the spectrometer without being detected (see Figure 4.21). Consequently the measured rigidities differed from the initial energies of the electrons at the top of the payload. To account for these effects a Bayesian unfolding procedure, as described in [D'Agostini, 2010], was applied to the count distributions of selected events binned according to their measured rigidities and divided by all selection efficiencies except those of the tracking system, the anti-counter selections and

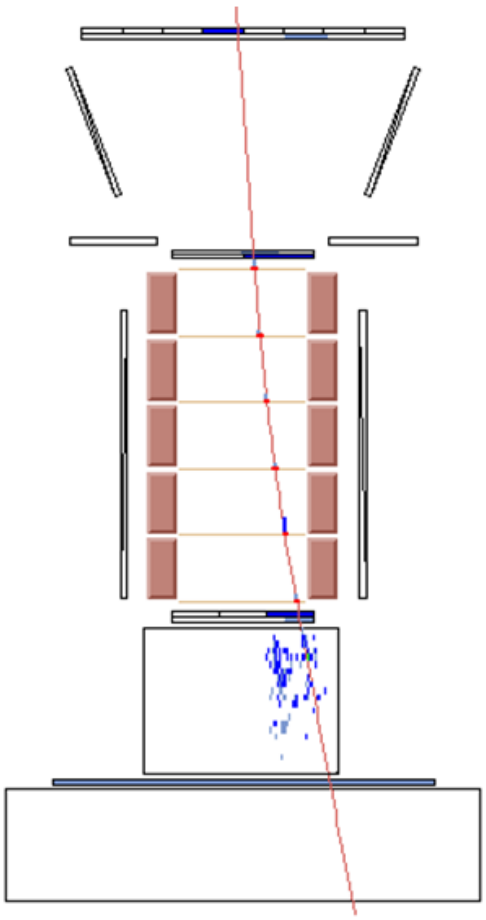

Figure 4.21: A flight electron which emits a bremsstrahlung photon. Both the electrons and the photon convert inside the calorimeter producing a double shower.

the calorimeter selection Criteria 13 - 14. As discussed in the previous section, these were, instead, applied to the unfolded count distribution.

The purpose of the unfolding is to find the "true" number of events in each bin (in this case the number of events in each energy, E_0, bin), given the observed spectrum (i.e. the number of events measured in each rigidity bin) and assuming some knowledge about the physical laws which connect the cause with the effect (spectrometer resolution and energy losses). The purpose of the Bayesian unfolding is to assess[5]:

$$P(x(C)|x(E), \Lambda) \tag{4.2}$$

5 The conditional probability of A given B, $P(A|B)$, is defined as the probability that the event A occurred given that (by assumption, presumption, assertion or evidence) the event B has occurred.

where $x(E_j)$ are the number of events of the observed spectrum in the j-th bin, called the effect bin, $x(C_i)$ the true number of events in the i-th bin, the cause bin, Λ stands for the smearing matrix which elements represent the migration probability of an event from the cause C_i to the effect E_j bin (see below). The goal of the analysis is the determination of the probability $P(C_i|E_j)$, i.e. the probability that several independent causes $(C_i; i = 1, 2, ..., n_C)$, can produce an observable response that is the effect $(E_j; j = 1, 2, ..., n_E)$. This quantity can be evaluated starting from the Bayes' theorem:

$$P(C_i|E_j) = \frac{P(E_j|C_i) \cdot P(C_i)}{\sum_i P(E_j|C_i) \cdot P(C_i)} \tag{4.3}$$

The formula links the probability $P(C_i|E_j)$ that the single observed event E_j has been due to the cause C_i, to the probability $P(E_j|C_i)$ that the cause i-th produces the j-th effect, times the a priori probability of the cause $P(C_i)$. To solve this equation two elements have to be known:

1. The smearing matrix elements $\lambda_{ji} \equiv P(E_j|C_i)$. The terms of the smearing matrix are obtained by Monte Carlo simulation: a large number of events are simulated in each bin and counted where they end up after a realistic simulation of the physics under analysis. The elements of the matrix are estimated with:

$$\lambda_{ij} = x(E_j)|^{MC}_{C_i} / x(C_i)^{MC} \tag{4.4}$$

   where $x(E_j)|^{MC}_{C_i}$ is the number of events in the j-th effect bin coming from the i-th cause bin.

2. The initial probability $P(C_i)$ (prior): an assumption on this quantity has to be done. Usually a constant probability is assumed considering the cause bins equally likely, in other words an initial flat spectra.

Once these quantities are known, having observed in the j-th bin $x(E_j)$ events, the best estimate of the expected number of events assignable to each of the cause is:

$$x(C_i) = \frac{1}{\epsilon_i} \sum_{j=1}^{n_E} P(C_i|E_j) \cdot x(E_j) \tag{4.5}$$

where ϵ_i is defined as:

$$\epsilon_i = \sum_{j=1}^{n_E} P(E_j|C_i) = \sum_{j=1}^{n_E} \lambda_{ij} = 1 - \lambda_{n_E+1,i} \tag{4.6}$$

The assumption to use a flat prior $P(C_i)$ can be justified since simulations on toy models show that the unfolded distribution reproduces

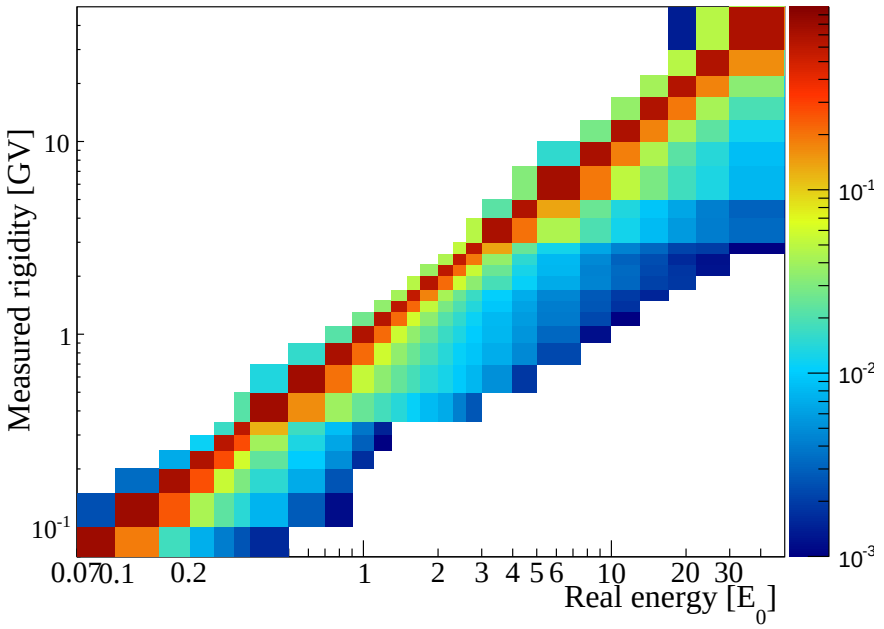

Figure 4.22: The unfolding matrix estimated with Monte Carlo electrons. Each bin corresponds to the probability for an event of initial energy E_0 to be reconstructed with a rigidity ρ due to interactions inside PAMELA (energy losses, tracker resolution).

rather well the true one. However for a more precise approximation an iterative procedure has been used. The posterior obtained after the first iteration, i.e. $\hat{P}(C_i) = \chi(C_i)/\sum_{j=1}^{n_E} \chi(C_j)$, is used as a prior in the subsequent unfolding. Empirically two or three steps are sufficient to recover accurately the true spectrum. A dedicated algorithm was implemented to perform the unfolding. The elements of the unfolding matrix has to be properly estimated with Monte Carlo simulation in order to correctly reconstruct the energy spectrum.

UNFOLDING MATRIX

In this analysis each element of the unfolding matrix represents the probability that an event, which had at the top of the payload an energy E_0, was reconstructed with a rigidity ρ due to the physical effects discussed above (energy losses, tracker resolution). The simulated positrons and electrons were used to estimate the unfolding matrix. In order to properly account for event migration, the unfolding matrix was built with the simulated events which survived the tracker selection Criteria 1-2, the quality track on χ^2, the anti-coincidence and

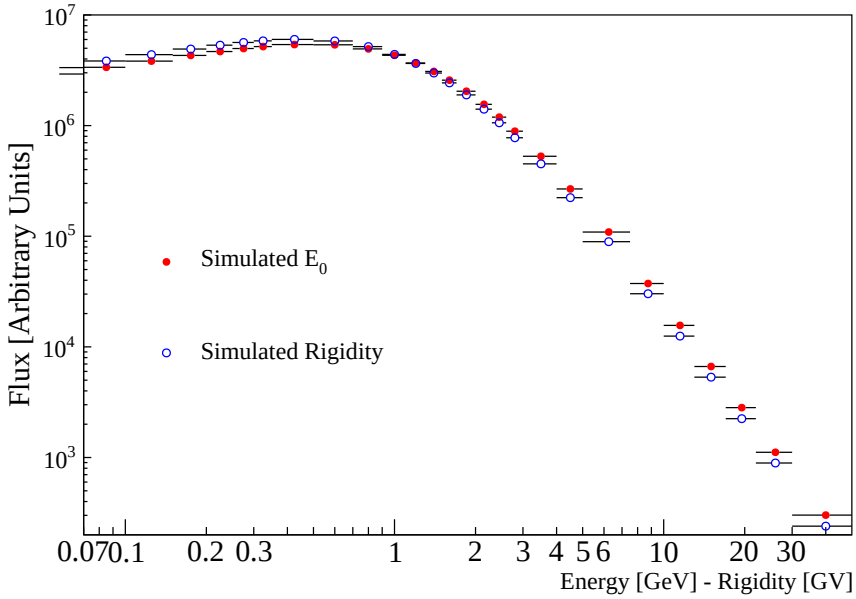

Figure 4.23: Red points correspond to the histogram filled with 10^{10} events following the shape of the electron Galactic spectrum. The blue points simulate how the simulated spectrum is distorted because of bremsstrahlung energy losses corresponding to the passage inside 0.1 radiation lengths (i.e. equal to the amount of material traversed by the particles inside and above the PAMELA instrument).

calorimeter selections 13-14, i.e. with the events selected as in the distribution which will be unfolded.

Figure 4.22 shows the normalized unfolding matrix evaluated with Monte Carlo electrons. Because of their probabilistic meaning, the matrix element of each column were normalized to one. Due to the limited energy (rigidity) range of the matrix, the sum of the element of the firsts and the last columns could give values lower than one since some events migrate outside the matrix range. This effect was treated as an efficiency ϵ and inserted in the Equation 4.5. The higher values of the unfolding matrix correspond to the diagonal elements. This means that the maximum probability for an event was to be reconstructed with its initial energy (within the bin width). The elements below the diagonal represent the probability for an event to be reconstructed with a rigidity lower with respect to its E_0. The migration probability decreases as the gap between E_0 and rigidity increases. Matrix elements above the diagonal represent those events that were reconstructed with a higher rigidity with respect to E_0 because of the tracker resolution.

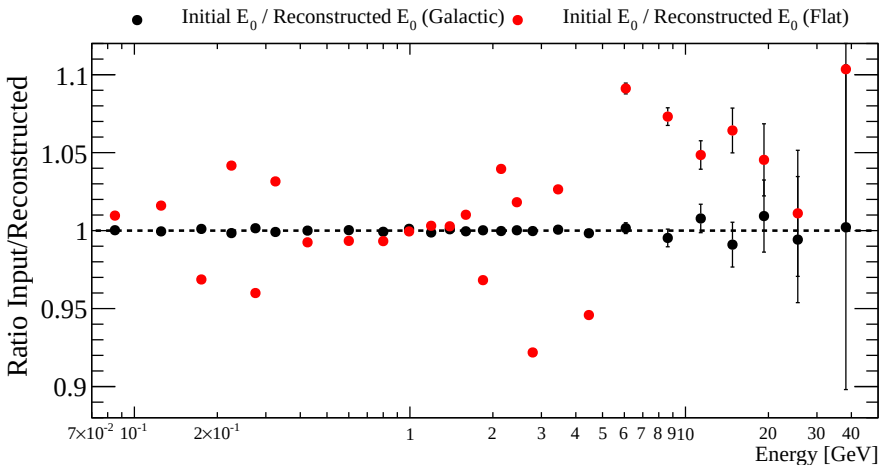

Figure 4.24: Results obtained with the toy model implemented to test the unfolding algorithm. Black points represent the ratio between the simulated and reconstructed E_0 spectrum obtained using the matrix generated using the Galactic spectrum shape. The unfolding reproduces the initial spectrum within the statistical errors. Red points were obtained with the smearing matrix generated using the flat spectrum. In this case structures well beyond statistical fluctuations were introduced.

Several checks were done to test the convergence of the unfolding algorithm and the consistency of the smearing matrix. A toy model was implemented creating a histogram binned as reported in Table 4.2 and filled with 10^{10} events according to the Galactic spectrum shape. The huge number of events ensured the statistical fluctuations to be negligible. This distribution was considered as an "E_0" spectrum and thus distorted with a e^{-x} law as an approximation of the bremsstrahlung energy losses above the tracking system, which corresponded to the passage through $x = 0.1$ radiation lengths of equivalent material. The resulting distribution was treated as a "rigidity" spectrum. Figure 4.23 shows the simulated E_0 spectrum and the resulting rigidity spectrum after the passage through matter. This picture shows how the electron flux is distorted because of the bremsstrahlung photon emission. The rigidity spectrum is higher at low energy (< 1 GV) than the E_0 spectrum due to the migration of higher energy events, consequently at high energy (> 1 GeV) the rigidity spectrum results lower. Two different unfolding matrices were created according to the simulated energy losses: the first filled with events extracted from a Galactic input spectrum, the second using a flat spectrum (i.e. $dN/dE = \text{const}$). The unfolding algorithm was then applied to the rigidity distribution to reproduce the E_0 spectrum. Figure 4.24 shows the ratio between the simulated and the reconstructed E_0 spectrum, black points represent

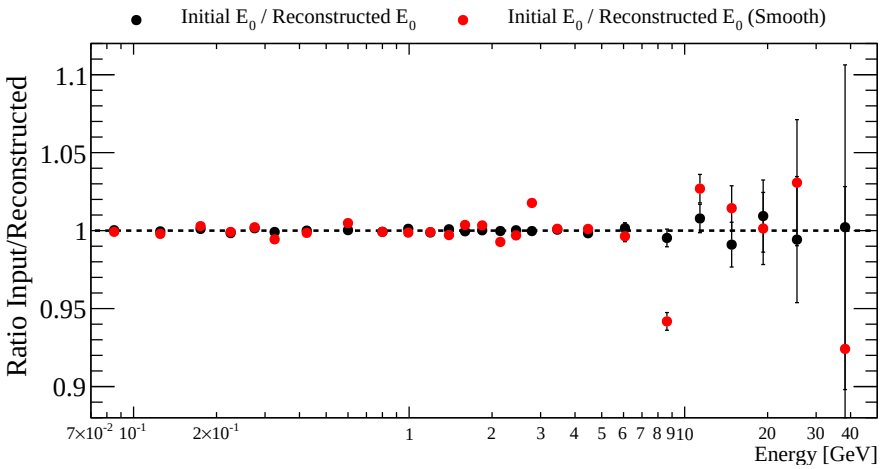

Figure 4.25: Test on the smoothing algorithm. Black points represent the ratio between the simulated and reconstructed E_0 spectrum obtained without applying the smoothing algorithm. Red points represent the result with the smoothing. In this case when the bin width was greater than 1 GV, structures well beyond the statistical fluctuations were introduced in the final result.

the first matrix (Galactic shape) and shows how the unfolding algorithm reproduced the initial E_0 spectrum within the statistical errors. The red points represent the result obtained with the flat matrix. Several structures well beyond the statistical fluctuations were introduced over the whole energy range. In this case the algorithm failed to reproduce the E_0 spectrum since the unfolding matrix overestimated the quantity of migrating events. As a consequence a wrong number of events were shifted from bin to bin, introducing fake structures. From this check it can be argued that to unfold an event distribution with strong variation within each energy bin (as the case of a power law), the matrix has to account for the shape of the spectrum in order to not (under)overestimate the amount of migrating events.

A smoothing is usually applied to the unfolding procedure in order to reduce possible structures introduced by the algorithm. A regularization method for one-dimensional problems consists of smoothing the posterior before using it as prior of the next iteration. Two different smoothing algorithms were tested in this analysis: a weight moving average method (WMA) and the one implemented by default in the ROOT[6] code [SMOOTHING, 1994]. Figure 4.25 shows the ratio between the simulated E_0 spectrum and the reconstructed spectrum obtained with the WMA smoothing. Red and black points referred respectively to the result obtained with and without the smoothing

6 All the analysis presented in this work was based on the C++ object oriented data analysis framework which was developed at CERN starting from 1994 [ROOT, 2015].

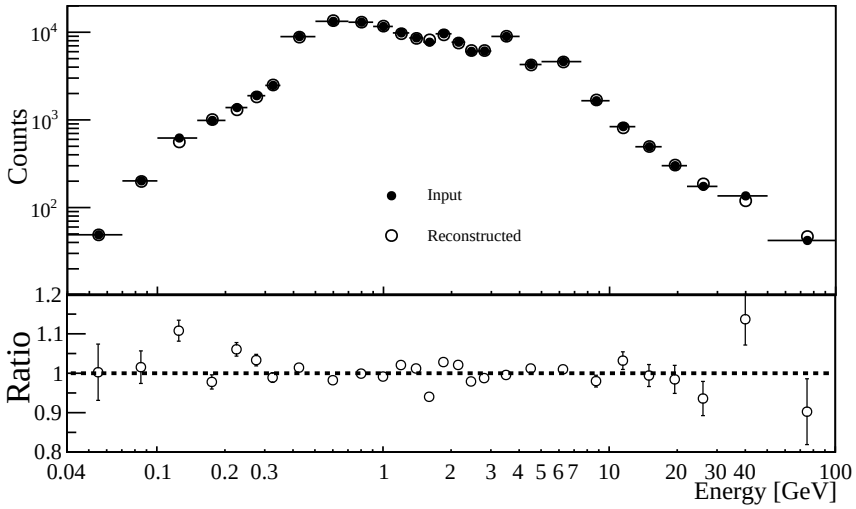

Figure 4.26: Top panel: comparison between the simulated electron energy spectrum (filled black points) and the reconstructed spectrum with the unfolding procedure (open black points). The statistics were of the same order of the flight electrons selected in 2006 in the first cutoff interval (i.e. to recreate the statistics of a typical experimental situation). Bottom panel: the ratio of the input and reconstructed spectrum. The unfolding reproduces the initial spectrum within 10% of uncertainties.

procedure. In the first case above ~ 2 GeV structures well beyond the statistical fluctuations were introduced in the spectrum. In fact it was observed that if the width of the bin was wider than ~ 0.5 GeV, the smoothing instead of reducing the structures increased them. For this reason it was decided to use the smoothing only when the width of the bin was smaller than 0.5 GeV, i.e. below 2 GV.

The unfolding represents a significant correction for the electron and positron fluxes, therefore, the corresponding uncertainties, were carefully evaluated. Two source of uncertainties were taken into account:

- the statistical fluctuations introduced by the limited statistics of the smearing matrix and the experimental spectrum;
- the systematic uncertainties related to the unfolding algorithm itself.

A set of Monte Carlo electrons was selected in order to reproduce the statistical fluctuations of the experimental data. The statistics and the spectral shape of the electrons selected in the first cutoff interval was used as reference. The rigidity distribution of the simulated events was

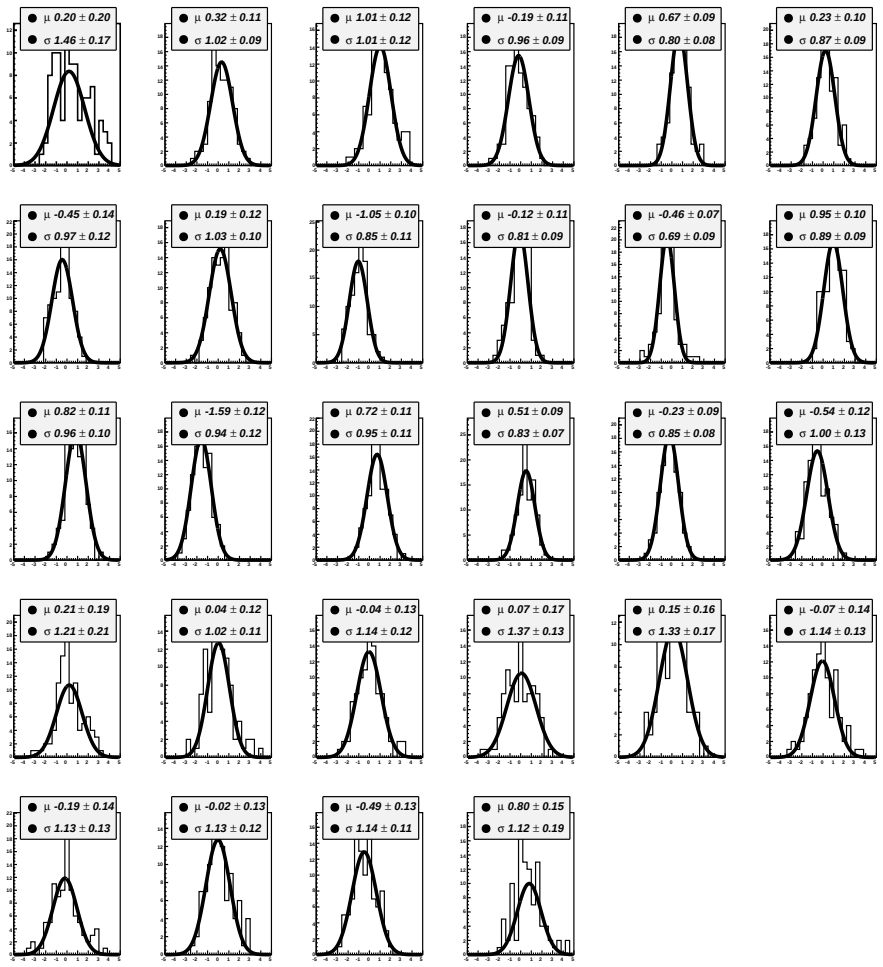

Figure 4.27: Pull distributions obtained unfolding 100 different sample of simulated electrons. The histograms represent the pull distribution of each energy bin. In the text is described how the pulls were estimated (see Equation 4.7).

then reconstructed and unfolded to be compared with the initial E_0 distribution. The result is illustrated in Figure 4.26 (top panel) which shows the initial E_0 spectrum (black filled points) and the reconstructed E_0 spectrum (open black points) while the bottom panel shows their ratio. The initial spectrum was reproduced with a maximum displacement of 10%.

A statistical test was performed to investigate if these fluctuations were consistent with the statistical uncertainties or were an indication of systematic uncertainties For this test a pull distribution was associated to each energy bin. If a random variable x is generated repeatedly

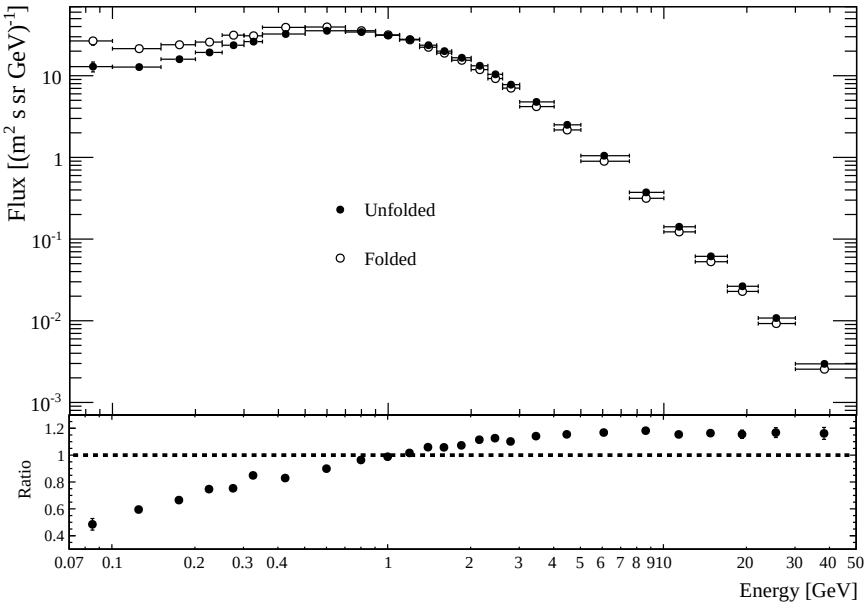

Figure 4.28: Top panel: distributions of the event counts before (open circles) and after (full circles) the unfolding procedure. Bottom panel: ratio between the unfolded and folded count distributions.

with a Gaussian distribution of mean Ξ and width ρ, the pull is defined as:

$$g = \frac{\Xi - x}{\rho} \tag{4.7}$$

and will be distributed as a standard Gaussian with mean (μ) zero and unit width (σ). A mean value of the pull distribution strongly different from zero implies a bias in the generated quantity x while a sigma smaller than one means that the associated errors were overestimated, and underestimated if greater.

In order to test the unfolding algorithm by means of the pull distribution, the simulated electrons were divided in 100 data sets each one containing a statistics comparable to the flight electrons selected inside the first cutoff interval. Each of the 100 rigidity distributions was unfolded and compared with the initial E_0 distribution. The reconstructed count distribution was considered as the random generated variable x, the value of the initial flux was the Ξ and the ρ corresponds to the statistical errors associated with x ($\rho = \sqrt{x}$). Figure 4.27 shows the pull distributions evaluated for each bin of the flux together with the means μ and sigmas σ obtained from a Gaussian fit. The estimated mean μ of many pulls was significantly different from one, suggesting the presence of a systematic bias in the unfolding procedure. Compar-

ing the distribution obtained in Figure 4.26 (bottom panel) with the pull distribution, a correspondence was noticed among the bins with the maximum displacement between the initial and reconstructed fluxes and the pulls distribution significantly displaced from zero, indicating the presence of systematic uncertainties introduced by the unfolding procedure. In the end from these checks it can be argued that the unfolding procedure was able to reproduce the initial energy distribution within maximal uncertainties of $\sim 10\%$. The detailed discussion of the systematics due to the unfolding procedure is discussed in Section 5.2.

Figure 4.28, top panel, shows the effect of the unfolding on the electron spectrum. The open black points represent the rigidity distribution (folded distribution) of experimental electrons selected in the first cutoff interval in 2006 while the filled black points represent the reconstructed E_0 distribution (unfolded distribution). The bottom panel shows the variation in each rigidity (in the spectrometer)/energy (at the top of the payload) bin resulting from the unfolding procedure. At high energy the effect was essentially constant, shifting up of about 20% the flux and leaving unaffected the slope of the spectrum (e.g. see Figure 4.23). At low energy, below ~ 1 GeV, the unfolded spectrum decreases up to 50% at 70 MeV. Moreover below 1 GeV the spectral shape changes as well.

The unfolding was performed on the rigidity distribution of the events selected in each of the cutoff intervals (after having divided for the rigidity efficiencies). Then, to each of the 16 energy distributions (one for each cutoff interval) of the seven time periods, the E_0 efficiencies were applied. At this step, each of the 16 electron and positron energy distributions were still a mix of Galactic and reentrant albedo particles. After the unfolding, the Galactic selection was performed.

4.5 GALACTIC SELECTION

Galactic CRs can be selected comparing the rigidity measured by the tracking system with the vertical rigidity cutoff associated to the PAMELA orbital position. If the particle's rigidity is greater than the vertical cutoff the event has a Galactic origin. The selection takes the form:

$$\rho > k \cdot R_{\perp} \tag{4.8}$$

where k is a constant to be determined as the minimum value that makes the selection efficient in rejecting all trapped particles. Moreover the value of k turns out to be greater than one since it has to take into account the uncertainties related to the vertical cutoff estimation. The latter depends on the precision of the Earth magnetic field provided by

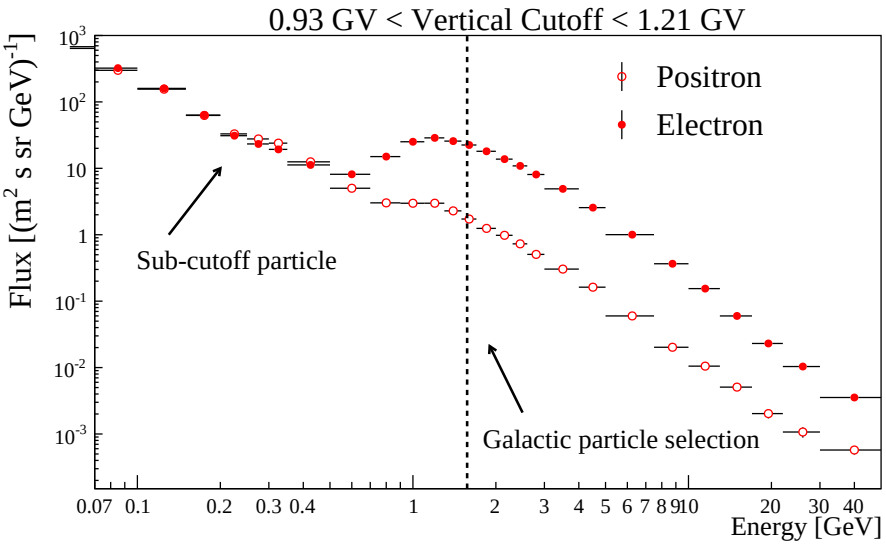

Figure 4.29: Graphical illustration of the Galactic particle selection for electrons (closed circles) and positrons (open circles). The dashed line indicates the energy regions where the Galactic electrons and positrons dominate and are unaffected by the Earth's magnetosphere. Around the geomagnetic cutoff, in the penumbra region, Galactic electrons are mixed with re-entrant albedo electrons that become the dominant component as the energies decrease. Below the vertical cutoff the electron and positron components reach approximately the same magnitude.

the IGRF model and the finite resolution related to the determination of the satellite position and inclination.

For this work a conservative value of $k = 1.3$ was chosen. This value was obtained by comparing the proton flux measured at the magnetic poles, where the cut-off rigidity was of the order of tens of MV and can be assumed as originate outside the Earth magnetosphere, with the flux measure by PAMELA at all the geomagnetic locations obtained by rejecting sub-cutoff particles with Equation 4.8, and found to be compatible [De Simone, 2007].

In order to take into account the event migration, the Galactic selection was performed on the unfolded spectra. If the selection would had been applied on the rigidity event distribution, several Galactic CRs would had been rejected as sub-cutoff particles. For example, a Galactic electron with $E_0 = 3$ GeV, reconstructed with $\rho = 1$ GV and detected at an orbital position corresponding to $R_\perp = 2$ GV, would have been misidentified as a sub-cutoff particle and rejected. Figure 4.29 illustrates how reentrant-albedo particles were rejected. The unfolded electron (filled red points) and positron (open red points) distributions measured inside the 7th cutoff intervall (i.e. between 0.93 and

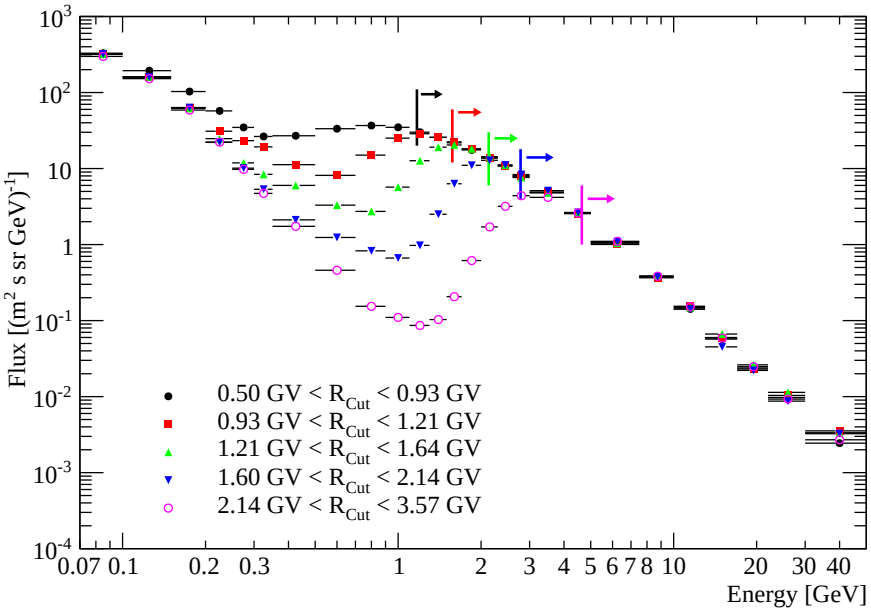

Figure 4.30: Electron energy spectrum measured by PAMELA at the five geomagnetic rigidity cutoff intervals specified in the figure.

1.21 GV) are shown. Two components can be clearly seen: at energies higher than the corresponding geomagnetic cutoff the Galactic component and at lower energies the re-entrant albedo one, with a transition region where the two components mix called the penumbra region. At the lowest energy the reentrant albedo electrons and positrons were approximatively of the same magnitude. The dashed line in Figure 4.29 indicates the energy region (1.3 times above the maximum vertical geomagnetic cutoff of the upper limit of the energy interval, i.e. $1.3 \cdot 1.21 = 1.57$ GeV) where the fluxes were assumed to be of Galactic origin and unaffected by the Earth's magnetosphere.

For each cutoff interval the Galactic selection was performed. Figure 4.30 shows the electron spectrum measured in five different geomagnetic regions and the corresponding Galactic selection represented by the arrows. The final electron spectrum was determined by combining the Galactic part of the fluxes of each geomagnetic cutoff interval weighted by its fractional live-time.

4.6 LIVE TIME

The live-time was provided by an on-board clock that timed the periods during which the apparatus was waiting for a trigger. The accuracy of

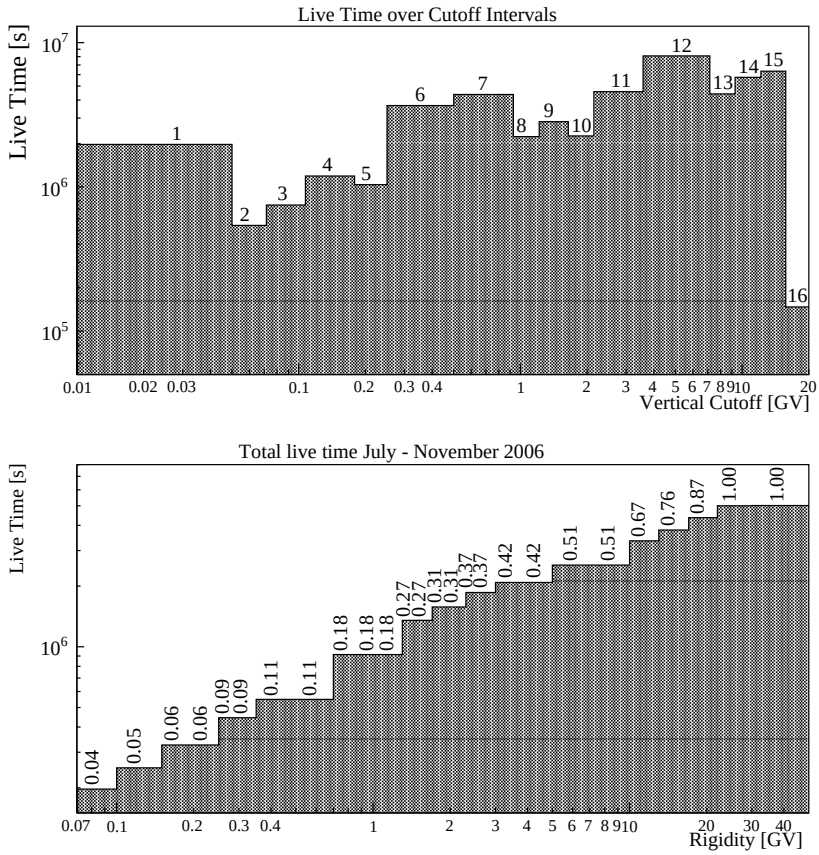

Figure 4.31: Top panel: the live-time evaluated between July and November 2006 in each geomagnetic cutoff interval of Table 4.1. The bin values correspond to the time spent by the satellite at the corresponding geomagnetic latitude interval. Bottom panel: the total PAMELA live-time as a function of the rigidity. The increase of the live-time with rigidity reflects the effect of the geomagnetic cutoff. The total live-time in 2006 was about 5×10^6 s above 20 GV, reducing to about 4% of this value at 70 MV.

the live-time determination was cross-checked by comparing different clocks available in flight, which showed a relative difference of less than 0.2%.

In order to account for the wide geomagnetic region spanned by the satellite, the live-time was separately measured for each of the sixteen cutoff intervals. The live-time evaluated during 2006 is shown in Figure 4.31 (top panel). Each bin corresponds to the time spent by the satellite within a certain geomagnetic latitude interval. The numbers over each bin refer to the geomagnetic cutoff intervals of Table 3.1. The energy dependence of the live-time was obtained combining the bin contents of Figure 4.31 (top panel) into a histogram binned according to Table 4.2. Each energy bin was filled with the sum of the livetimes of all

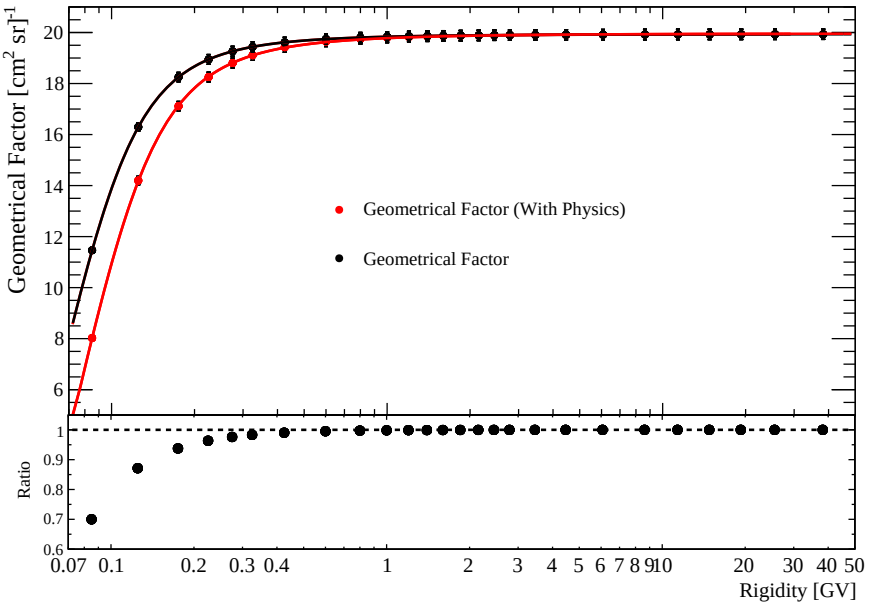

Figure 4.32: The PAMELA geometrical factor resulting from Monte Carlo simulation. The black points represent the acceptance evaluated without taking into account the physical interactions of particles with the instrument while red points account also for physical interaction. The latter results are lower since a part of the low energy particles which interacted with the instrument were prevented from triggering the apparatus.

the cutoff intervals in which PAMELA was able to measured Galactic particles as explained in Section 4.5. The result is shown on Figure 4.31 (bottom panel). For example the first bin of this histogram correspond to the live-time of just the first cutoff interval of Figure 4.31 (top panel) since only inside this orbital position PAMELA was able to measure Galactic particles with rigidities between 70 and 100 MeV. The live-time of the last two bins correspond to the total instrumental live-time since particles above 20 GeV could be detected over the whole orbit. For each bin of Figure 4.31 (bottom panel) the corresponding fraction of the total live-time was indicated. The total live-time in 2006 was about 5×10^6 s above 20 GV, reducing to about 4% of this value at 70 MV.

4.7 GEOMETRICAL FACTOR

The geometrical factor, i.e. the requirement of triggering and containment (at least 1.5 mm away from the magnet walls and the TOF-scintillator edges) was estimated with the full simulation of the appara-

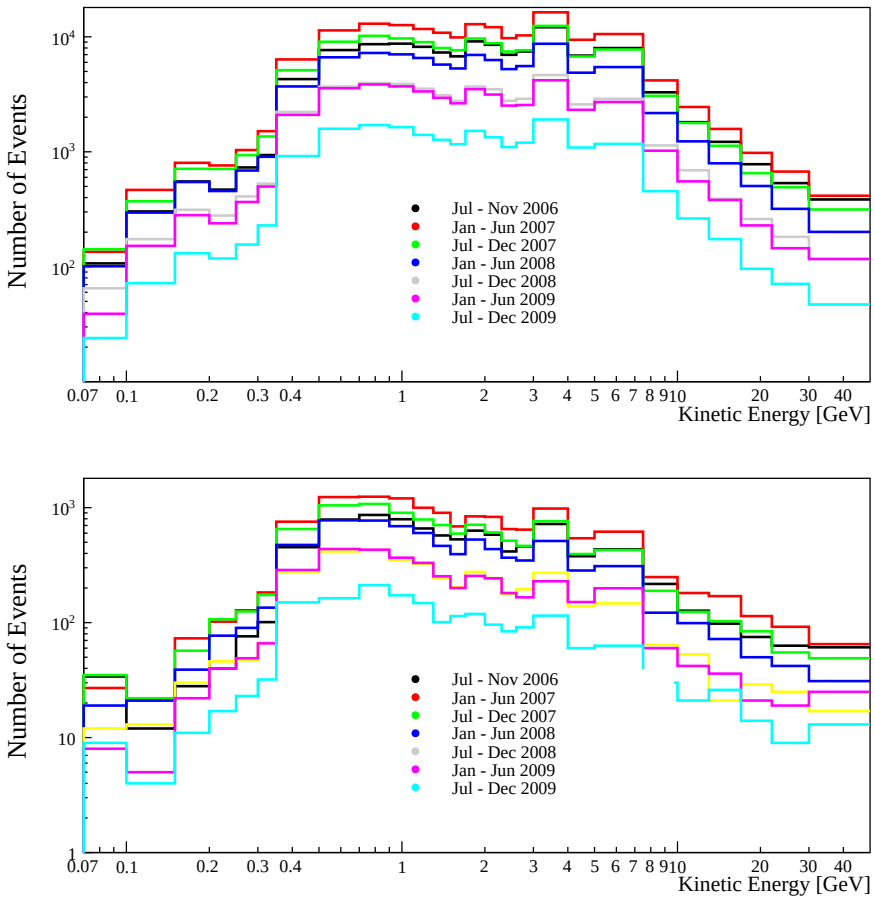

Figure 4.33: Number of selected electrons (top panel) and positrons (lower panel) after the selection Criteria 1 -14. The decrease in statistics over time reflects the decrease of the tracker efficiency.

tus. A large amount of particles was isotropically simulated over the 4π solid angle. The particles who triggered and were contained were then counted and compared to the initial numbers of particles to evaluate the geometrical factor. Figure 4.32 (top panel) shows the geometrical factor evaluated with the Monte Carlo simulation for the PAMELA instrument with a containment at 1.5 mm (black points). It was found to be constant at 19.9 cm^2 sr above 1 GeV, decreasing smoothly below this energy. This decrease was due to the increasing curvature of the electron tracks in the magnetic spectrometer. The black points of Figure 4.32 represent the geometrical factor evaluated accounting only for the PAMELA geometry and the magnetic field of the tracking system. However, at low energy, physical processes such energy losses, multiple scattering, etc.. had a non-negligible effect on the instrumental acceptance. Indeed these physical processes at the lowest rigidity pre-

vented many low energy particles from triggering the apparatus leading to a significant decrease in the acceptance. For example, since the multiple scattering increases as the energy decreases, a large number of low energy particles were deflected out and did not trigger. Red points in Figure 4.32 represent the geometrical factor evaluated accounting also for the physical interactions. Below 500 MV the acceptance decreases faster with respect to the previous case. The bottom panel of Figure 4.32 shows the ratio between the acceptance evaluated with and without the physical interactions. The variation of the acceptance was of the order of 30% at 70 MV thus representing a non-negligible correction.

The sharp acceptance decrease and the limited live-time result in a significant statistics reduction below a few hundreds of MeV. Figure 4.33 shows the number of Galactic electrons (top panel) and positrons (lower panel) selected in each of the six month time periods after applying all the selection criteria. The decrease in statistics over time reflects the degradation of the tracker efficiency. The statistics of 2006 was lower than 2007 despite the tracker efficiency being higher since December 2006 was excluded from the analysis.

The fluxes were evaluated according to the procedure described in the next Section.

4.8 FLUX ESTIMATION

The flux $\phi(E)$ (where E is the kinetic energy) was evaluated as follows:

$$\phi(E) = \frac{N(E)}{\epsilon(E) \times G(E) \times T \times \Delta E} \tag{4.9}$$

where $N(E)$ is the unfolded count distribution, $\epsilon(E)$ the energy efficiencies (χ^2, anticounter, tracking system and Criteria 13-14), $G(E)$ the geometrical factor, T the live-time and ΔE the width of the energy interval. Summarizing, the various steps that lead to the flux estimation were:

- select positrons and electrons among a vast hadron background by means of the selection criteria reported in Table 3.1;
- construct count distributions binned as shown in Table 4.2 for each of the 16 vertical geomagnetic cutoff intervals of Table 4.1;
- divide the folded count distributions for those efficiencies evaluated as a function of the rigidity;

- unfold each of the 16 rigidity distributions with the algorithm described in Section 4.4 in order to reconstruct the energy distributions;
- divide the unfolded count distributions for the efficiencies evaluated as a function of the energy (E_0);
- perform the Galactic selection as described in Section 4.5;
- sum the Galactic components of the 16 rigidity cutoff distributions;
- divide for the geometrical factor and the live-time.

The fluxes were evaluated for both the Criteria 2 and 2bis. Two sets of seven fluxes were measured for the positrons and two for the electrons. The final results were then obtained using Criterion 2bis up to 500 MeV and the significantly more efficient Criterion 2 at higher energies. Finally, a total of seven electron and seven positron spectra were evaluated during the 23-th solar minimun (July 2006 - December 2009). Multiple consistency checks were done in order to test the reliability of the results. A normalization at high energy, were the fluxes were assumed to be time-independent, was performed using the high energy proton fluxes. The consistency tests are presented in the next chapter together with the systematic uncertainties, the results and their interpretations.

5 RESULTS AND INTERPRETATION

INDEX

The last chapter of this thesis is devoted to presenting the results on the time-dependent electron and positron fluxes measured by PAMELA during the 23rd solar minimum. Before presenting the results, a few consistency checks made to test the reliability of the electron and positron fluxes are discussed. Furthermore, the normalization factors used to account for any not fully estimated time variations of the experimental environment, e.g. the tracking or other selection efficiencies, are presented. For this purpose a sample of high energy (30 - 50 GV) protons were used. The systematic uncertainties related to the efficiency estimation, the unfolding procedure and the normalization factors are then discussed.

Finally it is described how the 3D numerical solution of the Parker equation (see Sections 1.6 and 1.7) was tuned to reproduce the experimental fluxes. The numerical values and the energy dependence of the perpendicular and parallel diffusion coefficients, as well as the drift scale, needed to reproduce the PAMELA data, are presented. The physical meaning of these results are discussed and compared with those obtained in the analysis of the proton fluxes measured during the same period [Adriani et al., 2013b]. Because of the huge mass difference between electrons and protons, at the lowest energies, different propagation processes become dominant. Finally, the charge-sign dependence of the solar modulation is studied comparing the time variation of the electron, positron and proton fluxes. A different increase with time of the electron with respect to the positron and proton fluxes was found

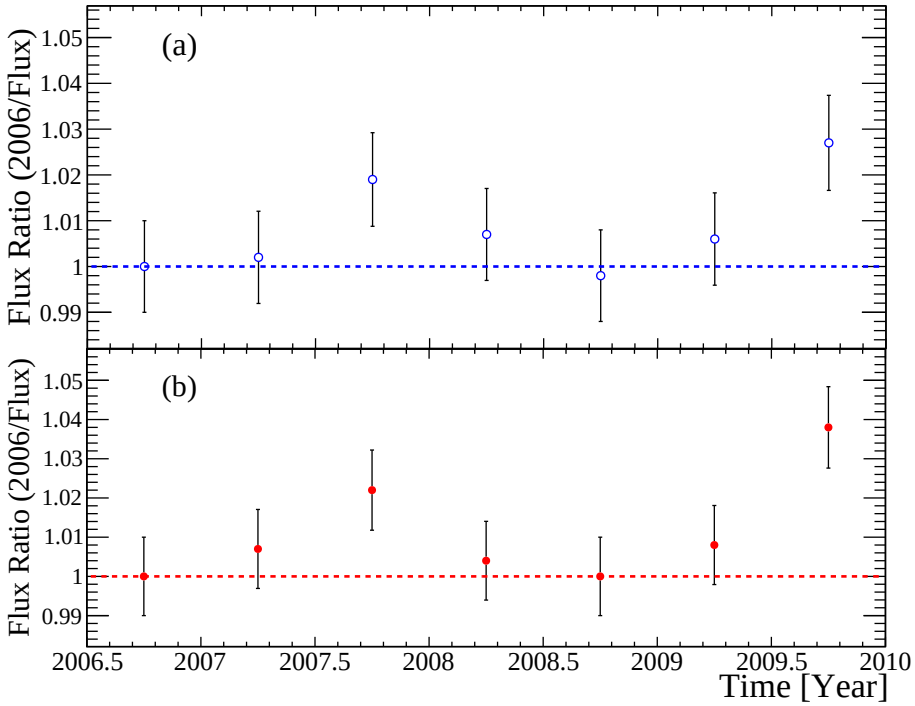

Figure 5.1: The high-energy (30-50 GeV) proton flux measured in July-November 2006 divided by the proton fluxes measured in each time interval. Proton events were selected with the same requirements of the electron analysis but the calorimeter selections using Criterion 2bis (a) and Criterion 2 (b).

and interpreted as an indication of the charge-sign dependence of the solar modulation.

5.1 FLUXES NORMALIZATION

As discussed in Section 1.6, above ~ 30 GeV, the modulation of the Galactic CR fluxes was significantly smaller than at the lowest energies. Above a few tens of GeV, in fact, the CR gyro-radius becomes close to the size of the heliosphere and the CR intensity decreases only a few percent with respect to the LIS (see Table 5.1). Moreover, since the period from 2006 to 2009 is a minimum for the solar activity, the time variation of high energy CRs was expected to be small. In fact, from the computed electron spectra presented in Section 5.5, a variation of the electron flux at high energy (30-50 GeV) between July-November 2006 and July-December 2009 of less than 0.4% can be estimated. For

this reason the CR electron and positron fluxes were assumed to be constant with time above 30 GeV.

Possible time-dependent variations of the high energy electron and positron fluxes, due to, e.g., not fully estimated time variations of the selection efficiencies, were studied as in the proton analysis [Adriani et al., 2013b]. A sample of protons at high energy, between 30-50 GeV, was selected with the same criteria as for the electron and positron analysis but the calorimeter selections. The tracking selection efficiencies were estimated with the same Monte Carlo code used for the electron and positron analysis. Then, the resulting fluxes measured in July-November 2006 were divided by the proton fluxes measured in the other time intervals. Figure 5.1 shows this ratio as a function of time for fluxes obtained with Criterion 2bis (a) and with Criterion 2 (b). It can be seen that the high-energy proton flux varies a maximum 2% over the years with the exception of the end of 2009 when the flux estimated with Criterion 2 differs by about 4%. The statistical errors associated to each normalization factor were treated as systematic uncertainties (see Section 5.2). Because of the lack of statistics it was not possible to use high energy electrons (positrons) to evaluate the normalization factors. In that case the uncertainties associated with the normalization factors were greater than the correction themselves.

The normalization obtained from the protons were used to normalize in each half-year time interval the electron fluxes measured using both Criteria 2 and 2bis. In conclusion, the final energy spectra were obtained by correcting the positron and electron fluxes with these normalization factors and using Criterion 2bis up to 500 MeV and the significantly more efficient Criterion 2 at higher energies. The systematic uncertainties related to the fluxes were estimated before performing the consistency checks.

5.2 SYSTEMATICS UNCERTAINTIES

All the sources of systematics errors were carefully studied and quantified. The overall errors associated to the fluxes consisted of the quadratic sum of the statistical and the systematic uncertainties. The systematics included:

- the statistical errors resulting from the finite size of the efficiency samples;
- the systematics related to the χ^2 efficiency, already discussed in Section 4.3;

- the statistical error associated to the normalization factor presented in Section 5.1;
- the systematics due to the unfolding procedure;
- the residual pion and proton contaminations discussed in Section 3.4.

Each of these contributions are discussed separately in the next paragraphs.

SYSTEMATIC FROM EFFICIENCIES

The selection efficiencies were obtained from flight and simulated data using efficiency samples. The statistical errors resulting from the finite size of such samples were included in the uncertainties of the flux measurements and treated as systematic uncertainties. As discussed in Section 4.3 the values of the efficiencies were obtained by fitting the simulated and flight distributions. The uncertainties related to the fit estimation were obtained evaluating the confidence intervals associated to the fitted values. The one sigma (68%) confidence intervals[1] were evaluated for the various fitted efficiencies presented in Section 4.3. In Figure 5.2 (top panel) the resulting contributions to the systematic uncertainties from each efficiency are shown. Except for the tracker efficiency below 300 MeV, the systematics related to the efficiencies were smaller than 1%. All these contributions were treated as independent uncertainties and quadratically summed to the overall systematics.

As already discussed in Section 4.3, the ratio between the Monte Carlo and the experimental efficiency for the quality track selection (Criteria 3 and 4) was considered as a systematic uncertainty. In Figure 5.2 (top panel) the dotted black line represents the contribution of this uncertainty to the overall systematics (about 2%). Also this uncertainty was quadratically added to the overall systematics.

SYSTEMATICS FROM THE NORMALIZATION FACTORS

As discussed in Section 5.1, the fluxes were normalized using factors obtained comparing the high-energy proton flux over time. The statistical errors on these factors amounted to less than 1% and were treated

1 The confidence limits of the fitted functions were evaluated with an existing routine of the ROOT framework. This routine calculates the confidence limit at each point of the fitted function at the required confidence level (one, two, three sigma). For more detail about this algorithm see https://root.cern.ch/root/html/tutorials/fit/ConfidenceIntervals.C.html.

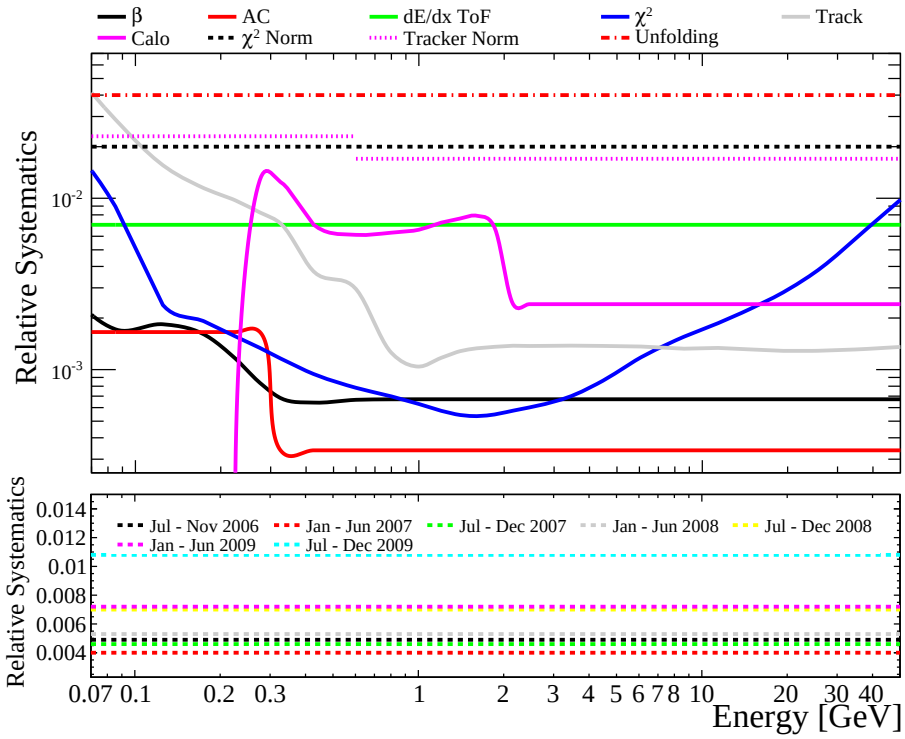

Figure 5.2: Top panel: the single contributions to the systematic uncertainties. The various colored lines represent the errors due to the efficiencies estimation, the χ^2 efficiency normalization and the unfolding procedure. Bottom panel: contribution to the systematics due to the statistical errors on the normalization factors presented in Section 5.1. The increase with time of this systematic reflects the decrease in the proton statistics due to the tracker efficiency decrease. Each contribution to the systematics is discussed in detail in Section 5.2.

as systematic uncertainties. In Figure 5.2 (bottom panel) the time variation of the statistical errors due to the normalization factor is shown. This systematic increases with time since the statistics of the proton sample used to evaluated the normalization factors decreases because of the tracker efficiency decrease. Since these normalizations accounted for the stability respect to the second half of 2006 of the fluxes estimated for the following time periods, a possible systematic uncertainty on the high-energy proton flux obtained for July-November 2006 and due to the tracking selection efficiency was studied as in [Adriani et al., 2011a]. An efficiency sample was obtained both from flight and simulated data selecting non-interacting minimum ionizing particles traversing the calorimeter. With this selection, protons with rigidities greater than 2 GV were selected. The resulting simulated and experimental tracking

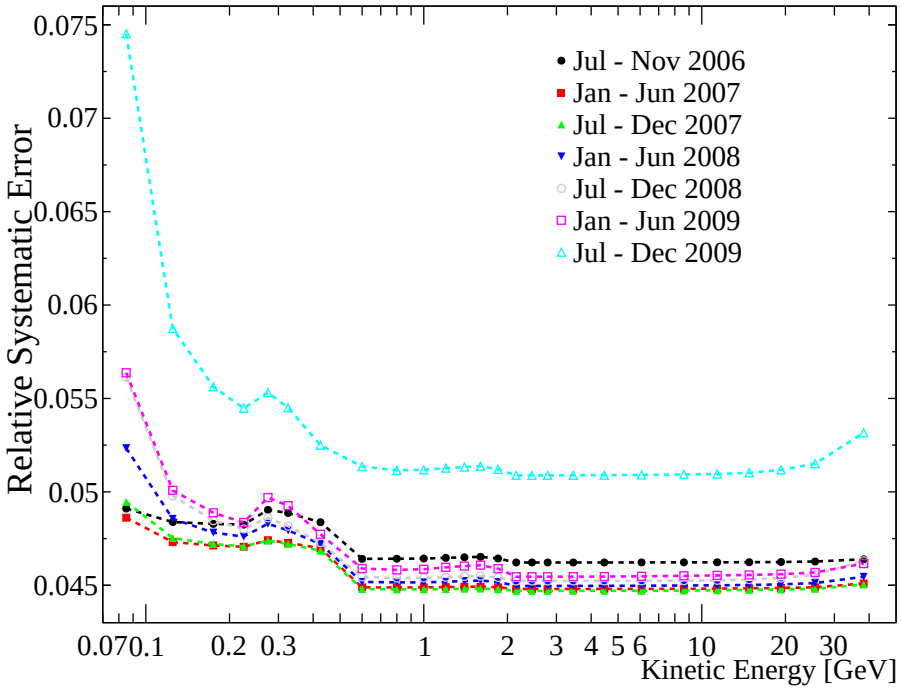

Figure 5.3: Overall (relative) systematic errors as a function of the rigidity for the seven time intervals. The systematics due to the residual hadron contamination were not included.

selection efficiency differed by 1.7% and 2.3% when using Criterion 2 and 2bis, respectively. The dotted magenta lines in Figure 5.2 represent these systematics. Considering that this experimental efficiency sample was not fully representative of the experimental condition for this analysis, this difference was treated as a systematic error. These uncertainties were quadratically added to the overall systematics.

SYSTEMATICS FROM THE UNFOLDING

The unfolding procedure was checked with Monte Carlo simulations analyzing the relative differences between the expected and reconstructed count distributions by means of pull distributions (see Section 4.4 and Figure 4.27). Nearly all of the pulls presented in Figure 4.27 followed the expected standard normal distribution with sigma consistent with one, hence the statistical errors properly accounted for the fluctuations in the flux values. Also the means fluctuated around zero indicating possible bias. The relative differences between the means of the expected and reconstructed count distributions could be approxi-

mated with a Gaussian distribution. Following D'Agostini and Raso [2000], the RMS of this distribution, amounting to 4%, was treated as one standard deviation systematic error due to the unfolding procedure. On Figure 5.2 the red dotted line represents the systematic due to the unfolding procedure.

SYSTEMATICS FROM RESIDUAL HADRON

As discussed in Section 3.4, both Monte Carlo and flight data were used to estimate the residual pion and (spillover) proton contamination. Figure 3.19 represents the residual spillover proton contamination after the whole electron selection criteria while Figure 3.20 represents the residual proton contamination after the positron selection criteria. As already discussed, a check performed on flight data did not confirm the abundance of residual spillover protons shown in Figure 3.19. Therefore this contamination was considered as a systematic uncertainty and quadratically summed to the electron systematics. Also the residual proton contamination in the positron sample shown in Figure 3.20 was quadratically summed to the positron systematics. The residual pion contamination is shown in Figure 3.22 for both electrons and positrons. Also this contamination was quadratically summed to the overall systematics.

OVERALL SYSTEMATICS

The systematics discussed in the previous paragraphs were considered as independent errors and thus quadratically summed to obtain the overall uncertainties. Figure 5.3 shows the relative errors resulting from the quadratic sum of the systematic uncertainties (residual hadron contaminations were not included in the figure). The systematic errors due to the efficiency estimation, the unfolding procedure and the normalization factors were supposed to be independent from the sign of the charge, thus the same uncertainties were associated to the electron and positron fluxes[2]. The increase over time of the overall systematics was essentially due to the decreasing efficiency of the tracking system which, reducing the statistics of the efficiency sample, increased the systematics related to the efficiency estimation. The systematic uncertainties were then quadratically summed to the statistic uncertainties to obtain the overall flux errors. After the systematics evaluation, three

2 Actually, a small difference between the positron and the electron systematic uncertainties, related to the estimation of the low energy efficiencies, was present. However, simulation shows that this difference, when present, was lower than 0.1% and thus was ignored.

consistency checks related to the flux estimation, are discussed. The results of these tests were found consistent within the systematic uncertainties, as explained in the next section.

5.3 CONSISTENCY CHECKS

Before presenting the time-dependent electron and positron spectra, three consistency checks performed on the final results are discussed. These were implemented in order to check all of the analysis chain that combined many different elements: event selection, efficiency estimation, unfolding and normalization.

- **Efficiency check**: a first check was done comparing the energy spectrum of each time interval obtained with Criterion 2 with the equivalent one obtained with Criterion 2bis. This was performed in order to check the consistency of the selection efficiencies (the ones which depend on the tracker selections). Figure 5.4 shows the ratios of the two sets of fluxes for each time interval. The solid lines indicate the overall systematics uncertainties associated to the flux estimation (see Section 5.2). Above 500 MeV, the ratio between the two sets of fluxes was consistent with one showing a excellent agreement within the systematic uncertainties. On the contrary, below 500 MeV, the fluxes obtained with Criterion 2 were consistently higher because of the contamination by spillover protons caused by the less stringent selection (see Section 3.2). As discussed in Section 4.3 all the efficiencies were evaluated starting from a sample of particles selected with both Criteria 2 and 2bis. The agreement between the two set of fluxes ensures that all the efficiencies were consistently evaluated. Moreover the agreement above 500 MeV indicates that also the normalization factor discussed in Section 5.1 were consistent for both the Criteria 2 and 2bis.

- **Low energy check**: an additional check was performed to validate the estimation of the low energy (< 1 GeV) fluxes. The low energy part of the re-entrant albedo electron spectrum was measured at the lowest geomagnetic latitude (vertical geomagnetic cutoff greater than 12.1 GV) in each time interval and it was compared to the same spectrum measured in the second half of 2006. It has been shown ([Lipari, P., 2002; Zuccon et al., 2003]) that, because of the East-West effect, re-entrant albedo electrons at low geomagnetic latitudes, i.e. high geomagnetic cutoffs, are mostly produced by high-energy (> 30 GeV) protons interacting with the Earth's atmosphere. Therefore, it can be inferred that the

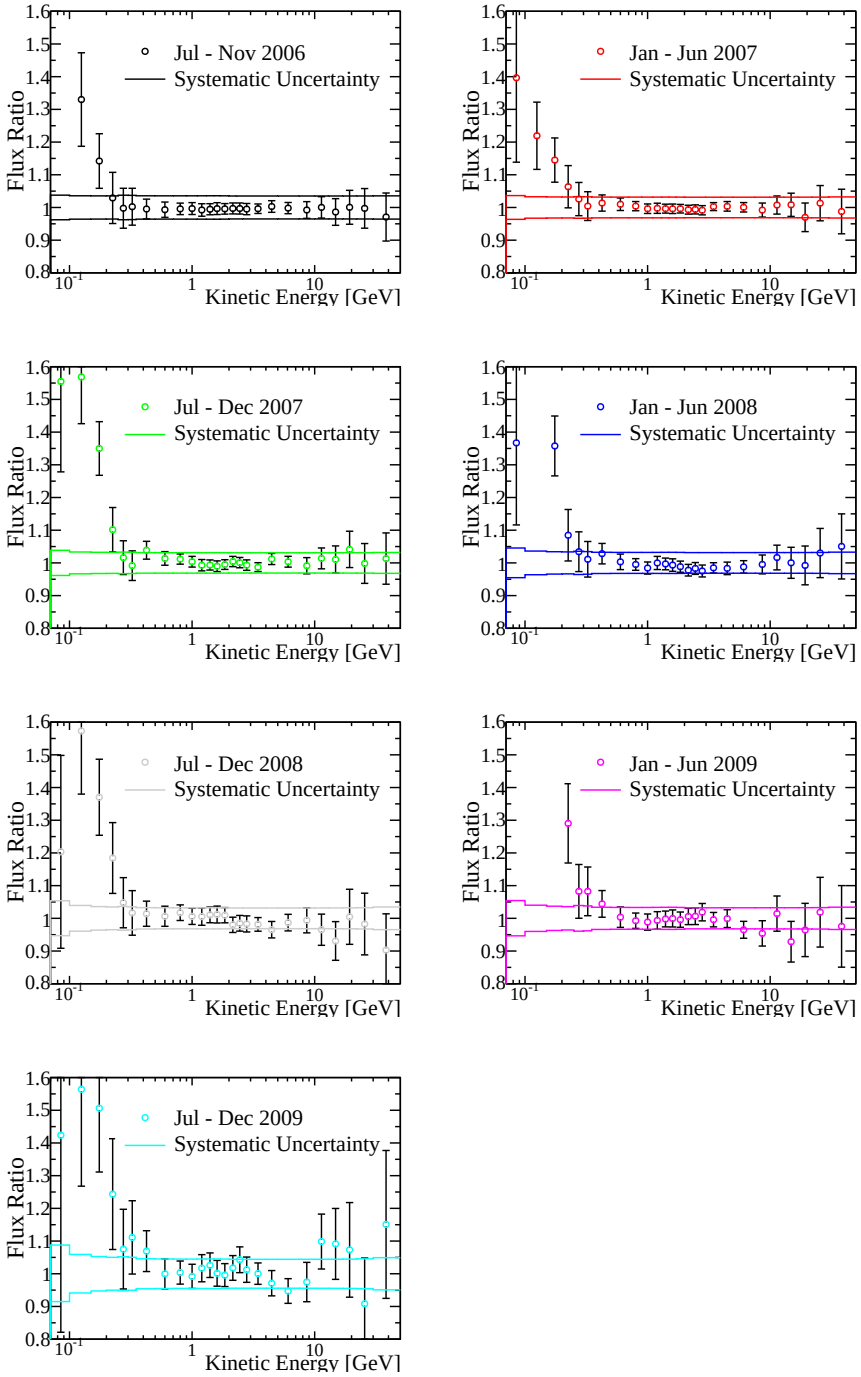

Figure 5.4: First consistency check. The electron fluxes measured in each time interval obtained with Criterion 2 divided by the equivalent ones obtained with Criterion 2bis. The solid lines indicate the systematic uncertainties associated with these data (see Figure 5.3). These ratios, above 500 MeV, show an agreement between the two set of fluxes within the systematic errors, suggesting that the efficiencies and the normalization factors were correctly evaluated. On the contrary, below 500 MeV, the fluxes obtained with Criterion 2 were consistently higher because of the contamination by spillover protons caused by the less stringent selection (see Section 3.2).

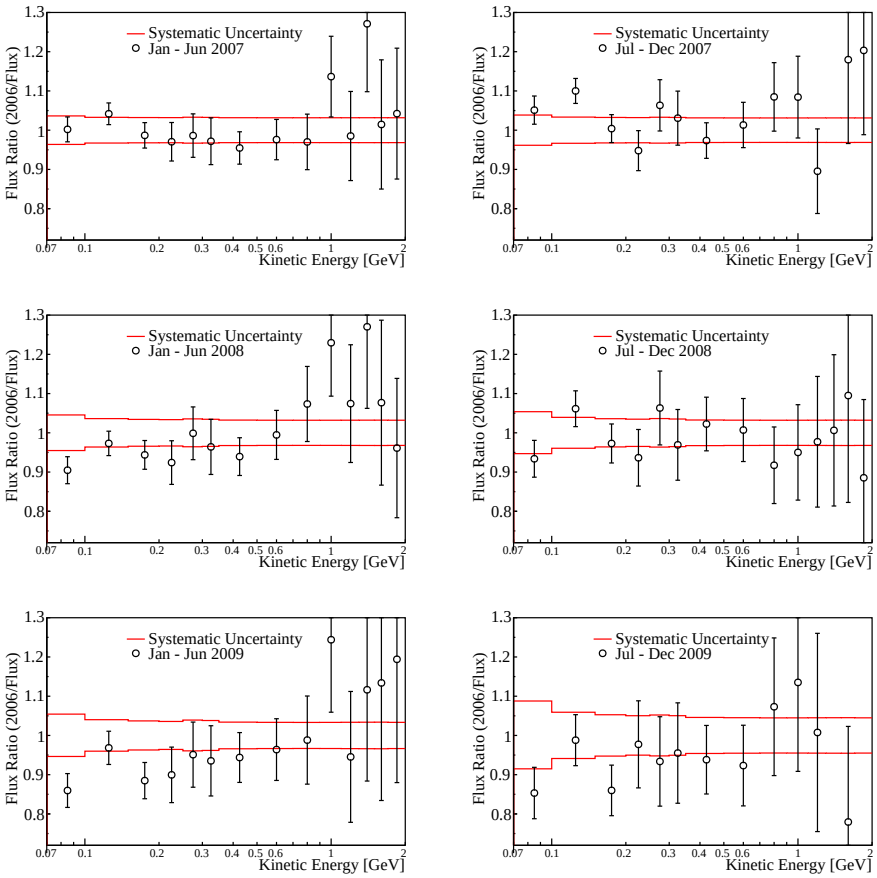

Figure 5.5: Second consistency check. The re-entrant albedo electron fluxes measured in July-November 2006 divided by the equivalent fluxes measured in the other time intervals. These events were selected for vertical geomagnetic cutoff greater than 12.1 GV. The solid lines indicate the systematic uncertainties associated with these data. This check was performed to validate the estimation of the low energy (< 1 GeV) fluxes, see text.

re-entrant albedo electrons energy spectrum should not show significant temporal variations due to solar modulation, and hence it can be used to check the temporal stability of the flux measurements at the lowest energies. Figure 5.5 shows the re-entrant albedo electron fluxes measured in July-November 2006 divided by the equivalent fluxes measured in the other time intervals. The solid lines indicate the systematic uncertainties discussed in the previous section. No significant time variation was found, indicating that the systematic uncertainties properly accounted for any residual time dependence down to the lowest measured energies.

- **Analysis chain**: as a final check, the full analysis chain described in Section 4.8 was cross-checked with simulations. Electron events were simulated at the top of the payload with isotropic arrival directions and with energy spectrum from 40 MeV to 100 GeV consistent with the reconstructed experimental spectrum for the first geomagnetic cutoff interval (0-0.055 GV). Essentially the spectral shape represented by the black points in Figure 4.2 (left panel) was used. Then, the events that, according to simulation, triggered the instrument were processed with the PAMELA data analysis software and consequently treated as in the experimental analysis (rigidity determination, selection based on criteria discussed in Section 3.3, efficiency and unfolding corrections, flux determination). The resulting energy spectrum was compared with the input one and a good agreement was found. The differences between the input and reconstructed fluxes at top of the payload were consistent with the uncertainties related to the unfolding procedure described in Section 4.4. Therefore, it was concluded that the unfolding procedure did not introduce additional uncertainties.

These three consistency checks were a good indication on the reliability of the results which are presented in the next section.

5.4 RESULTS

ELECTRON SPECTRA

Figure 5.6 shows the results on the electron energy spectra for the seven half-year periods. The error bars are the quadratic sum of the statistical and systematic errors. These results were published in [Adriani et al., 2015e]. The electron spectra for each time interval are overlaid with the corresponding computed spectra (solid lines). Moreover the electron local interstellar spectrum is shown (dashed lines). The LIS and the computed spectra are separately discussed in Section 5.5.

In Figure 5.7 the ratios between the measured half-year period electron fluxes from January 2007 until December 2009 and the fluxes measured in the first period of data taking (July-November 2006) are shown. With this representation the time variation of the electron flux, as a consequence of the solar activity decrease, is clearly visible. It follows from these ratios that the low-energy electron flux increased by a factor of $\sim$ 1.6 from 2006 to 2009 at 0.5 GeV and of a factor $\sim$ 4 at 0.1 GeV. The uncertainties on the electron spectra do not allow the effects of the solar modulation above $\sim$ 10GeV to be appreciated. The computed spectra

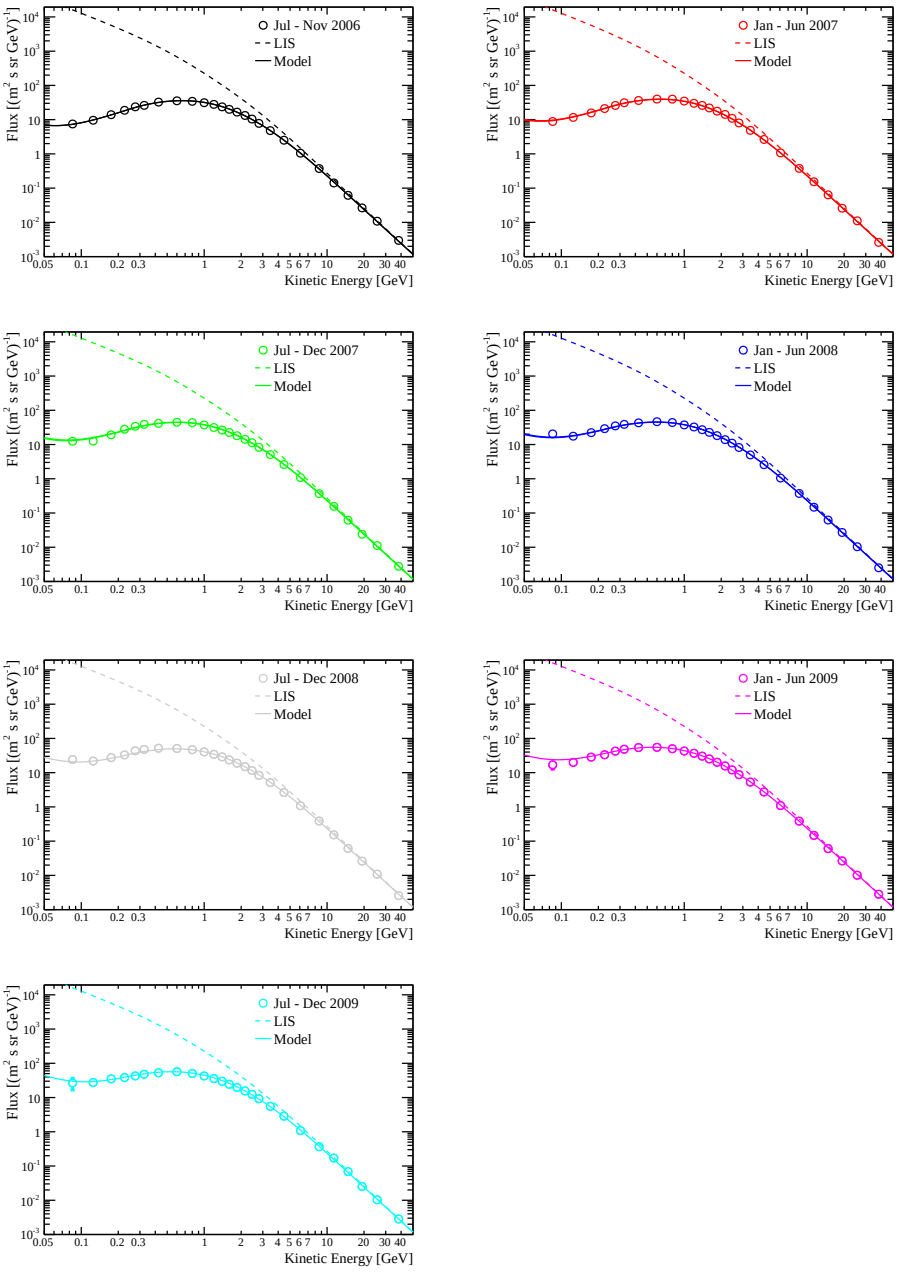

Figure 5.6: The measured electron energy spectrum for the seven time periods from the second half of 2006 to the end of 2009. Time progresses from top to bottom, left to right. The error bars are the quadratic sum of the statistical and systematic errors. If not visible, they lie inside the data points. The solid lines represent the computed spectra while the dashed line represents the LIS used for the computation (see Section 5.5).

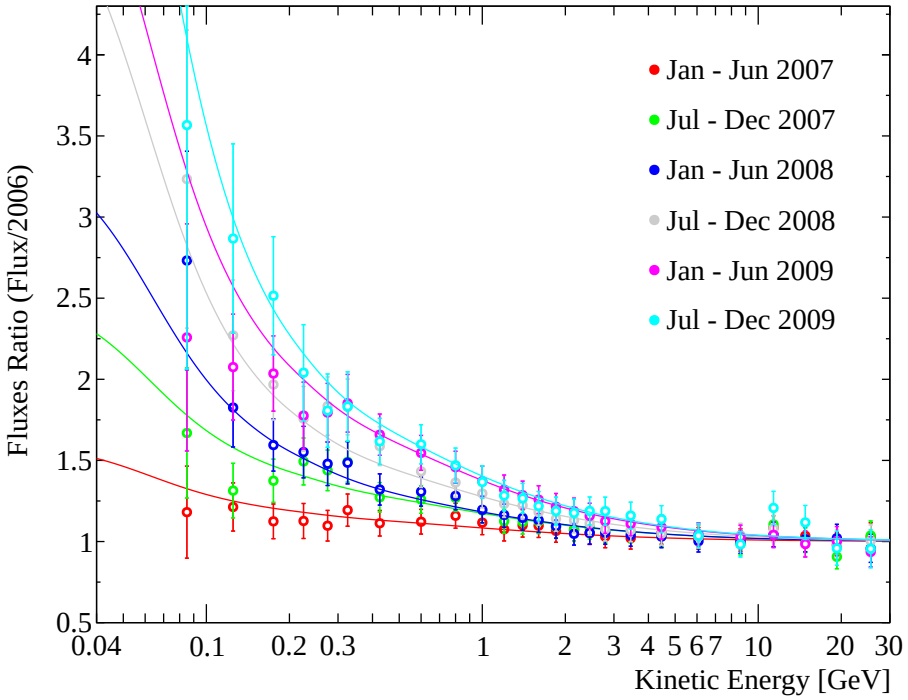

Figure 5.7: The ratios as a function of energy between the measured half-years electron fluxes from January 2007 till December 2009 and the measured fluxes for the period July-November 2006 overlaid with the corresponding computed spectra (solid lines). The error bars are the quadratic sum of the statistical and systematic errors.

(see Section 5.5) shows that at 10 GeV the increase of the electron flux from July-November 2006 to July-December 2009 should be of the order of 3%. Above 10 GeV the variation was even smaller.

No other instruments measured the low energy CR electron spectra at Earth during the 23th solar minimum. However Evenson and Clem [2011], in 2009 performed the LEE experiment, a balloon-borne instrument launched from Kiruna on the 17 May of 2009 which flew for 4 days. This instrument measured the all electron spectrum (electron plus positron) from 20 MeV to 5 GeV. Figure 5.8 shows the comparison between the electron spectrum for January-June 2009 presented in this work and the all electron spectrum measured by Evenson and Clem. Since the LEE instrument measured the all electron spectrum (the result should be roughly 10% higher with respect to a pure electron spectra), and since the PAMELA result was averaged over a period of time significantly longer than the LEE flight duration, a direct comparison between the two sets of data is difficult. However, Figure 5.8 shows that the shape of the PAMELA and the LEE spectra were in

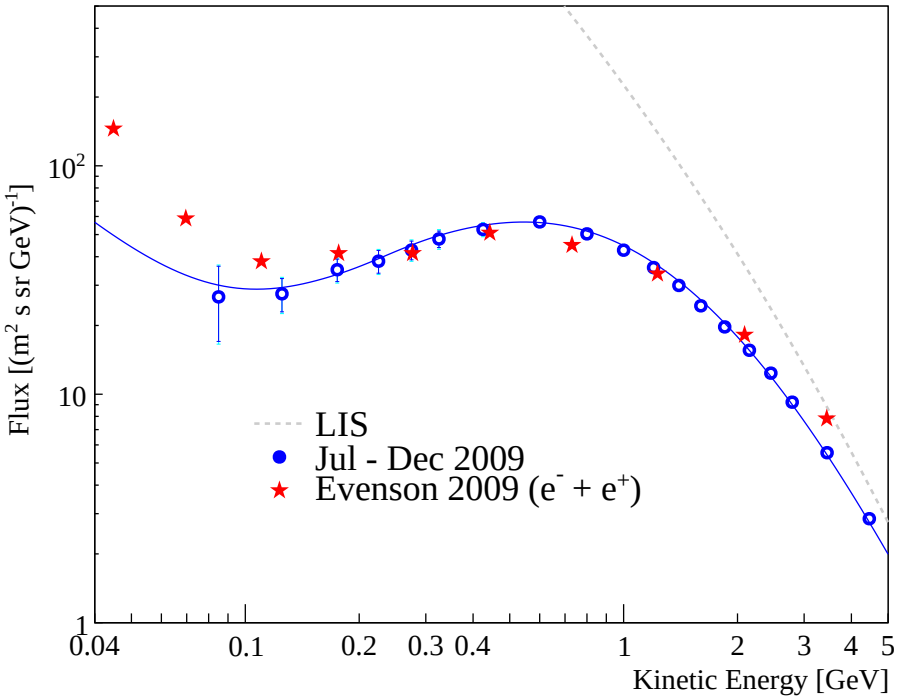

Figure 5.8: Comparison between the electron spectra for January-June 2009 presented in this work and the electron plus positron spectra measured by Evenson and Clem [2011] between the 17 and 21 May of 2009 with the LEE instrument.

good agreement above 200 MeV. Below 200 MeV the LEE data were significantly higher than both the PAMELA results and the computed spectrum. This could be the result of a residual contamination by low energy secondary electrons and positrons produced in the residual atmosphere above the LEE balloon, which flew at an altitude of $\sim$ 42 km, corresponding to $\sim$ 3 g cm^{-2}. Moreover below 50 MeV, electrons observed at Earth should included Jovian electrons [Potgieter and Nndanganeni, 2013] which would led the electron fluxes to increase with respect to a pure Galactic spectra.

In order to compare the electron fluxes presented in this thesis with the previous published PAMELA results [Adriani et al., 2011a], a total electron flux was evaluated averaging the half-year fluxes over the whole time period (July 2006-December 2009). The resulting energy spectrum is shown in Figure 5.9 (red points) where is compared to the previously PAMELA published results [Adriani et al., 2011a] (black points). This new estimation yields fluxes whose absolute values are approximately 10% higher than in the previous work. This difference stems from an improved treatment both in the data and in the simula-

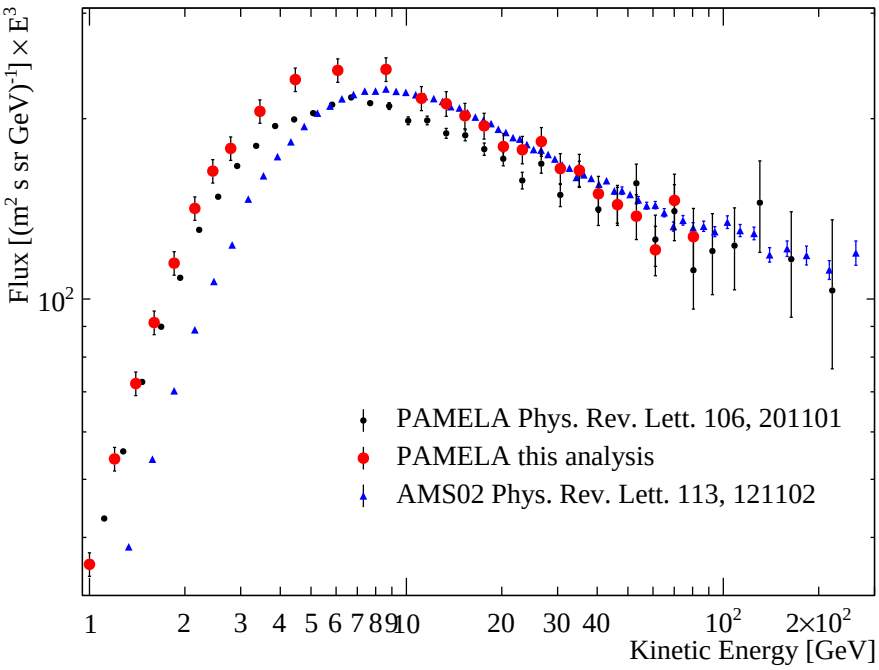

Figure 5.9: Comparison between various sets of electron spectra. The fluxes are multiplied by the energy to the power of three in order to better display the high energy fluctuations. Red points represent the electron flux obtained averaging the fluxes evaluated in the seven-time periods presented in Figure 5.6. Black points represent the electron PAMELA flux published in [Adriani et al., 2011a]. Blue points represent the AMS02 result published in [Aguilar et al., 2014].

tion of the time dependence of the tracking system performances and the unfolding procedure. A difference of the order of 5-6% arises from the Monte Carlo tracker efficiency averaged over the whole period of time (Criteria 1 and 2), which for this analysis was found to be lower than the previous simulated efficiency. The remaining differences were due to the unfolding procedure that, above 1 GeV, produced fluxes about 4% higher than the previous analysis. In Figure 5.9 the new results are also compared with the last results from the AMS02 collaboration on the electron flux (blue triangles) [Aguilar et al., 2014]. The old set of PAMELA electrons differs of about 10% with respect the AMS02 results above 10 GeV. The results presented in this work are in good agreement with the AMS02 results. Below 10 GeV the PAMELA and AMS02 results differ significantly since they were obtained for different period of solar activity (see Section 1.9).

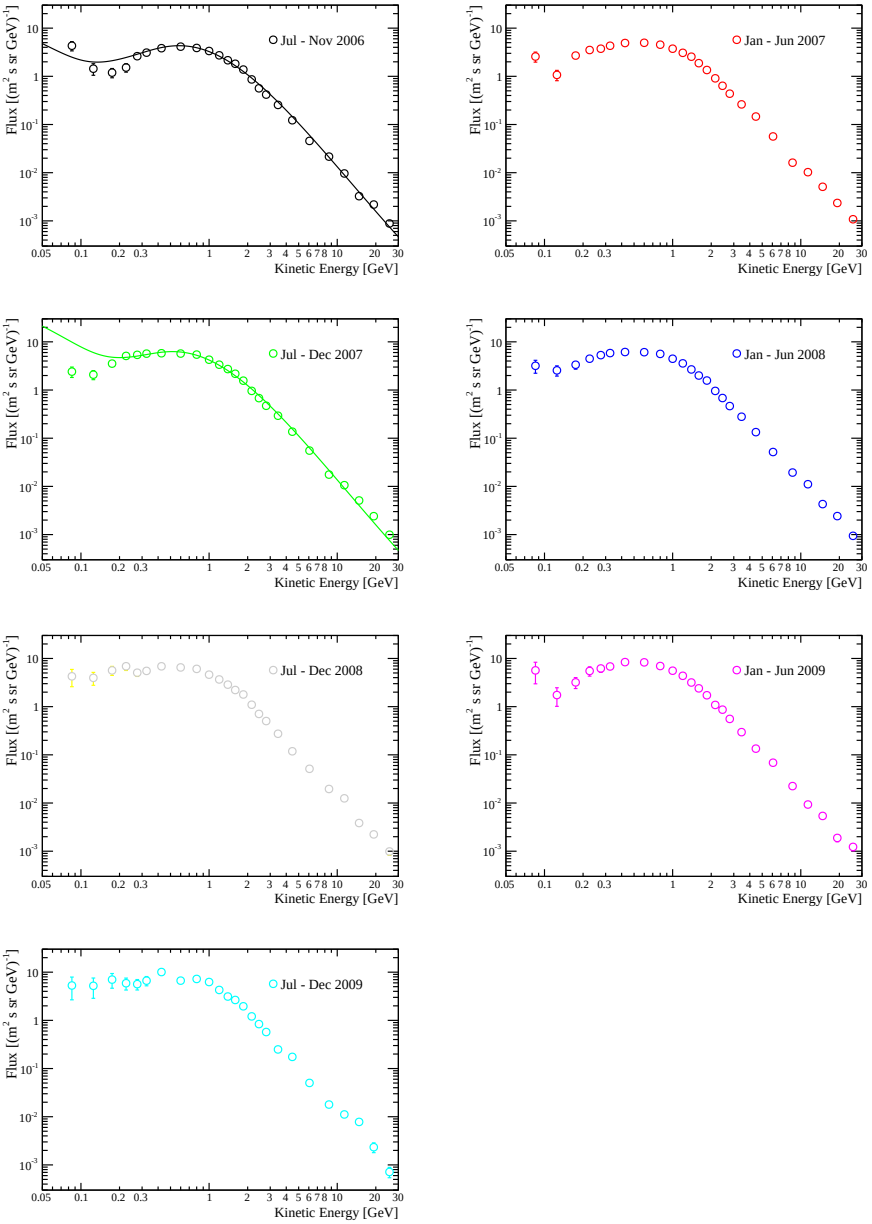

Figure 5.10: The measured positron energy spectrum for the seven time periods from the second half of 2006 to the end of 2009. Time progresses from top to bottom, left to right. The error bars are the quadratic sum of the statistical and systematic errors. If not visible, they lie inside the data points. The computed spectra are shown only for July-November 2006 and July-December 2007 since the modeling work is still ongoing.

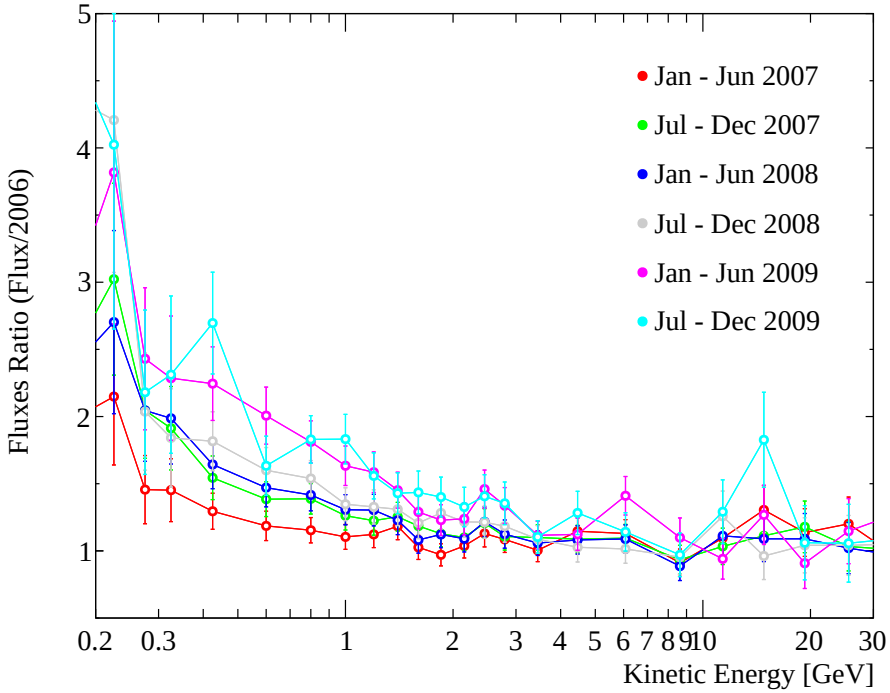

Figure 5.11: The ratios as a function of energy between the measured half-years positron fluxes from January 2007 till December 2009 and the measured fluxes for the period July-November 2006. The error bars are the quadratic sum of the statistical and systematic errors. The ratio are shown down to 200 MeV (see text).

POSITRON SPECTRA

Figure 5.10 shows the positron energy spectra for the seven half-year periods. The error bars are the quadratic sum of the statistical and systematic errors. The statistical fluctuations were much more pronounced with respect to the electron spectra (the statistics is about ten times smaller in this case). The statistical fluctuations are particularly relevant below 500 MeV, where the geometrical factor sharply decreased, and for the last three time period, where the statistics was lower due to the decreased efficiency of the tracking system.

The positron modeling work is still on-going and no final results are yet available. However, in Figure 5.10, some preliminary results on the July-November 2006 and July-December 2007 computed positron spectra are shown (solid lines). It can be noticed that, below 200 MeV, the experimental data largely differ from the reconstructed spectra. These differences could arise from an incorrect determination of the various modulation processes or problems with the experimental estimation of the positron fluxes. For this reasons, the results on the positron spec-

tra were considered reliable only above 200 MeV. Below this energy the analysis is still on-going. Residual hadron contamination or low energy efficiencies not properly estimated are currently under study.

Figure 5.11 shows the ratios between the measured positron fluxes from January 2007 until December 2009 and the fluxes measured in the first period of data taking (July-November 2006). As for the electron fluxes, the positron fluxes increase with time as a consequence of the decrease in the solar activity. It follows from these ratios that, the low-energy positron flux, increased by a factor of ~ 2.4 from 2006 to 2009 at 0.5 GeV. At the same energy the electron fluxes increased by a factor ~ 1.6. This difference is an indication of the charge-sign dependence of the solar modulation which will be further discussed in Section 5.6. The model used to reproduced the experimental electron spectra is now presented.

5.5 INTERPRETATION

As briefly discussed in Section 1.10, the curves shown in Figure 1.25 were obtained with a comprehensive model implemented to study the solar modulation of the proton fluxes between 2006 and 2009. These results allowed a better understanding of the basic processes responsible for solar modulation during the 23rd solar minimum. The model used to reproduce the PAMELA results on the CR protons was formally identical the one discussed in Section 1.7. This model was applied to the study of the solar modulation of electron spectra measured by PAMELA and presented in this thesis. For a complete and more exhaustive discussion about the model details and the theoretical implications of the results see [Potgieter et al., 2015]. Concerning positrons, since below 200 MeV the analysis is still ongoing, the modeling results are not yet published. As soon as the experimental positron data are final an experimental and modeling paper will be published. In this thesis, a preliminary work on the positron modeling was shown (see Figure 5.10).

In order to reproduce the experimental data, the heliospheric modulation condition, as a prerequisite for applying the modulation model, were studied in detail.

HELIOSPHERIC MODULATION CONDITION

In Figure 5.12 the relevant heliospheric modulation condition based on a selection of observations are illustrated from the year 2000 to 2012. The top panel shows the mean sunspot number, that, as discussed in

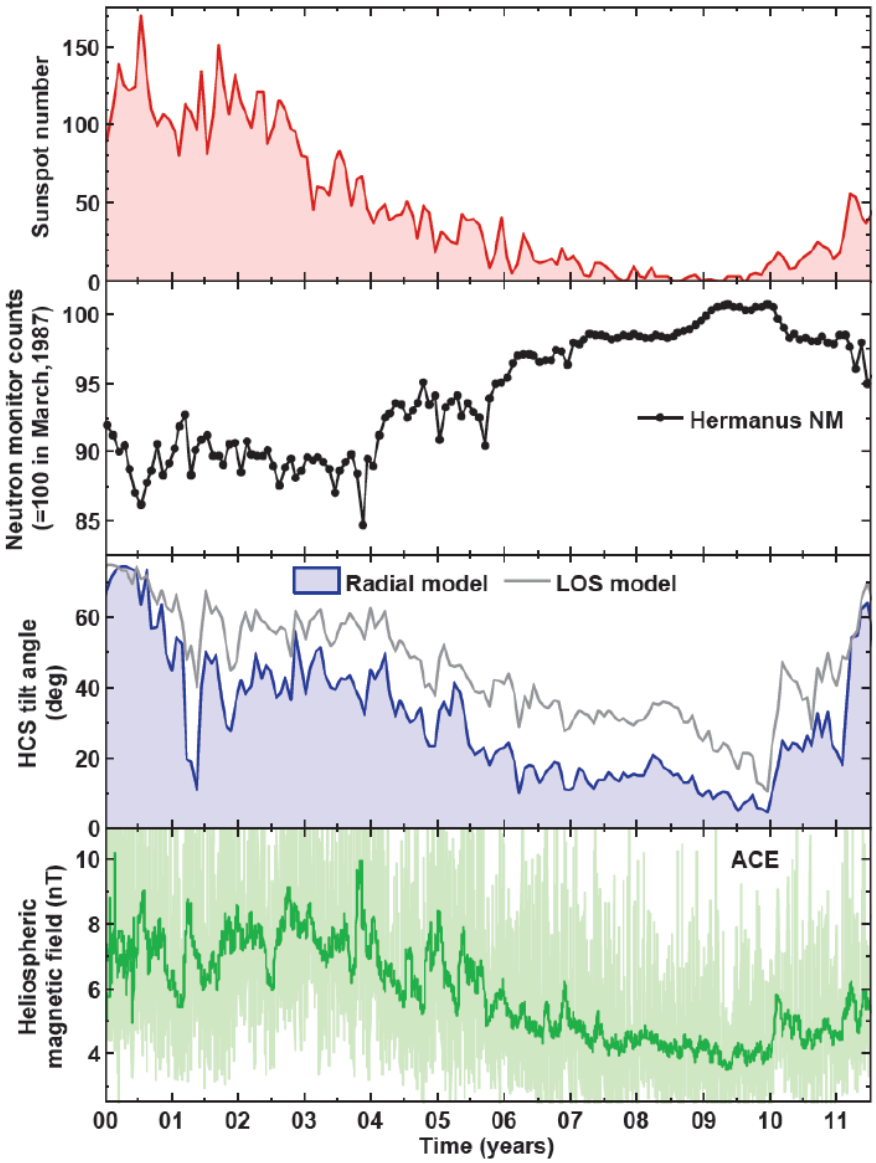

Figure 5.12: Heliospheric modulation conditions from the year 2000 up to 2012. First panel: the observed sunspot numbers (http://sidc.oma.be/). Second panel: the count rate of the Hermanus neutron monitor (NM) normalized to March 1987 (http://www.nwu.ac.za/content/neutron-monitor-data). Third panel: the heliospheric current sheet tilt angle based on two approaches (radial model and LOS model; see http://wso.stanford.edu/). Fourth panel: the monthly (dark green line) and daily (light green line) heliospheric magnetic fields (HMF) averages observed at Earth by ACE (http://nssdc.gsfc.nasa.gov/).

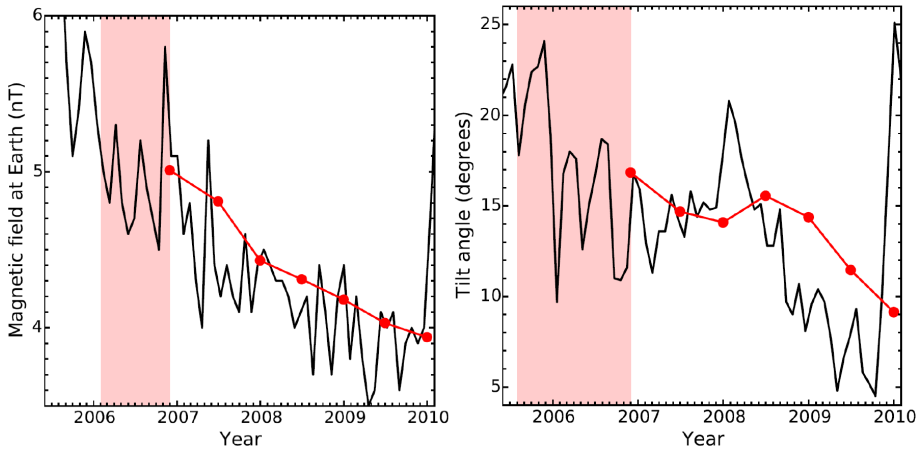

Figure 5.13: Left panel: the observational HMF at Earth (black curve) from Figure 5.12 and the averaged value for the selected seven time intervals for the modeling study (red curve). The first red point is the average value for the preceding 10 months as indicated by the colored band). The same was done for the other six time periods. Right panel: same as the left panel for the observational tilt angle. The average values (red points) are evaluated for the preceding 16 months.

Section 1.5, is a good proxy for the solar activity. Already in 2007 the sunspot number became quite low and remained very low till the end of 2009 when a new sunspot cycle started. The second panel of Figure 5.12 shows the count rate of the Hermanus Neutron Monitor (see Section 1.8). These data show a steep increase in the CR intensity between 2006 and 2007 followed by a plateau in 2008 and a maximum from early to late 2009. As the solar activity started to increase in 2010, the NM count began to decrease. The third panel of Figure 5.12 shows the tilt angle of the heliosperic current sheet which is, as the sunspot number, a good indication of the solar activity. The last panel of Figure 5.12 shows the daily HMF value which dropped below 4 nT for an extended period of time, in contrast to the previous cycle. This was considered as unusual (see the review by Kóta [2013]).

For a modeling perspective the most relevant quantities were: the change in the tilt angle and the HMF variations. In order to reproduce electron spectra at Earth for a specific period of time with the 3D model discussed in the first chapter, the averaged tilt angle and HMF values were required for the preceding 16 months (as a maximum) to 10 months (as a minimum) as input parameters to the model. This was required because CRs respond to the modulation condition between the modulation boundary, assumed to be the heliopause, and the point of observation, the Earth. For this reason the heliosperic modulation condition between Earth and HP had to be estimated based on the ob-

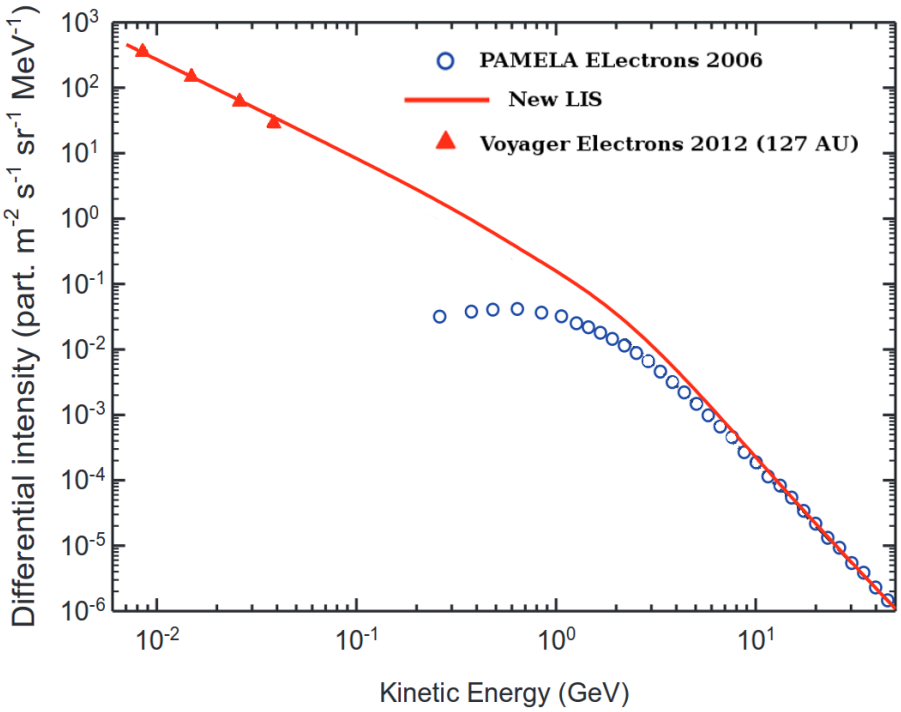

Figure 5.14: The electron local interstellar spectrum used for this work. At low energies the LIS was tuned to reproduce the Voyager 1 data measured at 122 AU (red triangles) while above 30 GeV to reproduce the PAMELA results (open blue points).

servations of, at least, the 10 months before the observational time. On Figure 5.13 the procedure is summarized: the red points represent the averaged 10 months value for the HMF (left panel) and the averaged 16 month value tilt angle (right panel) for the seven time periods considered for the electron flux evaluation. These average values were used as observational input for the model. In addition to these observational conditions also the LIS spectrum had to be specified as an initial condition.

LOCAL INTERSTELLAR SPECTRUM

A very local electron interstellar spectrum was needed as the input spectrum which, then, was modulated to reproduce the observed electrons at Earth. Below a few GeV, where modulation effects were important, the value of the LIS is rather contentious. The situation has improved significantly when Voyager 1 crossed the heliopause (HP) on August 2012 (see Section 1.5) measuring electron CRs between 5 and 50 MeV [Stone et al., 2013]. The LIS used in this work is shown in Figure 5.14. This new local interstellar spectrum was tuned in order to

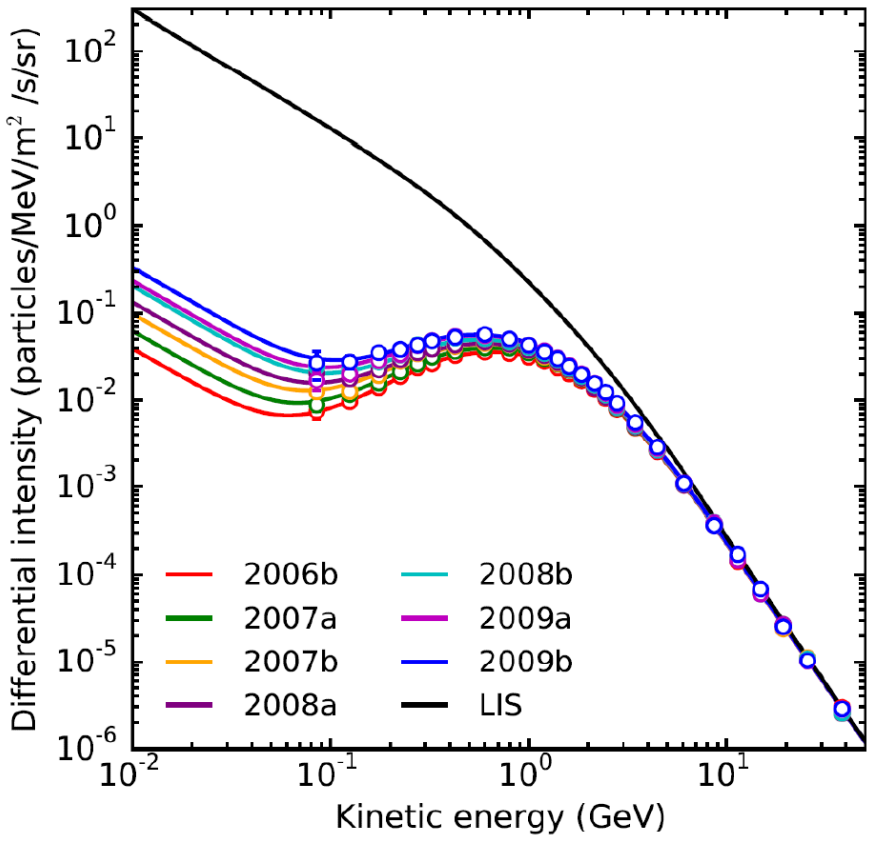

Figure 5.15: The observed seven electron spectra from Figure 5.6 overlaid by the corresponding computed spectra (colored solid lines). The black line represent the LIS specified at 122 AU.

reproduce the low energy Voyager data measured outside the HP (below 50 MeV) and the PAMELA observation above 30 GeV (where the solar modulation was considered to have negligible effects). The dotted colored lines in Figure 5.6 correspond to this electron LIS. Once the LIS was specified it was modulated to reproduce the electron spectra measured at Earth by PAMELA.

MODELING RESULTS

As already discussed, in order to compute the electron fluxes at Earth, a full three-dimensional model based on the heliospheric transport equation (see Equation 1.13) was used. To solve the transport equation for the seven time periods, the calculated tilt angle and HMF magnitude at Earth were averaged as discussed in the previous paragraphs. The transport equation was numerically solved as discussed in Section 1.7. The computed spectra are shown in Figure 5.15. They well reproduced

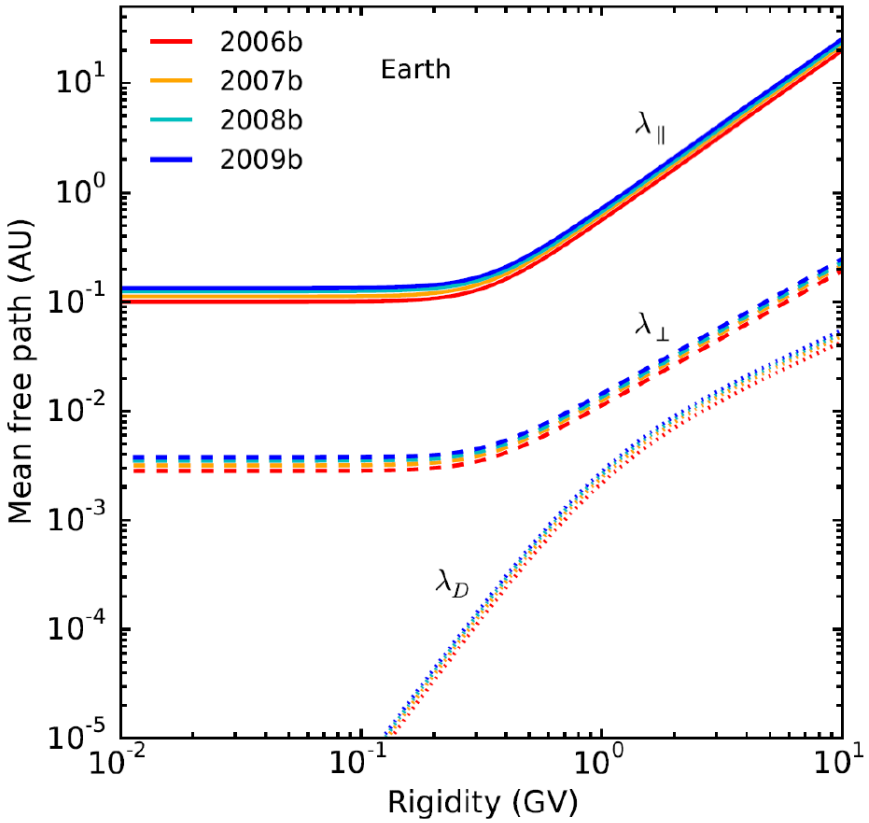

Figure 5.16: The assumed rigidity dependence of the main mean free path (which are related to the diffusion coefficients by Equation 1.16) and of the drift scale at the Earth. Here, the corresponding parallel $\lambda_{\parallel}$ and perpendicular mean free paths $\lambda_{\perp} = \lambda_{\perp r} = \lambda_{\perp \theta}$ and the drift scale λ_d, all in AU, are depicted with colored lines, indicative of the changes needed to reproduce the observations from July 2006 (lower lines, beginning with red curves) to January 2009 (upper lines, ending with blue curves).

the basic features of the experimental spectra represented by the colored points. From 2006 to 2009, as can be argued from Figure 5.13, the tilt angle changed from $\sim$ 15.8° to $\sim$ 10° and the HMF at Earth from $\sim$ 5.05 nT to 3.94 nT. However, since the three mean free paths (related to the diffusion coefficients by means of Equation 1.16) and the drift scale depend on the HMF (see Equation 1.17), these small changes had significant modulation effects as can be seen in Figures 5.7 and 5.15

The rigidity dependence of the perpendicular and parallel mean free path, as well as the drift scale values, used to reproduce the PAMELA data, are shown in Figure 5.16. This figure shows also the changes in the coefficients needed to reproduce the temporal variation of the electron fluxes. The parallel mean free path changed about 30%, from 1×10^{-1} AU in July-December 2006 to 1.35×10^{-1} AU in July-December

Table 5.1: The modulation factor (MF) as the ratio of the electron LIS intensity to the computed intensity at the Earth. The MF is shown for various energies for the periods July-December 2006, July-December 2008 and July-December 2009.

E [GeV]	0.05	0.2	0.8	2	5	10	20	40
Jul-Dec 06′	4825	292	10.6	2.81	1.49	1.20	1.08	1.03
Jul-Dec 08′	1700	180	8.5	2.56	1.44	1.18	1.07	1.03
Jul-Dec 09′	762	128	7.18	2.31	1.38	1.15	1.06	1.02

2009. The perpendicular mean free path, as well as the drift scale, had proportionally the same increase. These relatively small adjustments were sufficient to reproduce the observed electron spectra. A change of 30% in the diffusion coefficient was responsible for an increase of a factor ~ 4 in the electron fluxes at 100 MeV.

As already discussed in Section 1.6, based on turbulence theory, predictions have been made over the years on the rigidity dependence of the diffusion coefficients (see e.g. [Teufel, A. and Schlickeiser, R., 2003]. For the electron propagation through the heliosphere, in contrast with protons, a flattening of the parallel and perpendicular diffusion coefficient was found below 500 GV. These basic predictions were confirmed by the comparison of the PAMELA results with the comprehensive model.

In order to quantify the amount of solar modulation, a Modulation Factor (MF), defined as the ratio of the intensity of the LIS and the intensity of the electron fluxes at Earth, was introduced. The MFs based on the computed electron spectra shown in Figure 5.15 and the LIS of Figure 5.14 are presented in Table 5.1. The MF is shown for three time periods: July-December 2006, July-December 2008 and July-December 2009. As the solar activity decreased, for a fixed energy, the MF decreased as well. At 40 GeV a residual effect of the solar modulation of a few percent was still present. However as already discussed, the experimental results are not sufficiently precise to appreciate such an effect. At the lowest energy, as a consequence of the flattening of the diffusion coefficient, below a few tens of MeV, the MF became nearly constant. This happened because below this energy the propagation of the electrons became diffusive dominated. On the contrary, below a few hundreds of MeV, the protons experience much larger adiabatic losses and the spectral shape is approximatively a power law with index $\gamma \simeq 1$ (see Figure 1.25).

The computed drift scale, as can be seen from Figure 5.16, became negligible below 100 MeV . Below this energy the drift effects were negligible with respect to the other modulation processes. On the other

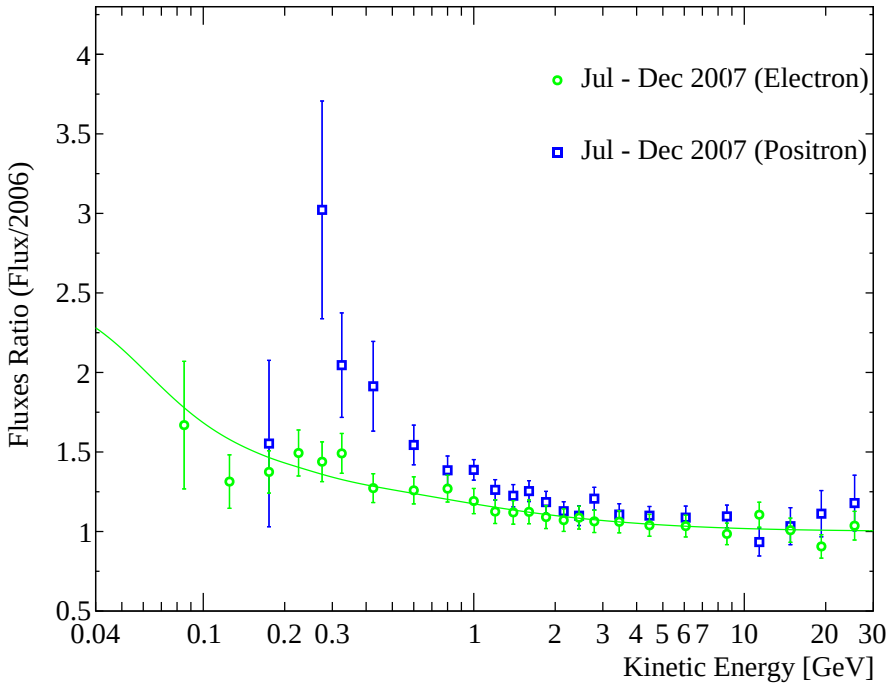

Figure 5.17: Comparison between the ratios of the measured half-year positron and electron fluxes for July-December 2007 and the measured fluxes for the period July-November 2006. The error bars are the quadratic sum of the statistical and systematic errors. During the considered time period, the positron flux increased more than the electron flux. This charge-sign dependence is interpreted as an indication of the drift effects (see text).

hand as can be seen in Figure 1.21, electron and positron drift was expected to have maximum effects between ~ 100 MeV and 5 GeV.

Charge-sign dependence of the solar modulation was observed comparing the time variation of the positron with respect to the electron fluxes.

5.6 CHARGE-SIGN DEPENDENCE

Figure 5.17 shows the comparison between the ratio of the electron fluxes with respect to the ratio of the positron fluxes (July-November 2007 divided by July-November 2006). Below ~ 3 GeV the positron ratio was higher with respect to the electron ratio. This difference suggested that the solar modulation behaved differently on electrons and positrons during this period of time. Being the particle drift the only

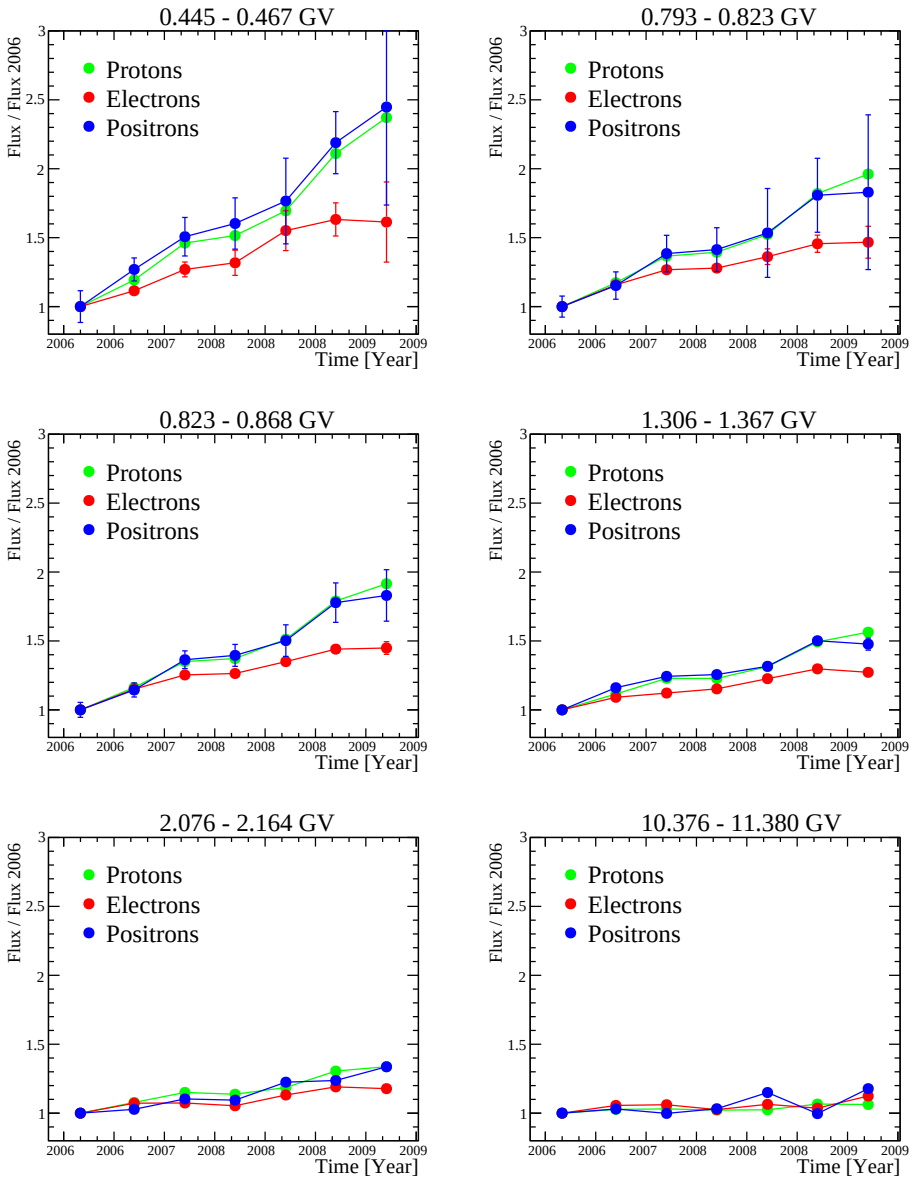

Figure 5.18: The increase with respect to July-November 2006 of the positron, electron and proton fluxes evaluated for the seven time periods. Each panel represents the increase of the fluxes evaluated in a different rigidity intervals. These values are normalized to 1 in July-November 2006. The different increase of the electron fluxes with respect to the positron and proton fluxes, together with the good agreement between positron and proton data, are good indication of the charge-sign dependence of the solar modulation.

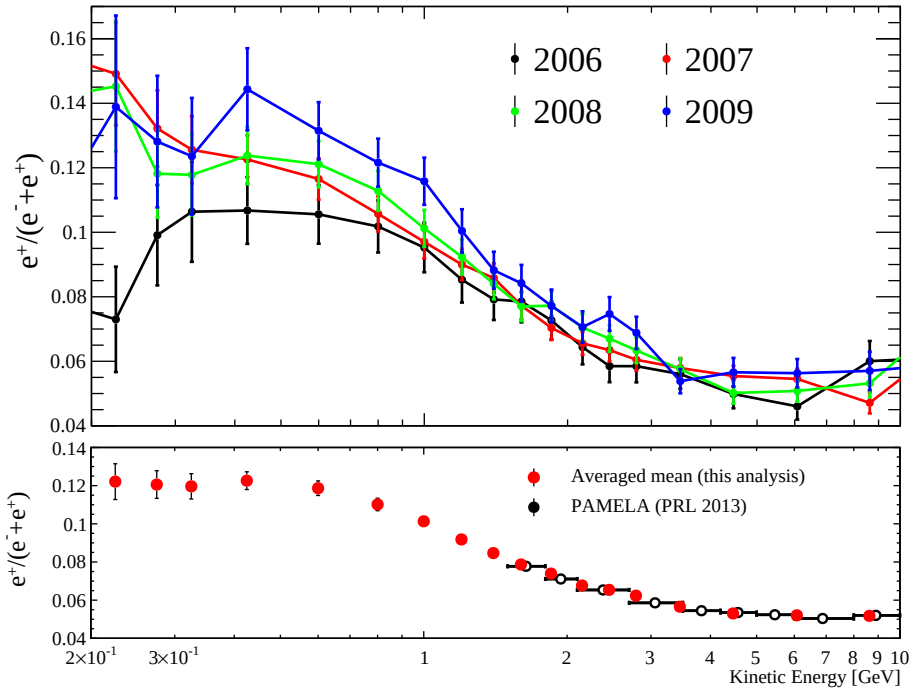

Figure 5.19: Top panel: the yearly average positron fraction evaluated from the electron and positron fluxes presented in this thesis. Below a few GeV the positron fraction increases with time as expected from the charge-sign dependence of the solar modulation. Bottom panel: the 2006 - 2009 averaged positron fraction from this analysis (red points) compared to the positron fraction measure by PAMELA in [Adriani et al., 2013a] (black points). A good agreement with the previous result is observed.

solar modulation mechanism which depends on the sign of the charge, the differences shown in Figure, 5.17 were ascribed to this process.

The effects of drift are evident in Figure 5.18 where, for different rigidity intervals, the increase with respect to July-November 2006 of the positron, electron and proton fluxes, evaluated for the seven time periods, is shown. These values were normalized to 1 in July-November 2006. The increase with time of the positron and proton intensities was in good agreement while the increase in the electron flux was systematically lower. Except for the first rigidity interval (0.445-0.467 GV), possible effects in the solar modulation due to the different velocity (positrons respect to protons) was negligible. From this consideration, the different amount of modulation for the positively with respect to the negatively charged particles, was ascribed to the drift effects. As mentioned in Section 1.6, during $A < 0$ cycles electrons drift towards

the Earth mostly, but not exclusively, through the polar regions of the heliosphere, eluding the impact of the wavy HCS on CR modulation (see Figure 1.20). This causes charge-sign dependent modulation, implying that CR electrons should experience less modulation with respect to positrons and protons over the same period. In fact, positrons and protons during $A < 0$ cycles, mainly drift from the equatorial to the polar region, inward along the heliosperic current sheet and thus are more sensitive to the changes in the tilt angle and experience more solar modulation during the same period of time. As a consequence, during this solar minimum, the intensity of positrons at Earth was expected to increase more than the intensity of electrons, as actually shown in Figure 5.18.

Because of the charge-sign dependence of the solar modulation, a time variation of the positron fraction is expected below some GeV. Figure 5.19 (top panel) shows the yearly averaged positron fraction from 2006 to 2009. As can be noticed, approximatively below 3 GeV, the positron fraction increases with time: its value in 2006 is lower than the value measured in 2007 and so on. In Figure 5.19 (bottom panel) is also shown the positron fraction averaged from 2006 to 2009 overlaid with the previous PAMELA result [Adriani et al., 2013a]. A good agreement with the previous result is observed.

5.7 CONCLUSION AND PERSPECTIVE

The solar modulation of Galactic CR electrons and positrons during the 23rd solar minimum measured by the PAMELA experiment were presented. In Chapter 1, the basic concepts about the transport of CRs through the heliosphere were described. The physical processes which, approximatively below 30 GeV, contribute to the modulation of the Galactic CRs inside the heliosphere, were detailed. Processes such as the convection with the solar wind or the diffusion in the heliosperic magnetic field irregularities, made the intensity of the Galactic CRs decrease at Earth with respect to the LIS. Moreover, as a consequence of the change in the solar activity, the CRs intensity measured at Earth was not constant with time. In order to reproduce the electron and positron spectra measured by PAMELA, a comprehensive three-dimensional model based on the Parker equation was developed. The numerical solution of this model, by means of the appropriate initial conditions, allows us to derive the energy dependence and the values for the basic modulation parameters, as well as the diffusion coefficients and the drift scale. Furthermore, the computed spectra provide important information, which leads to a better understanding of each processes to the solar modulation of the Galactic CRs.

The PAMELA experiment, thanks to its long flight duration, was particularly suited to measure the time variation of the low energy CRs at Earth. In Chapter 2 a brief introduction of the PAMELA instrument was given. The key aspects of each sub-detector relevant to the measure of the electron and positron CRs were discussed. The electromagnetic calorimeter was presented with particular attention (see also Appendix A).

In Chapter 3, a set of criteria, developed to select clean samples of electrons and positrons, was discussed. The residual contamination, in the final particle samples, was evaluated with the experimental and Monte Carlo data. For this purpose, a set of protons and pions was simulated by means of a toolkit based on the GEANT4 code. This reproduce the geometry of the entire PAMELA apparatus and the interaction of particles with it.

In Chapter 4 the flux estimation was described. This consisted of several parts: the efficiency measurements, the unfolding procedure, the Galactic CR selection, the live time and the geometrical factor evaluation. The selection efficiencies of the whole set of criteria were evaluated using both the Monte Carlo and the experimental electrons and positrons. The unfolding procedure, entirely based on the simulations, was a fundamental step since it allowed us to reconstruct the spectra as a function of the real particle energy. This did not coincide with the rigidity reconstructed by the PAMELA tracking system because of energy losses inside the instruments.

The time dependent CR electron and positron fluxes were presented in Chapter 5, together with a discussion on the systematic uncertainties and a few consistency checks made to test the reliability of the results. These fluxes were measured over a six-month time period, from July 2006 to January 2009, for a total of seven spectra. Below $\sim$ 30 GeV, as expected from the decrease in the solar activity, the electron and positron fluxes increased with time. The electron flux increased by a factor of 1.6 at 500 MeV from 2006 to 2009 while the positron flux, at the same energy, increased by a factor of 2.4. Such a difference in the amount of modulation is a clear indication of the charge-sign dependence of the solar modulation which is introduced by the drift motion. The comprehensive model based on the Parker equation was then used to calculate the electron spectrum. The numerical solutions well reproduce the experimental results. The assumed energy dependence of the diffusion coefficients and the drift scale were presented. Differently from the low energy protons, which experience large adiabatic energy losses, the electrons below $\sim$ 100 MeV become diffusive dominated, and the diffusion coefficient becomes energy independent. The modeling work for positrons is still ongoing thus, only a few preliminary results, were shown. Furthermore below 200 MeV the positron spectra

were found to be not reliable (residual contamination, wrong efficiency estimation) and are currently under investigation.

In conclusion, the experimental data presented in this work improve the understanding on the propagation of electrons and positrons through the heliospere, reducing the uncertainties on the solar modulation effects. Furthermore the results at low energy are fundamental to reduce the uncertainties on the computed positron LIS. As discussed in Section 1.10 the energy spectra of the antiparticle CRs are particularly relevant for indirect searches of dark matter annihilation or decay. The charge-sign dependence of the solar modulation was directly observed comparing the increase with time of electrons with respect to positrons and protons during the same period of time.

At the current date (March 2016), the PAMELA instrument, is still orbiting around the Earth taking data. A full set of data is available for the time period from 2010 to 2015. Moreover a new algorithm for track reconstruction was implemented. This will allow to increase the electron and positron statistics with respect to the ones of late 2009. The time evolution of the positron and electron fluxes will be measured also for the time period after the 2009, i.e. during the solar maximum phase. If PAMELA continues to take data till the end of 2017, the solar modulation of CRs will be measured over an entire solar cycle. The period of time after 2009 allows the modeling of the modulation of CR electrons and positrons during solar maximum condition and thus, will helps to understand which modulation processes are dominant during such a period. Moreover, as discussed in Section 1.9, the models predict a sharp change in the positron fraction during the polarity inversion, which took place between 2013 and 2014. A direct measurement will improve the previous experimental results (see Table 1.1) and the understanding on the significance of the polarity inversion on the propagation of charged particles inside the heliosphere.

5.8 AUTHOR'S CONTRIBUTION

My personal contribution to the analysis described in this thesis consisted on:

- develop and test the set of Criteria used to select the samples of positrons and electrons (Section 3.3);
- estimate the residual proton and pion contamination in the final electron and positron samples (Section 3.4);
- evaluate the selection efficiencies and their temporal dependences (Section 4.3);

- create the unfolding matrix and test the consistency of the unfolding algorithm (Section 4.4);
- combine all the elements needed to evaluate the positron and electron fluxes (Section 4.8);
- evaluate the normalization factors of the electron and positron fluxes (Section 5.1);
- evaluate the source of systematic errors related to the efficiencies, the unfolding and the normalization factors (Section 5.2);
- test the results on the positron and electron fluxes with three consistency checks (Section 5.3);

5.9 ACKNOWLEDGMENTS

I would like to acknowledge Mirko Boezio who supervised my work during these three year of PhD and helped me with good and helpful advice. He also actively participated to this analysis measuring the systematic errors related to the tracker efficiency (Section 5.2). I express my thanks to Valeria di Felice who worked on the simulation and produced the set of electrons, positrons and protons which were extensively used in this analysis. Thanks to Valerio Formato who wrote the ROOT routine used for the flux unfolding. Thanks to professor Marius Potgieter and Etienne Voss who worked on the modeling of the experimental electron results of this analysis. Thanks to professor Steve Stochaj who allowed me to spend two months (in 2014) at the New Mexico State University (Las Cruces, New Mexico) and to collaborate with professor Bill Webber. Thanks again to Marius Potgieter who invited me two times (2013 and 2015) at the North-West University (Potchesfroom, Sud Africa) and helped me to understand the theory describing the solar modulation of Galactic CRs. Thanks to Mark Pearce who hosted me at KTH (Stockholm) for two months in 2012.

5.10 PUBLICATIONS

The author of the thesis appears in the following publications: [Mori et al., 2015a], [Adriani et al., 2015d], [Adriani et al., 2015e], [Potgieter et al., 2015], [Adriani et al., 2015a], [Munini et al., 2015], [Koldobskiy et al., 2015b], [Mori et al., 2015b], [Karelin et al., 2015b], [Usoskin et al., 2015], [Karelin et al., 2015a], [Adriani et al., 2015c], [Mikhailov et al., 2015], [Koldobskiy et al., 2015a], [Adriani et al., 2015b], [Panico et al.,

2014], [Bruno et al., 2014], [Adriani et al., 2015f], [Adriani et al., 2014b], [Boezio et al., 2014], [Formato et al., 2014], [Adriani et al., 2014a], [Mocchiutti et al., 2014], [Formato et al., 2014], [Martucci et al., 2014], [Potgieter et al., 2013], [Adriani et al., 2013a].

A RADIATION THROUGH MATTER

INDEX

This appendix concerns the basic reactions which occur when radiation encounters matter and the effects produced by these processes. From an experimental point of view the knowledge of these interactions is of paramount importance since these processes are the basis of all current particle detection devices. Indeed, the operational principle of the electromagnetic calorimeters is based on the shower development induced from the interacting particle. In order to understand the phenomenology of electromagnetic showers, Section A.1 briefly introduce the QED processes which describe the interactions of electrons and photons with matter. Once the fundamental physics is well understood, the main features of the particle cascade can be parametrized with simple empirical functions as reported in Section A.2. The main features of the PAMELA calorimeter are presented in relation to the quantities which characterize the shower development. The information obtained from the calorimeter output allows PAMELA to reach excellent positron and electron identification amongst the huge hadron background.

A.1 ELECTRON AND PHOTON ENERGY LOSSES

ELECTRONS

Figure A.1 (left panel) shows various physical processes of energy losses for electrons and positrons traversing lead as a function of the particle energy. At low energies, electrons lose their energy mainly through collisions with the atoms and molecules of the material thus giving rise to ionization and thermal excitation. For low energies positrons, other

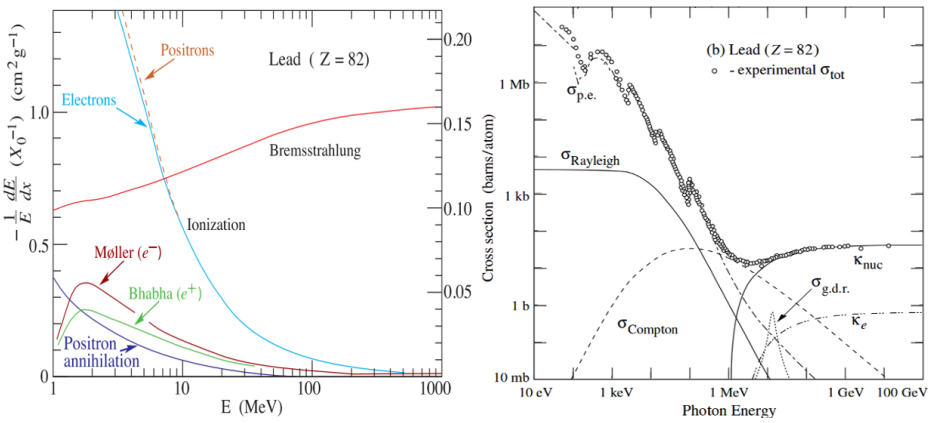

Figure A.1: Left panel: electron and positron energy losses due to the various physical interactions through matter (lead $Z = 82$) as a function of the particle energy. Right panel: the photon cross section for different physical interaction through matter (lead $Z = 82$) as a function of energy. Pictures adapted from [PDG, a].

processes contribute like positron-annihilation or Bhabha scattering[1] [Uehling, 1954]. However these processes becomes negligible above few hundreds of MeV (see Figure A.1).

For an electron, the average energy loss per unit path length through ionization, i.e. due to atomic electron collisions, is described by the well known Bethe-Bloch formula which from quantum-mechanical calculation results to be [Leo, 1994][2]:

$$-\frac{dE}{dx} = 2\pi N_a r_e^2 m_e c^2 \, \rho \frac{z^2}{\beta^2}\frac{Z}{A}\left[\ln\left(\frac{2m_e\gamma^2 v^2 W_{max}}{I^2}\right) - 2\beta^2 - \delta - 2\frac{C}{Z}\right] \quad \text{(A.1)}$$

where N_a is the Avogadro number, r_e the classical electron radius, m_e the electron mass, c the speed of light, ρ is the density, Z the atomic number and A the atomic weight of absorbing material, $z = qe$ the charge of incident particle (e is the charge of the electron), β the particle velocity v divided by the speed of light c, γ is the Lorentz factor, δ and C the density and shell correction respectively, $W_{max} = 2m_e c^2\beta^2\gamma^2$ the maximum energy transfer in a single collision and I the mean atomic excitation potential of the absorbing material which is experimentally determined. The product of the terms $2\pi N_a r_e^2 m_e c^2$ is ~ 0.1535 MeVcm^2/g.

The energy dependence of dE/dx is shown in Figure A.2 which plots the energy losses of charge-one particles as a function of $\beta\cdot\gamma$ for several different materials. At non-relativistic energies, dE/dx is dominated by the $1/\beta^2$ factor and decreases with increasing velocity. When

1 In quantum electrodynamics, Bhabha scattering is the electron-positron scattering process.

2 For a complete and exhaustive discussion of the Bethe-Block formula see [Leo, 1994].

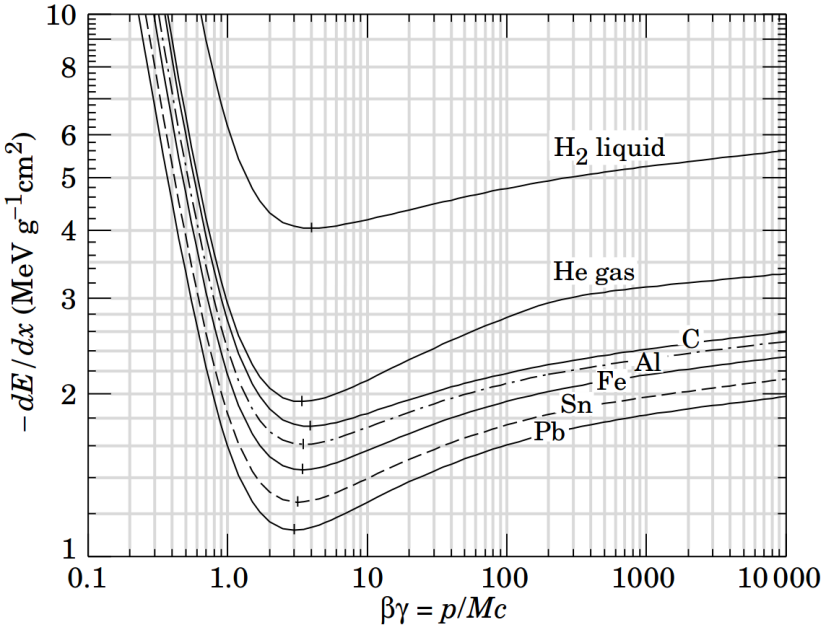

Figure A.2: Mean energy loss rate in liquid (bubble chamber) hydrogen, gaseous helium, carbon, aluminum, iron, tin, and lead. Picture adapted from [PDG, a].

particles become relativistic ($\beta \sim 1$) the energy loss is almost energy-independent. Such particles are referred to as minimum ionizing. The logarithmic dependence on β would predict a rise as the energy increases. However the relativistic rise is partially canceled by the second order correction (density and shell correction). For this reason the ionization energy losses of relativistic particles can be considered energy-independent with good approximation. When dE/dx is expressed in units of mass thickness, i.e. $d\epsilon = dx \cdot \rho$ [g/cm^2], it is almost material independent since the ratio Z/A varies little over a wide range of materials. For this reasons it is very common to use the mass thickness instead of the length to indicate the amount of traversed material. From now on the material thickness is expressed in terms of mass thickness.

As can be seen from Figure A.1 (left panel) for energies larger than ~ 10 MeV, the main source of energy loss for electrons is bremsstrahlung, i.e. the emission of electromagnetic radiation (photon) arising from scattering in the electric field of a nucleus. As a practical matter, electrons and positrons are the only particles in which bremsstrahlung contributes substantially to the energy loss of the particle below a few TeV. The emission probability, in fact, varies as the inverse square of the particle mass. Radiation loss by muons (m = 106 MeV), for example,

Table A.1: Atomic and nuclear property of the tungsten.

Tungsten Property				
		Units		Units
Atomic Number	74			
Atomic mass	183	[g mole^{-1}]		
Density	19.3	[g cm^{-3}]		
Nuclear interaction length	192	[g cm^{-2}]	9.94	cm
Radiation length	6.76	[g cm^{-2}]	0.35	cm
Critical Energy	7.97	[MeV]		
Molière Radius	18	[g cm^{-2}]	0.93	cm
Hadronic lateral extent	192	[g cm^{-2}]	9.94	cm

is $4 \cdot 10^4$ times smaller than that for electrons. The energy loss due to radiation can be expressed as:

$$\frac{dE}{dx} = \frac{E}{X_0} \tag{A.2}$$

This relation indicates that electrons loose energy by bremsstrahlung at a rate proportional to their energy. The quantity X_0 is referred to as radiation length and one possible parametrization is [PDG, a]:

$$X_0(g/cm^2) = \frac{716\ g/cm^2 A}{Z(Z+1)\ln(287/\sqrt{Z})} \tag{A.3}$$

where Z and A are the atomic number and weight of the material, respectively. In Table A.1 is reported the values of X_0 in the case of tungsten. Resolving the differential Equation A.2 yelds:

$$E = E_0 e^{-\frac{x}{X_0}} \tag{A.4}$$

The radiation length thus governs the rate at which electrons lose energy by bremsstrahlung, since it represents the average distance x that an electron needs to travel in a material to reduce its energy to $1/e$ of its original energy E_0. Another quantity which is very useful to the electromagnetic shower parametrization is the critical energy E_c defined as the energy at which the radiation loss equals the ionization loss. This energy depends on the features of the material and is approximately given, using Rossi [1952] definition, by :

$$E_c = \frac{610\ MeV}{Z + 1.24} \tag{A.5}$$

The critical energy for tungsten is reported in Table A.1. The interaction of photons in matter will now briefly discussed since it is of fundamental importance to understand the physics of electromagnetic shower development.

Table A.2: Numerical values of the main features for the PAMELA electromagnetic calorimeter.

PAMELA calorimeter				
		Units		Units
Number of tungsten planes	22			
Single Plane Thickness	0.26	cm		
Plane radiation length	0.74	X_0	5.02	[g cm^{-2}]
Plane interaction length	0.026	X_0	5.02	[g cm^{-2}]
Total radiation length	16.2	X_0	110	[g cm^{-2}]
Total interaction length	0.6	X_0	110	[g cm^{-2}]
Pitch of Si strips	0.24	cm		
Molière radius	4	Si strips		
Hadronic lateral extent	41	Si strips		

PHOTONS

Figure A.1 (right panel) shows the interaction cross section of photons with matter (lead) for various process. At low energies, approximately below 1 MeV, the photoelectric effect dominates, although Compton scattering, Rayleigh scattering, and photonuclear absorption also contribute. Above $\sim$ 1 MeV the interaction cross section of pair production dominates over the others. The process of pair production involves the transformation of a photon into an electron-positron pair. In order to conserve momentum, this can only occur in the presence of a third body, usually a nucleus. Moreover, to create the pair, the photon must have at least an energy of $\sim$ 1 MeV. Theoretically, pair production is related to bremsstrahlung by a simple substitution rule, so that once the calculations for one process are made, results for the other immediately follow. It can be shown that a photon beam of initial intensity I_0 traversing a block of material reduce its intensity as:

$$I = I_0 e^{-\frac{7}{9}\frac{x}{X_0}} \tag{A.6}$$

The photons intensity thus decrease of a factor $1/e$ after a distance $x = 9/7\ X_0$. In this way a simple relation between the radiation length and the photons absorption coefficient is found. The pair production from high energy photons is the dominant reaction that combined with the bremsstrahlung emission by high energy electrons, contributes to the formation of electron-photon showers.

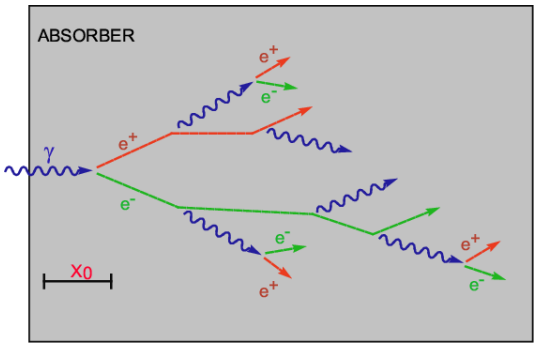

Figure A.3: Graphical representation of the analytic model introduced to parametrize the electromagnetic shower induced by electrons and photons.

A.2 ELECTROMAGNETIC SHOWERS

When a high-energy electron or photon is incident on a thick absorber, it initiates an electromagnetic cascade as pair production and bremsstrahlung generate more electrons and photons with lower energy. A simple analytic model which only gives a rough qualitative picture of the shower development can be describe using the notion of radiation length. Suppose an energetic photon (electron) of energy E_0 traverses matter. On average, the photon will convert into an electron positron pair after one radiation length. Similarly the electron will emit one photons via Bremsstrahlung after one radiation length. This process triggers a multiplication of particles which double its number after each radiation length. Figure A.3 schematically represents the multiplication process. After t radiation lengths the number of particles is $N = 2^t$ and assuming that the shower stops abruptly at the critical energy E_c, the maximum penetration depth of the cascade, i.e. the depth at which the largest number of secondary particles is produced, is $t_{max} \cong \ln(E_0/E_c)$. This simple model, of course, only gives a rough qualitative picture of the shower. To make more precise calculation Monte Carlo simulations and experimental data are required. From experimental measurements the thickness containing 95% of the shower energy is parametrized by [Fabjan and Gianotti, 2003]:

$$t_{95\%} = t_{max} + 0.08 \cdot Z + 9.6 \quad \text{with} \quad t_{max} \cong \ln\frac{E_0}{E_c} + t_0 \tag{A.7}$$

where $t_0 = -0.5$ $(+0.5)$ for electrons (photons). Due to the logarithmic dependence of t_{max} on the initial energy, calorimeters with limited thickness can contain the maximum of high energy particle showers. In calorimeters with thickness 25 X_0, the shower longitudinal leakage beyond the end of the active detector is much less than 1% up to incident electron energies of 300 GeV. The PAMELA calorimeter is about

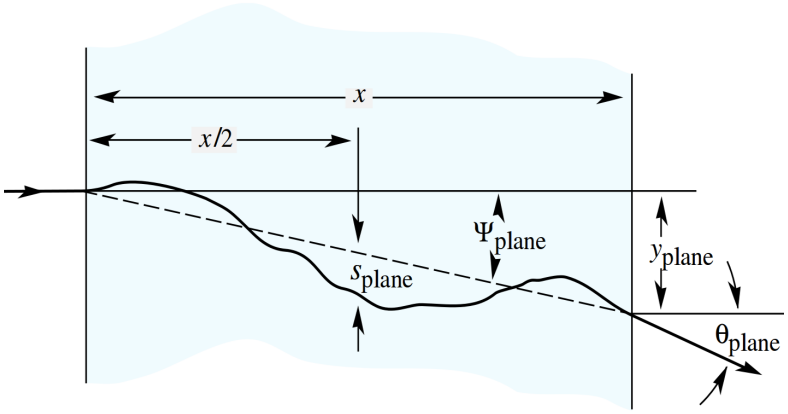

Figure A.4: Pictorial representation of multiple-scattering of a charged particles traversing a material with thickness x. Pictures adapted from [PDG, a].

$16X_0$ and is not able to fully contain the electromagnetic shower produced by electrons above few tens of GeV. However the main goal of the PAMELA calorimeter is not the energy determination but to reconstruct the topological development of the particle shower. For example in order to reject hadrons from leptons it is important to reconstruct the lateral and longitudinal profile of the particle cascade at least up to the shower maximum, which, as can be seen from Figure A.5, is contained within 16 X_0 up to 1 TeV.

An useful parameter is the lateral dispersion of the shower which is mainly due to multiple scattering of electrons and positrons away from the shower axis. Bremsstrahlung photons emitted by these electrons and positrons can also contribute to the shower spread but with smaller contribution[3]. Charged particles passing through matter suffer repeated elastic Coulomb scatterings from nuclei as illustrated in Figure A.4. These Coulomb scattering is well represented by the theory of Molière [Bethe, 1953]. The problem can be treated statistically to obtain the probability distribution for the net angle of deflection as a function of the thickness. Usually a Gaussian well approximates the scattering angle probability distribution. It can be shown that the mean squared scattering angle for relativistic electrons of energy E_e traversing a thickness of material x is:

$$\sqrt{<\theta^2>} = \frac{21.2\ \text{MeV}}{E_e}\sqrt{\frac{x}{X_0}} \tag{A.8}$$

3 The mean squared scattering angle $<\theta^2>$ for Bremsstrahlung and pair production corresponds to $\simeq 1/\gamma$ thus very small also for electron at the critical energy E_c

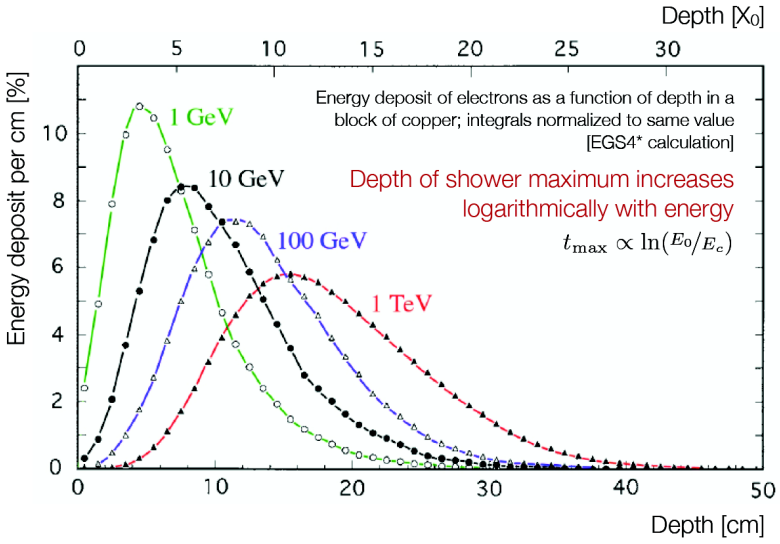

Figure A.5: An EGS4 simulation for the lateral profile of an electron-induced cascade in copper. Picture adapted from http://www.kip.uni-heidelberg.de/~coulon/Lectures/Detectors/Free_PDFs/Lecture9.pdf.

This quantity can be related with the transverse development of electromagnetic showers which scales fairly accurately with the Molière radius R_M, given by [Nelson et al., 1966]:

$$R_M\ (g/cm^2) = \frac{21\ MeV}{E_c} X_0 \tag{A.9}$$

On average, about 90% of the shower energy is contained in a cylinder with R_M around the shower axis. The fraction increases to 99% of the shower energy if a cylinder of 3.5 R_M is considered. The value of R_M for tungsten is reported in Table A.1. Since for most calorimeters R_M is of the order of a few centimeters, electromagnetic showers are quite narrow. In addition, the transversal size of the electromagnetic shower is roughly energy independent. The cells of a segmented calorimeter must be smaller than one R_M if the calorimeter is to be used for precision measurements of the shower topology. Table A.2 shows that for the PAMELA calorimeter, one R_M corresponds to the extension of about four silicon strips and thus the lateral extension of the electromagnetic shower can be resolved and studied with great resolution.

The mean longitudinal profile is more complex to parametrize and can be described reasonably well by the model proposed by Longo and Sestili [1975]:

$$\frac{dE}{dt} = E_0\ b \frac{(bt)^{a-1} e^{-bt}}{\Gamma(a)} \tag{A.10}$$

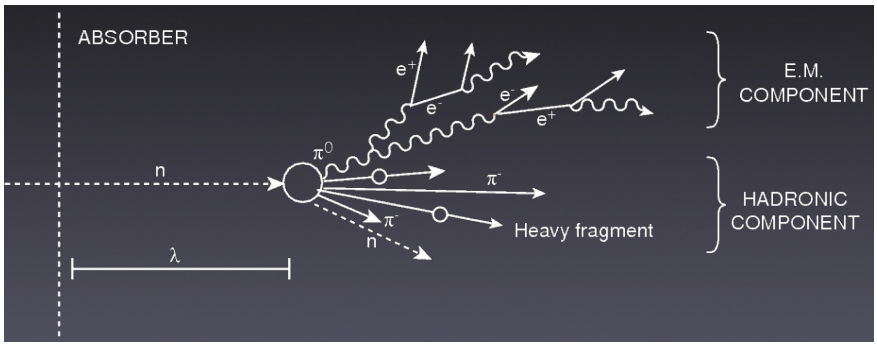

Figure A.6: Graphical representation of a hadronic shower inside matter. The electromagnetic component resulting from the decay of neutral pions is also shown.

where $t = x/X_0$ is the depth inside the material in radiation lengths and a and b are parameters dependent on the material. Figure A.5 shows an EGS4[4] simulation for electron-induced cascade in copper. The histogram shows fractional energy deposition per radiation length. As can be noticed, since the energy deposition is proportional to the number of particles in the cascade, the number of secondaries in an electron-photon shower rises exponentially to a relatively broad maximum after which it declines gradually over many radiation lengths, rather than stopping abruptly as in the simple model above.

All the quantities presented in this section allow the main features of an electromagnetic cascade inside matter to be parametrized. In a highly segmented device as the PAMELA calorimeter the knowledge of these quantities can be used to define variables related to the topological development and the energy released pattern as the quantities introduced in Section 3.3. Combining several variables the electromagnetic showers can be fully characterized and separated from the hadronic cascade with a great rejection power. The complexity of the nuclear processes produces a multitude of effects which make the hadronic shower much more complicated to parametrize.

A.3 HADRONIC SHOWERS

This section intends to give a brief overview of the main features of the hadronic shower development inside matter, emphasizing the main differences with respect to the electromagnetic cascade.

The hadronic showering process is dominated by a succession of inelastic hadronic interactions. At high energy, these are characterized

4 Electron gamma shower, is a Monte Carlo code implemented for the simulation of electromagnetic shower in material [Nelson et al., 1985]

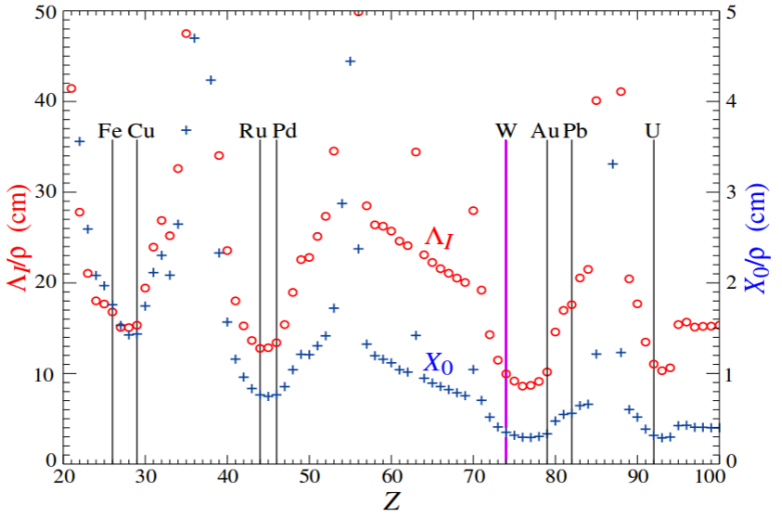

Figure A.7: Nuclear interaction length λ_I/ρ (circles) and radiation length X_0/ρ in cm for the chemical elements with $Z > 20$. The tungsten is indicated by the magenta line. Pictures adapted from [PDG, b].

by multi-particle production and particle emission originating from nuclear decay of excited nuclei. Most of the secondary particles are pions and because of the charge independence of hadronic interactions, on average one third will be neutral pions which decay into two photons, $\pi_0 \rightarrow \gamma\gamma$, before having a chance to re-interact hadronically. Thus in a hadron shower, on average one third of the energy is converted, via π_0 decay, into electromagnetic showers as shown in Figure A.6. However, a consistent part of the primary energy is consumed in nuclear processes such as excitation, nucleon evaporation, spallation, fission and neutrino emission, resulting in particles with characteristic nuclear energies at the MeV scale. Since a significantly fraction of the initial energy cannot be measured, the hadron energy resolution in a calorimeter is worse than the electrons and photons.

Overall, the nuclear processes which govern the hadronic shower development are complex and a simple calculation is not possible. Monte Carlo based simulations yield empirical relations for the longitudinal and transverse shower development. In analogy to the radiation length introduced for the electromagnetic shower, the basic quantity for the hadronic shower is the nuclear interaction length which can be parametrized as:

$$\lambda_I = 35\ A^{\frac{1}{3}}\ \frac{g}{cm^2} \tag{A.11}$$

This quantity describes the mean free path between secondary production and scales as 1/3 power of the atomic mass of the absorbing material. The value of λ_I for tungsten is reported in Table A.1. The interaction probability for hadrons traversing a material can be expressed

as in Equation A.4 where the absorption coefficient is replaced with λ_I. For example the total width of the PAMELA calorimeter is about 0.6 λ_I meaning that about $(1 - e^{-0.6}) \cdot 100 = 45\%$ of the incident protons will interact in the calorimeter. Figure A.5 shows the comparison between the radiation and the interaction length for material with $Z > 20$. It can be noticed that the interaction length is significantly larger than the radiation length for the same material. Thus deeper devices are needed to contain the hadronic showers. The maximum of the hadronic shower take place approximatively at:

$$t_{max}(\lambda_I) = 0.2 \cdot \ln E(\text{GeV}) + 0.7 \tag{A.12}$$

Hadronic showers are much broader then electromagnetic ones due to secondary products which can be produced with large angle with respect to the shower axis. The lateral extent at shower maximum is well represented by λ_I. About 95% of the shower is contained in a cylinder of one λ_I around the shower axis and as for the Molière radius is energy-independent. Comparing the values reported in Table A.1 the average lateral extent of a hadronic shower in tungsten is about ten time broader than the electromagnetic shower. Section 3.3 introduced many calorimeter variables based on the topological development of the electromagnetic and hadronic shower. These variables intend to emphasize the different features of the hadronic and electromagnetic shower. Combining several selections based on these quantities a high rejection power for hadronic cascade was obtained ($\sim 10^4$).

BIBLIOGRAPHY

Lipari, P. The fluxes of sub-cutoff particles detected by AMS, the cosmic ray albedo and atmospheric neutrinos. *Astroparticle Physics*, 16(3):295 – 323, 2002. http://www.sciencedirect.com/science/article/pii/S0927650501001347. (Cited at page 138.)

Teufel, A. and Schlickeiser, R. Analytic calculation of the parallel mean free path of heliospheric cosmic rays. *Astronomy and Astrophysics*, 397(1):15–25, 2003. http://dx.doi.org/10.1051/0004-6361:20021471. (Cited at pages 26 e 154.)

Accardo, L. et al. High statistics measurement of the positron fraction in primary cosmic rays of 0.5-500 GeV with the Alpha Magnetic Spectrometer on the International Space Station. *Phys. Rev. Lett.*, 113:121101, 2014. http://link.aps.org/doi/10.1103/PhysRevLett.113.121101. (Cited at page 6.)

Ackermann, M. et al. Measurement of separate cosmic-ray electron and positron spectra with the fermi large area telescope. *Phys. Rev. Lett.*, 108:011103, 2012. http://link.aps.org/doi/10.1103/PhysRevLett.108.011103. (Cited at page 6.)

Ackermann, M. et al. Detection of the Characteristic Pion-Decay Signature in Supernova Remnants. *Science*, 339(6121):807–811, 2013. http://www.sciencemag.org/content/339/6121/807.abstract. (Cited at pages 8 e 9.)

Adriani, O. et al. An anomalous positron abundance in cosmic rays with energies 1.5 - 100 GeV. *Nature*, 458:607–609, 2009a. http://www.nature.com/nature/journal/v458/n7238/full/nature07942.html. (Cited at pages 6 e 34.)

Adriani, O. et al. Measurements of quasi-trapped electron and positron fluxes with PAMELA. *Journal of Geophysical Research (Space Physics)*, 114(A13):12218, 2009b. http://onlinelibrary.wiley.com/doi/10.1029/2009JA014660/full. (Cited at page 58.)

Adriani, O. et al. PAMELA results on the cosmic-ray antiproton flux from 60 MeV to 180 GeV in kinetic energy. *Phys. Rev. Lett.*, 105:121101, 2010. http://journals.aps.org/prl/abstract/10.1103/PhysRevLett.105.121101. (Cited at page 3.)

Adriani, O. et al. The cosmic-ray electron flux measured by the PAMELA experiment between 1 and 625 GeV. *Phys. Rev. Lett.*, 106:201101, 2011a. http://journals.aps.org/prl/abstract/10.1103/PhysRevLett.106.201101. (Cited at pages 3, 75, 135, 144 e 145.)

Adriani, O. et al. Observations of the 2006 December 13 and 14 Solar Particle Events in the 80 MeV/n – 3 GeV/ n Range from Space with the PAMELA Detector. *The Astrophysical Journal*, 742(2):102, 2011b. http://stacks.iop.org/0004-637X/742/i=2/a=102. (Cited at page 87.)

Adriani, O. et al. PAMELA Measurements of Cosmic-Ray Proton and Helium Spectra. *Science*, 332(6025):69–72, 2011c. http://www.sciencemag.org/content/332/6025/69.abstract. (Cited at pages 3 e 92.)

Adriani, O. et al. The cosmic-ray positron energy spectrum measured by PAMELA. *Phys. Rev. Lett.*, 111:081102, 2013a. http://link.aps.org/doi/10.1103/PhysRevLett.111.081102. (Cited at pages 3, 157, 158 e 162.)

Adriani, O. et al. Time dependence of the proton flux measured by pamela during the july 2006 - december 2009 solar minimum. *The Astrophysical Journal*, 765(2):91, 2013b. http://stacks.iop.org/0004-637X/765/i=2/a=91. (Cited at pages 36, 131 e 133.)

Adriani, O. et al. Measurement of boron and carbon fluxes in cosmic rays with the pamela experiment. *The Astrophysical Journal*, 791:93, 2014a. http://stacks.iop.org/0004-637X/791/i=2/a=93. (Cited at page 162.)

Adriani, O. et al. The PAMELA Mission: Heralding a new era in precision cosmic ray physics. *Physics Reports*, 544(4):323 – 370, 2014b. http://www.sciencedirect.com/science/article/pii/S0370157314002087. (Cited at pages 39 e 162.)

Adriani, O. et al. New upper limit on strange quark matter abundance in cosmic rays with the pamela space experiment. *Phys. Rev. Lett.*, 115:111101, 2015a. http://link.aps.org/doi/10.1103/PhysRevLett.115.111101. (Cited at page 161.)

Adriani, O. et al. Pamela's measurements of magnetospheric effects on high energy solar particles. *The Astrophysical Journal Letters*, 801:L3, 2015b. http://stacks.iop.org/2041-8205/801/i=1/a=L3. (Cited at page 161.)

Adriani, O. et al. Reentrant albedo proton fluxes measured by the pamela experiment. *Journal of Geophysical Research: Space Physics*, 120:3728–3738, 2015c. http://dx.doi.org/10.1002/2015JA021019. (Cited at page 161.)

Adriani, O. et al. Search for Anisotropies in Cosmic-ray Positrons Detected by the Pamela Experiment. *Astrophys.J.*, 811:21, 2015d. http://stacks.iop.org/0004-637X/811/i=1/a=21. (Cited at page 161.)

Adriani, O. et al. Time Dependence of the e^- Flux Measured by PAMELA during the July 2006-December 2009 Solar Minimum. *The Astrophysical Journal*, 810:142, 2015e. http://stacks.iop.org/0004-637X/810/i=2/a=142. (Cited at pages 141 e 161.)

Adriani, O. et al. Trapped proton fluxes at low earth orbits measured by the pamela experiment. *The Astrophysical Journal Letters*, 799:L4, 2015f. http://stacks.iop.org/2041-8205/799/i=1/a=L4. (Cited at page 162.)

Aguilar, M. et al. Electron and positron fluxes in primary cosmic rays measured with the alpha magnetic spectrometer on the international space station. *Phys. Rev. Lett.*, 113:121102, 2014. http://link.aps.org/doi/10.1103/PhysRevLett.113.121102. (Cited at page 145.)

Alcaraz, J. et al. Leptons in near earth orbit. *Phys. Lett. B*, 484:10, 2000. https://ams.cern.ch/AMS/Publications/AMS-03_PLB484_10.pdf. (Cited at pages 3, 6 e 34.)

Anand, K. C., Daniel, R. R., and Stephens, S. A. Cosmic-ray electron spectrum above 50 BeV and its implications for cosmic-ray confinement. *Phys. Rev. Lett.*, 20:764–768, 1968. http://link.aps.org/doi/10.1103/PhysRevLett.20.764. (Cited at page 2.)

Baade, W. and Zwicky, F. Cosmic rays from super-novae. *Proc. Nat. Acad. of Sciences of United States of America*, 20:259, 1934. http://www.pnas.org/content/20/5/259.full.pdf. (Cited at page 3.)

Barwick, S. W. et al. Measurements of the Cosmic-Ray Positron Fraction from 1 to 50 GeV. *The Astrophysical Journal Letters*, 482(2):L191, 1997. http://stacks.iop.org/1538-4357/482/i=2/a=L191. (Cited at pages 3 e 34.)

Berezinskii, V. S., Bulanov, S. V., Dogiel, V. A., and Ptuskin, V. S. *Astrophysics of cosmic rays*. 1990. http://adsabs.harvard.edu/abs/1990acr..book.....B. (Cited at page 10.)

Bethe, H. A. Molière theory of multiple scattering. *Phys. Rev.*, 89:1256–1266, 1953. http://link.aps.org/doi/10.1103/PhysRev.89.1256. (Cited at page 169.)

Blasi, P. The origin of galactic cosmic rays. *The Astronomy and Astrophysics Review*, 21(1), 2013. http://dx.doi.org/10.1007/s00159-013-0070-7. (Cited at page 9.)

Boezio, M. et al. The Cosmic-Ray Electron and Positron Spectra Measured at 1 AU during Solar Minimum Activity. *Astrophys. J.*, 532:653, 2000. http://iopscience.iop.org/article/10.1086/308545/fulltext/. (Cited at pages 3, 6 e 34.)

Boezio, M. et al. The pamela experiment and antimatter in the universe. 228:101–109, 2014. http://dx.doi.org/10.1007/s10751-014-1049-0. (Cited at page 162.)

Bongi, M. *Data analysis of cosmic rays at ground level with the PAMELA experiment*. Ph.D. thesis, Università degli studi di Firenze, 2005. http://hep.fi.infn.it/PAMELA/tesi/pdf/phd_bongi.pdf. (Cited at page 46.)

Bruno, A. *Cosmic ray antiprotons measured in the PAMELA experiment*. Ph.D. thesis, Università degli studi di Bari, 2008. (Cited at page 60.)

Bruno, A. Estimate of the pion contamination in the pamela antiproton measurements. *Proocedings of the 31st ICRC, Lodz*, 2009. http://pamela.roma2.infn.it/index.php?option=com_docman&task=doc_view&gid=464. (Cited at page 58.)

Bruno, A. et al. Back-tracing and flux reconstruction for solar events with PAMELA. *arXiv:1412.1765 [astro-ph.IM].*, 2014. http://arxiv.org/abs/1412.1765. (Cited at page 162.)

Buchmüller, W. et al. Gravitino dark matter in r-parity breaking vacua. *Journal of High Energy Physics*, 2007:037, 2007. http://stacks.iop.org/1126-6708/2007/i=03/a=037. (Cited at page 7.)

Charbonneau, P. Solar dynamo theory. *Annual Review of Astronomy and Astrophysics*, 52:251–290, 2014. http://www.annualreviews.org/doi/abs/10.1146/annurev-astro-081913-040012. (Cited at page 14.)

Chardonnet, P., Orloff, J., and Salati, P. The production of anti-matter in our galaxy. *Physics Letters B*, 409:313 – 320, 1997. http://www.sciencedirect.com/science/article/pii/S0370269397008708. (Cited at page 54.)

Cheng, H., Feng, J. L., and Matchev, K. T. Kaluza-klein dark matter. *Phys. Rev. Lett.*, 89:211301, 2002. http://link.aps.org/doi/10.1103/PhysRevLett.89.211301. (Cited at page 7.)

Cirelli, M., Kadastik, M., Raidal, M., and Strumia, A. Model-independent implications of the , cosmic ray spectra on properties of Dark Matter. *Nuclear Physics B*, 813:1 – 21, 2009. http://www.sciencedirect.com/science/article/pii/S0550321308006627. (Cited at page 7.)

Clem, J. and Evenson, P. Positron abundance in galactic cosmic rays. *The Astrophysical Journal*, 568(1):216, 2002. http://stacks.iop.org/0004-637X/568/i=1/a=216. (Cited at page 34.)

Clem, J. and Evenson, P. Observations of cosmic ray electrons and positrons during the early stages of the a- magnetic polarity epoch. *Journal of Geophysical Research*, 109, 2004. http://dx.doi.org/10.1029/2003JA010361. (Cited at page 34.)

Clem, J. and Evenson, P. Balloon-borne observations of the galactic positron fraction during solar minimum negative polarity. *Journal of Geophysical Research*, 114, 2009. http://dx.doi.org/10.1029/2009JA014225. (Cited at pages 32, 33 e 34.)

Clem, J. M., Clements, D. P., Esposito, J., Evenson, P., Huber, D., L'Heureux, J., Meyer, P., and Constantin, C. Solar Modulation of Cosmic Electrons. *Astrophysical Journal*, 464:507, 1996. http://adsabs.harvard.edu/abs/1996ApJ...464..507C. (Cited at pages 33, 34, 35 e 38.)

Clem, J. M. et al. Charge sign dependence of cosmic ray modulation near a rigidity of 1 GV. *Journal of Geophysical Research*, 105, 2000. http://dx.doi.org/10.1029/2000JA000097. (Cited at page 34.)

D'Agostini, G. Improve iterative bayesian unfolding. *arXiv:1010.0632v1 [physics.data-an]*, 2010. http://arxiv.org/abs/1010.0632. (Cited at page 112.)

D'Agostini, G. and Raso, M. Uncertainties due to imperfect knowledge of systematic effects: general considerations and approximate formulae. *arXiv:hep-ex/0002056*, 2000. http://arxiv.org/abs/hep-ex/0002056. (Cited at page 137.)

Daniel, R. and Stephen, S. Electron component of the primary cosmic radiation at energies 15 GeV. *Phys. Rev. Lett.*, 15:769–772, 1965. http://adsabs.harvard.edu/abs/1965PhRvL..15..769D. (Cited at page 2.)

Daugherty, J., Hartman, R., and Schmidt, P. A measurement of cosmic-ray positron and negatron spectra between 50 and 800 MV. *The Astrophysical Journal*, 198:493–505, 1975. http://adsabs.harvard.edu/abs/1975ApJ...198..493D. (Cited at page 34.)

De Shong, J. A., Hildebrand, R., and Meyer, P. Ratio of electrons to positrons in the primary cosmic radiation. *Phys. Rev. Lett.*, 12:3 – 6, 1964. http://link.aps.org/doi/10.1103/PhysRevLett.12.3. (Cited at pages 2 e 32.)

De Simone, N. *Messa in orbita dell'apparato PAMELA e prime misure di raggi cosmici.* Master's thesis, Università degli studi di Roma "Tor Vergata, 2007. (Cited at page 123.)

Delahaye, T., Cerdeno, D. G., and Lavalle, J. Cosmic-ray antiproton constraints on light singlino-like dark matter candidates. *Nucl. Phys. B*, 854(3):738 – 779, 2012. http://www.sciencedirect.com/science/article/pii/S0550321311005426. (Cited at page 53.)

Delahaye, T., Lavalle, J., Lineros, R., Donato, F., and Fornengo, N. Galactic electrons and positrons at the Earth: new estimate of the primary and secondary fluxes. *Astronomy and Astrophysics*, 524:A51, 2010. http://dx.doi.org/10.1051/0004-6361/201014225. (Cited at pages 4, 5, 11 e 13.)

Earl, J. A. Cloud-chamber observations of primary cosmic-ray electrons. *Phys. Rev. Lett.*, 6:125–128, 1961. http://link.aps.org/doi/10.1103/PhysRevLett.6.125. (Cited at pages 2 e 4.)

Erdélyi, R. and Ballai, I. Heating of the solar and stellar coronae: a review. *Astronomical Notes*, 2007. http://onlinelibrary.wiley.com/doi/10.1002/asna.200710803/abstract;jsessionid=27A4C757C7D0E4685C74C9F797AB8E50.f02t04. (Cited at page 14.)

ESA. Solar wind speeds measured by Ulysses. 2008. http://www.esa.int/spaceinimages/Images/2008/06/Solar_wind_speeds_measured_by_Ulysses.

Etienne, E. V. *Cosmic ray modulation processes in the heliosphere*. Ph.D. thesis, Potchefstroom Campus of the North-West University, 2011. (Cited at pages 16, 17, 18, 25, 30 e 36.)

Evenson, P. and Clem, j. Cosmic ray electron spectrum in 2009. *Prooceedings of the 32st ICRC, Beijing*, 2011. http://www.ihep.ac.cn/english/conference/icrc2011/paper/proc/vb/vb_0596.pdf. (Cited at pages 143 e 144.)

EXPLORER. 1963. http://history.nasa.gov/explorer.html. (Cited at page 24.)

Fabjan, C. W. and Gianotti, F. Calorimetry for particle physics. *Rev. Mod. Phys.*, 75:1243–1286, 2003. http://link.aps.org/doi/10.1103/RevModPhys.75.1243. (Cited at page 168.)

Fang, K., Kotera, K., and Olinto, A. V. Ultrahigh energy cosmic ray nuclei from extragalactic pulsars and the effect of their galactic counterparts. *Journal of Cosmology and Astroparticle Physics*, 2013(03):010, 2013. http://stacks.iop.org/1475-7516/2013/i=03/a=010. (Cited at page 9.)

Fanselow, J. L., Hartman, R. C., Hildebrad, R. H., and Meyer, P. Charge Composition and Energy Spectrum of Primary Cosmic-Ray Electrons. *The Astrophysical Journal*, 158:771, 1969. http://adsabs.harvard.edu/abs/1969ApJ...158..771F. (Cited at page 34.)

Fermi, E. On the origin of the cosmic radiation. *Phys. Rev.*, 75:1169–1174, 1949. http://link.aps.org/doi/10.1103/PhysRev.75.1169. (Cited at page 7.)

Ferreira, S. E. S. and Potgieter, M. S. Long-term cosmic-ray modulation in the heliosphere. *Astrophysical Journal*, 603:744–752, 2004. http://iopscience.iop.org/0004-637X/603/2/744. (Cited at page 30.)

Fichtner, H., Potgieter, M., Ferreira, S., and Burger, A. On the propagation of Jovian electrons in the heliosphere: Transport modelling in 4-D phase space. *Geophysical Research Letters*, 27(11):1611–1614, 2000. http://dx.doi.org/10.1029/2000GL003765. (Cited at page 24.)

Formato, V. et al. Measurement of hydrogen and helium isotopes flux in galactic cosmic rays with the {PAMELA} experiment. *Nuclear Instruments and Methods in Physics Research Section A: Accelerators, Spectrometers, Detectors and Associated Equipment*, 742:273 – 275, 2014. http://www.sciencedirect.com/science/article/pii/S0168900213015040. (Cited at page 162.)

Formato, V. et al. Solar modulation of galactic protons and helium with the PAMELA experiment. In *Astroparticle, Particle, Space Physics and Detectors for Physics Applications - Proceedings of the 14th ICATPP Conference*, pages 182–188. 2014. http://adsabs.harvard.edu/abs/2014apsp.conf..182F. (Cited at page 162.)

GALPROP. 2011. http://galprop.stanford.edu/code.php?option=manual. (Cited at page 13.)

GEANT4. Geant4: a toolkit for the simulation of the passage of particles through matter. 2015. https://geant4.web.cern.ch/geant4. (Cited at page 58.)

Giacalone, J. and Jokipii, J. R. The Transport of Cosmic Rays across a Turbulent Magnetic Field. *The Astrophysical Journal*, 520:204–214, 1999. http://iopscience.iop.org/0004-637X/520/1/204/fulltext/. (Cited at page 25.)

Giesen, G., Boudaud, M., Génolini, Y., Poulin, V., Cirelli, M., Salati, P., and Serpico, P. D. AMS-02 antiprotons, at last! Secondary astrophysical component and immediate implications for Dark Matter. *Journal of Cosmology and Astroparticle Physics*, 2015(09):023, 2015. http://stacks.iop.org/1475-7516/2015/i=09/a=023. (Cited at pages 37 e 38.)

Ginzburg, V. *Prog. Element. Cosmic Ray Phys.*, 4, 1958. (Cited at page 2.)

Ginzburg, V. L. and Syrovatskii, S. I. The Origin of Cosmic Rays. 1964. http://adsabs.harvard.edu/abs/1964ocr..book.....G. (Cited at page 3.)

Giuliani, A. et al. Neutral Pion Emission from Accelerated Protons in the Supernova Remnant W44. *The Astrophysical Journal Letters*, 742(2), 2011. http://stacks.iop.org/2041-8205/742/i=2/a=L30. (Cited at page 9.)

Golden, R. L. et al. Observation of cosmic ray positrons in the region from 5 to 50 GeV. *Astronomy and Astrophysics*, 188:145–154, 1987. (Cited at page 34.)

Golden, R. L. et al. Measurement of the Positron to Electron Ration in the Cosmic Rays above 5 GeV. *Astrophys. J.*, 457:L103, 1996. http://people.roma2.infn.it/~morselli/A29apj_TS93_e.pdf. (Cited at page 3.)

Hale, G. E. and Nicholson, S. The law of sun-spot polarity. *Astrophysical Journal*, 62, 1925. (Cited at page 15.)

Hartman, R. C. and Pellerin, C. J. Cosmic-ray positron and negatron spectra between 20 and 800 MeV measured in 1974. *The Astrophysical Journal*, 204:927–933, 1976. http://adsabs.harvard.edu/abs/1976ApJ...204..927H. (Cited at page 34.)

Heber, B., Clem, J., Muller-Mellin, R., Kunow, H., Ferreira, S., and Potgieter, M. Evolution of the galactic cosmic ray electron to proton ratio: Ulysses COSPIN/KET observations. *Geophysical Research Letters*, 30, 2003. http://onlinelibrary.wiley.com/doi/10.1029/2003GL017356/pdf. (Cited at page 35.)

Heber, B. and Potgieter, M. Cosmic rays at high heliolatitudes. *Space Science Reviews*, 127(1-4):117–194, 2006. http://dx.doi.org/10.1007/s11214-006-9085-y. (Cited at page 29.)

Hillas, A. M. Cosmic rays: Recent progress and some current questions. *arXiv:astro-ph/0607109*, 2006. http://arxiv.org/abs/astro-ph/0607109. (Cited at page 9.)

IGRF. The international association of geomagnetism and aeronomy. 2014. http://www.ngdc.noaa.gov/IAGA/vmod/igrf.html. (Cited at page 55.)

Jokipii, J. R. Cosmic-Ray Propagation. I. Charged Particles in a Random Magnetic Field. *Astrophysical Journal*, 146:480, 1966. http://adsabs.harvard.edu/full/1966ApJ...146..480J. (Cited at page 25.)

Jokipii, J. R. and Kóta, J. The polar heliospheric magnetic field. *Geophysical Research Letters*, 16(1):1–4, 1989. http://dx.doi.org/10.1029/GL016i001p00001. (Cited at page 20.)

Kamae, T., Karlsson, N., Mizuno, T., Abe, T., and Koi, T. Parameterization of γ, $e^{+/-}$, and Neutrino Spectra Produced by p-p Interaction in Astronomical Environments. *Astrophysical Journal*, 647:692–708, 2006. http://adsabs.harvard.edu/abs/2006ApJ...647..692K. (Cited at page 5.)

Kamionkowski, M., Jungman, G., and Griest, K. Supersymmetric dark matter. *Physics Reports*, 267(5-6):195–373, 1996. http://www.sciencedirect.com/science/article/pii/0370157395000585. (Cited at page 7.)

Karelin, A. et al. Detection of a change in the north-south ratio of count rates of particles of high-energy cosmic rays during a change in the polarity of the magnetic field of the sun. *JETP Letters*, 101:228–231, 2015a. http://dx.doi.org/10.1134/S0021364015040086. (Cited at page 161.)

Karelin, A. et al. Measurement of the large-scale anisotropy of cosmic rays in the pamela experiment. *JETP Letters*, 101:295–298, 2015b. http://dx.doi.org/10.1134/S0021364015050136. (Cited at page 161.)

Kobayashi, T., Komori, Y., Yoshida, K., and Nishimura, J. The most likely sources of high energy cosmic-ray electrons in supernova remnants. *Astrophys. J.*, 601:340–351, 2004. http://iopscience.iop.org/article/10.1086/380431/pdf. (Cited at page 11.)

Koldobskiy, S. et al. Measuring the albedo deuteron flux in the pamela satellite experiment. *Bulletin of the Russian Academy of Sciences: Physics*, 79:294–297, 2015a. http://dx.doi.org/10.3103/S1062873815030326. (Cited at page 161.)

Koldobskiy, S. A. et al. Study of deuteron spectra under radiation belt with pamela instrument. *Journal of Physics: Conference Series*, 632:012060, 2015b. http://stacks.iop.org/1742-6596/632/i=1/a=012060. (Cited at page 161.)

Kóta, J. Theory and modeling of galactic cosmic rays: Trends and prospects. *Space Science Reviews*, 176(1-4):391–403, 2013. http://dx.doi.org/10.1007/s11214-012-9870-8. (Cited at pages 21, 23 e 150.)

Leo, W. R. *Techiques for Nuclear and Particle Physics Experiments: A How to approach*. 1994. (Cited at page 164.)

Longo, E. and Sestili, I. Monte Carlo calculation of photon-initiated electromagnetic showers in lead glass. *Nuclear Instruments and Methods*, 128(2):283 – 307, 1975. http://www.sciencedirect.com/science/article/pii/0029554X75906795. (Cited at page 170.)

LUNA1. Luna 1. 1959. http://nssdc.gsfc.nasa.gov/nmc/spacecraftDisplay.do?id=1959-012A. (Cited at page 16.)

Martucci, M. et al. Analysis on h spectral shape during the early 2012 {SEPs} with the {PAMELA} experiment. *Nuclear Instruments and Methods in Physics Research Section A: Accelerators, Spectrometers, Detectors and Associated Equipment*, 742:158 – 161, 2014. http://www.sciencedirect.com/science/article/pii/S0168900213016434. (Cited at page 162.)

Maurin, D. et al. Cosmic Rays below Z=30 in a diffusion model: new constraints on propagation parameters. *The Astrophysical Journal*, 555(2):585, 2001. http://stacks.iop.org/0004-637X/555/i=2/a=585. (Cited at page 5.)

Mikhailov, V. et al. Searching for anisotropy of positrons and electrons in the pamela experiment. *Bulletin of the Russian Academy of Sciences: Physics*, 79:298–301, 2015. http://dx.doi.org/10.3103/S1062873815030375. (Cited at page 161.)

Mocchiutti, E. et al. PAMELA: Mission Status and Future Analysis Development. In *Astroparticle, Particle, Space Physics and Detectors for Physics Applications - Proceedings of the 14th ICATPP Conference*, pages 78–84. 2014. http://adsabs.harvard.edu/abs/2014apsp.conf...78M. (Cited at page 162.)

Mori, N. et al. The {PAMELA} experiment and cosmic ray observations. *Nuclear and Particle Physics Proceedings*, 265–266:242 – 244, 2015a. http://www.sciencedirect.com/science/article/pii/S2405601415004046. (Cited at page 161.)

Mori, N. et al. Pamela measurements of the boron and carbon spectra. *Journal of Physics: Conference Series*, 632:012017, 2015b. http://stacks.iop.org/1742-6596/632/i=1/a=012017. (Cited at page 161.)

Moskalenko, I. V. and Strong, A. W. Production and propagation of cosmic-ray positrons and electrons. *The Astrophysical Journal*, 493(2):694, 1998. http://stacks.iop.org/0004-637X/493/i=2/a=694. (Cited at page 6.)

Munini, R. *Time dependence of the cosmic-ray electron and positron spectra measured by PAMELA experiment during the last solar minimum*. Ph.D. thesis, Università degli studi di Trieste, 2011. (Cited at pages 72 e 91.)

Munini, R. et al. Solar modulation of GCR electrons over the 23rd solar minimum with PAMELA. *Journal of Physics: Conference Series*, 632:012073, 2015. http://stacks.iop.org/1742-6596/632/i=1/a=012073. (Cited at page 161.)

NASA. Heliospheric Magnetic Field. 2015. http://interstellar.jpl.nasa.gov/interstellar/probe/interaction/interaction.html. (Cited at page 20.)

Nelson, W., Hirayama, H., and Rogers, D. The EGS4 Code System. *SLAC*-265, 1985. http://www.slac.stanford.edu/cgi-wrap/getdoc/slac-r-265.pdf. (Cited at page 171.)

Nelson, W. R., Jenkins, T. M., McCall, R. C., and Cobb, J. K. Electron-induced cascade showers in copper and lead at 1 gev. *Phys. Rev.*, 149:201–208, 1966. http://link.aps.org/doi/10.1103/PhysRev.149.201. (Cited at page 170.)

Ness, N. et al. Initial results of the Imp 1 Magnetic Field Experiment. *Journal of Geophysical Research*, 69(17):3531–3569, 1964. (Cited at page 24.)

Osteria, G., Barbarino, G., Boscherini, M., Campana, D., Di Meo, P., Di Pietro, M., Menn, W., Orazi, M., Rocco, R., Simon, M., and Weber, E. The ToF and Trigger electronics of the PAMELA experiment. *Nuclear Instruments and Methods in Physics Research A*, 518:161–163, 2004. http://adsabs.harvard.edu/abs/2004NIMPA.518..161O. (Cited at page 48.)

Osteria, G., Campana, D., Barbarino, G., Boscherini, M., Menn, W., Mitchell, J., Rossi, G., Russo, S., Simon, M., and Streitmatter, R. The time-of-flight system of the pamela experiment on satellite. *Nuclear Instruments and Methods in Physics Research Section A: Accelerators, Spectrometers, Detectors and Associated Equipment*, 535(1-2):152 – 157, 2004. http://www.sciencedirect.com/science/article/pii/S016890020401592X. (Cited at page 47.)

Panico, B. et al. A method to detect positron anisotropies with Pamela data. *Nuclear Physics B - Proceedings Supplements*, 256–257:173 – 178, 2014. http://www.sciencedirect.com/science/article/pii/S092056321400214X. (Cited at page 161.)

Panov, A. D. Electrons and positrons in cosmic rays. *Journal of Physics: Conference Series*, 409(1):012004, 2013. http://stacks.iop.org/1742-6596/409/i=1/a=012004. (Cited at pages 10 e 12.)

Parker, E. N. Cosmic-ray modulation by solar wind. *Physical Review Letters*, 1958. http://journals.aps.org/pr/abstract/10.1103/PhysRev.110.1445. (Cited at pages 16 e 20.)

Parker, E. N. The scattering of charged particles by magnetic irregularities. *Journal of Geophysical Research*, 69(9):1755–1758, 1964. http://dx.doi.org/10.1029/JZ069i009p01755. (Cited at page 24.)

Parker, E. N. The passage of energetic charged particles through interplanetary space. *Planetary and Space Science*, 30:9–49, 1965. (Cited at page 22.)

PDG. Particle data group. 2015a. http://pdg.lbl.gov/2015/reviews/rpp2014-rev-passage-particles-matter.pdf. (Cited at pages 164, 165, 166 e 169.)

PDG. Particle data group. 2015b. http://pdg.lbl.gov/2015/reviews/rpp2014-rev-particle-detectors-accel.pdf. (Cited at page 172.)

Peaceman, D. W. and Rachford, H. H. The numerical solution of parabolic and elliptic differential equations. *Journal of the Society for Industrial and Applied Mathematics*, 3(1):28–41, 1955. http://www.jstor.org/stable/2098834. (Cited at page 30.)

Phillips, J. L. et al. Ulysses solar wind plasma observations from pole to pole. *Geophysical Research Letters*, 22:3301–3304, 1995. http://dx.doi.org/10.1029/95GL03094. (Cited at page 17.)

Picozza, P. and Marcelli, L. Electron cosmic ray measurements in space. *Astroparticle Physics*, 53:160 – 165, 2014. http://www.sciencedirect.com/science/article/pii/S0927650513000224. (Cited at page 3.)

Potgieter, M. and Nndanganeni, R. The solar modulation of electrons in the heliosphere. *Astrophysics and Space Science*, 345:33 – –40, 2013. http://dx.doi.org/10.1007/s10509-013-1365-x. (Cited at page 144.)

Potgieter, M., Vos, E., Nndanganeni, R., Boezio, M., and Munini, R. A very local interstellar spectrum for galactic electrons. *arXiv:1308.1666 [astro-ph.SR]*, 2013. http://arxiv.org/abs/1308.1666. (Cited at page 162.)

Potgieter, M. S. Solar modulation of cosmic rays. *Living Reviews in Solar Physics*, 10(3), 2013. http://www.livingreviews.org/lrsp-2013-3. (Cited at page 30.)

Potgieter, M. S., Vos, E. E., Munini, R., Boezio, M., and Di Felice, V. Modulation of Galactic Electrons in the Heliosphere during the Unusual Solar Minimum of 2006–2009: A Modeling Approach. *The Astrophysical Journal*, 810(2):141, 2015. http://stacks.iop.org/0004-637X/810/i=2/a=141. (Cited at pages 148 e 161.)

ROOT. 2015. https://root.cern.ch/. (Cited at page 118.)

Rossi, B. *High-Energy Particles*. New York: Prentice-Hall, 1952. (Cited at page 166.)

Rothschild, R. E. et al. Evidence of X-Ray Synchrotron emission from electrons accelerated to 40 TeV in the Supernova Remnant Cassiopeia A. *The Astrophysical Journal*, 487, 1997. http://iopscience.iop.org/1538-4357/487/1/L97/pdf/1538-4357_487_1_L97.pdf. (Cited at page 4.)

Schlickeiser, R. *Cosmic ray astrophysics*. 2002. http://www.springer.com/in/book/9783540664659. (Cited at page 24.)

Serpico, P. D. Astrophysical models for the origin of the positron "excess". *Astroparticle Physics*, 39-40:2 – 11, 2012. http://www.sciencedirect.com/science/article/pii/S0927650511001654. (Cited at page 7.)

Sheeley, N. R. et al. Measurements of Flow Speeds in the Corona Between 2 and 30 R_{sun}. *The Astrophysical Journal*, 484:472, 1997. http://stacks.iop.org/0004-637X/484/i=1/a=472. (Cited at page 17.)

Smart, D. F. and Shea, M. A. A review of geomagnetic cutoff rigidities for earth-orbiting spacecraft. *Advances in Space Research*, 36:2012–2020, 2004. http://engineering.dartmouth.edu/~d76205x/research/Shielding/docs/Smart_06.pdf. (Cited at page 55.)

SMOOTHING. 1994. https://root.cern.ch/doc/master/classTH1.html#a0d08651c37b622f4bcc0e1a0affefb33. (Cited at page 118.)

Stone, E. C., Cummings, A. C., McDonald, F. B., Heikkila, B. C., Lal, N., and Webber, W. R. Voyager 1 observes low-energy galactic cosmic rays in a region depleted of heliospheric ions. *Science*, 341(6142):150–153, 2013. http://www.sciencemag.org/content/341/6142/150.abstract. (Cited at page 151.)

Straulino, S., Adriani, O., Bonechi, L., Bongi, M., Bottai, S., Castellini, G., Fedele, D., Grandi, M., Papini, P., Ricciarini, S., Spillantini, P., Taccetti, F., Taddei, E., and Vannuccini, E. Spatial resolution of double-sided silicon microstrip detectors for the PAMELA apparatus . *Nuclear Instruments and Methods in Physics Research Section A: Accelerators, Spectrometers, Detectors and Associated Equipment*, 556(1):100 – 114, 2006. http://www.sciencedirect.com/science/article/pii/S0168900205019315. (Cited at page 44.)

Tan, L. C. and Ng, L. K. Parametrisation of hadron inclusive cross sections in p-p collisions extended to very low energies. *Journal of Physics G: Nuclear Physics*, 9:1289, 1983. http://stacks.iop.org/0305-4616/9/i=10/a=015. (Cited at page 5.)

Uehling, E. *Ann. Rev. Nucl. Sci.*, 4:315, 1954. (Cited at page 164.)

Usoskin, I. et al. Force-field parameterization of the galactic cosmic ray spectrum: Validation for Forbush decreases. *Advances in Space Research*, 55:2940 – 2945, 2015. http://www.sciencedirect.com/science/article/pii/S0273117715001921. (Cited at page 161.)

Webber, W. R. et al. At Voyager 1 Starting on about August 25, 2012 at a Distance of 121.7 AU From the Sun, a Sudden Disappearance of Anomalous Cosmic Rays and an Unusually Large Sudden Increase of Galactic Cosmic Ray H and He Nuclei and Electron Occurred. *arXiv:1212.0883*, 2012. http://arxiv.org/abs/1212.0883. (Cited at page 18.)

Yoshida, K. High-energy cosmic-ray electrons in the Galaxy. *Advances in Space Research*, 42:477 – 485, 2008. http://pcams01.mib.infn.it/grandi/varie/work/bobik/ele_galaxy.pdf. (Cited at page 3.)

Zuccon, P. et al. Atmospheric production of energetic protons, electrons and positrons observed in near Earth orbit. *Astroparticle Physics*, 20(2):221 – 234, 2003. http://www.sciencedirect.com/science/article/pii/S0927650503001609. (Cited at page 138.)